UNIVERSITÀ DEGLI STUDI DI ROMA “LA SAPIENZA”
Dottorato di Ricerca in Fisica - XVI Ciclo

Measurement of the $b \to s\gamma$ Branching Ratio Studying the Recoil of Fully Reconstructed B s with the BABAR Experiment

Fabio Bellini

Direttore della Ricerca:
Prof. Fernando Ferroni
Dott. Riccardo Faccini

Coordinatore del
Dottorato di Ricerca:
Prof. Guido Martinelli

ANNO ACCADEMICO 2002/2003

Contents

Introduction

Weak decays of the B mesons are an ideal environment to measure the elements of the CKM quark-mixing matrix and test the Standard Model.

Rare processes, like the $b \to s\gamma$ radiative decay, are of great interest since they represent an ideal framework for the study of flavour physics and a laboratory for perturbative QCD. The $B \to X_s\gamma$ branching fraction and direct CP asymmetry are sensitive to contributions from new physics that could enter at one loop level. Moreover, the measurement of the $B \to X_s\gamma$ branching fraction allows the extraction of the CKM matrix element V_{ts}.

The shape of the photon spectrum is used to extract the theoretical parameters m_b and μ_π^2 in the framework of the Heavy Quark Effective Theory (HQET). These parameters are universal in B meson inclusive decay spectra with massless partons in the final state and they are needed for a better determination of the CKM matrix element V_{ub} in $B \to X_u\ell\nu$ decays.

Theoretically, inclusive radiative rates can be calculated reliably at the parton level. Non-perturbative effects play a subdominant role and they are under control thanks to the heavy mass expansion and the assumption of quark–hadron duality [8]. The theoretical error on the total inclusive $B \to X_s\gamma$ branching ratio is of the order of 10%.

The extraction of $BR(B \to X_s\gamma)$ is a challenge for experiments. The main problem is the separation of the signal from a huge background (1000 times bigger). Selection criteria, applied to achieve this separation, generally make the theoretical extrapolation to the full decay rate more difficult and introduce very large uncertainties and model dependence.

Several $BR(B \to X_s\gamma)$ measurements exist in scientific literature that exploit different techniques to isolate the signal decay from background. The analysis presented here is based on a novel technique consisting in the study of high energy photons recoiling to fully reconstructed B 's.

This reconstruction allows for the measurement of the B momentum and thus a transformation to the rest frame of the recoiling B meson; this information is beneficial for signal selection since the photon spectrum is not smeared from the unknown boost of the B mesons in the $\Upsilon(4S)$ frame like fully inclusive analysis. The reconstruction also results in a very clean sample of $B\overline{B}$ events and determines the flavor and the charge of the reconstructed B meson allowing to measure $BR(B \to X_s\gamma)$ and the direct CP asymmetry in B^0 and $B^\pm$ separately. Moreover the absolute luminosity of the sample and B reconstruction efficiencies are not needed since normalization is taken from the number of reconstructed B's. T

Since the reconstruction efficiency of one B in a fully hadronic decay is very low $\sim 0.4\%$, the B factories, thanks to their very high luminosity, represent the ideal environment for the study of the $B \to X_s\gamma$ decay with this technique.

A $B \to X_s\gamma$ decay of the recoil B meson is identified by the presence of an isolated high energy photon in the event. Detailed studies have been performed on the reconstruction and efficiency of high energetic photons and selection

criteria are applied in order to ensure well known efficiencies and minimal backgrounds. To reject the huge background coming mainly from $q\overline{q}$ events a multivariate analysis technique (Fisher) is used combining information for the event decay topology. The $B \to X_s\gamma$ signal yield is finally extracted from a fit to the photon energy E_γ distribution on events that fulfill the selection criteria.

Due to the lower level of background, the signal spectrum is measured down to $1.9\,\mathrm{GeV}$, a value never reached in previous measurements. This allows to reduce the theoretical uncertainties due to the extrapolation in the unmeasured part of the energy spectrum.

The direct CP asymmetry is extracted with the same technique and event selection in B^0 and $B^\pm$ separately.

The first chapter describes the theoretical background of the inclusive rare radiative B decays, particularly the $b \to s\gamma$ decay. A brief introduction to the Standard Model and CP mechanism is given. Existing measurement of $B \to X_s\gamma$ are reviewed.

The second chapter is a description of the PEP-II B Factory and *BABAR* detector. Details on the tracking system, neutral reconstruction, and particle identification relevant to this analysis are given.

The first half of the third chapter is an overview of the tracks and neutrals selection and meson reconstruction used in this measurement. In the second half of the chapter the reconstruction of a B in a fully hadronic decay is detailed.

The fourth chapter describes the bulk of the analysis: the selection criteria applied to isolate the $B \to X_s\gamma$ decays, their optimization, the Data-MonteCarlo agreement, the measurement technique and the results obtained.

The fifth chapter is devoted to systematics studies. Conclusions and perspectives are summarized in the sixth chapter.

1

Radiative B Decays

The first section presents a brief overview of the Standard model and CP violation mechanism. In Sec.1.2, 1.3 a theoretical review of inclusive radiative $\boldsymbol{B}$ decays is given. The $\boldsymbol{B \to X_s \gamma}$ decay model used in this analysis is detailed in Sec.1.4. Finally, Sec.1.5 and Sec.1.6 are on overview of the existing results.

1.1 Standard Model and the Cabibbo-Kobayashi-Maskawa matrix

The electroweak sector of the SM is a gauge theory based on the local group $SU_L(2) \otimes U_Y(1)$, which describes the symmetries of the matter fields. The Yang-Mills electroweak lagrangian is [1]:

$$\mathcal{L} = -\frac{1}{4}\Sigma_A W^A_{\mu\nu} W^{A\mu\nu} - \frac{1}{4} B_{\mu\nu} B^{\mu\nu} + \bar{\Psi}_L i\gamma^\mu \mathcal{D}_\mu \Psi_L + \bar{\Psi}_R i\gamma^\mu \mathcal{D}_\mu \Psi_R. \tag{1.1}$$

where, the spinors Ψ_L and Ψ_R represent the matter fields in their chiral components, and the field strength tensors are given by:

$$W_{\mu\nu} = \partial_\mu W_\nu - \partial_\nu W_\mu - g\epsilon_{ABC} W^B_\mu W^C_\nu \text{ and } B_{\mu\nu} = \partial_\mu B_\nu - \partial_\nu B_\mu \tag{1.2}$$

Here W^A, and B are the SU(2) and U(1) gauge fields, with the coupling constants g and g', and ϵ_{ABC} is the totally anti-symmetric Levi-Civita tensor. The corresponding covariant derivate is:

$$\mathcal{D}_\mu \Psi_{L,R} = \left[\partial_\mu + ig\Sigma t^A_{L,R} W_{A\mu} + ig'\frac{1}{2} Y_{L,R} B_\mu\right] \Psi_{L,R}, \tag{1.3}$$

where $t^A_{L,R}$ and $1/2Y_{L,R}$ are the SU(2) (weak isospin) and U(1) (hypercharge) generators. The electric charge generator is related to the isospin and hypercharge by:

$$Q = t^3_L + \frac{1}{2} Y_L = t^3_R + \frac{1}{2} Y_R. \tag{1.4}$$

The left and the right fermion components have different properties under the gauge group. The left components behave as doublets while the right as singlets. In the symmetric limit the two chiral component cannot interact each other, and thus mass term for fermions (of the form $\bar{\Psi}_L \Psi_R$) are forbidden. To give mass terms to fermions as well as to gauge bosons, the electroweak theory is realized with a vacuum state only invariant under the $U_{EM}(1)$ electric charge gauge transformation (spontaneous symmetry breaking). The gauge theories spontaneous broken allow to introduce mass terms for the gauge boson and the fermion fields without spoiling the gauge invariance, and the renormalizability of the theory. The mechanism by which, starting from a degenerate vacuum state, mass terms are introduced is known as Higgs mechanism [2]. The Higgs lagrangian term is:

$$\mathcal{L}_{Higgs} = (\mathcal{D}_m u\phi)^\dagger (\mathcal{D}^\mu \phi) - V(\phi^\dagger \phi) - \bar{\Psi}_L \Gamma \Psi_R \phi - \bar{\Psi}_R \Gamma^\dagger \Psi_L \phi^\dagger, \tag{1.5}$$

where ϕ is the isospin doublet of the Higgs scalar fields and the quantities Γ (which include all coupling constants) are matrices that make the Yukawa couplings invariant under the Lorentz and gauge groups. The general form of the Higgs potential is:

$$V(\phi^\dagger \phi) = \mu^2 \phi^\dagger \phi + \lambda(\phi^\dagger \phi)^2, \tag{1.6}$$

and it is not possible to include terms with higher dimension without breaking the renormalizability of the SM. To have a vacuum state (the minimum of the potential) degenerate, the μ^2 coefficient should be negative, while the coefficient λ should be positive to guarantee the potential bound from below. Under these hypotheses the vacuum state of the Higgs field satisfies $|\phi^2| = -\mu^2/2\lambda = v^2$. The field ϕ can be expanded around one of its ground states; in choosing a particular ground state ($\phi_0 = \begin{pmatrix} 0 \\ \mathrm{v} \end{pmatrix}$), the $SU_{L,R}(2) \otimes U_Y(1)$ symmetry is spontaneously broken.

The mass terms for the gauge bosons are coming from the kinetic part of the Higgs lagrangian once it is expanded around the Higgs vacuum state. The correct quantum numbers of the Higgs field are fixed by the requirement that the Lagrangian 1.5 is gauge invariant.

Family			Quantum Numbers			
1	2	3	T	T_3	Y	$Q = Y/2 + T_3$
$\begin{pmatrix} \nu_e \\ e \end{pmatrix}_L$	$\begin{pmatrix} \nu_\mu \\ \mu \end{pmatrix}_L$	$\begin{pmatrix} \nu_\tau \\ \tau \end{pmatrix}_L$	$1/2$	$+1/2$	-1	0
			$1/2$	$-1/2$	-1	-1
e_R	μ_R	τ_R	0	0	-2	-1
$\begin{pmatrix} u \\ d \end{pmatrix}_L$	$\begin{pmatrix} c \\ s \end{pmatrix}_L$	$\begin{pmatrix} t \\ b \end{pmatrix}_L$	$1/2$	$+1/2$	$+1/3$	$+2/3$
			$1/2$	$-1/2$	$+1/3$	$-1/3$
u_R	c_R	t_R	0	0	$4/3$	$+2/3$
d_R	s_R	b_R	0	0	$-2/3$	$-1/3$

Table 1-1. *Electroweak interaction multiplets.*

Since the $SU_L(2) \otimes U_Y(1)$ symmetry is spontaneously broken into $U_{EM}(1)$, only the linear combination of gauge fields with the quantum numbers of the photon remains massless. A general linear combination between the gauge bosons associated to the generator in Eq. 1.4 can be written:

$$\begin{pmatrix} A_\mu \\ Z_\mu \end{pmatrix} = \begin{pmatrix} -\sin\theta_W & \cos\theta_W \\ \cos\theta_W & \sin\theta_W \end{pmatrix} \begin{pmatrix} W_\mu^3 \\ B_\mu \end{pmatrix}. \tag{1.7}$$

where the angle θ_W is known as the Weak or Weinberg mixing angle. Once the symmetry is spontaneously broken through the interaction with the Higgs field, A_μ remains massless while Z_μ, W_μ^+ and W_μ^- acquire a mass term. W_μ^+ and W_μ^- are defined as:

$$W_\mu^\pm = \frac{1}{\sqrt{2}}(W_\mu^1 \pm iW_\mu^2). \tag{1.8}$$

The bilinear terms in the fields Z_μ and $W_\mu^\pm$ in Eq. 1.5 can be identified as the mass terms:

$$M_Z^2 = \frac{v^2 g^2}{2cos^2\theta_W} \tag{1.9}$$

$$M_W^2 = cos^2\theta_W M_Z^2 \tag{1.10}$$

which implies $\tan\theta_W = g'/gY_\phi$. In therms of these new fields the fermionic currents are:

$$J_\mu^\pm = \mathbf{\Sigma_f}\bar{\Psi}^f(1-\gamma_5)\gamma_\mu t^\pm \Psi^f \tag{1.11}$$

$$J_\mu^0 = \Sigma_f \bar{\Psi}^f \gamma_\mu \left[(1-\gamma_5)t^3 - 2Q\sin^2\theta_W\right]\Psi^f, \tag{1.12}$$

$$J_\mu^{em} = \mathbf{\Sigma_f}\bar{\Psi}^f\gamma_\mu Q\ \Psi^f, \tag{1.13}$$

where Ψ^f represents the isospin doublet for the fermions fields (Tab. 1-1) with f acting as a family index, $(1-\gamma_5)$ is the left-handed chiral projector, and $t^\pm$ are the isospin generator associated to the fields $W^\pm$. The first current describes interactions which change the electric charge, while the other two, produce transitions charge-conserving. The lagrangian 1.2 could be rewritten in two terms: one including interactions between the neutral current and the A_μ and Z_μ bosons, and another describing the interactions of the the $W_\mu^\pm$ with the charged current:

$$\mathcal{L}_{\mathcal{ED}} = \mathcal{L}_{\mathcal{CC}} + \mathcal{L}_{\mathcal{NC}}, \tag{1.14}$$

$$\mathcal{L}_{\mathcal{CC}} = \frac{g_2}{2\sqrt{2}}(J_\mu^+ W_\mu^+ + J_\mu^- W_\mu^-), \tag{1.15}$$

$$\mathcal{L}_{\mathcal{NC}} = -eJ_\mu^{em}A^\mu + \frac{g_2}{2\cos\theta_W}J_\mu^0 Z^\mu, \tag{1.16}$$

where e is defined as $e = g_2\sin\theta_W$.

Starting from the same doublet which gives masses to the gauge bosons it is possible to introduce mass terms for the fermion fields. This imposes others restrictions on the Higgs field. To obtain fermion mass terms like:

$$-\bar{\Psi}_L\Gamma\Psi_R\phi - \bar{\Psi}_R\Gamma\Psi_L\tilde{\phi} \quad \text{where} \quad \tilde{\phi} = i\sigma^2\phi^\dagger, \tag{1.17}$$

invariant under $SU_{L,R}(2)$ transformations, the Higgs field is required to have isospin equal to 1/2. The Γ matrices contain the Yukawa constants, which determine the strength of the fermion couplings to the Higgs fields.

The fermion mass matrix is obtained from the Yukawa couplings expanding ϕ around the vacuum state:

$$M = \bar{\psi}_L\ \mathcal{M}\psi_R + \bar{\psi}_R\mathcal{M}^\dagger\psi_L\ , \tag{1.18}$$

with

$$\mathcal{M} = \Gamma\cdot v\ . \tag{1.19}$$

It is important to observe that by a suitable change of basis we can always make the matrix $\mathcal{M}$ Hermitian, γ_5-free, and diagonal. In fact, we can make separate unitary transformations on ψ_L and ψ_R according to

$$\psi_L' = L\psi_L, \quad \psi_R' = R\psi_R, \tag{1.20}$$

and consequently

$$\mathcal{M} \to \mathcal{M}' = L^\dagger\mathcal{M}R\ . \tag{1.21}$$

This transformation does not alter the general structure of the fermion couplings in $\mathcal{L}$.

Weak charged currents are the only tree level interactions in the SM that may induce a change of flavour. By emission of a W an up-type quark is turned into a down-type quark, or a ν_l neutrino is turned into a l^- charged lepton. If we start from an up quark that is a mass eigenstate, emission of a W turns it into a down-type quark state d' (the weak isospin partner of u) that in general is not a mass eigenstate. In general, the mass eigenstates and the weak eigenstates do not in fact coincide and a unitary transformation connects the two sets:

$$\begin{pmatrix} d' \\ s' \\ b' \end{pmatrix} = V \begin{pmatrix} d \\ s \\ b \end{pmatrix}, \tag{1.22}$$

V is the Cabibbo-Kobayashi-Maskawa matrix[3]. Thus in terms of mass eigenstates the charged weak current of quarks is of the form:

$$J_\mu^+ \propto \bar{u}\gamma_\mu(1-\gamma_5)t^+ V d, \tag{1.23}$$

Since V is unitary (i.e. $VV^\dagger = V^\dagger V = 1$) and commutes with T^2, T_3 and Q (because all d-type quarks have the same isospin and charge) the neutral current couplings are diagonal both in the primed and unprimed basis. If the Z down-type quark current is abbreviated as $\bar{d}'\Gamma d'$ then, by changing basis we get $\bar{d}V^\dagger\Gamma V d$ and V and Γ commute; it follows that $\bar{d}'\Gamma d' = \bar{d}\Gamma d$. This is the GIM mechanism that ensures natural flavour conservation of the neutral current couplings at the tree level.

With three fermion generations the matrix V could be expressed in terms of three angles and one irremovable complex phase[4]. The CKM matrix is usually represented as:

$$V = \begin{pmatrix} V_{ud} & V_{us} & V_{ub} \\ V_{cd} & V_{cs} & V_{cb} \\ V_{td} & V_{ts} & V_{tb} \end{pmatrix}. \tag{1.24}$$

The irremovable phase in the CKM matrix allows possible CP violation.

The measurement of the elements of the CKM matrix is fundamental to test the validity of the Standard Model. Many of them (actually the first two rows of the matrix) are measured directly, namely by tree-level processes. Using unitary relations one can put constraints on the top mixing $|V_{ti}|$. Moreover the B mixing measurements, that involve box diagrams, can give information also about V_{td} and V_{tb}.

The CKM-matrix can be expressed in terms of four Wolfenstein parameters (λ, A, ρ, η) with $\lambda = |V_{us}| = 0.22$ playing the role of an expansion parameter and η representing the CP-violating phase [5]:

$$V = \begin{pmatrix} 1-\frac{\lambda^2}{2} & \lambda & A\lambda^3(\rho - i\eta) \\ -\lambda & 1-\frac{\lambda^2}{2} & A\lambda^2 \\ A\lambda^3(1-\rho-i\eta) & -A\lambda^2 & 1 \end{pmatrix} + O(\lambda^4). \tag{1.25}$$

λ is small, and for each element in V, the expansion parameter is actually λ^2.

The Wolfenstein parametrization offers a transparent geometrical representation of the structure of the CKM matrix. The unitarity of the matrix implies various relations among its elements. Three of them are very useful for understanding the Standard Model predictions for CP violation:

$$V_{ud}V_{us}^* + V_{cd}V_{cs}^* + V_{td}V_{ts}^* = 0, \tag{1.26}$$

$$V_{us}V_{ub}^* + V_{cs}V_{cb}^* + V_{ts}V_{tb}^* = 0, \tag{1.27}$$

$$V_{ud}V_{ub}^* + V_{cd}V_{cb}^* + V_{td}V_{tb}^* = 0. \tag{1.28}$$

Each of these three relations requires the sum of three complex quantities to vanish and so can be geometrically represented in the complex plane as a triangle. These are "the unitarity triangles". If the CP symmetry is violated the area of the triangles is not zero. The B physics is related to the third triangle at least for what the B Factory can access. The study of the parameters of this triangle encompasses the physics of CP violation in Standard Model. The openness of this triangle, due to the fact that all the three sides are of the same order of magnitude, predicts large CP asymmetries.

It should be remarked that the Wolfenstein parametrization is an approximation and neglecting $O(\lambda^4)$ terms could be wrong in particular processes. An improved approximated parametrization of the original Wolfenstein matrix is given in [6]. Defining

$$V_{us} = \lambda, \quad V_{cb} = A\lambda^2, \quad V_{ub} = A\lambda^3(\rho - i\eta), \tag{1.29}$$

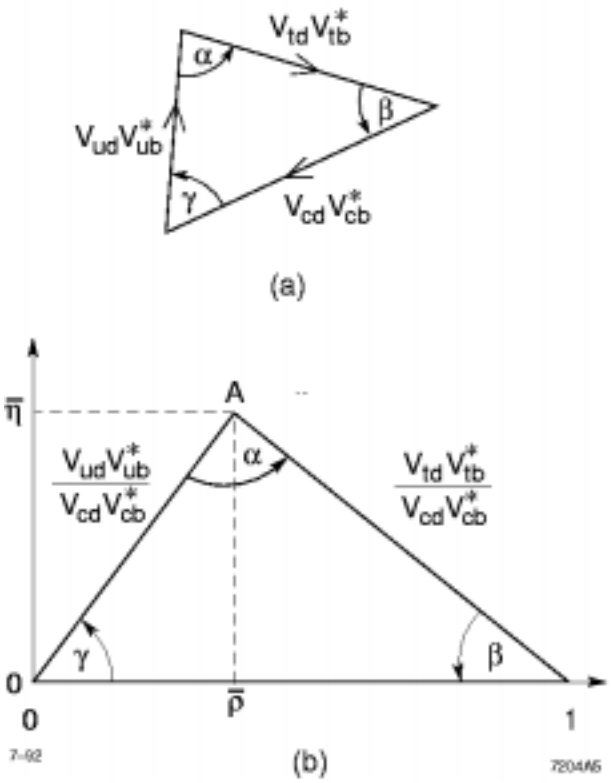

Figure 1-1. *The rescaled Unitarity Triangle, all sides divided by $V_{cb}^* V_{cd}$.*

one can then write

$$V_{td} = A\lambda^3(1 - \bar{\rho} - i\bar{\eta}), \tag{1.30}$$

$$Im(V_{cd}) = -A^2\lambda^5\eta, \quad Im(V_{ts}) = -A\lambda^4\eta, \tag{1.31}$$

where

$$\bar{\rho} = \rho(1 - \lambda^2/2), \quad \bar{\eta} = \eta(1 - \lambda^2/2), \tag{1.32}$$

turn out to be excellent approximations to the exact expressions. Depicting the rescaled Unitarity Triangle in the $(\bar{\rho}, \bar{\eta})$ plane, the lengths of the two complex sides are

$$R_b \equiv \sqrt{\bar{\rho}^2 + \bar{\eta}^2} = \frac{1 - \lambda^2/2}{\lambda}\left|\frac{V_{ub}}{V_{cb}}\right|, \quad R_t \equiv \sqrt{(1 - \bar{\rho})^2 + \bar{\eta}^2} = \frac{1}{\lambda}\left|\frac{V_{td}}{V_{cb}}\right|. \tag{1.33}$$

The rescaled Unitarity Triangle (Fig. 1-1) is derived from Eq. 1.28 by:

- choosing a phase convention such that $(V_{cd}V_{cb}^*)$ is real,
- dividing the lengths of all sides by $|V_{cd}V_{cb}^*|$,
- aligns one side of the triangle with the real axis,
- makes the length of this side 1.

The form of the triangle is unchanged. Two vertices of the rescaled Unitarity Triangle are thus fixed at (0,0) and (1,0). The coordinates of the remaining vertex are denoted by $(\bar{\rho}, \bar{\eta})$.

This triangle is very important in B Physics. Both angles and sides can be measured in a B factory and they can offer an independent test of the Standard Model. The incompatibility of the new measurements with a triangle would be a probe of new Physics.

1.2 Radiative B Decays

Flavour physics is governed by the interplay of strong and weak interactions. One of the main difficulties in examining the observables in flavour physics is the influence of the strong interactions. For matrix elements dominated by long-distance strong interactions, there is no adequate quantitative estimate available in quantum field theory. The resulting hadronic uncertainties restrict the opportunities in flavour physics significantly, in particular within the indirect search for new physics.

The B system represents an ideal framework for the study of flavour physics. Since the b quark mass is much larger than the typical scale of the strong interaction Λ_{QCD}, long-distance strong interactions could be generally taken under control, thanks to the expansion in that heavy mass [7]. In particular, inclusive rare B decays play the most important role; they are, in fact, theoretically clean and represent a theoretical laboratory of perturbative QCD.

In particular, the decay width $\Gamma(B \to X_s\gamma)$ is well approximated by the partonic decay rate $\Gamma(b \to s\gamma)$, which can be analyzed in renormalization-group-improved perturbation theory:

$$\Gamma(B \to X_s\gamma) = \Gamma(b \to s\gamma) + \Delta^{nonpert.} \tag{1.34}$$

Non-perturbative effects, $\Delta^{nonpert.}$, play a subdominant role and are under control thanks to the heavy mass expansion and the assumption of quark–hadron duality [8](see Sec. 1.2.1).

The SM leading order diagrams for $b \to s\gamma$, shown in Fig. 1-2, are called 'penguin diagram'.

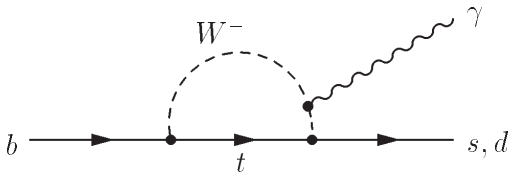

Figure 1-2. *Feynman diagram for the electromagnetic penguins $b \to s\gamma$ and $b \to d\gamma$. The photon can be emitted from the W (shown) or from any of the quarks.*

In contrast to the exclusive rare B decay modes, the inclusive ones are theoretically clean observables, because no specific model is needed to describe the hadronic final states.

The inclusive modes $B \to X_s\gamma$ can be easily measured in the electron–positron colliders (B factories, CLEO) with their kinematic constraints and their controlled background, while they are more difficult to measure at hadronic machines.

1.2.1 Heavy quark effective theory (HQET)

The heavy-quark effective theory (HQET) is constructed to provide a simplified description of processes where a heavy quark interacts with light degrees of freedom predominantly by the exchange of soft gluons. In these systems

typical momenta exchanged between the heavy and light constituents are of order $\Lambda_{\rm QCD} \sim 0.2\,{\rm GeV}$. The heavy quark is surrounded by a complicated, strongly interacting cloud of light quarks, antiquarks, and gluons. In this case it is the fact that the Compton wavelength of the heavy quark $\lambda_Q \sim 1/m_Q$ is much smaller than the size of the hadron $R_{\rm had} \sim 1/\Lambda_{\rm QCD}$, which leads to simplifications. To resolve the quantum numbers of the heavy quark there would require a hard probe; the soft gluons exchanged between the heavy quark and the light constituents can only resolve distances much larger than λ_Q. Therefore, the light degrees of freedom are blind to the flavour (mass) and spin orientation of the heavy quark. They experience only its colour field, which extends over large distances because of confinement, relativistic effects such as colour magnetism vanish as $m_Q \to \infty$.

These hadronic bound states are therefore characterized by a large separation of mass scales. The goal of the HQET is to separate the physics associated with these two scales, in such a way that all dependence on the heavy-quark mass becomes explicit. The framework in which to perform this separation is the operator product expansion (OPE) [9, 10].

After the separation of short- and long-distance phenomena a big portion of the relevant physics (i.e. all short-distance effects) could be computed using perturbation theory and renormalization-group techniques, taking under control all logarithmic dependence on the heavy-quark mass, and it may happen that the long-distance physics simplifies due to approximate symmetries, which imply non-trivial relations between observables.

Compared with most effective theories, in which the degrees of freedom of a heavy particle are removed completely from the low-energy theory, the HQET is special in that its purpose is to describe the properties and decays of hadrons which do contain a heavy quark. Hence, it is not possible to remove the heavy quark completely from the effective theory. What is possible is to integrate out the "small components" in the full heavy-quark spinor, which describe the fluctuations around the mass shell.

The odinary QCD lagrangian for a heavy-quark field Ψ with mass m

$$\mathcal{L} = \bar{\Psi} i \not{D} \Psi - m \bar{\Psi} \Psi, \tag{1.35}$$

with the covariant derivative

$$D_\mu = \partial_\mu - igT^a A^a_\mu, \tag{1.36}$$

could be expressed [12, 13] in term of the large- and small-component fields, h_v and H_v,

$$\Psi(x) = e^{-imv\cdot x} \left(h_v(x) + H_v(x) \right), \tag{1.37}$$

where the heavy-quark momentum has been decomposed as

$$p = mv + k, \tag{1.38}$$

with v being the 4-velocity of the heavy *hadron*. Once mv, the large kinematical part of the momentum is singled out, the remaining component k is determined by the soft QCD bound state interactions, and thus $k = \mathcal{O}(\Lambda_{QCD}) \ll m$.

Eq. 1.35 could be re-written as:

$$\mathcal{L}_{\rm eff} = \bar{h}_v \, iv\cdot D \, h_v + \frac{1}{2m_Q} \bar{h}_v \, (iD_\perp)^2 \, h_v + \frac{g_s}{4m_Q} \bar{h}_v \, \sigma_{\mu\nu} \, G^{\mu\nu} \, h_v + O(1/m_Q^2) \, . \tag{1.39}$$

The first term in 1.39 describes the "residual" QCD dynamics of the heavy quark once the kinematic dependence on m is separated out. Since there is no longer any reference to the mass m, the only parameter to distinguish quark flavours, this term is flavour symmetric: the dynamics is the same for b and c quarks in the static limit. Since the operator $v \cdot D$ contains no γ-matrices, which would act on the spin degrees of freedom, the leading HQET Lagrangian also exhibits a spin symmetry. This corresponds to the decoupling of the heavy-quark spin in the $m \to \infty$ limit [11].

The second term describes the non relativistic kinetic energy arising from the off-shell residual motion of the heavy quark, and the third represents the chromo-magnetic coupling of the heavy-quark spin to the gluon field.

The following definitions are used in literature [13]:

$$\lambda_1 \equiv \frac{\langle B|\bar{h}(iD)^2 h|B\rangle}{2m_B} \qquad \lambda_2 \equiv \frac{1}{6}\frac{\langle B|\bar{h}g\sigma\cdot Gh|B\rangle}{2m_B}. \tag{1.40}$$

The same parameters appear in the heavy-quark expansion of meson masses. Introducing the spin-averaged masses $\overline{m}_B = \frac{1}{4}(m_B + 3m_{B^*})$ and $\overline{m}_D = \frac{1}{4}(m_D + 3m_{D^*})$, one finds

$$\begin{aligned} m_b - m_c &= (\overline{m}_B - \overline{m}_D)\left(1 + \frac{(-\lambda_1)}{2\overline{m}_B\overline{m}_D} + \ldots\right), \\ m_{B^*}^2 - m_B^2 &= 4\lambda_2 + \ldots \end{aligned} \tag{1.41}$$

where the factors in parenthesis represent higher-order terms in the heavy-quark expansion. From the second relation, it follows that $\lambda_2 = 0.128 \pm 0.007\,\mathrm{GeV}^2$. The kinetic-energy parameter λ_1, on the other hand, is given in terms of a difference of quark masses and cannot be determined from hadron spectroscopy. Various model approaches have been used to obtain values for λ_1; however, since λ_1 is not a physical quantity, it is hard to compare the results from different methods. The range of predictions obtained from a variety of methods is $0.1\ \mathrm{GeV}^2 < -\lambda_1 < 0.6\ \mathrm{GeV}^2$ [14].

Inclusive decay rates determine the probability for the decay of a particle into the sum of all possible final states with a given set of global quantum numbers. From a theoretical point of view, inclusive decays of hadrons containing a heavy quark offer two advantages [15, 16]. First, bound-state effects related to the initial state (such as the "Fermi motion" of the heavy quark inside the hadron [17, 18]) can be accounted for in a systematic way using the heavy-quark expansion. Secondly since the energy released into the final state by the decay of the heavy b quark is large compared to the QCD scale, the final hadronic state need not to be dominated by a few sharp resonances. If resonances are indeed unimportant, then there is a factorization between the short distance part of the decay (the disappearance of the b quark) and the long distance part (the eventual hadronization of the decay products). This factorization implies that for sufficiently inclusive quantities it is enough to consider the short distance part of the process, with the subsequent hadronization taking place with unit probability. This factorization, known as *local parton-hadron duality*, is an example of a crucial assumption which lies outside of the HQE itself. Local duality must hold as $m_b \to \infty$ with all other masses held fixed. In this limit, wavelengths associated with the b quark decay are arbitrarily short and cannot interfere coherently with the hadronization process. On the other hand, it is not known how to estimate the size of corrections to local duality for m_b large but finite. There is no analog of the heavy quark expansion appropriate to this question, and no way to estimate systematically deviations from the limit $m_b \to \infty$. Although an expansion in powers $1/m_b$ in the calculation of inclusive quantities is incorporated, the behavior of this expansion does not address directly the issue of violations of duality. The duality hypothesis, while entirely reasonable for inclusive B decays, is not independently verifiable except by the direct confrontation of theoretical calculations with the data. The assumption of duality is basically that cross sections and decay rates, which are defined in the physical region (*i.e.*, the region of time-like momenta), are calculable in QCD after a "smearing" or "averaging" procedure has been applied [19].

The inclusive decay width of an heavy hadron Γ_H, could be expressed [13], using the optical theorem, as: Γ_H

$$\Gamma_H = \frac{1}{2m_H}\langle H|\mathcal{T}|H\rangle \equiv \langle\mathcal{T}\rangle, \tag{1.42}$$

where the transition operator $\mathcal{T}$ is defined as

$$\mathcal{T} = \mathrm{Im}\; i\int d^4x\, T\,\mathcal{H}_{eff}(x)\mathcal{H}_{eff}(0), \tag{1.43}$$

with $\mathcal{H}_{eff}$ being the effective weak Hamiltonian. Eqs. 1.42, 1.43 express the total decay rate as the absorptive part of the forward scattering amplitude $H \to H$ under the action of $\mathcal{H}_{eff}$. Eq. 1.42 and 1.43 could be re-written in a more

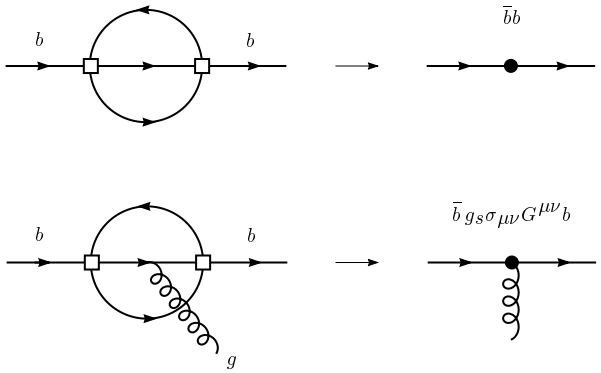

Figure 1-3. *Perturbative contributions to the transition operator* **T** *(left), and the corresponding operators in the operator product expansion (right). The open squares represent a four-fermion interaction of the effective weak Lagrangian $\mathcal{L}_{\rm eff}$, while the black circles represent local operators in the $1/m_b$ expansion.*

directly understandable form by inserting a complete set of states $\sum_\alpha |X\rangle\langle X|$ between the two factors of $\mathcal{H}_{eff}$ in Eq. 1.43 and removing the T-product by explicitly taking the absorptive part. This yields

$$\Gamma_H \sim \sum_\alpha \langle H|\mathcal{H}_{eff}|X\rangle\langle X|\mathcal{H}_{eff}|H\rangle, \tag{1.44}$$

where one immediately recognizes the decay rate as the modulus squared of the decay amplitude (summed over all final states X). The reason to introduce (1.43) is that the T-product, by means of Wick's theorem, allows for a direct evaluation in terms of Feynman diagrams.

In order to compute Γ_H an operator product expansion is applied to Eq. 1.43, resulting in a series of local operators of increasing dimension. The coefficients of these operators are correspondingly suppressed by increasing powers of $1/m_b$.

The leading contributions to the transition operator are shown in Fig. 1-3. The large mass of the b quark means that the momenta flowing through the internal propagator lines are large. It is thus possible to construct an OPE for the two-point function **T**, in which it is represented as a series of local operators containing the b-quark fields. The operator with the lowest dimension is $\bar{b}b$; it arises from contracting the internal lines in the first diagram. The only gauge-invariant operator with dimension four is $\bar{b}\, iD\!\!\!/\, b$; however, the equations of motion imply that this operator can be replaced by $m_b\bar{b}b$. The first operator with a different structure has dimension four and contains the gluon field-strength tensor. Finally, from dimension four on, a large number of new operators appear. For dimensional reasons, the matrix elements of these operators are suppressed by inverse powers of the b-quark mass. Thus, any inclusive decay rate may be written in the form [20, 21]

$$\Gamma(H_b \to X_f) = \frac{G_F^2 m_b^5}{192\pi^3}\left\{c_3^f\,\langle\bar{b}b\rangle_H + c_5^f\,\frac{\langle\bar{b}\,g_s\sigma_{\mu\nu}G^{\mu\nu}b\rangle_H}{m_b^2} + \ldots\right\}, \tag{1.45}$$

where the prefactor arises from the loop integrations, c_n^f are calculable short-distance coefficient functions (which also contain the relevant CKM matrix elements) depending on the quantum numbers f of the final states, and $\langle O\rangle_H$ are the (normalized) forward matrix elements of local operators, written using the short-hand notation

$$\langle O\rangle_H = \frac{1}{2m_{H_b}}\,\langle H_b|\,O\,|H_b\rangle\,. \tag{1.46}$$

These matrix elements, which contain all the long-distance contributions, can be systematically expanded in powers of $1/m_b$ using HQET parameters defined in Eq. 1.42. For the particular case of B mesons ($H_b = B$), the result is

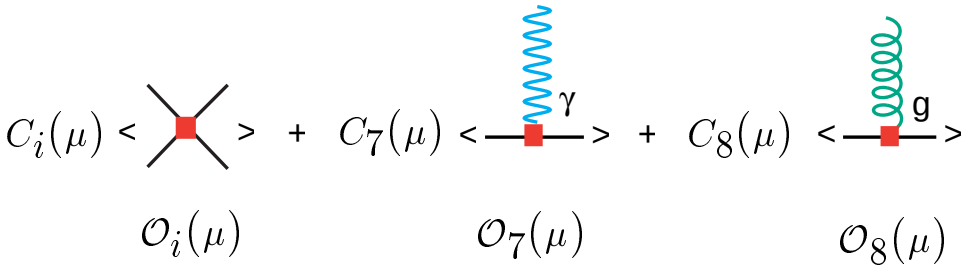

Figure 1-4. *Effective Hamiltonian in the case of $B \to X_{s,d}\gamma$.*

[20, 22, 23]

$$\begin{aligned} \langle \bar{b} b \rangle &= 1 + \frac{\lambda_1 + 3\lambda_2}{2m_b^2} + \mathcal{O}(1/m_b^3)\,, \\ \frac{\langle \bar{b}\, g_s \sigma_{\mu\nu} G^{\mu\nu} b \rangle}{m_b^2} &= \frac{6\lambda_2}{m_b^2} + \mathcal{O}(1/m_b^3)\,. \end{aligned} \tag{1.47}$$

Inserting the results of Eq. 1.47 into Eq. 1.45 yields

$$\Gamma(\overline{B} \to X_f) = \frac{G_F^2 m_b^5}{192\pi^3} \left\{ c_3^f \left(1 + \frac{\lambda_1 + 3\lambda_2}{2m_b^2} \right) + c_5^f \frac{6\lambda_2}{m_b^2} + \ldots \right\}. \tag{1.48}$$

The main result of the HQE for inclusive decay rates is the observation that the free quark decay (*i.e.*, the parton model) provides the first term in a systematic $1/m_b$ expansion [15]. For dimensional reasons, the corresponding rate is proportional to the fifth power of the b-quark mass.

The nonperturbative corrections, which arise from bound-state effects inside the B meson, are suppressed by at least two powers of the heavy-quark mass, *i.e.*, they are of relative order $(\Lambda_{\rm QCD}/m_b)^2$. The absence of first-order power corrections is a consequence of the equations of motion, as there is no independent gauge-invariant operator of dimension four that could appear in the operator product expansion.

The fact that bound-state effects in inclusive decays are strongly suppressed explains *a posteriori* the success of the parton model in describing such processes [24, 25].

1.2.2 $B \to X_s\gamma$ theoretical predictions

The general Eq. 1.48 can describe the inclusive $B \to X_s\gamma$ decays. In this case it could be written as

$$\Gamma_{B\to X_s\gamma} = \frac{G_F^2 m_b^5}{32\pi^4} |V_{tb}V_{ts}|^2 C_7^2(m_b)(1 + \frac{1}{2}\lambda_1 - \frac{9}{2}\lambda_2). \tag{1.49}$$

where $C_7^2(m_b)$ is the Wilson coefficient for the dipole-operator shown in Fig. 1-4. The resulting $\mathcal{O}(\Lambda_{QCD}^2/m_b^2)$ non perturbative correction amounts to around 3% with respect to the partonic decay [26].

The Wilson coefficients in Eq. 1.49 encodes information on the short-distance QCD effects due to hard gluon exchanges between the quark lines of the leading one-loop electroweak diagrams (Fig. 1-5). Such effects enhance the branching ratio $B \to X_s\gamma$ by roughly a factor of three [27, 28]. Moreover, it is sensitive to the top quark mass, and more generally, to any kind of new physics beyond the standard model.

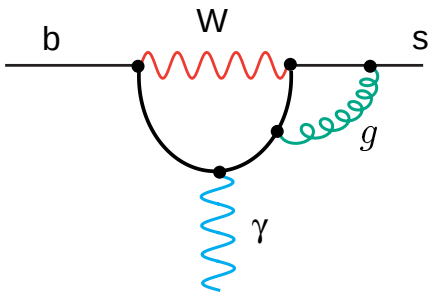

Figure 1-5. *QCD corrections to the decay $b \to s\gamma$.*

The leading order (LO) $\Gamma[b \to s\gamma]$ result [29] was dominated by a large renormalization scale dependence at the $\pm 25\%$ level, which already indicated the importance of the next to leading order calculation(NL0), that was completed in 1997, thanks to the effort of many different groups ([30, 31, 32]). The theoretical error of the previous L0 result was substantially reduced, to $\pm 10\%$, and the central value of the partonic decay rate increased by about 20%.

The theoretical prediction for the branching ratio of $b \to s\gamma$, is [32] :

$$\mathcal{B}(b \to s\gamma) = (3.28 \pm 0.33) \times 10^{-4}. \tag{1.50}$$

Including the resummed QED corrections and the non-perturbative corrections discussed above, one ends up with the following theoretical prediction for the $B \to X_s\gamma$ branching ratio [33]:

$$\mathcal{B}(B \to X_s\gamma) = (3.32 \pm 0.30) \times 10^{-4}, \tag{1.51}$$

where the error has two sources, the uncertainty regarding the μ scale dependences and the uncertainty due to the input parameters. In the latter the uncertainty due to the parameter m_c/m_b is dominant. This prediction almost coincides with the prediction of Kagan and Neubert [34].

In reference [35] it was shown that the strong enhancement of the branching ratio by QCD logarithms is mainly due to the b-quark mass evolution in the top-quark sector. This leads to a better control over the residual scale dependence at NL0. Secondly, quark mass effects were further analysed in particular the definitions of the quark masses m_c and m_b in the two-loop matrix element of the four-quark operators $\mathcal{O}_{1,2}$. Since the charm quark in the matrix element $\mathcal{O}_{1,2}$ are dominantly off-shell, it is argued that the running charm mass should be chosen instead of the pole mass. The latter choice was used in all previous analyses [30, 32, 33, 34].

$$m_c^{pole}/m_b^{pole} \qquad \Rightarrow \qquad m_c^{\overline{MS}}(\mu)/m_b^{pole}, \;\; \mu \in [m_c, m_b]. \tag{1.52}$$

Numerically, the shift from $m_c^{pole}/m_b^{pole} = 0.29 \pm 0.02$ to $m_c^{\overline{MS}}(\mu)/m_b^{pole} = 0.22 \pm 0.04$ is rather important and leads to a $+11\%$ shift of the central value of the $B \to X_s\gamma$ branching ratio. The error in the charm mass within the $\overline{MS}$ scheme, is due to the uncertainty resulting from the scale variation and due to the uncertainty in $m_c^{\overline{MS}}$.

With the new choice of the charm mass renormalization scheme, the theoretical prediction for the 'total' branching ratio is

$$\mathcal{B}(B \to X_s\gamma)_{E\gamma > 1.6\,\mathrm{GeV}} = (3.60 \pm 0.30) \times 10^{-4}, \tag{1.53}$$

The previous predictions are computed considering the photon spectrum with $E_\gamma > (1-\delta)E_\gamma^{max} = (1-\delta)\frac{m_b}{2}$ with $\delta = 0.9$, thus resulting $E_\gamma > 0.25\,\mathrm{GeV}$. Normalize Eq. 1.53 to that range we get $\mathcal{B}(B \to X_s\gamma) = (3.73 \pm 0.30) \times 10^{-4}$. The theoretical error might be larger due to non perturbative corrections.

The renormalization scheme for m_c is an NNL0 issue, and the $\overline{MS}$ mass of the charm quark is a short-distance quantity which does not suffer from non-perturbative ambiguities, in contrast to its pole mass. Therefore the central value resulting within this scheme, is definitely favoured and should be regarded as the present theoretical prediction.

1.3 Extrapolation of the photon spectrum

As shown in the previous section, the theoretical error on the total inclusive $B \to X_s\gamma$ branching ratio is of the order of 10%. Unfortunately most of the theoretical uncertainty in an inclusive branching fraction measurement derives from other sources. In order to isolate the signal region from the large background (1000 times bigger) a cut on the phase space region is applied. The extrapolation to the full phase space may introduce very large uncertainties and model dependence. Only the high part of the $B \to X_s\gamma$ photon spectrum is accessible from an experimental point of view. Therefore only the branching ratio for $B \to X_s\gamma$ with $E_\gamma > E_\gamma^{\min}$ could be directly measured. To obtain the total branching ratio, one has to know the fraction R of the $B \to X_s\gamma$ events with $E_\gamma > E_\gamma^{\min}$.

The uncertainty on this fraction R is regarded as a *theoretical* uncertainty. The photon energy spectrum cannot be calculated directly using the heavy mass expansion, because the operator product expansion breaks down in the high-energy part of the spectrum, where $E_\gamma \approx m_b/2$.

The fraction R was calculated, for the first time, in [36] using a phenomenological model [37], where the motion of the b quark in the B meson is characterized by two parameters, the average momentum p_F of the b quark and the average mass m_q of the spectator quark.

A theoretical analysis of the problem was presented in [34]. The residual motion of the b quark inside the B meson caused by its soft interactions with the light constituents leads to a modification of the photon energy spectrum, the so called "Fermi motion". Since the endpoint of the photon energy spectrum the operator product expansion breaks down, the Fermi motion is included in the heavy-quark expansion by resumming an infinite set of leading-twist corrections into a shape function $F(k_+)$, which governs the light-cone momentum distribution of the heavy quark inside the B meson defined in Eq. [17].

The shape function is a universal, i.e. process-independent characteristic of the B meson governing the inclusive decay spectra in processes with massless partons in the final state, such as $B \to X_s\gamma$ and $B \to X_u\,\ell\,\nu$. It is important to note that this function does not describe in an accurate way the distributions in decays into massive partons such as $B \to X_c\,\ell\,\nu$. Therefore, the shape function cannot be determined using the lepton spectrum in semileptonic decays of B mesons, for which high-precision data exist.

On the other hand, there is some useful theoretical information on the moments of the shape function, which are related to the forward matrix elements of local operators:

$$A_n = \int \mathrm{d}k_+\, k_+^n\, F(k_+) = \frac{1}{2m_B}\,\langle B|\,\bar{b}\,(iD_+)^n b\,|B\rangle\,. \tag{1.54}$$

The first three moments satisfy $A_0 = 1$, $A_1 = 0$ and $A_2 = \frac{1}{3}\mu_\pi^2$, where $\mu_\pi^2 = -\lambda_1$ is related to the kinetic energy of the b quark inside the B meson (Sec. 1.2). The condition $A_1 = 0$, which is a consequence of the equations of motion, ensures that the quark mass m_b entering the theoretical expressions is the pole mass.

Let $P_{\mathrm{p}}(y_{\mathrm{p}})$ be the photon energy spectrum in the parton model, where $y_{\mathrm{p}} = 2E_\gamma/m_b$ with $0 \le y_{\mathrm{p}} \le 1$. The result of including the effects of Fermi motion and calculating the physical spectrum $P(y)$ as a function of the variable

$y = 2E_\gamma/m_B$, to the leading-twist approximation,is given by the convolution [17]

$$P(y)\,\mathrm{d}y = \int \mathrm{d}k_+\, F(k_+) \left[P_{\mathrm{p}}(y_{\mathrm{p}})\,\mathrm{d}y_{\mathrm{p}}\right]_{y_{\mathrm{p}}=y_{\mathrm{p}}(k_+)}, \tag{1.55}$$

where $y_{\mathrm{p}}(k_+)$ is obtained by replacing m_b in the definition of y_{p} with the "effective mass" $m_b^* = m_b + k_+$, i.e. $y_{\mathrm{p}}(k_+) = 2E_\gamma/m_b^* = ym_B/m_b^*$. Because the support of the shape function is restricted to the range $-m_b \le k_+ \le m_B - m_b$, it follows that $0 \le y \le 1$. Denoting $B_{\mathrm{p}}(\delta_{\mathrm{p}})$ the integrated branching ratio calculated in the parton model, which is given by an integral over the spectrum $P_{\mathrm{p}}(y_{\mathrm{p}})$ with a cutoff δ_{p} defined by the condition that $E_\gamma \ge \frac{1}{2}(1-\delta_{\mathrm{p}})m_b$, from Eq. 1.55, follows that the corresponding physical quantity $B(\delta)$ is given by:

$$B(\delta) = \int\limits_{m_B(1-\delta)-m_b}^{m_B-m_b} \mathrm{d}k_+\, F(k_+)\, B_{\mathrm{p}}\left(1 - \frac{m_B(1-\delta)}{m_b+k_+}\right). \tag{1.56}$$

This relation is such that $B(1) = B_{\mathrm{p}}(1)$, implying that the total branching ratio is not affected by Fermi motion; indeed, the $1/m_Q^2$ corrections are the only power corrections to the total branching ratio.

A simple ansatz for the distribution function is:

$$F(k_+) = N(1-x)^a e^{(1+a)x}; \quad x = \frac{k_+}{\bar{\Lambda}} \le 1 \quad and \quad a = f(\bar{\Lambda}, \lambda_1), \tag{1.57}$$

where $\bar{\Lambda} = m_B - m_b$. The parameters N, a chosen such that the first three moments of $F(k_+)$ satisfy the relations mentioned after Eq. 1.54. and the parameter a can be related to the second moment, yielding $A_2 = \frac{1}{3}\mu_\pi^2 = \bar{\Lambda}^2/(1+a)$. Thus, the b-quark mass (or $\bar{\Lambda}$) and the quantity μ_π^2 (or a) are the two parameters of this function.

For a graphical illustration of the sensitivity of the results to the parameters of the shape function, the predictions for the Standard Model branching ratio as a function of the energy cutoff $E_\gamma^{\min}$ are shown in Fig. 1-6. The gray line shows the result obtained using the same parameters as for the solid line, but with a Gaussian ansatz $F(k_+) = N\,(1-x)^a e^{-b(1-x)^2}$ for the shape function.

Comparing the two upper plots in Fig. 1-6, it's clear that the uncertainty due to the value of the b-quark mass is the dominant one. Variations of the parameter μ_π^2 have a much smaller effect on the partially integrated branching ratio, and also the sensitivity to the functional form adopted for the shape function turns out to be small. This behaviour is a consequence of global quark–hadron duality, which ensures that even partially integrated quantities are rather insensitive to bound-state effects. The strong remaining dependence on the b-quark mass is simply due to the transformation by Fermi motion of phase-space boundaries from parton to hadron kinematics.

The spread of results obtained by varying m_b between 4.65 and 4.95 GeV/c^2 (with μ_π^2 adjusted as described above) represents the amount of model dependence resulting from the inclusion of Fermi motion.

An important observation is that the shape of the photon spectrum is practically insensitive to physics beyond the SM. A precise measurement of the photon spectrum allows to determine the parameters of the shape function.

The latter information is an important input for the determination of the CKM matrix element V_{ub}. One takes advantage of the universality of the shape function to lowest order in Λ_{QCD}/m_b. The same shape function occurs in the description of nonperturbative effects in the endpoint region of the $B \to X_s\gamma$ photon spectrum and of the $B \to X_u\ell\nu$ charged-lepton spectrum up to higher $1/m_b$ corrections. Thus, from the photon spectrum one can determine the shape function; with the help of the latter and of the measurement of the charged-lepton spectrum of $B \to X_u\ell\nu$, one can extract a value for V_{ub}.

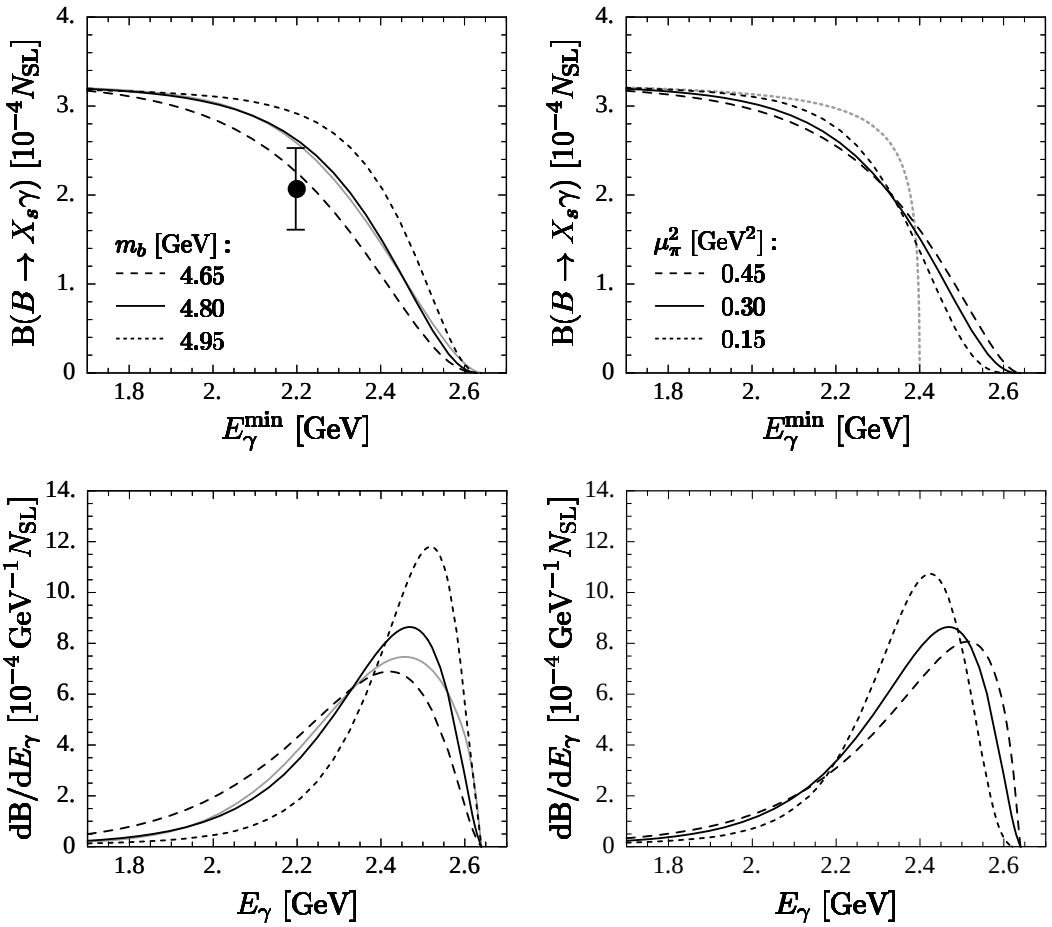

Figure 1-6. *The model dependence of the E_γ spectrum in the B meson rest frame, taken from the paper by Kagan and Neubert [34]. The spectra are shown for different choices of b quark mass and Fermi momentum. Also shown are the integrals of the spectra as a function of the lower bound of integration, E_γ^{min}. The data point represents the first CLEO measurement, as provided to Kagan and Neubert by private communication.*

1.4 $B \to X_s\gamma$ decay model

In order to simulate the $B \to X_s\gamma$ decay it is necessary to determine the shape of the photon and m_{X_s} spectrum. Theoretical predictions are based on a non-resonant model, i.e. resonances in the m_{X_s} spectrum have widths exceeding their spacing and thus overlapping. This assumption is not valid for the $K^*(892)$, whose width has been measured in [44, 45, 46] to be $50.8\ \mathrm{MeV}$. This resonance needs to be incorporated in the decay model with width and branching ratio set to the measured value. This issue will be adressed in the next two sections.

Table 1-2. *Mean masses and widths of the lowest-lying hadronic states accessible in $B \to X_s\gamma$ decays, and the corresponding photon energies (errors refer to changing M_H by $\pm\Gamma_H$)*

State H	M_H [GeV/c^2]	Γ_H [MeV]	E_γ [GeV]
$K\,(n\pi)$	≥ 0.629	continuum	≤ 2.60
$K^*(892)$	0.894	50	2.56 ± 0.01
$K_1(1270)$	1.273	90	2.49 ± 0.02
$K_1(1400)$	1.402	174	2.45 ± 0.05
$K^*(1410)$	1.412	227	2.45 ± 0.06
$K_2^*(1430)$	1.428	103	2.45 ± 0.03
$K_2(1580)$	1.580	110	2.40 ± 0.03
$K_1(1650)$	1.650	150	2.38 ± 0.05
$K^*(1680)$	1.714	323	2.36 ± 0.10
$K_2(1770)$	1.773	186	2.34 ± 0.06

1.4.1 Non-resonant contribution

In the B rest frame, the non-resonant spectrum can be described equivalently in terms of the photon energy or the invariant mass of the hadronic system X_s. The relation between the two spectra can be related from kinematics:

$$E_\gamma = \frac{m_B^2 - m_{X_s}^2}{2m_B}. \tag{1.58}$$

It is necessary to recall that the theoretical predictions for the photon energy and hadronic mass spectra must be understood in the sense of quark–hadron duality. In particular, the true hadronic mass spectrum in the low-mass region may have resonance structures due to low-lying kaon states. Two kinematic regions could be defined: the "endpoint region" and the "resonance region".

The endpoint region of the photon energy spectrum is characterized by the condition that $E_\gamma^{\max} - E_\gamma = O(\bar{\Lambda})$, where $\bar{\Lambda} = m_B - m_b$. It is in this region that the effects of Fermi motion are relevant and determine the shape of the spectrum. In the endpoint region, the invariant mass of the hadronic final state is of order $m_B\bar{\Lambda} \gg \Lambda_{\rm QCD}^2$, implying that a large number of final states are kinematically accessible. Under such circumstances, local quark–hadron duality ensures that the photon and hadronic mass spectra are similar to the corresponding inclusive spectra predicted by the heavy-quark expansion even without applying a smearing procedure.

In the resonance region, on the other hand, the invariant mass of the hadronic final state is of order $\Lambda_{\rm QCD}^2$, implying that the photon energy is very close to the kinematic endpoint: $E_\gamma^{\max} - E_\gamma = O(\Lambda_{\rm QCD}^2/m_B)$. The heavy-quark expansion does not allow to make model-independent predictions for the structure of the individual resonance contributions.

The X_s state can decay through a number of resonances given in Tab. 1-2. There are six resonances plus a continuum contribution feeding the photon spectrum in the energy interval between 2.4 and 2.6 GeV. Hence, an average over this interval should be calculable using global quark–hadron duality, although a much finer resolution cannot be obtained. In the hadronic mass spectrum, the $K^*(892)$ peak is clearly separated from the rest; however, the next resonances already have widths exceeding the level spacing and hence are overlapping. Therefore only this resonance will be considered separately. The prescription given in [34] consists of a single Breit–Wigner peak for the $K^*(892)$ followed by a continuum above a threshold $M_{\rm cont}$, which is dual to the higher resonance contributions and given by the inclusive spectrum calculated using the heavy-quark expansion.

This gives

$$\frac{\mathrm{dB}}{\mathrm{d}M_H} = \frac{2M_H N_{K^*}\,\mathrm{B}(B\to K^*\gamma)}{(M_H^2-m_{K^*}^2)^2+m_{K^*}^2\Gamma_{K^*}^2} + \Theta(M_H-M_{\mathrm{cont}})\,\frac{\mathrm{dB_{incl}}}{\mathrm{d}M_H}\,, \tag{1.59}$$

where

$$N_{K^*} = \frac{m_{K^*}\Gamma_{K^*}}{\arctan\left(\dfrac{m_{K^*}}{\Gamma_{K^*}}\right)+\dfrac{\pi}{2}}. \tag{1.60}$$

is the normalization of the Breit–Wigner distribution.

The continuum threshold M_{cont} is then fixed by the requirement that the total branching ratio be the same as that predicted by the heavy-quark expansion, yielding the condition

$$\int_0^{M_{\mathrm{cont}}} \mathrm{d}M_H\,\frac{\mathrm{dB_{incl}}}{\mathrm{d}M_H} = \mathrm{B}(B\to X_s\gamma)\Big|_{E_\gamma>E_{\mathrm{cont}}} = \mathrm{B}(B\to K^*\gamma)\,, \tag{1.61}$$

where $E_{\mathrm{cont}} = \frac{1}{2}(m_B^2 - M_{\mathrm{cont}}^2)/m_B$.

The ratio of resonant over non-resonant branching fraction, as well as the cut-off mass, depends on the input parameter λ and m_b. The result is shown in Fig. 1-7.

In this analysis, the $B \to K^*(892)\gamma$ over the non-resonant ratio is fixed to the experimental measurements. The weighted average of the *BABAR* measurements for the two charge states [44] gives, for the resonant branching ratio:

$$\mathcal{B}(B\to K^*\gamma) = (4.03\pm0.43)\times10^{-5}. \tag{1.62}$$

The world weighted average, for the non-resonant branching ratio, is (see Sec. 1.5):

$$\mathcal{B}(B\to X_s\gamma) = (3.34\pm0.38)\times10^{-4}. \tag{1.63}$$

This gives a $B \to K^*(892)\gamma$ over the non-resonant ratio of $\sim 12\%$.

The parameters, from which the shape function is computed, see Eq. 1.57, are set to the following values: $m_b = 4.8\,\mathrm{GeV}/c^2$, $\mu_\pi^2 = 0.3\,\mathrm{GeV}^2$, $m_B = 5.2788\,\mathrm{GeV}/c^2$. The minimum energy of the photon is given by $E_\gamma \geq \frac{1}{2}(1-\delta)m_b$ where the cutoff parameter δ is set to be 0.9. The renormalization scale μ_b is set at the b-quark mass m_b. The ratio of the charm and beauty quark masses $z = m_c/m_b$ is set to 0.22 in agreement with the most recent theoretical calculation [35]

The m_{X_s} cut-off is computed in agreement with the Kagan-Neubert prescription described above, resulting $m_{X_s}^{cut-off} = 1.03\,\mathrm{GeV}/c^2$. Making use of Eq. 1.58 , this leads to an upper cut-off for the energy photon at $E_\gamma = 2.54\,\mathrm{GeV}$.

In this analysis we rely on the signal model primarily to compute our efficiency and the effect on it varying the model; only the shape and the ratio of resonant over non-resonant matters for this.

This model is also used for the optimization of the selection criteria. This is the only place where an assumed inclusive branching fraction matters. But in this context, neither that assumption nor using a "wrong" model can cause any bias; at worst they result in slightly non-optimum selection cuts.

The error on the experimental measurement, and on the used model will be taken into account in the systematics effect.

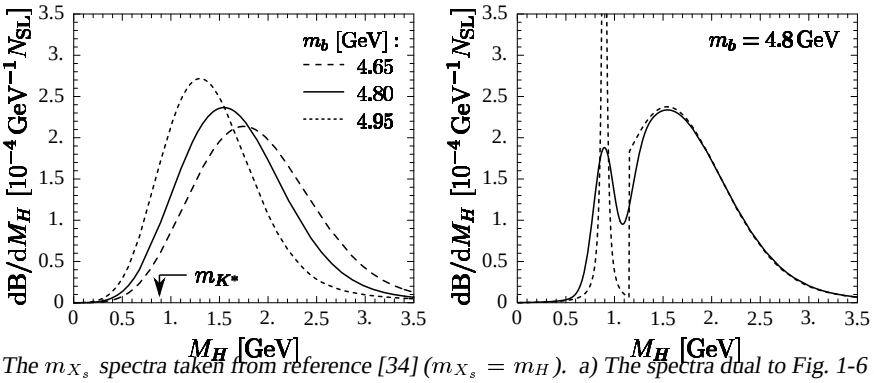

Figure 1-7. *The m_{X_s} spectra taken from reference [34] ($m_{X_s} = m_H$). a) The spectra dual to Fig. 1-6 using Eq. 1.58 for different m_b choices; b) one of the m_{X_s} spectra modified to include the $K^*(892)$ resonance [34].*

1.4.2 Resonant contribution

The branching fractions of the decay $B^\pm \to K^{*\pm}(892)\gamma$ and $B^0 \to K^{*0}(892)\gamma$ have been measured [44, 45, 46] to be:

$$\mathcal{B}(B^\pm \to K^{*\pm}(892)\gamma) = (3.83 \pm 0.62(\text{stat.}) \pm 0.22(\text{syst.})) \times 10^{-5}\,,$$
$$\mathcal{B}(B^0 \to K^{*0}(892)\gamma) = (4.23 \pm 0.40(\text{stat.}) \pm 0.22(\text{syst.})) \times 10^{-5}\,.$$

These numbers are not well predicted by theory because they require the difficult calculation of a heavy-to-light form factor at $q^2 = 0$. In fact recent calculations give values of $\sim 7 \times 10^{-5}$ which are large compared to the experimental measurement. As already discussed in the previous section the $B \to K^*\gamma$ is modeled by a Breit–Wigner function with peak and width fixed, from the experimental, to be respectively 892 MeV and 50.8 MeV and the branching ratio set to the weighted average of the *BABAR* measurements:

$$\mathcal{B}(B \to K^*\gamma) = (4.03 \pm 0.43) \times 10^{-5}. \tag{1.64}$$

1.5 Existing measurements of $B \to X_s\gamma$

In this section a short review of the existing measurement of $B \to X_s\gamma$ is presented both for published and preliminary results, focusing on the experimental aspects of each technique and giving an idea of the theoretical uncertainties associated to them.

The $B \to X_s\gamma$ decay was measured by several independent e^+e^- experiments, mostly at the $\Upsilon(4S)$ resonance, [47, 48, 49, 50, 51, 52]. In 1994 the first inclusive $B \to X_s\gamma$ measurement was done by the CLEO collaboration through the measurement of its characteristic photon energy spectrum in 1994 using a sample of $2.2 \times 10^6\, B\bar{B}$ events.

Only the high part of the $B \to X_s\gamma$ photon spectrum is observed. Some lower cut-off in the photon energy was imposed in order to suppress the background from other B decay processes. The $B\bar{B}$ background mainly arises from the processes $B \to \pi^0 X$ and $\pi^0 \to \gamma_1\gamma_2$ or $B \to \eta X$ and $\eta \to \gamma_1\gamma_2$, where γ_1 has high energy and γ_2 either has energy too low to be observed or is not in the geometric acceptance of the detector. Moreover, there is a small component ($\sim 5\%$) from the process $B \to \bar{n}X$ or $B \to K_L X$, where the anti-neutron or the neutral kaon interacts hadronically with the electromagnetic calorimeter, faking a photon.

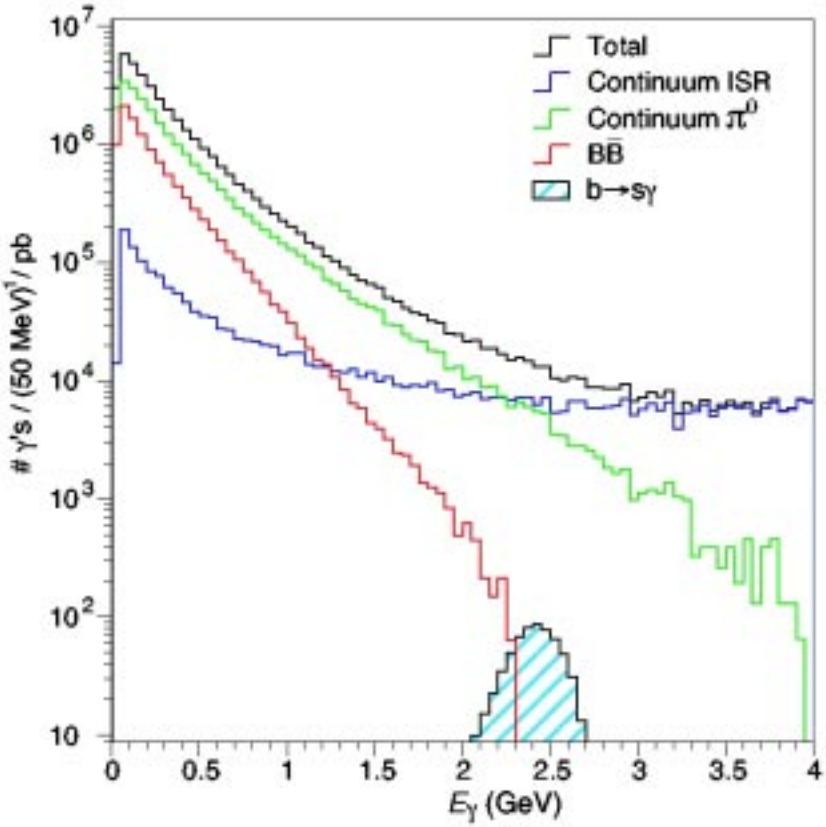

Figure 1-8. *Levels of inclusive photons from various background processes at $\Upsilon(4S)$ and the expected signal from $b \to s\gamma$: ISR, $B\bar{B}$ and π^0 backgrounds are shown (from the bottom to the top at $E_\gamma = 0.5$), from [54].*

As explained in Sec. 1.2, to obtain the total branching ratio, an extrapolation to the full photon spectrum has to be done. In the first Cleo measurement a phenomenological model [37] model was used, resulting in a large systematic error for this model dependence: [47]

$$\mathcal{B}(B \to X_s\gamma) = (2.32 \pm 0.57_{stat} \pm 0.35_{syst}) \times 10^{-4}. \tag{1.65}$$

The first error is statistical and the second is systematic (including model dependence).

Besides the high energy cut-off to suppress the background from other B decays, two different techniques were used to suppress the continuum background in this first CLEO measurement. In the first (semi-inclusive) technique all products were reconstructed as in the exclusive measurement. The background in the measurement of exclusive modes is naturally low, because of kinematical constraints and of the beam energy constraint. In order to reduce the combinatoric background, only $K(n\pi)\gamma$, with $n \leq 4$ and at most one π^0, were chosen as final states in this analysis, which accounts for $\sim 50\%$ of the inclusive rate. In the second (fully inclusive) technique, only the photon was explicitly reconstructed. As shown in Fig. 1-8, there are very large backgrounds, both from the initial-state-radiation (ISR) process $e^+e^- \to q\bar{q}\gamma$, where one of the beam electrons radiates a hard photon before annihilation, and from inclusive π^0/η production in which one of the photons from the decay is not detected. Background suppression was therefore more difficult with this technique. For this purpose, topological differences between the spherical $B\bar{B}$ events and the two jets $e^+e^- \to q\bar{q}$ as shown in Fig. 1-9 were used. While the signal events are spherical because the B mesons are almost at rest at the $\Upsilon(4S)$ resonance, the continuum events have a jet-like structure. With the help of a neural network, several event-shape variables were combined into a single one, which tends toward $+1$ for $b \to s\gamma$ and toward -1 for the ISR and $q\bar{q}$ processes; the signal was extracted from a one-parameter fit to that variable.

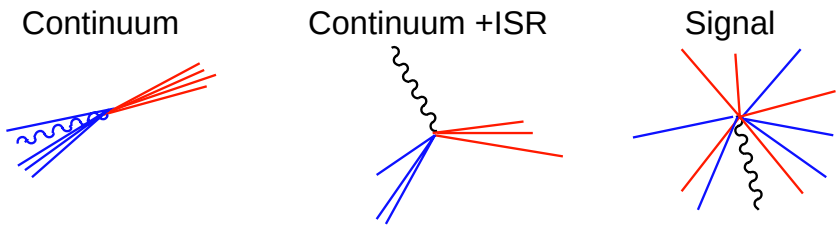

Figure 1-9. *Examples of idealized event shapes. The straight lines indicate hadrons and the wavy lines photons, from [55].*

The signal efficiency (32%) was very high with respect to the first technique (9%). However the first technique has a better signal-to-noise ratio, so that the two methods had nearly equal sensitivity. The branching ratio reported above represents the average of the two technique measurements, taking into account the correlation.

In 2001, CLEO published a new measurement [48], based on three times more data (10×10^6 events). The spectrum down to 2.0 GeV was used, which includes almost 90% of the $B \to X_s\gamma$ yield. This also leads to a significant background from B decay processes other than $B \to X_s\gamma$, located within 2.0 – 2.2 GeV. The continuum background was suppressed with the same two approaches as in the first measurement, but within a fully integrated analysis. What remained of the continuum background was subtracted using off-resonance data.

In order to obtain the corrected branching ratio of $B \to X_s\gamma$, two extrapolations were necessary. What was directly measured was the branching fraction for $B \to X_s\gamma$ plus $B \to X_d\gamma$. The $B \to X_d\gamma$ part was subtracted by using the theory input statement that, according to the SM expectation, the $B \to X_d\gamma$ and the $B \to X_s\gamma$ branching fractions are in the ratio $|V_{td}/V_{ts}|^2$. Therefore the branching ratio was corrected down by $(4.0 \pm 1.6)\%$ of itself - assuming the validity of the SM suppression factor $|V_{td}/V_{ts}|^2$. In this measurement, the corresponding fraction was estimated to be $R = 0.915^{+0.027}_{-0.055}$ using the model of Kagan and Neubert[34], which allowed for the extrapolation of the measured branching ratio to the total $B \to X_s\gamma$ branching ratio ($E_\gamma > 0.25$ GeV). The present CLEO measurement for the $B \to X_s\gamma$ branching ratio is

$$\mathcal{B}(B \to X_s\gamma) = (3.21 \pm 0.43_{stat} \pm 0.27_{syst} {}^{+0.18}_{-0.10\,mod}) \times 10^{-4}. \tag{1.66}$$

The errors represent statistics, systematics, and the model dependence (due to the extrapolation below $E_\gamma = 2.0$ GeV) respectively.

There are also data at the Z^0 peak from the LEP experiments. The ALEPH collaboration [49] has measured the inclusive branching ratio based on 0.8×10^6 $b\bar{b}$ pairs.

$$\mathcal{B}(H_b \to X_s\gamma) = (3.11 \pm 0.80_{stat} \pm 0.72_{syst}) \times 10^{-4}. \tag{1.67}$$

The signal was isolated in lifetime-tagged $b\bar{b}$ events by the presence of a hard photon associated with a system of high momentum and high rapidity hadrons. It should be noted that the branching ratio in 1.67 involves a weighted average of the B mesons and Λ_b baryons produced in Z^0 decays (hence the symbol H_b) different from the corresponding one given by CLEO, which has been measured at the $\Upsilon(4S)$ resonance.

BELLE has also presented a measurement [50] based on 6.07×10^{-6} $B\bar{B}$ events at the $\Upsilon(4S)$ resonance. A semi-inclusive analysis was used to reconstruct the $B \to X_s\gamma$ decay from a primary photon, a kaon and multiple pions (no more than one π^0). The background reduction includes an effective $E_\gamma > 2.24$ GeV photon energy cut-off which corresponds to a cut in the hadronic mass spectrum of $M_{X_s} = 2.05$ GeV/c^2 as quoted in [50]; $E_\gamma = (M_B^2 - M_{X_s}^2)/(2M_B)$:

$$\mathcal{B}(B \to X_s\gamma) = (3.37 \pm 0.53_{stat} \pm 0.42_{syst} \pm 0.54_{mod}) \times 10^{-4}, \tag{1.68}$$

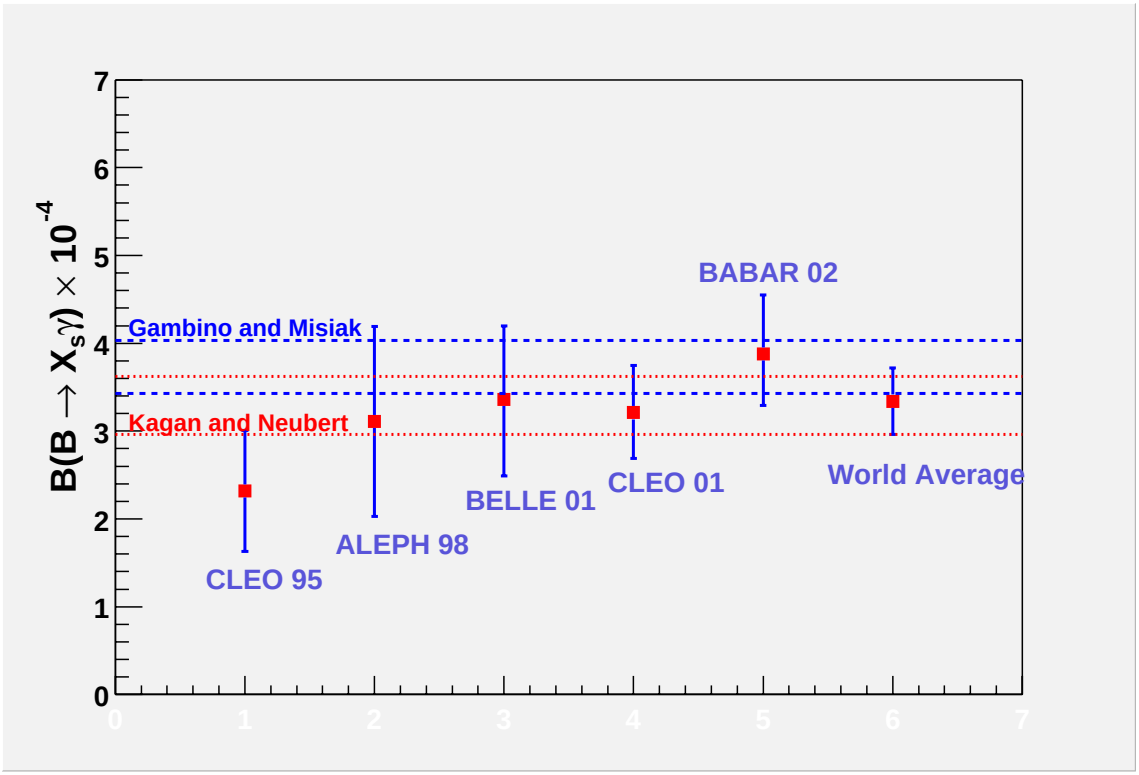

Figure 1-10. *$B \to X_s\gamma$ measurements versus theoretical predictions, from [51].*

which is consistent with previous measurements.

BABAR presented two preliminary analyses on the $B \to X_s\gamma$ branching ratio, a fully inclusive and a semi-inclusive one [51]. The fully inclusive BABAR measurement has used the largest number of B mesons, so far. It is based on almost 60×10^6 $B\bar{B}$ events at the $\Upsilon(4S)$ resonance. The method of extracting the signal from the data is similar to what was done for previous measurements: the continuum background was subtracted with the help of off-resonance data. The $B\bar{B}$ contribution was deduced from MonteCarlo predictions.

However, the high statistics available in this BABAR measurement allowed for additional techniques: a lepton tag on a high-momentum electron or muon was also required to suppress continuum backgrounds. For the $B \to X_s\gamma$ signal events, the lepton arises from the semi-leptonic decay of the other B meson. Leptons also occur in the continuum background, most notably from the semi-leptonic decays of charm hadrons, but their production is less frequent and their momentum lower than those from a B decay. Because a lepton tag is imposed on the other B meson, one can reject the continuum background without introducing any model dependence since no requirement is imposed on the signal decay. A $\times 1200$ reduction of the background was achieved at the cost of 5% efficiency of the lepton tag. This effective method to suppress the continuum background was possible because of the high statistics of the new BABAR measurement.

The systematic precision was limited by the size of the $B\bar{B}$ background control samples scaling in proportion to the signal sample. The systematic precision limited the lower bound to $E_\gamma > 2.1$ GeV (measured in the e^+e^- center-of-mass system). The preliminary BABAR measurement is

$$\mathcal{B}(B \to X_s\gamma) = (3.88 \pm 0.36_{stat} \pm 0.37_{syst}{}^{+0.43}_{-0.23\,mod}) \times 10^{-4}. \quad (1.69)$$

Besides this fully inclusive analysis, BABAR also presented a semi-inclusive analysis where twelve exclusive $b \to s\gamma$ decays were fully reconstructed, which led to the following measurement of the inclusive branching ratio:

$$\mathcal{B}(B \to X_s\gamma) = (4.4 \pm 0.5_{stat} \pm 0.8_{syst} \pm 1.3_{mod}) \times 10^{-4}. \tag{1.70}$$

The error is much larger than the one of the previous semi-inclusive measurements, but includes also less final states; only states including $1-3$ pions rather than $1-4$ pions were reconstructed.

As Fig. 1-10 shows, all the measurements of the 'total' $B \to X_s\gamma$ branching ratio available so far are consistent with each other and also consistent with the SM predictions (see Sec. 1.3). A weighted average of the available experimental measurements is problematic, because the model dependence errors (and also the systematic errors) are correlated and differ within the various measurements. A recent analysis taking into account the correlations leads to the following world average [56]:

$$\mathcal{B}(B \to X_s\gamma) = (3.34 \pm 0.38) \times 10^{-4}. \tag{1.71}$$

1.6 CP asymmetry in $B \to X_s\gamma$ decays

The CKM mechanism that predicts CP violation introducing one single phase has passed its first precision test in the golden B mode, $B_d \to J/\psi K_S$, at the 5% level. Nevertheless, there is still room for non-standard CP phases, especially in the FCNC $\Delta S = 1$ modes.

The direct *normalized* CP asymmetries of the inclusive decay modes is given by [1]:

$$\alpha_{CP} = \frac{\Gamma(b \to s\gamma) - \Gamma(\bar{b} \to \bar{s}\gamma)}{\Gamma(b \to s\gamma) + \Gamma(\bar{b} \to \bar{s}\gamma)}. \tag{1.72}$$

Such an asymmetry can be different from zero only if the decay is due to two or more amplitudes with different strong and weak phases.

Since the Standard Model rate is dominated by a single diagram, it predicts a CP asymmetry of less than 1 %. Some non-SM models allow the CP asymmetry to be above 10% without changing the inclusive branching fraction [43].

It is important to distinguish between $b \to s\gamma$ and $b \to d\gamma$ in making these measurements. The Standard Model predicts in fact much larger CP asymmetries in $b \to d\gamma$ ($\approx$ 10%), but in the sum of $b \to s\gamma$ and $b \to d\gamma$ the CP asymmetries exactly cancel. This is also true in minimal flavour violating extensions of the Standard Model. Theoretical NLL QCD predictions of the *normalized* CP asymmetries of the inclusive channels (see [43]) within the SM can be expressed by the approximate formula:

$$\begin{aligned} \alpha_{CP}(B \to X_s\gamma) &\approx 0.334 \times \Im[\epsilon_s] \approx +0.6\%\,, \\ \alpha_{CP}(B \to X_d\gamma) &\approx 0.334 \times \Im[\epsilon_d] \approx -16\%. \end{aligned} \tag{1.73}$$

where

$$\epsilon_s = \frac{V_{us}^* V_{ub}}{V_{ts}^* V_{tb}} \simeq -\lambda^2(\rho - i\eta), \qquad \epsilon_d = \frac{V_{ud}^* V_{ub}}{V_{td}^* V_{tb}} \simeq \frac{\rho - i\eta}{1 - \rho + i\eta}. \tag{1.74}$$

[1] This is the sign convention that is generally adopted in theory and experiment, which implies $\alpha_{CP}(B^0) = (\Gamma(\bar{B}^0 \to X_s^0\gamma) - \Gamma(B^0 \to X_{\bar{s}}^0\gamma))/(\Gamma(\bar{B}^0 \to X_s^0\gamma) + \Gamma(B^0 \to X_{\bar{s}}^0\gamma))$ and $(\alpha_{CP}(B^\pm) = (\Gamma(B^- \to X_s^-\gamma) - \Gamma(B^+ \to X_{\bar{s}}^+\gamma))/(\Gamma(B^- \to X_s^-\gamma) + \Gamma(B^+ \to X_{\bar{s}}^+\gamma))$.

The two CP asymmetries are connected by the relative factor $\lambda^2\left((1-\rho)^2+\eta^2\right)$. The small SM prediction for the CP asymmetry in the decay $B \to X_s\gamma$ is a result of three suppression factors. There is an α_s factor needed in order to have a strong phase; moreover, there is a CKM suppression of order λ^2 and there is a GIM suppression of order $(m_c/m_b)^2$ reflecting the fact that in the limit $m_c = m_u$ any CP asymmetry in the SM would vanish.

The first measurement of an inclusive CP asymmetry was performed by CLEO [38] using two distinct methods of flavour-tagging. The first method requires only a high energy photon (between 2.2 and 2.7 GeV) and a lepton from the other B to give the flavour tag. In this method the dominant source of mistags arises from $B^0 - \bar{B}^0$ mixing. The method does not distinguish between $b \to s\gamma$ and $b \to d\gamma$. Their second method employs "pseudo-reconstruction" of a possible X_s system which is self-tagging. Their final direct CP asymmetry measurement is a weighted average of the two methods, and hence a weighted average of the asymmetries in $b \to s\gamma$ and $b \to d\gamma$ They quote:

$$A_{CP} = 0.965 A_{CP}(b \to s\gamma) + 0.02 A_{CP}(b \to d\gamma) = (-0.079 \pm 0.108 \pm 0.022)\cdot(1.0 \pm 0.030). \tag{1.75}$$

The first (and by far largest) error is statistical, the second is an additive systematic, and the third a multiplicative systematic. This result rules out some of the more extreme non–Standard Model predictions.
Belle has recently presented a CP asymmetry in the an inclusive measurement [42] based on $\sim 140\,\mathrm{fb}^{-1}$ finding:

$$\alpha_{CP} = -0.004 \pm 0.051 \pm 0.038. \tag{1.76}$$

for $B \to X_s\gamma$ events having recoil mass smaller than $2.1\,\mathrm{GeV}/c^2$ and using a sum of exclusive final states which are lepton-tagged by the other B. This corresponds to $-0.107 < \alpha_{CP} < 0.099$ at 90% confidence level, where the statistical and systematic errors are added in quadrature, Gaussian errors are assumed. Large effects are thus already excluded.

The same conclusion can be deduced from the measurements of the CP asymmetry in the exclusive mode $B \to K^*(892)\gamma$ of CLEO [40], $\alpha_{CP} = +0.08 \pm 0.13_{stat} \pm 0.03_{syst}$, of BABAR [41], $\alpha_{CP} = -0.044 \pm 0.076 \pm 0.082$, and of BELLE [39], $\alpha_{CP} = -0.022 \pm 0.048 \pm 0.017$. The preliminary measurement of BELLE is the best by far, based on 65.4×10^6 B meson pairs and implies that, at 90% confidence level, α_{CP} in the exclusive $B \to K^*\gamma$ lies between $-0.106 < \alpha_{CP} < +0.062$.

From an experimental point of view, there are several ways in which an α_{CP} analysis differs from the branching fraction analysis: the need to allow for mistagging; the possibility of asymmetries in the backgrounds or selection efficiencies; and the different way in which model-dependent uncertainties affect the result.

The flavor of the decaying $B \to X_s\gamma$ is determined from the tagging requirements on the non-signal B . A fraction ω of the tags for signal events will be assigned the wrong charge; ω is referred to as the *mistag fraction*. There are two contributions to ω. First, for B^0 and $\overline{B}^0$ decays there is a probability of an oscillation taking place before decay, leading to an incorrect flavor tag. The mistag fraction from this source is equal to the time-integrated B^0 - $\overline{B}^0$ mixing probability, χ, the world average value of which is 0.181 ± 0.004 [60]. This is an irreducible source of mistagging. Second, for both B^0 and $B^\pm$ mesons there are decays where the flavour of the b quark within the meson is incorrectly tag.

In the analysis described in this thesis, one B is fully reconstructed in a hadronic decay, allowing the tagging of the flavour of the b quark with negligible mistag fraction and the separation of charged and neutral B mesons. This implies that the only contribution to the mistag ratio is due to neutral B oscillation. Also this measurement doesn't separate $B \to X_s\gamma$ decays from $B \to X_d\gamma$ although it will be possible to do so with higher statistics by looking for the K_s in the X system.

The value of α_{CP}^{meas} , in neutral B mesons tag events, must be corrected for the mistag fraction to yield the underlying asymmetry, α_{CP}:

$$\alpha_{CP} = \frac{\alpha_{CP}^{meas}}{(1-2\chi)}\ . \tag{1.77}$$

This means that the statistical precision of α_{CP} is diluted by a factor of $(1-2\chi)$.

No correction needs to be applied in the case of charged B mesons tagged events.

The last consideration is the relative importance of statistical, systematic and model dependent errors in the α_{CP} analysis. As discussed in Sec. 1.3 the branching fraction analysis has a significant model dependence which decreases as more of the spectrum is included by lowering the minimum requirement on E_γ. For the α_{CP} measurement this model dependence cancels out to first order for any requirement on E_γ.

1.7 $B \to X_s\gamma$ with a fully reconstructed B

The analysis presented in this thesis is based on a novel technique consisting in the study of high energy photons recoiling to fully reconstructed B 's. This technique offers many advantages:

- A very clean environment. One of the two B mesons from the decay of the $\Upsilon(4S)$ is reconstructed in a fully hadronic mode. We will refer it as B_{reco} . The remaining particles of the event originate from the other B , are referred as B_{recoil} .
- The B_{recoil} 4-vector is measured, and hence all relevant kinematic quantities are known in the B_{recoil} rest frame. This information is advantageous for signal selection since the photon spectrum is not smeared from the unknown boost of the B mesons in the $\Upsilon(4S)$ frame like fully inclusive analysis.

  In the analysis we will refer as E_γ to the photon energy in B rest frame.
- Absolute luminosity and B reconstruction efficiencies are not needed since normalization is taken from the number of reconstructed B's before applying any selection. This avoids errors from incorrectly luminosity estimates.
- The purity of the B_{reco} sample can be adjusted selecting only a sub-sample of the reconstructed modes on the tag side.
- Continuum events can be subtracted on the B_{reco} side performing a fit toM_{ES} as explained in Sec. 3.4.4 without using off-resonance data, of which much fewer statistics than on-peak data are available.
- Since the kinematic is over-constrained, the resolution on the reconstructed quantities, such as the mass of the hadronic system m_{X_s}, can be improved by using a kinematic fit.
- The fully hadronic reconstruction of one B in the decay determines the tagging of the charge and flavour of the B 's allowing to measure $BR(B \to X_s\gamma)$ and α_{CP} in B^0 and B^+ separately.

The only drawback of this technique is that the reconstruction efficiency of one B in a fully hadronic mode is very low $\sim 0.4\%$ (see Sec. 3.5). The B factories, thanks to their very high luminosity, represent therefore, the ideal environment for the study of the $B \to X_s\gamma$ decay with this technique.

A $B \to X_s\gamma$ decay of the recoil B meson is identified by the presence of an isolated high energy photon in the event. Detailed studies have been performed on the reconstruction and efficiency of high energetic photons and selection criteria are applied in order to ensure well known efficiencies and minimal backgrounds.

The amount of continuum events in the signal region can be estimated and subtracted from a fit to the M_{ES} distribution as explained in Sec. 3.4.4, but it is still important to reduce this background in order to minimize the statistical error of the measurement. To reject those events a multivariate analysis technique (Fisher) is used combining information for the event decay topology.

The $B \to X_s\gamma$ signal yield is finally extracted from a fit to the photon energy E_γ distribution on events that fulfill the selection criteria.

Due to the lower level of background, the signal spectrum is measured down to $1.9\,\mathrm{GeV}$, a value never reached in previous measurements. This allows to reduce the theoretical uncertainties due to the extrapolation in the unmeasured part of the spectrum.

The direct CP asymmetry α_{CP} is then extracted with the same technique and event selection in B^0 and $B^\pm$ separately.

2

BABAR Experiment at PEP-II

2.1 Introduction

The primary goal of the BABAR experiment is the study of CP-violating asymmetries in the decay of neutral B meson. Secondary goals are precision measurement of decays of bottom and charm mesons and of τ leptons, searches for rare processes accessible because of the high luminosity of PEP II B Factory.

The PEP-II B Factory is an e^+e^- asymmetric collider running at a center of mass energy of 10.58 GeV corresponding to the mass of the $\Upsilon(4S)$ resonance. The electron beam in the High Energy Ring (HER) has 9.0 GeV and the positron beam in the Low Energy Ring (LER) has 3.1 GeV. The $\Upsilon(4S)$ is therefore produced with a Lorentz boost of $\beta\gamma = 0.56$. This boost makes it possible to reconstruct the decay vertices of the two B mesons, to determine their relative decay times Δt, and thus to measure the time dependence of their decay rates, since, without boost, this distance would be too small ($\sim 30\ \mu$) to be measured by any vertex tracker.

The BABAR detector [57] has been optimized to reach the primary goal of the CP asymmetry measurement. This measurement needs the complete reconstruction of a B decay in a CP eigenstate, the flavour identification (tagging) of the non-CP B and a measure of the distance of the two decay vertices. To fulfill these needs, a very good vertex resolution, both transverse and parallel to the beam direction, excellent reconstruction efficiency for charged particles and a very good momentum resolution, efficient electron and muon identification, with low misidentification probabilities for hadrons, are required.

A longitudinal section of the BABAR detector is shown in Fig. 2-1.The detector innermost part is reserved for the silicon vertex tracker (SVT), then there is the drift chamber (DCH), the Čerenkov light detector (DRC) and the CsI electromagnetic calorimeter (EMC). All those detector sub-systems are surrounded by a solenoidal superconductor magnetic field. The iron used for the return flux has been instrumented (IFR) for muons and neutral hadrons, like K_L and neutrons, detection.

The detector geometry is cylindrical in the inner zone and hexagonal in the outermost zone: the central part of the structure is called *barrel* and it's closed forward and backward by *end caps*. The covered polar angle ranges from 350 mrad, in the forward, to 400 mrad in the backward directions (defined with respect to the high energy beam direction). The *BABAR* coordinate system has the z axis along the boost direction (or the beam direction): the y axis is vertical and the x axis is horizontal and goes toward the external part of the ring. In order to maximize the geometrical acceptance for $\Upsilon(4S)$ decays the whole detector is offset, with respect to the beam-beam interaction point (IP), by 0.37 m in the direction of the lower energy beam.

A trigger system is used to separate collisions producing interesting events from those that constitutes the noise, or the background, for instance, beam interactions with residual gas. The trigger system is divided in two consequent levels: the level one trigger ($L1$) is hardware based and is designed to have a maximum output rate of $2\ kHz$ and a maximum time delay of 12 μs, while the other level ($L3$), software based, has a throughput rate limited to $120Hz$ in order to permit an easy storage and processing of collected data.

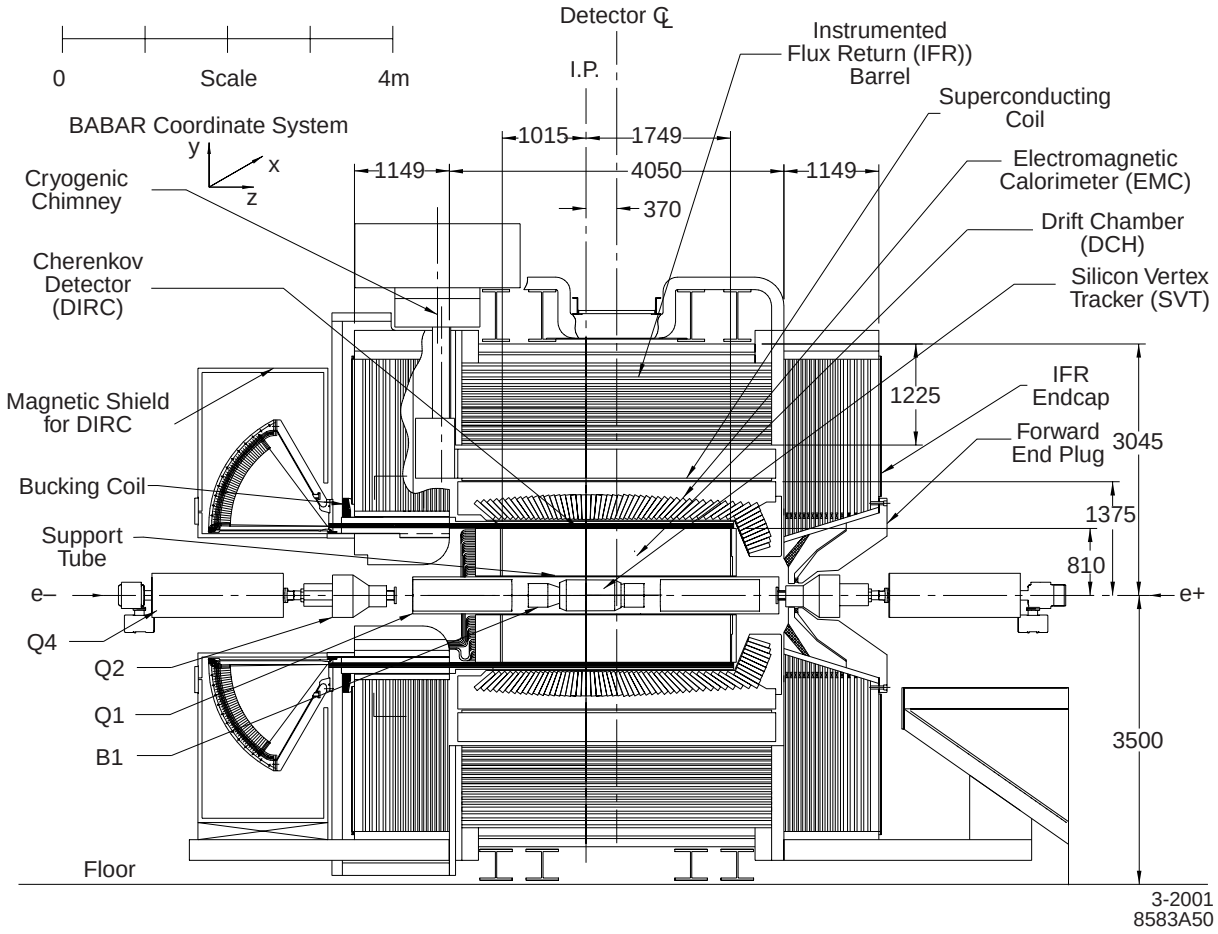

Figure 2-1. BABAR *detector longitudinal section.*

2.2 PEP-II B Factory

PEP-II is a system consisting of two accumulating asymmetric rings designed in order to operate at a center of mass energy of the $\Upsilon(4S)$ resonance mass, 10.58 GeV. Tab. 2-1 shows the various sub-systems parameters: a comparison between typical and design values is presented. As can be easily seen from the table, PEP-II parameters have overcome the project ones in terms of instant luminosity and daily integrated luminosity achieving recently the peak value of $6.8 \times 10^{33}\ cm^{-2}\ s^{-1}$ with a daily integrated luminosity of $370\ pb^{-1}$.

Data is mostly collected at $\Upsilon(4S)$ peak energy. Tab. 2-2 shows the active processes cross sections breakdown at peak energy. From now on the production of light quark pairs (u, d, s) and $charm$ quark pairs will be referred to as "continuum production". In order to study this non-resonant production $\sim 12\%$ of data is collected with a center of mass energy 40 MeV below the $\Upsilon(4S)$ mass value.

PEP-II measures radiative Bhabha scattering to provide a luminosity fast monitor useful for operations. *BABAR* derives the absolute luminosity offline from other QED processes, mainly e^+e^- and $\mu^+\mu^-$ pairs: the systematic uncertainty on the absolute value of the luminosity is estimated to be about 1.5%. This error is dominated by uncertainties in the MonteCarlo generator and the simulation of the detector.

Parameters	Design	Typical
Energy HER/LER (GeV)	9.0/3.1	9.0/3.1
Current HER/LER (A)	0.75/2.15	0.7/1.3
# of bunch	1658	553-829
bunch time separation (ns)	4.2	6.3-10.5
σ_{Lx} (μm)	110	120
σ_{Ly} (μm)	3.3	5.6
σ_{Lz} (μm)	9000	9000
Luminosity ($10^{33}\ cm^{-2}s^{-1}$)	3	4.5
Daily average integrated luminosity (pb^{-1}/d)	135	300

Table 2-1. *PEP-II beam parameters. Design and typical values are quoted and are referred to the fourth year of machine running.*

$e^+e^- \rightarrow$	Cross section (nb)
$b\bar{b}$	1.05
$c\bar{c}$	1.30
$s\bar{s}$	0.35
$u\bar{u}$	1.39
$d\bar{d}$	0.35
$\tau^+\tau^-$	0.94
$\mu^+\mu^-$	1.16
e^+e^-	~ 40

Table 2-2. *Various processes cross sections at $\sqrt{s} = M_{\Upsilon(4S)}$. $Bhabha$ cross section is an effective cross section, within the experimental acceptance.*

The beam energies of the two beams are calculated from the total magnetic bending strength and the average deviations of the accelerating frequencies from their central values. The systematic error on the PEP-II calculation of the absolute beam energies is estimated to be $5 - 10$ MeV, while the relative energy setting for each beam is accurate and stable to about 1 MeV.

The interaction region design, with the two beams crossing in a single interaction point with particles trajectories modified in order to have head on collisions, is realized with a magnetic field, produced by a dipole magnetic system, acting near the interaction point. The collision axis is off-set from the z-axis of the *BABAR* detector by about 20 mrad in the horizontal plane to minimize the perturbation of the beams by the solenoidal field. In this configuration the particles and the beams are kept far apart in the horizontal plane outside the interaction region and parassite collisions are minimized. Magnetic quadrupoles included inside the detector's magnetic field, and hence realized in Samarium-Cobalt, are strongly focusing the beams inside the interaction region.

In order to keep track of PEP-II beams displacement with respect to the *BABAR* detector, the interaction point position is computed on periodic intervals, using two tracks events. Interaction region dimensions (beam-spot) computed in that way are $\sim 150\ \mu m$ along x, $\sim 50\ \mu m$ along y and $1\ cm$ along z axis. The y dimension estimate is completely dominated by tracking resolution and can be improved by looking at luminosity variations as a function of relative beams position. In particular, knowing the beam currents and the x beam-spot dimension, it is possible to get a

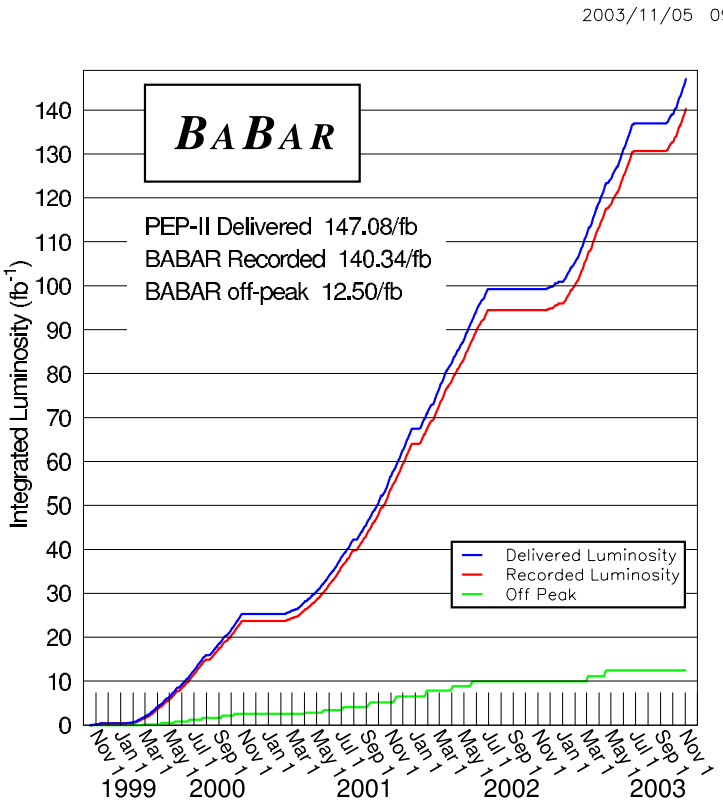

Figure 2-2. *Integrated luminosity and obtained by PEP-II and collected by BABAR from 1999 to 2003.*

resolution on y $(\sigma_y) \sim 5\ \mu m$, value that remain stable within 10% in a one hour time scale. Those measurements can be also verified offline by measuring multi hadrons events primary vertexes[1].

Fig. 2-2 shows the integrated luminosity obtained by PEP-II and collected by *BABAR* from the beginning of data taking (November 1999) to the end of November 2003. This analysis will make use only of data collected in **Run 1** and **Run 2** data taking periods (before November 2002).

2.3 Tracking system

The charged particle tracking system consists of two different components: the silicon vertex tracker (SVT) and the drift chamber (DCH): the main purpose of this tracking system is the efficient detection of charged particles and the measurement of their momentum and angles with high precision. These track measurements are important for the extrapolation to the DIRC, the EMC and the IFR: at lower momenta, the DCH measurements are more important while at higher momenta the SVT dominates.

[1]By reconstructing all the tracks in one event it is possible to have an estimate of primary vertex position: $\Upsilon(4S)$ decay point in transversal plane. Given that the boost along the z axis produces a relative displacement of the two B mesons this method has a relative poor resolution that get worse in presence of long-lived particles.

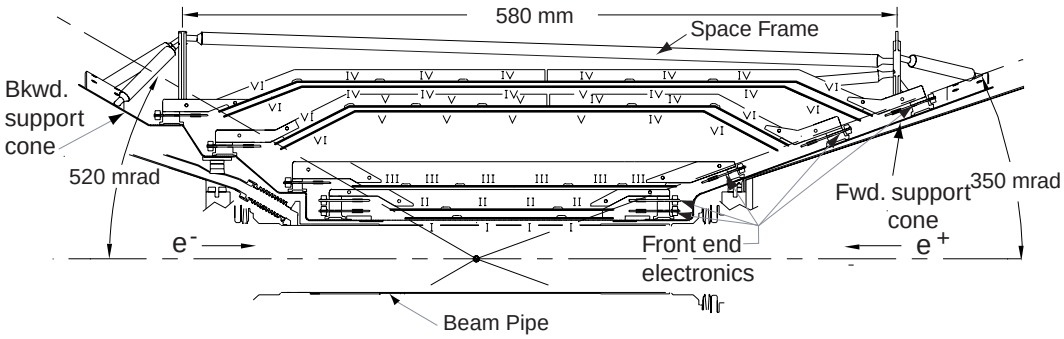

Figure 2-3. SVT *schematic view: longitudinal section*

2.3.1 The Silicon Vertex Tracker: SVT.

The vertex detector has a radius of $20\,cm$ from the primary interaction region: it is placed inside the support tube of the beam magnets and consists of five layers of double-sided silicon strip sensors detectors to provide five measurements of the positions of all charged particles with polar angles in the region $20.1^\circ < \theta < 150^\circ$. Because of the presence of a $1.5\,T$ magnetic field, the charged particle tracks with transverse momenta lower than $\sim 100\ \mathrm{MeV}/c$ cannot reach the drift chamber active volume. So the SVT has to provide stand-alone tracking for particles with transverse momentum less than $120\ \mathrm{MeV}/c$, the minimum that can be measured reliably in the DCH alone: this feature is essential for the identification of slow pions from D^*-meson decays. Because of these, the SVT has to provide redundant measurements.

Beyond the stand-alone tracking capability, the SVT provides the best measurement of track angles which is required to achieve design resolution for the Čerenkov angle for high momentum tracks. The SVT is very close to the production vertex in order to provide a very precise measure of points on the charged particles trajectories on both longitudinal (z) and transverse directions. The longitudinal coordinate information is necessary to measure the decay vertex distance, while the transverse information allows a better separation between secondary vertices coming from decay cascades.

More precisely, the design of the SVT was carried out according to some important guidelines:

- The number of impact points of a single charged particle has to be greater than 3 to make a stand-alone tracking possible, and to provide an independent momentum measure.
- The first three layers are placed as close as possible to the impact point to achieve the best resolution on the z position of the B meson decay vertices.
- The two outer layers are close to each other, but comparatively far from the inner layers, to allow a good measurement of the track angles.
- The SVT must withstand 2 MRad of ionizing radiation: the expected radiation dose is 1 Rad/day in the horizontal plane immediately outside the beam pipe and 0.1 Rad/day on average.
- Since the vertex detector is inaccessible during normal detector operations, it has to be reliable and robust.

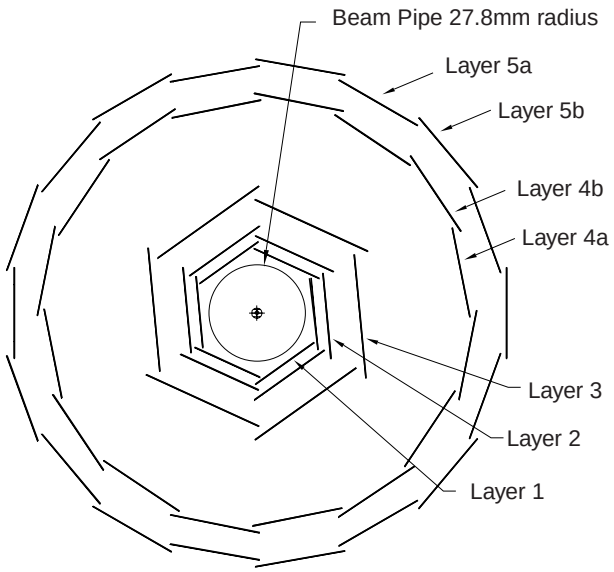

Figure 2-4. *Cross-sectional view of the SVT in a plane perpendicular to the beam axis.*

These guidelines have led to the choice of a SVT made of five layers of double-sided silicon strip sensors: the spatial resolution, for perpendicular tracks must be $10 - 15\ \mu m$ in the three inner layers and about $40\ \mu m$ in the two outer layers. The three inner layers perform the impact parameter measurement, while the outer layers are necessary for pattern recognition and low p_t tracking. The silicon detectors are double-sided (contain active strips on both sides) because this technology reduces the thickness of the materials the particles have to cross, thus reducing the energy loss and multiple scattering probability compared to single-sided detectors. The sensors are organized in modules (Fig. 2-3). The SVT five layers contain 340 silicon strip detectors with AC-coupled silicon strips.

Each detector is $300\ \mu m$-thick but sides range from $41\ mm$ to $71\ mm$ and there are 6 different detector types. Each of the three inner layers has a hexagonal transverse cross-section and it is made up of 6 detector modules, arrayed azimuthally around the beam pipe, while the outer two layers consist of 16 and 18 detector modules, respectively. The inner detector modules are barrel-style structures, while the outer detector modules employ the novel arch structure in which the detectors are electrically connected across an angle. This arch design was chosen to minimize the amount of silicon required to cover the solid angle while increasing the solid angle for particles near the edges of acceptance: having incidence angles on the detector closer to 90 degrees at small dip angles insures a better resolution on impact points. One of the main features of the SVT design is the mounting of the readout electronics entirely outside the active detector volume.

The strips on the two sides of the rectangular detectors in the barrel regions are oriented parallel (ϕ strips) or perpendicular (z strips) to the beam line: in other words, the inner sides of the detectors have strips oriented perpendicular to the beam direction to measure the z coordinate (z-size), whereas the outer sides, with longitudinal strips, allow the ϕ-coordinate measurement (ϕ-side). In the forward and backward regions of the two outer layers, the angle between the strips on the two sides of the trapezoidal detectors is approximately 90° and the ϕ strips are tapered.

The inner modules are tilted in ϕ by 5°, allowing an overlap region between adjacent modules: this provide full azimuthal coverage and is convenient for alignment. The outer modules are not tilted, but are divided into sub-layers and placed at slightly different radii (see Fig. 2-4).

The total silicon area in the SVT is $0.94\ m^2$ and the number of readout channels is about $150\,000$. The geometrical acceptance of SVT is 90% of the solid angle in the c.m. system and typically 80% are used in charged particle tracking.

The z-side strips are connected to the read-out electronics with flexible *Upilex* fanout circuits glued to the inner faces of half-modules: as a matter of fact, each module is divided into two electrically separated forward and backward half-modules. The fanout circuits consist of conductive traces on a thin flexible insulator (copper traces on Kapton): the traces are wire-bonded to the end of the strips.

In the two outer layers, in each module the number of z strips exceeds the number of read-out channels, so that a fraction of the strips is "ganged", i.e., two strips are connected to the same read-out channel. The "ganging" is performed by the fanout circuits. The length of a z strip is about $50\,\mu m$ (case of no ganging) or $100\,\mu m$ (case of two strip connected): the ganging introduces an ambiguity on the z coordinate measurement, which must be resolved by the pattern recognition algorithms. The ϕ strips are daisy-chained between detectors, resulting in a total strip length of up to $26\,cm$. Also, for the ϕ-side, a short fanout extension is needed to connect the ends of the strips to the read-out electronics.

Table 2-3. *Parameters of the SVT layout: these characteristics are shown for each layer.*

	1st layer	2nd layer	3rd layer	4th layer	5th layer
radius (mm)	32	40	54	91-127	114-144
modules/layer	6	6	6	16	18
wafers/module	4	4	6	7	8
read-out pitch (μm)					
ϕ	50-100	55-110	55-110	100	100
z	100	100	100	210	210

The signals from the read-out strips are processed using a new technique, bringing in several advantages. After amplification and shaping, the signals are compared to a preset threshold and the time they exceed this threshold (time over threshold, or ToT) is measured. This time interval is related to the charge induced in the strip by the charged particle crossing it. Unlike the traditional peak-amplitude measurement in the shaper output, the ToT has the advantage of an approximately logarithmic relation of the time interval to the charge signal. This compresses the active dynamic range of the signal, ensuring a good sensitivity in the lower range. When a particle crosses a silicon detector a cluster of adjoining strips producing a signal is formed. The good signal resolution in the lower range ensures a good determination of the tails of the cluster thus improving the resolution on the impact point measurement.

The electronic noise measured is found to vary between 700 and 1500 electrons ENC (equivalent noise charge), depending on the layer and the readout view: this can be compared to the typical energy deposition for a minimum ionizing particle at normal incidence, which is equivalent to ~ 24000 electrons.

During normal running conditions, the average occupancy of the SVT in a time window of $1\,\mu s$ is about 2% for the inner layers, where it is dominated by machine backgrounds, and less than 1% for the outer layers, where noise hits dominate.

The cluster reconstruction is based on a cluster finding algorithm: first the charge pulse height of a single pulse is calculated form the ToT value and clusters are formed grouping adjacent strips with consistent times. The position x of a cluster formed by n strips is evaluated with an algorithm called "head-to-tail" algorithm:

$$x = \frac{(x_1 + x_n)}{2} + \frac{p}{2}\frac{(Q_n - Q_1)}{(Q_n + Q_1)}$$

where x_i and Q_i are the position and the collected charge of i-th strip and p is the read-out pitch. This formula always gives a cluster position within $p/2$ of the geometrical center of the cluster. The cluster pulse height is simply the sum of the strip charges, while the cluster time is the average of the signal times.

The SVT efficiency can be calculated for each half-module by comparing the number of associated hits to the number of tracks crossing the active area of the half-module. Excluding defective readout sections (9 over 208), the combined hardware and software efficiency is 97%.

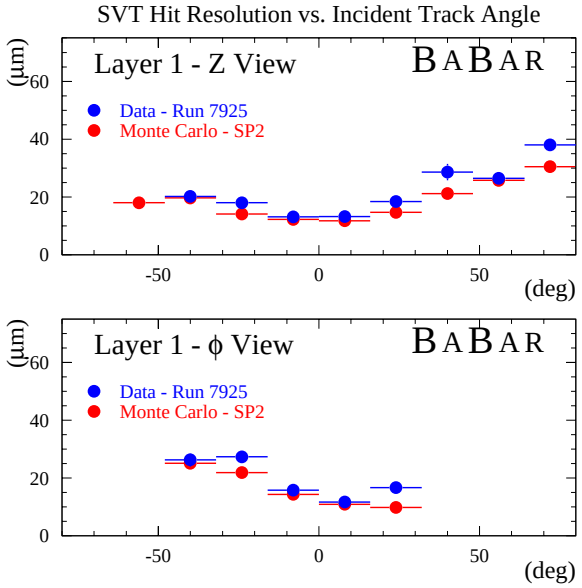

Figure 2-5. *SVT hit resolution in the z and ϕ coordinate in microns, plotted as functions of the track incident angle in degrees.*

The spatial resolution of SVT hits is calculated by measuring the distance (in the plane of the sensor) between the track trajectory and the hit, using high-momentum tracks in two prong events: the uncertainty due to the track trajectory is subtracted from the width of the residual distribution to obtain the hit resolution. The track hit residuals are defined as the distance between track and hit, projected onto the wafer plane and along either the ϕ or z direction. The width of this residual distribution is then the SVT hit resolution. Fig. 2-5 shows the SVT hit resolution for z and ϕ side hits as a function of the track incident angle: the measured resolutions are in very good agreement with the MonteCarlo expected ones. Over the whole SVT, resolutions are raging from $10 - 15\ \mu m$ (inner layers) to $30 - 40\ \mu m$ (outer layers) for normal tracks.

For low-momentum tracks ($p_t < 120$ MeV/c), the SVT provides the only particle identification information. The measure of the ToT value enables to obtain the pulse height and hence the ionization dE/dx: the value of ToT are converted to pulse height using a look-up table computed from the pulse shapes. The double-sided sensors provide up to ten measurements of dE/dx per track: with signals from at least four sensors, a 60% truncated mean dE/dx is calculated. For MIPs, the resolution on the truncated mean dE/dx is approximately 14%: a 2σ separation between kaons and pions can be achieved up to momentum of 500 MeV/c and between kaons and protons beyond 1 GeV/c.

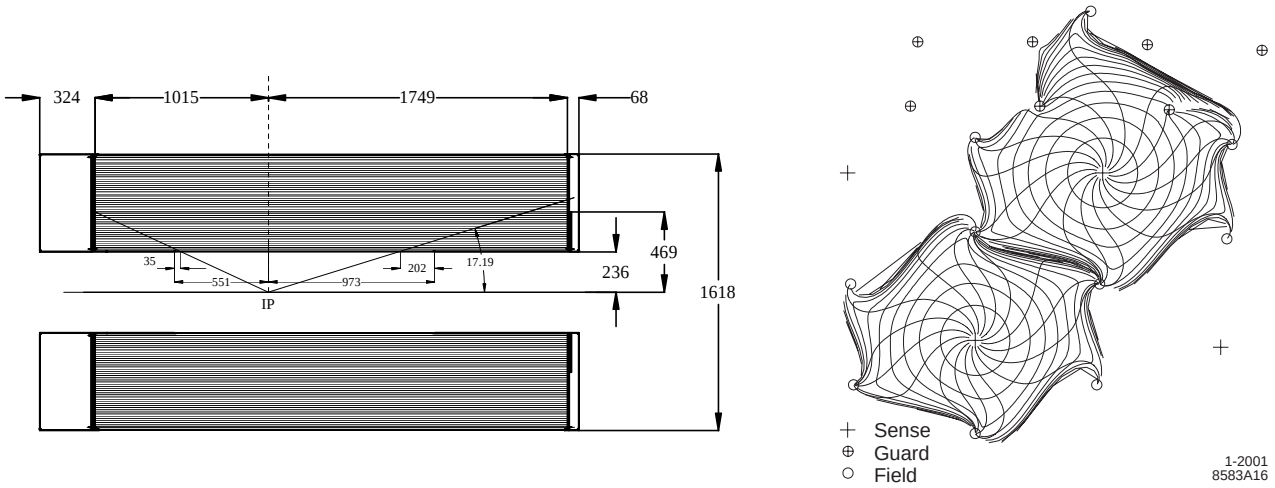

Figure 2-6. *Side view of the BABAR drift chamber (the dimensions are in mm) and isochrones (i.e. contours of equal drift time of ions) in cells of layer* 3 *and* 4 *of an axial super-layer. The isochrones are spaced by* $100\ ns$.

2.3.2 The drift chamber: DCH.

The drift chamber is the second part of *BABAR* tracking system: its principal purpose is the efficient detection of charged particles and the measurement of their momenta and angles with high precision. The DCH complements the measurements of the impact parameter and the directions of charged tracks provided by the SVT near the impact point (IP). At lower momenta, the DCH measurements dominate the errors on the extrapolation of charged tracks to the DIRC, EMC and IFR. The reconstruction of decay and interaction vertices outside of the SVT volume, for instance the K^0_S decays, relies only on the DCH. For these reasons, the chamber should provide maximal solid angle coverage, good measurement of the transverse momenta and positions but also of the longitudinal positions of tracks with a resolution of $\sim 1\,mm$, efficient reconstruction of tracks at momenta as low as $100\ \mathrm{MeV}/c$ and it has to minimally degrade the performance of the calorimeter and particle identification devices (the most external detectors). The DCH also needs to supply information for the charged particle trigger. For low momentum particles, the DCH is required to provide particle identification by measuring the ionization loss (dE/dx). A resolution of about 7% allows π/K separation up to $700\ \mathrm{MeV}/c$. This particle identification (PID) measurement is complementary to that of the DIRC in the barrel region, while in the extreme backward and forward region, the DCH is the only device providing some discrimination of particles of different mass. The DCH should also be able to operate in presence of large beam-generated backgrounds having expected rates of about $5\,kHz$/cell in the innermost layers.

To meet the above requirements, the DCH is a $280\,cm$-long cylinder (see left plot in Fig. 2-6), with an inner radius of $23.6\,cm$ and an outer radius of $80.9\,cm$: it is bounded by the support tube at its inner radius and the particle identification device at its outer radius. The flat end-plates are made of aluminum: since the *BABAR* events will be boosted in the forward direction, the design of the detector is optimized to reduce the material in the forward end. The forward end-plate is made thinner ($12\,mm$) in the acceptance region of the detector compared to the rear end-plate ($24\,mm$), and all the electronics is mounted on the rear end-plate. The device is asymmetrically located with respect to the IP: the forward length of 174.9 cm is chosen so that particles emitted at polar angles of 17.2° traverse at least half of the layers of the chamber before exiting through the front end-plate. In the backward direction, the length of 101.5 cm means that particles with polar angles down to 152.6° traverse at least half of the layers.

The inner cylinder is made of $1\,mm$ beryllium and the outer cylinder consists of two layers of carbon fiber glued on a Nomex core: the inner cylindrical wall is kept thin to facilitate the matching of SVT and DCH tracks, to improve the track resolution for high momentum tracks and to minimize the background from photon conversions and interactions.

Material in the outer wall and in the forward direction is also minimized in order not to degrade the performance of the DIRC and the EMC.

The region between the two cylinders is filled up by a gas mixture consisting of Helium-isobutane ($80\% : 20\%$): the chosen mixture has a radiation length that is five times larger than commonly used argon-based gases. 40 layers of wires fill the DCH volume and form 7104 hexagonal cells with typical dimensions of $1.2 \times 1.9\, cm^2$ along the radial and azimuthal directions, respectively (see right plot in Fig. 2-6). The hexagonal cell configuration has been chosen because approximate circular symmetry can be achieved over a large portion of the cell. Each cell consist of one sense wire surrounded by six field wires: the sense wires are $20\, \mu m$ gold-plated tungsten-rhenium, the field wires are $120\, \mu m$ and $80\, \mu m$ gold-plated aluminum. By using the low-mass aluminum field wires and the helium-based gas mixture, the multiple scattering inside the DCH is reduced to a minimum, representing less than $0.2\% X_0$ of material. The total thickness of the DCH at normal incidence is $1.08\% X_0$.

The drift cells are arranged in 10 super-layers of 4 cylindrical layers each: the super-layers contain wires oriented in the same direction: to measure the z coordinate, axial wire super-layers and super-layers with slightly rotated wires (*stereo*) are alternated. In the stereo super-layers a single wire corresponds to different ϕ angles and the z coordinate is determined by comparing the ϕ measurements from axial wires and the measurements from rotated wires. The stereo angles vary between ± 45 mrad and ± 76 mrad.

While the field wires are at ground potential, a positive high voltage is applied to the sense wires: an avalanche gain of approximately 5×10^4 is obtained at a typical operating voltage of $1960\, V$ and a $80 : 20$ helium:isobutane gas mixture.

In each cell, the track reconstruction is obtained by the electron time of flight: the precise relation between the measured drift time and drift distance is determined from sample of e^+e^- and $\mu^+\mu^-$ events. For each signal, the drift distance is estimated by computing the distance of closest approach between the track and the wire. To avoid bias, the fit does not include the hit of the wire under consideration. The estimated drift distances and the measured drift times are averaged over all wires in a layer.

The DCH expected position resolution is lower than $100\, \mu m$ in the transverse plane, while it is about $1\, mm$ in the z direction. The minimum reconstruction and momentum measure threshold is about $100\ \mathrm{MeV}/c$ and it is limited by the DCH inner radius. The design resolution on the single hit is about $140\, \mu m$ while the achieved weighted average resolution is about $125\, \mu m$. Left plot in Fig. 2-7 shows the position resolution as a function of the drift distance, separately for the left and the right side of the sense wire. The resolution is taken from Gaussian fits to the distributions of residuals obtained from unbiased track fits: the results are based on multi-hadron events for data averaged over all cells in layer 18.

The specific energy loss (dE/dx) for charged particles through the DCH is derived from the measurement of the total charge collected in each drift cell: the specific energy loss per track is computed as a truncated mean from the lowest 80% of the individual dE/dx measurements. Various corrections are applied to remove sources of bias: these corrections include changes in gas pressure and temperature ($\pm 9\%$ in dE/dx), differences in cell geometry and charge collection ($\pm 8\%$), signal saturation due to space charge buildup ($\pm 11\%$), non-linearities in the most probable energy loss at large dip angles ($\pm 2.5\%$) and variation of cell charge collection as a function of the entrance angle ($\pm 2.5\%$).

Right plot in Fig. 2-7 shows the distribution of the corrected dE/dx measurements as a function of track momenta: the superimposed Bethe-Bloch predictions have been determined from selected control samples of particles of different masses. The achieved dE/dx rms resolution for Bhabha events is typically 7.5%, limited by the number of samples and Landau fluctuations, and it is close to the expected resolution of 7%.

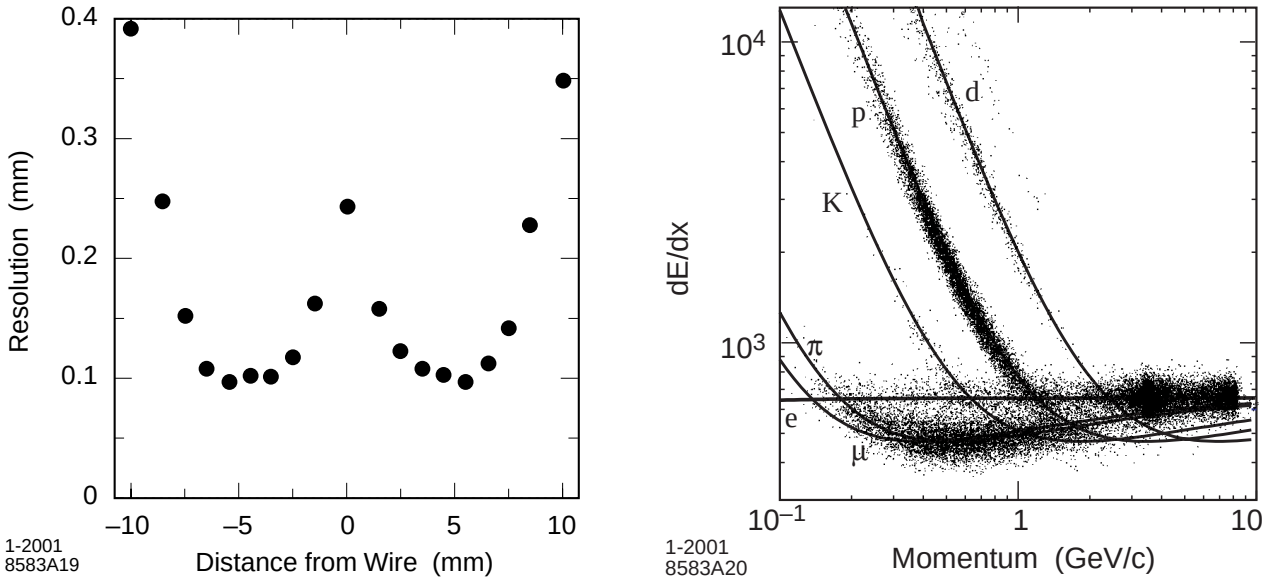

Figure 2-7. *Left plot: DCH position resolution as a function of the drift chamber in layer* 18*, for tracks on the left and right side of the sense wire. The data are averaged over all cells in the layer. Right plot: measurement of* dE/dx *in the DCH as a function of the track momenta. The data include large samples of beam background triggers as evident from the high rate of protons. The curves show the Bethe-Bloch predictions derived from selected control samples of particles of different masses.*

2.3.3 The charged particle tracking system.

As already said, the *BABAR* tracking system is based on SVT and DCH detectors: charged particle tracking has been studied with large samples of cosmic ray muons, e^+e^-, $\mu^+\mu^-$ and $\tau^+\tau^-$ events, as well as multi-hadrons.

Charged tracks are defined by five parameters (d_0, ϕ_0, ω, z_0 and $\tan\lambda$) and their associated error matrix: these parameters are measured at the point of closest approach to the z-axis and d_0 and z_0 are the distances of this point from the origin of the coordinate system (in the $x-y$ plane and on the z axix, respectively). The angle ϕ_0 is the azimuth of the track, λ is the dip angle relative to the transverse plane and ω is the curvature. d_0 and ω have signs that depend on the particle charge.

The track finding and the fitting procedure make use of the Kalman filter algorithm that takes into account the detailed description of material in the detector and the full map of the magnetic field. First of all, tracks are reconstructed with DCH hits through a stand-alone DCH algorithm: the resulting tracks are then extrapolated into the SVT and SVT track segments are added and a Kalman fit is performed to the full set of DCH and SVT hits. Any remaining SVT hits are then passed to the SVT stand-alone track finding algorithms. Finally, an attempt is made to combine tracks that are only found by one of the two tracking systems and thus recover tracks scattered in the material of the support tube.

The efficiency for track reconstruction in the DCH has been measured as a function of transverse momentum, polar and azimuthal angles in multi-track events. These measurement rely on specific final states and exploit the fact that the track reconstruction can be performed independently in the SVT and the DCH. The absolute DCH tracking efficiency is determined as the ratio of the number of reconstructed DCH tracks to the number of tracks detected

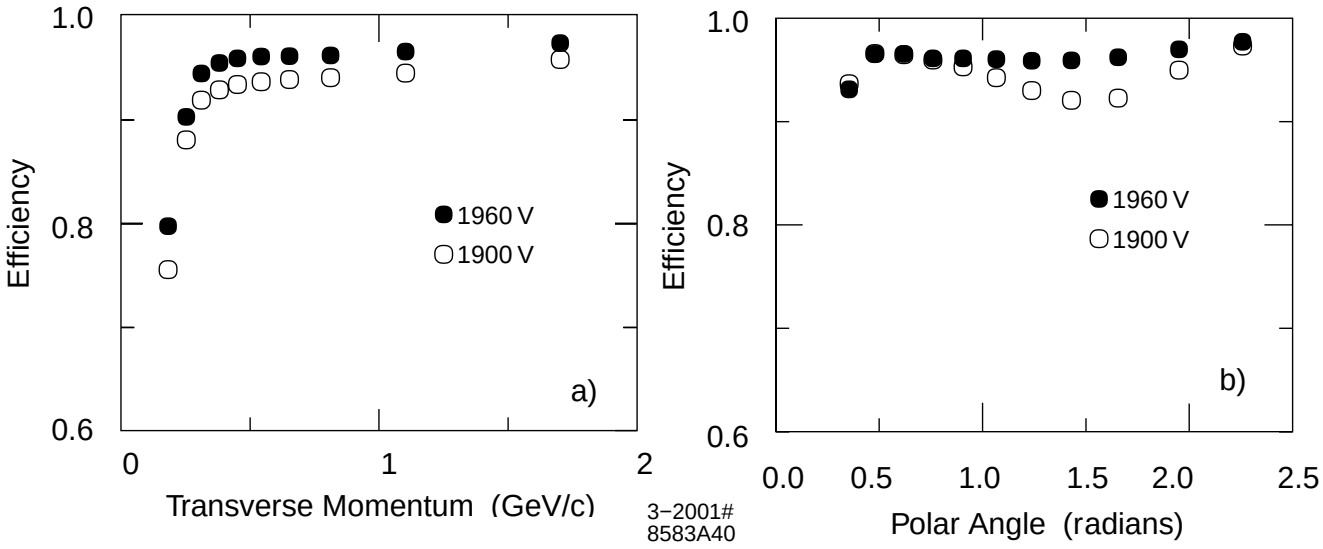

Figure 2-8. *Track reconstruction efficiency in the DCH at operating voltages of $1960\,V$ and $1900\,V$ as a function of transverse momentum (left plot) and of polar angle (right plot). The efficiency is measured in multi-hadron events.*

in the SVT with the requirement that they fall within the acceptance of the DCH. Left plot in Fig. 2-8 shows the efficiency in the DCH as a function of transverse momentum in multi-hadron events.

At design voltage of $1960\,V$, the efficiency averages $98 \pm 1\%$ per track above $200\ \mathrm{MeV}/c$: the data recorded at $1900\,V$ show a reduction in efficiency by about 5% for tracks almost at normal incidence, indicating that the cells are not fully efficient at this voltage (see right plot in Fig. 2-8).

The stand-alone SVT tracking algorithms have a high efficiency for tracks with low transverse momentum: to estimate the tracking efficiency for these low momentum tracks, a detailed MonteCarlo study was performed. The pion spectrum was derived from simulation of the inclusive D^* production in $B\bar{B}$ events and MonteCarlo events were selected in the same way as the data: since the agreement with MonteCarlo is very good, the detection efficiency has been derived from MonteCarlo simulation. The SVT extends the capability of the charge particle reconstruction down to transverse momenta of $\sim 50\ \mathrm{MeV}/c$ (see left plot in Fig. 2-9).

The resolution in the five track parameters is monitored using e^+e^- and $\mu^+\mu^-$ pair events: the resolution is derived from the difference of the measured parameters for the upper and lower halves of the cosmic ray tracks traversing the DCH and the SVT. On this sample with transverse momenta above $3\ \mathrm{GeV}/c$, the resolution for single tracks is $23\,\mu m$ in d_0 and $29\,\mu m$ in z_0. To study the dependence of resolution from transverse momentum, a sample of multi-hadron events is used: the resolution is determined from the width of the distribution of the difference between the measured parameters (d_0 and z_0) and the coordinates of the vertex reconstructed from the remaining tracks in the event: right plot in Fig. 2-9 shows the dependence of the resolution in d_0 and z_0 as a function of p_t. The measured resolutions are about $25\,\mu m$ in d_0 and $40\,\mu m$ in z_0 for p_t of $3\ \mathrm{GeV}/c$: these values are in good agreement with the MonteCarlo studies and in reasonable agreement also with the results from cosmic rays.

2.4 Čerenkov **light detector:** *DIRC*

The particle identification system is crucial for *BABAR* since the *CP* violation analysis requires the ability to fully reconstruct one of the B meson and to tag the flavour of the other B decay: the momenta of the kaons used for flavour

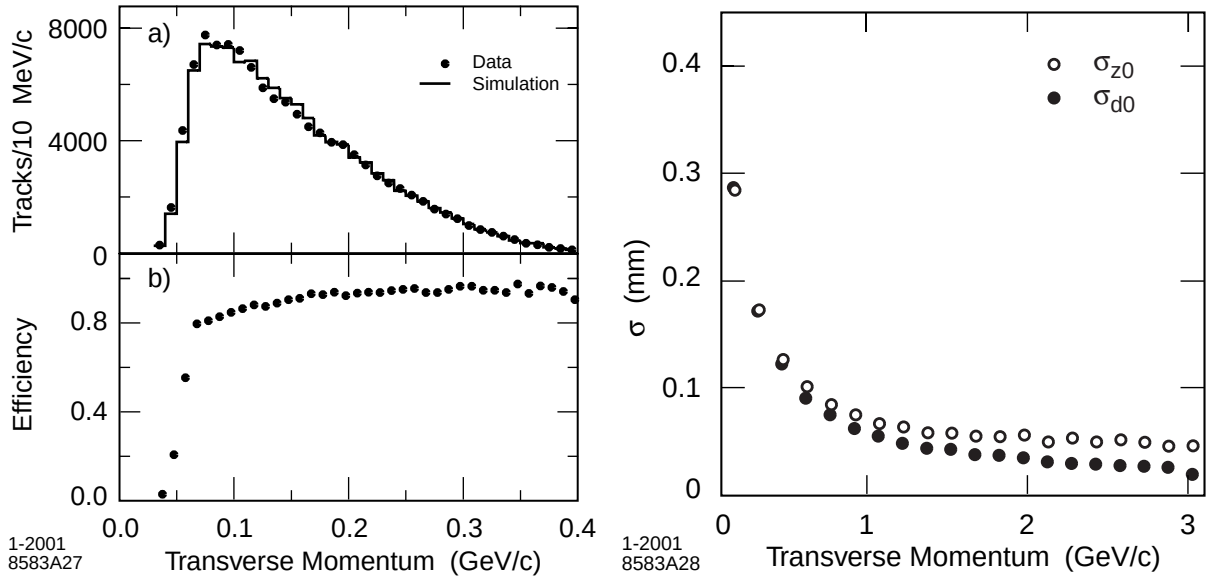

Figure 2-9. *Left plot: MonteCarlo studies of low momentum tracks in the SVT on $D^{*+} \rightarrow D^0\pi^+$ events. a) comparison with data in $B\bar{B}$ events and b) efficiency for slow pion detection derived from simulated events. Right plot: resolution in the parameters d_0 and z_0 for tracks in multi-hadron events as a function of the transverse momentum.*

tagging extend up to about $2\ \mathrm{GeV}/c$ with most of them below $1\ \mathrm{GeV}/c$. On the other hand, pions and kaons from the rare two-body decays $B^0 \rightarrow \pi^+\pi^-$ and $B^0 \rightarrow K^+\pi^-$ must be well separated: they have momenta between 1.7 and $4.2\ \mathrm{GeV}/c$ with a strong momentum-polar angle correlation of the tracks (higher momenta occur at more forward angles because of the c.m. system boost). So the particle identification system should be:

- thin and uniform in term of radiation lengths to minimize degradation of the calorimeter energy resolution,
- small in the radial dimension to reduce the volume (cost) of the calorimeter,
- with fast signal response,
- able to tolerate high background.

DIRC stands for Detection of Internally Reflected Čerenkov light and it refers to a new kind of ring-imaging Čerenkov detector which meets the above requirements. The particle identification in the *DIRC* is based on the Čerenkov radiation produced by charged particles crossing a material with a speed higher than light speed in that material. The angular opening of the Čerenkov radiation cone depends on the particle speed:

$$\cos\theta_c = \frac{1}{n\beta}$$

where θ_c is the Čerenkov cone opening angle, n is the refractive index of the material and β is the particle velocity over c. The principle of the detection is based on the fact that the magnitudes of angles are maintained upon reflection from a flat surface.

Since particles are produced mainly forward in the detector because of the boost, the *DIRC* photon detector is placed at the backward end: the principal components of the *DIRC* are shown in Fig. 2-10. The *DIRC* is placed in the barrel region and consists of 144 long, straight bars arranged in a 12-sided polygonal barrel. The bars are $1.7\,cm$-thick,

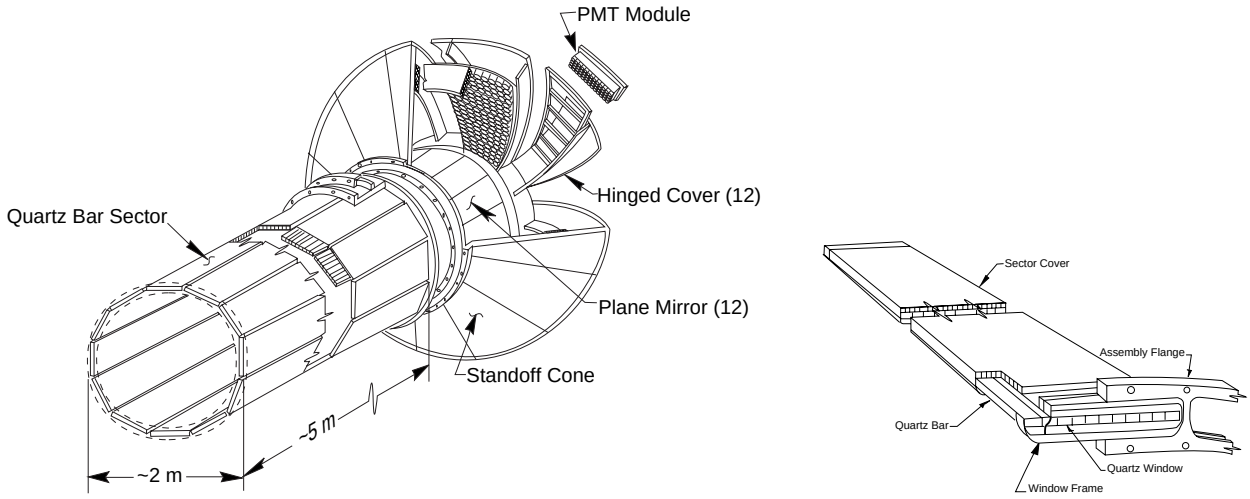

Figure 2-10. *Mechanical elements of the DIRC and schematic view of bars assembled into a mechanical and optical sector.*

$3.5\,cm$-wide and $4.90\,m$-long: they are placed into 12 hermetically sealed containers, called *bar boxes*, made of very thin aluminum-hexcel panels. Within a single bar box, 12 bars are optically isolated by a $\sim 150\,\mu m$ air gap enforced by custom shims made from aluminum foil.

The radiator material used for the bars is synthetic fused silica: the bars serve both as radiators and as light pipes for the portion of the light trapped in the radiator by total internal reflection. Synthetic silica has been chosen because of its resistance to ionizing radiation, its long attenuation length, its large index of refraction, its low chromatic dispersion within its wavelength acceptance.

The Čerenkov radiation is produced within these bars and is brought, through successive total internal reflections, in the backward direction outside the tracking and magnetic volumes: only the backward end of the bars is instrumented. A mirror placed at the other end on each bar reflects forward-going photons to the instrumented end. The Čerenkov angle at which a photon was produced is preserved in the propagation, modulo some discrete ambiguities (the forward-backward ambiguity can be resolved by the photon arrival-time measurement, for example). The $DIRC$ efficiency grows together with the particle incidence angle because more light is produced and a larger fraction of this light is totally reflected. To maximize the total reflection, the material must have a refractive index (fused silica index is $n = 1.473$) higher than the surrounding environment (the $DIRC$ is surrounded by air with index $n = 1.0002$).

Once photons arrive at the instrumented end, most of them emerge into a water-filled expansion region (see Fig. 2-11), called the *Standoff Box*: the purified water, whose refractive index matches reasonably well that of the bars ($n_{H_2O} = 1.346$), is used to minimize the total internal reflection at the bar-water interface.

The standoff box is made of stainless steel and consists of a cone, cylinder and 12 sectors of PMTs: it contains about 6000 liters of purify water. Each of the 12 PMTs sectors contains 896 PMTs in a close-packed array inside the water volume: the PMTs are linear focused $2.9\,cm$ diameter photo-multiplier tubes, lying on an approximately toroidal surface.

The $DIRC$ occupies only $8\,cm$ of radial space, which allows for a relatively large radius for the drift chamber while keeping the volume of the CsI Calorimeter reasonably low: it corresponds to about $17\%\,X_0$ at normal incidence. The angular coverage is the 94% of the ϕ azimuthal angle and the 83% of $\cos\theta_{CM}$.

Čerenkov photons are detected in the visible and near-UV range by the PMT array. A small piece of fused silica with a trapezoidal profile glued at the back end of each bar allows for significant reduction in the area requiring

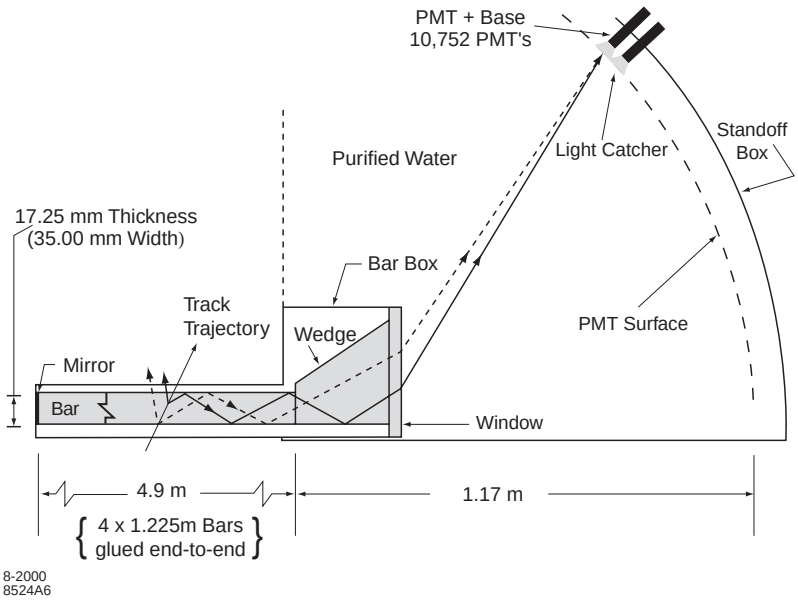

Figure 2-11. *Schematics of the DIRC fused silica radiator bar and imaging region. Not shown is a 6 mrad angle on the bottom surface of the wedge.*

instrumentation because it folds one half of the image onto the other half. The PMTs are operated directly in water and are equipped with light concentrators: the photo-multiplier tubes are about $1.2\,m$ away from the end of the bars. This distance from the bar end to the PMTs, together with the size of the bars and PMTs, gives a geometric contribution to the single photon Čerenkov angle resolution of about 7 mrad. This is a bit larger than the resolution contribution from Čerenkov light production (mostly a 5.4 mrad chromatic term) and transmission dispersions. The overall single photon resolution expected is about 9 mrad.

The image from the Čerenkov photons on the sensitive part of the detector is a cone cross-section whose opening angle is the Čerenkov angle modulo the refraction effects on the fused silica-water surface. In the most general case, the image consists of two cone cross-sections out of phase one from the other by a value related to an angle which is twice the particle incidence angle. In order to associate the photon signals with a track traversing a bar, the vector pointing from the center of the bar end to the center of each PMT is taken as a measure of the photon propagation angles α_x, α_y and α_z. Since the track position and angles are known from the tracking system, the three α angles can be used to determine the two Čerenkov angles θ_C and ϕ_C. In addition, the arrival time of the signal provides an independent measurement of the propagation of the photon and can be related to the propagation angles α. This over-constraint on the angles and the signal timing are useful in dealing with ambiguities in the signal association and high background rates.

The expected number of photo-electrons (N_{pe}) is ~ 28 for a $\beta = 1$ particle entering normal to the surface at the center of a bar and increases by over a factor of of two in the forward and backward directions.

The time distribution of real Čerenkov photons from a single event is of the order of $50\,ns$ wide and during normal data taking they are accompanied by hundreds of random photons in a flat background distribution within the trigger acceptance window. The Čerenkov angle has to be determined in an ambiguity that can be up to 16-fold: the goal of the reconstruction program is to associate the correct track with the candidate PMT signal with the requirement that the transit time of the photon from its creation in the bar to its detection at the PMT be consistent with the measurement error of about $1.5\,ns$.

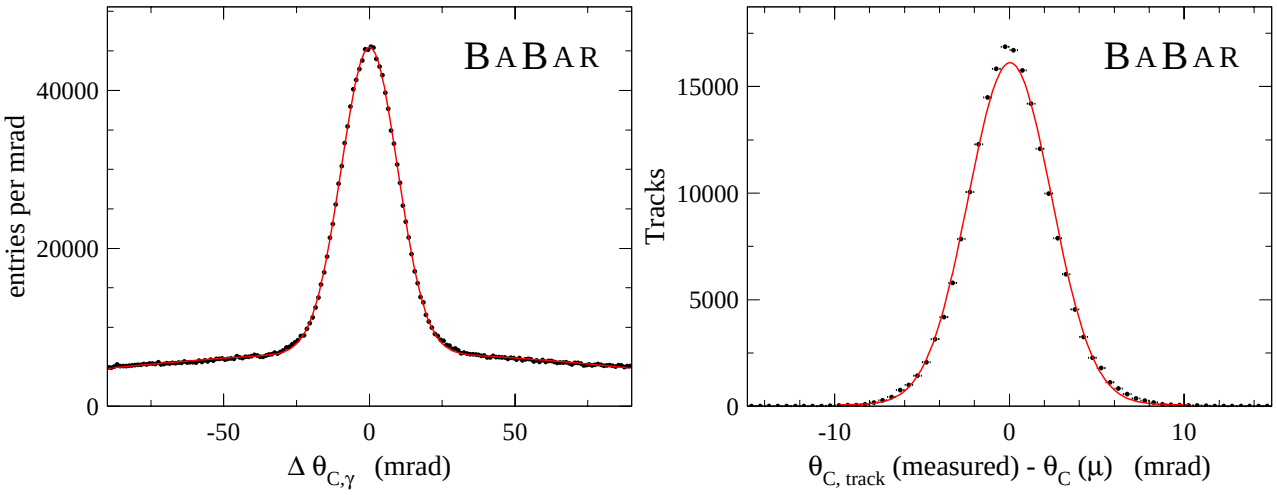

Figure 2-12. *From di-muon data events, left plot: single photon Čerenkov angle resolution. The distribution is fitted with a double-Gaussian and the width of the narrow Gaussian is* 9.6 *mrad. Right plot: reconstructed Čerenkov angle for single muons. The difference between the measured and expected Čerenkov angle is plotted and the curve represents a Gaussian distribution fit to the data with a width of* 2.4 *mrad.*

An unbinned maximum likelihood formalism is used to take into account all information provided by the $DIRC$: the reconstruction routine provides a likelihood value for each of the five stable particle types (e, μ, π, K and p) if the track passes through the active volume of the $DIRC$. These likelihood probabilities are calculated in an iterative process by maximizing the likelihood value for the entire event while testing different hypotheses for each track. If enough photons are found, a fit of θ_C and the number of observed signal and background photons are calculated.

In the absence of correlated systematic errors, the resolution ($\sigma_{C,\text{track}}$) on the track Čerenkov angle should scale as

$$\sigma_{C,\text{track}} = \frac{\sigma_{C,\gamma}}{\sqrt{N_{pe}}}$$

where $\sigma_{C,\gamma}$ is the single photon angle resolution. This angular resolution (obtained from di-muon events) can be estimated to be about 10.2 mrad, in good agreement with the expected value (see left plot in fig. 2-12). The measured time resolution is $1.7\,ns$ close to the intrinsic $1.5\,ns$ time spread of the PMTs. In di-muon event data, the number of photo-electrons varies between 20 for small polar angles at the center of the barrel and 65 at large polar angles: this is variation is well reproduced by MonteCarlo and can be understood by the fact that the number of Čerenkov photons varies with the path length of the track in the radiator (smaller path length at perpendicular incidence at the center of the barrel). Also the fraction of photons trapped by total internal reflection rises with larger values of $|\cos(\theta_{\text{track}})|$: this increase in the number of photons for forward going tracks corresponds also to an increase in momentum of the tracks and thus an improvement of the $DIRC$ performance.

The width of the track Čerenkov angle resolution for di-muon events is 2.4 mrad compared to the design goal of 2.2 mrad (see right plot in Fig. 2-12). From the measured single track resolution versus momentum in d-muon events and from the difference between the expected Čerenkov angles of charged pions and kaons, the pion-kaon separation power of the $DIRC$ can be evaluated: the expected separation between pions and kaons at 3 GeV/c is about 4.2σ, within 15% of the design goal.

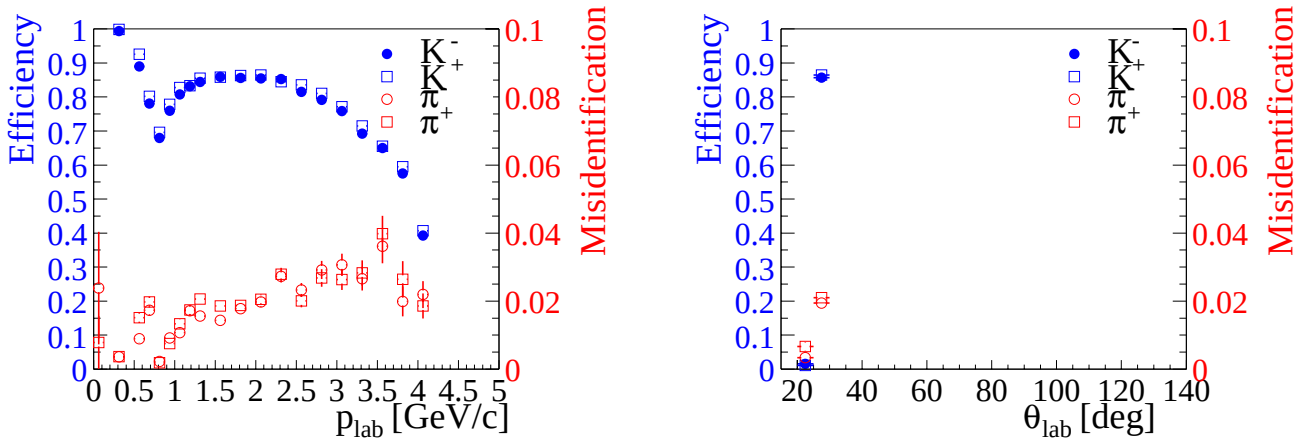

Figure 2-13. *Charged kaon identification and pion misidentification probabilit y for the tight kaon micro selector as a function of momentum (left) and polar angle (right). The solid markers indicate the efficiency for positive particles, the empty markers the efficiency for negative particles. Note the different scales for identification and misidentification on the left and right ordinates, respectively.*

The charged kaon efficiency is compared to the charged pion misidentification in Fig. 2-13. In the reconstruction of the invariant mass of the hadronic system, given the difference in the kaon momentum spectrum, Fig. 2-13, a ch arged track is identified as kaon if $p_K > 300\,\mathrm{MeV}$.

2.5 Electromagnetic calorimeter: *EMC*

The understanding of CP violation in the B meson system requires the reconstruction of final state containing a direct π^0 or that can be reconstructed through a decay chain containing one or more daughter $\pi^0 s$. The electromagnetic calorimeter is designed to measure electromagnetic showers with excellent efficiency and energy and angular resolution over the energy range from 20 MeV to 9 GeV. This capability should allow the detection of photons from π^0 and η decays as well as from electromagnetic and radiative processes. By identifying electrons, the EMC contributes to the flavour tagging of neutral B mesons via semi-leptonic decays. The upper bound of the energy range is given by the need to measure QED processes like $e^+e^- \to e^+e^-(\gamma)$ and $e^+e^- \to \gamma\gamma$ for calibration and luminosity determination. The lower bound is set by the need for highly efficient reconstruction of B-meson decays containing multiple π^0s and η^0s. The measurement of very rare decays containing π^0s in the final state (for example, $B^0 \to \pi^0\pi^0$) puts the most stringent requirements on energy resolution, expected to be of the order of $1-2\%$. Below 2 GeV energy, the π^0 mass resolution is dominated by the energy resolution, while at higher energies, the angular resolution becomes dominant and it is required to be of the order of few mrad. The EMC is also used for electron identification and for completing the IFR output on μ and K^0_L identification. It also has to operate in a $1.5\,T$ magnetic field.

The EMC has been chosen to be composed of a finely segmented array of thallium-doped cesium iodide (CsI(Tl)) crystals. The crystals are read out with silicon photo-diodes that are matched to the spectrum of scintillation light. The energy resolution of a homogeneous crystal calorimeter can be described empirically in terms of a sum of two terms added in quadrature:

$$\frac{\sigma_E}{E} = \frac{a}{\sqrt[4]{E(\mathrm{GeV})}} \oplus b$$

where E and σ_E refer to the energy of a photon and its rms error, measured in GeV. The energy dependent term $a(\sim 2\%)$ arises basically from the fluctuations in photon statistics, but also from the electronic noise of the photon

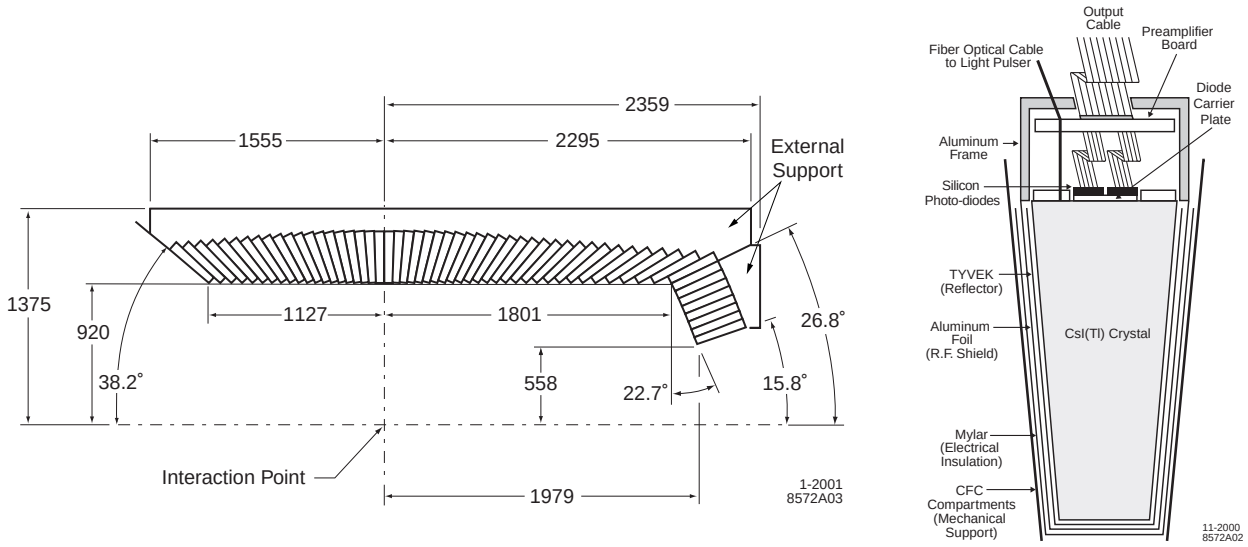

Figure 2-14. *The electromagnetic calorimeter layout in a longitudinal cross section and a schematic view of the wrapped CsI(Tl) crystal with the front-end readout package mounted on the rear face (not to scale).*

detector and electronics and from the beam-generated background that leads to large numbers of additional photons. This first term dominates at low energy, while the constant term $b(\sim 1.8\%)$ is dominant at higher energies (> 1 GeV). It derives from non-uniformity in light collection, leakage or absorption in the material in front of the crystals and uncertainties in the calibration.

The angular resolution is determined by the transverse crystal size and the distance from the interaction point: it can be empirically parameterized as a sum of an energy dependent and a constant term

$$\sigma_\theta = \sigma_\phi = \frac{c}{\sqrt{E(\mathrm{GeV})}} + d$$

where E is measured in GeV and with $c \sim 4$ mrad and $d \sim 0$ mrad.

In CsI(Tl), the intrinsic efficiency for the detection of photons is close to 100% down to a few MeV, but the minimum measurable energy in colliding beam data is about 20 MeV for the EMC: this limit is determined by beam and event-related background and the amount of material in front of the calorimeter. Because of the sensitivity of the π^0 efficiency to the minimum detectable photon energy, it is extremely important to keep the amount of material in front of the *EMC* to the lowest possible level.

Thallium-doped CsI has high light yield and small Molière radius in order to allow for excellent energy and angular resolution. It is also characterized by a short radiation length for shower containment at *BABAR* energies. The transverse size of the crystals is chosen to be comparable to the Molière radius achieving the required angular resolution at low energies while limiting the total number of crystals and readout channels.

The *BABAR* *EMC* (left plot in Fig. 2-14) consists of a cylindrical barrel and a conical forward end-cap: it has a full angle coverage in azimuth while in polar angle it extends from $15.8°$ to $141.8°$ corresponding to a solid angle coverage of 90% in the CM frame. Radially the barrel is located outside the particle ID system and within the magnet cryostat: the barrel has an inner radius of $92\,cm$ and an outer radius of $137.5\,cm$ and it's located asymmetrically about the interaction point, extending $112.7\,cm$ in the backward direction and $180.1\,cm$ in the forward direction. The barrel contains 5760 crystals arranged in 48 rings with 120 identical crystals each: the end-cap holds 820 crystals arranged in eight rings, adding up to a total of 6580 crystals. They are truncated-pyramid CsI(Tl) crystals (right plot in Fig. 2-14): they are tapered along their length with trapezoidal cross-sections with typical transverse dimensions of

$4.7 \times 4.7\,cm^2$ at the front face, flaring out toward the back to about $6.1.0\,cm^2$. All crystals in the backward half of the barrel have a length of $29.6\,cm$: toward the forward end of the barrel, crystal lengths increase up to $32.4\,cm$ in order to limit the effects of shower leakage from increasingly higher energy particles. All end-cap crystals are of $32.4\,cm$ length. The barrel and end-cap have total crystal volumes of $5.2\,m^3$ and $0.7\,m^3$, respectively. The CsI(Tl) scintillation light spectrum has a peak emission at $560\,nm$: two independent photodiodes collect this scintillation light from each crystal. The readout package consists of two silicon PIN diodes, closely coupled to the crystal and to two low-noise, charge-sensitive preamplifiers, all enclosed in a metallic housing.

A typical electromagnetic shower spreads over many adjacent crystals, forming a *cluster* of energy deposit: pattern recognition algorithms have been developed to identify these clusters and to discriminate single clusters with one energy maximum from merged clusters with more than one local energy maximum, referred to as *bumps*. The algorithms also determine whether a bump is generated by a charged or a neutral particle. Clusters are required to contain at least one seed crystal with an energy above 10 MeV: surrounding crystals are considered as part of the cluster if their energy exceeds a threshold of 1 MeV or if they are contiguous neighbors of a crystal with at least 3 MeV signal. The level of these thresholds depends on the current level of electronic noise and beam-generated background.

A bump is associated with a charged particle by projecting a track to the inner face of the calorimeter: the distance between the track impact point and the bump centroid is calculated and if it is consistent with the angle and momentum of the track, the bump is associated with this charged particle. Otherwise it is assumed to originate from a neutral particle.

On average, 15.8 clusters are detected per hadronic event: 10.2 are not associated to any charged particle. Currently, the beam-induced background contributes on average with 1.4 neutral clusters with energy above 20 MeV.

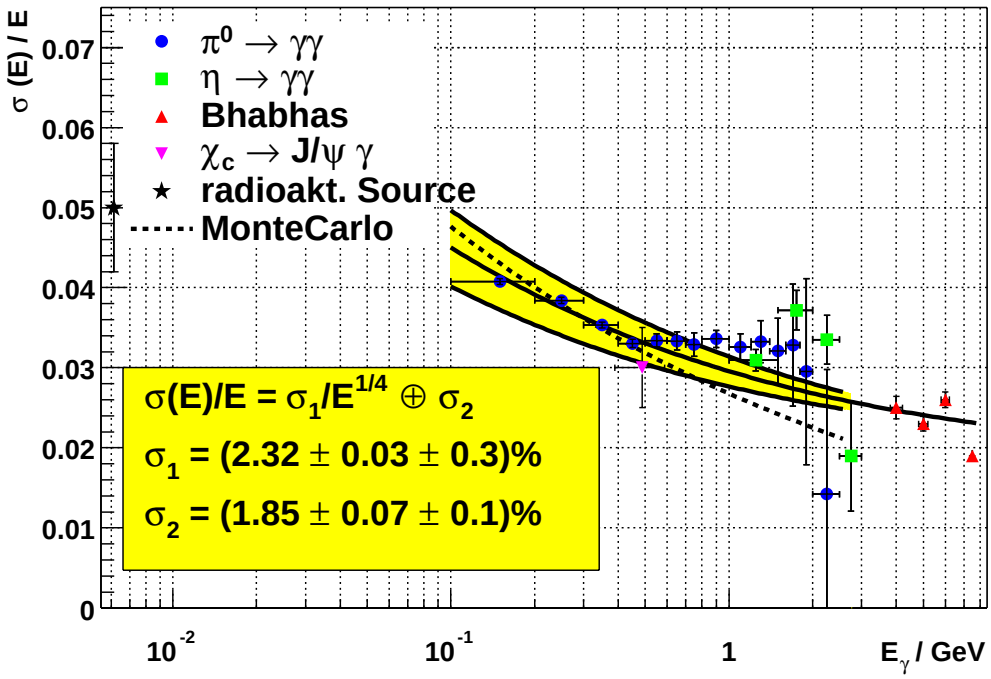

Figure 2-15. EMC *resolution as a function of the energy.*

At low energy, the energy resolution of the *EMC* is measured directly with a 6.13 MeV radioactive photon source (a neutron-activated fluorocarbon fluid) yielding $\sigma_E/E = 5.0 \pm 0.8\%$. At high energy, the resolution is derived from Bhabha scattering where the energy of the detected shower can be predicted from the polar angle of the electrons and positrons. The measured resolution is $\sigma_E/E = 1.9 \pm 0.1\%$ at 7.5 GeV. Fig. 2-15 shows the energy resolution on data

compared with expectations from MonteCarlo. From a fit to the experimental results to eq.2.5, $a = 2.32 \pm 0.30\%$ and $b = 1.85 \pm 0.12\%$ are obtained. The constant term comes out to be greater than expected: this is mainly caused by a cross talk effect, still not corrected, in the front-end electronics.

The measurement of the angular resolution is based on Bhabha events and ranges between 12 mrad and 3 mrad going from low to high energies. A fit to eq. 2.5 results in $c = (3.87 \pm 0.07)\ mrad$ and $d = (0.00 \pm 0.04)\ mrad$.

Different criteria are established to select electrons with different level of purity. Electrons are primarily separated from charged hadrons on the basis of the ratio of the energy E deposited in the EMC to the track momentum p ($\frac{E}{p}$). This quantity should be compatible with the unity for electrons since they deposit all the energy in the calorimeter. The other charged tracks should appear as MIP (minimal ionizing particles) unless they have hadronic interactions in the calorimer crystals. To further separate hadrons a variable describing the shape of the energy deposition in the EMC (LAT) is used. In addition, the $\mathrm{d}E/\mathrm{d}x$ energy loss in the DCH and the DIRC Čerenkov angle are required to be consistent with an electron and it offers a good separation in a wide range.

The track selection criteria are tightened for electrons selection to suppress background and to ensure a reliable momentum measurement and identification efficiency: there are requirements in addition for the transverse momentum $p_\perp > 0.1\,\mathrm{GeV}/c$, and $N_{Dch} \geq 12$ for the number of associated drift chamber hits. Furthermore, only tracks with a polar angle in the range $0.360 < \theta_{lab} < 2.37$ and electron candidates with a laboratory momentum $p_{lab} > 0.5\,\mathrm{GeV}/c$ are considered.

Electrons are identified using the a likelihood-based selector [75], which uses a number of discriminating variables:

- E_{cal}/p_{lab}, the ratio of E_{cal}, the energy deposited in the EMC, and p_{lab} the momentum in the laboratory rest frame measured using the tracking system; LAT, the lateral shape of the calorimeter deposit; $\Delta\Phi$, the azimuthal distance between the centroid of the EMC cluster and the impact point of the track on the EMC; and N_{cry}, the number of crystals in the EMC cluster;
- dE/dx, the specific energy loss in the DCH;
- the Čerenkov angle θ_C and N_C, the number of photons measured in the DIRC.

First, muons are eliminated based on dE/dx and the shower energy relative to the momentum. For the remaining tracks, likelihood functions are computed assuming the particle is an electron, pion, kaon, or proton. These likelihood functions are based on probability density functions that are derived from pure particle data control samples for each of the discriminating variables. For hadrons, we take into account the correlations between energy and shower-shapes. Using combined likelihood functions

$$\begin{aligned} L(\xi) &= P(E/p, LAT, \Delta\Phi, dE/dx, \theta_C|\xi) \\ &= P_{Emc}(E/p, LAT, \Delta\Phi|\xi)\ \ P_{Dch}(dE/dx|\xi)\ \ P_{DRC}(\theta_C|\xi) \end{aligned}$$

for the hypotheses $\xi \in \{e, \pi, K, p\}$, the fraction

$$F_\mathrm{e} = \frac{f_\mathrm{e} L(\mathrm{e})}{\sum_\xi f_\xi L(\xi)}\,, \tag{2.1}$$

is defined, where, for the relative particle fractions, $f_\mathrm{e} : f_\pi : f_\mathrm{K} : f_\mathrm{p} = 1 : 5 : 1 : 0.1$ is assumed. A track is identified as an electron if $F_\mathrm{e} > 0.95$.

The electron identification efficiency has been measured using radiative Bhabha events, as function of laboratory momentum p_{lab} and polar angle θ_{lab}. The misidentification rates for pions, kaons, and protons are extracted from selected data samples. Pure pions are obtained from kinematically selected $K^0_S \to \pi^+\pi^-$ decays and three prong $\tau^\pm$ decays. Two-body Λ and D^0 decays provide pure samples of protons and charged kaons.

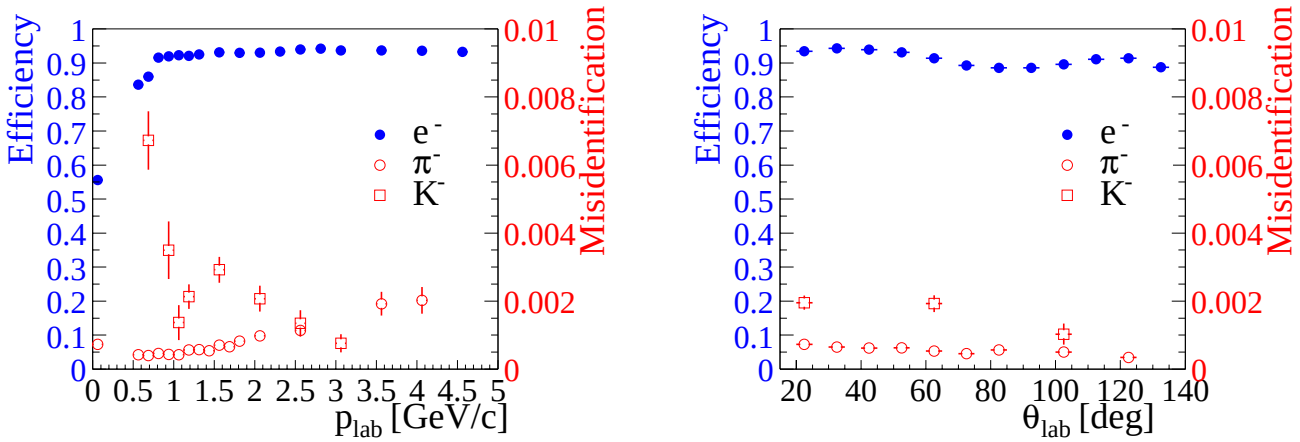

Figure 2-16. *Electron identification and hadron misidentification probability for the likelihood-based electron selector as a function of momentum (left) and polar angle (right). Note the different scales for identification and misidentification on the left and right ordinates, respectively. The measurements are for luminosity-averaged rates for Run-1 and Run-2.*

The performance of the likelihood-based electron identification algorithm is summarized in Figure 2-16, in terms of the electron identification efficiency and the per track probability that a hadron is misidentified as an electron.

The average hadron fake rates per track are determined separately for positive and negative particles, taking into account the relative abundance from Monte Carlo simulation of $B\overline{B}$ events, with relative systematic uncertainties of 3.5%, 15% and 20% for pions, kaons, and protons, respectively. The resulting average fake rate per hadron track of $p_{lab} > 1.0\,\mathrm{GeV}/c$, is of the order of 0.05% for pions and 0.2% for kaons.

2.6 Instrumented Flux Return: *IFR*

IFR (*Instrumented Flux Return*) detector is dedicated to muon identification and neutral hadrons detection (mainly K_L^0) in a wide range of momentum and angles.

The IFR, as all the other *BABAR* subsystems, has an asymmetric structure with a polar angle coverage that is $17° \leq \theta_{lab} \leq 150°$. The IFR (Fig. 2-17) is made of 19 layers of Resistive Plate Chambers (RPC) in the barrel region and 18 layers in forward and backward regions, that are placed inside the iron layers used for the solenoidal magnetic field return joke. The iron structure is subdivided in three main parts: the barrel one surrounding the solenoid, made of 6 sextants covering the radial distance between $1.820\ m$ and $3.045\ m$ with a length of $3.750\ m$ (along the z axis); the forward end-cap and backward end-cap covering the forward (positive z axis) and backward regions. Moreover, two cylindrical RPC layers have been installed between the calorimeter and the magnet cryostat in order to reveal particles exiting from the EMC. Those layers should cover the ϕ regions not covered by the barrel. Cylindrical layers are subdivided in four sections, each of them covering one fourth of the circumference: each of them has four RPC groups with orthogonal readout strips. $u - v$ helicoidal strips are placed inside along module's diagonals while ϕ and z parallel strips are placed outside. The summary of IFR readout segmentation is given in Tab. 2-4.

Each end-cap has an hexagonal shape and is vertically subdivided in two halves in order to allow internal subsystems access, if necessary: vacuum tube and PEP-II focusing elements are placed in the middle. Iron plates have a thickness ranging from 2 cm, for the inner ones placed nearest to the interaction region, to 10 cm for the outer ones; this means a total tickness of steel at normal incidence of ~ 65 cm (nearly corresponding to ~ 4 interaction lengths) in the barrel and ~ 60 cm in the end-caps. Nominal distance between iron layers in the inner barrel region is 3.5 cm while is 3.2 cm everywhere else. The increased granularity of inner layers with respect to the outer ones is due to the fact that the

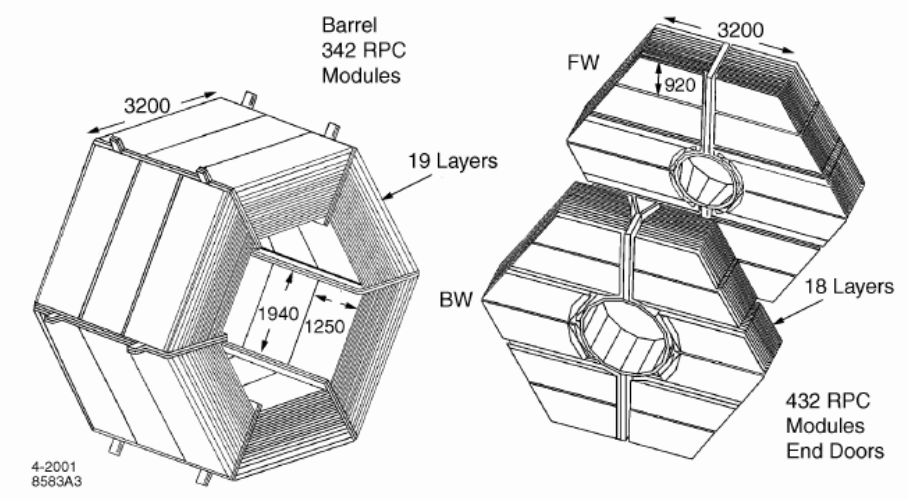

Figure 2-17. IFR *view*

section	# di sectors	coor.	readout # layer	# strip layer/sector	strip len. (cm)	strip larg. (mm)	total # channel
barrel	6	ϕ	19	96	350	19.7-32.8	$\approx$ 11k
		z	19	96	190-318	38.5	$\approx$ 11k
end-cap	4	y	18	6x32	124-262	28.3	13,824
		x	18	3x64	10-180	38.0	$\approx$ 15k
cyl.	4	ϕ	1	128	370	16.0	512
		z	1	128	211	29.0	512
		u	1	128	10-422	29.0	512
		v	1	128	10-423	29.0	512

Table 2-4. IFR *readout segmentation. Total number of channels is* $\sim 53k$.

largest part of particles detected inside the IFR are interacting in the very first material layers. Chosen segmentation is also the result of a compromise between the subsystem cost (proportional to the volume) and the need of a good efficiency for low momentum ($> 700\,\mathrm{MeV}$) muon detection, minimizing, at the same time, fraction of K_L^0's that are not interacting inside the IFR. Result of this optimization is a not uniform segmentation with iron plates that have thickness increasing with distance from beam line. RPC section is shown in Fig. 2-18.

In each barrel sextant layers are kept together by a structure that reduces the coverage of solid angle with active detectors of $\sim 7\%$. Active coverage of IFR detector is $\approx 2000\ m^2$, for a total RPC modules number that is ~ 900. Signals produced by particles crossing the gas gap inside the RPCs are collected on both sides of the chamber by using thin strips (thickness $\sim 40\ \mu m$) with witdh of the order of a centimeter. Strips are applied in two orthogonal directions on insulating planes $200\ \mu m$ thick, in order to have a bi-dimensional view. In each barrel sextant each gap is hosting a chamber. This consist of a set of 3 RPC modules of rectangular shape. Each module is ~ 125 cm long along beams direction with variable width in order to completely fill the gap. Each chamber is equipped with 96 $\phi - strip$ placed along z axis that are measuring the ϕ angle inside the barrel and 96 $z - strip$ orthogonal to beams direction that are measuring z coordinate. $z - strips$ are subdivided into 3 panels of 32 strips with largeness, function

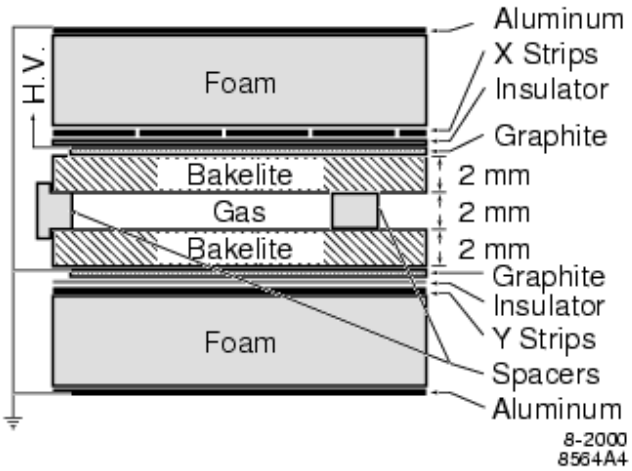

Figure 2-18. *Planar RPC section with HV connection scheme.*

of chamber radial position, ranging between 1.78 and 3.37 cm. This projective geometry allows a constant number of strips for all the various layers without decreasing detector resolution (each strip covers the same azimuthal angle). The used gas mixture is made of 56.7% Argon, 38.8% Freon-134a and 4.5% Isobutane. Working voltage for RPCs is $\sim 7.5\,kV$. Iron layers keeping apart RPC planes are chilled by a water system that keeps the temperature $\sim 20^oC$. RPC efficiencies have been measured by using cosmics taken on a weekly base.

Mean efficiency during 2000 run has been $\sim 78\%$ for the barrel and $\sim 87\%$ for the forward end-cap, less than that one measured in June 1999 ($\sim 92\%$). During the Summer 1999 the ambient temperature increased very much reaching about 32° to 38° inside the iron. During such period the IFR had problems to run the full detector because the dark current drawn by the chambers exceeded the total current limit provided by the power supply. All the chambers drawing more than $200\,\mu$A were disconnected. In October the chambers were re-connected but they didn't recover the full efficiency. The forward end-cap has been completely reconstructed and installed in the Summer 2002: 5 intermediate RPC layers were replaced by 2.54 cm of brass, 10 cm of steel were added after the last RPC layer, an RPC(layer 19) was added in front of the forward end-cap, an RPC belt was added in the barrel–end-cap overlap region. Barrel efficiencies are still decreasing and are at $\sim 40\%$ level while in the new forward end-cap, they are greater than 90%.

Muons are identified by measuring the number of traversed interaction lengths in the entire detector and comparing it with the number of expected interaction lengths for a muon of a given momentum. Moreover, the projected intersections of a track with the RPC planes are computed and, for each readout plane, all strips clusters detected within a predefined distance from the predicted intersection are associated with the track: the average number and the r.m.s. of the distribution of RPC strips per layer gives additional μ/π discriminating power. We expect in fact the average number of strips per layer to be larger for pions producing an hadronic interaction than for muons. Other variables exploiting clusters distribution shapes are constructed. Selection criteria based on all these variables are applied to select muons. The performance of the muon selection has been tested on samples of kinematically identified muons from $\mu\mu ee$ and $\mu\mu\gamma$ final states and pions from three-prong τ decays and $K_S \to \pi^+\pi^-$ decays.

The muon selection procedure is as follows:

- tight criteria on tracking: $p_\perp > 0.1\,\mathrm{GeV}/c$, $N_{DCH} \geq 12$, $0.360 < \theta_{lab} < 2.37$ and $p_{lab} > 1.0\,\mathrm{GeV}/c$
- the energy deposited in the EMC is required to be consistent with the minimum ionizing particle: $50\,\mathrm{MeV} < E_{cal} < 400\,\mathrm{MeV}$;

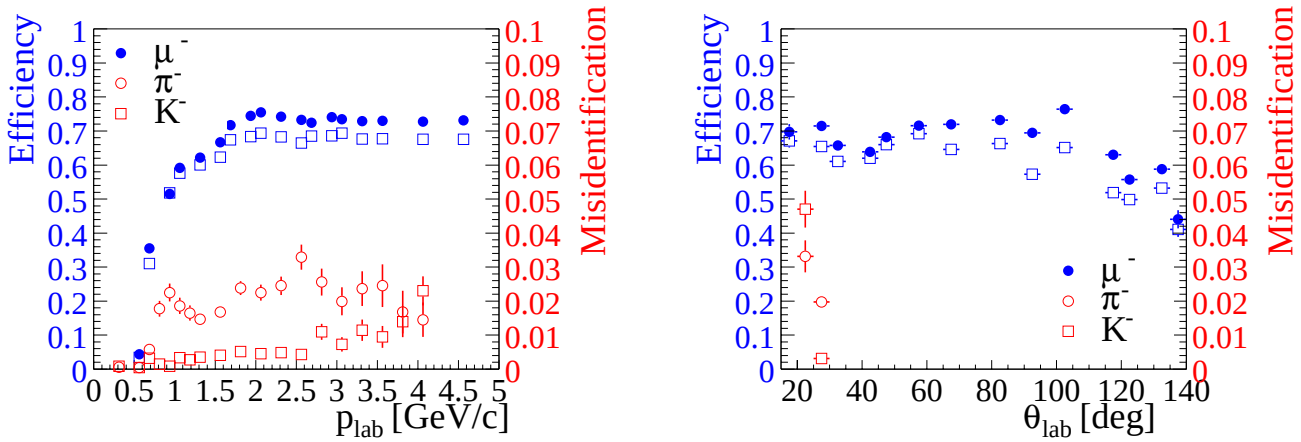

Figure 2-19. *Muon identification and hadron misidentification probability for the tight muon selector as a function of momentum (left) and polar angle (right). The solid markers indicate the efficiency in 2000, the empty markers the efficiency in 2001. Note the different scales for identification and misidentification on the left and right ordinates, respectively.*

- the number of IFR layers associated with the track has to be $N_L \geq 2$.
- the interaction lengths of material traversed by the track has to be $\lambda_{meas} > 2.2$.
- The number of interaction lengths expected for a muon of the measured momentum and angle to traverse is estimated by extrapolating the track up to the last *active* layer of the IFR. This estimate takes into account the RPC efficiencies which are routinely measured and stored. We require the difference $\Delta\lambda = \lambda_{exp} - \lambda_{meas}$ to be < 1.0, for tracks with momentum greater than 1.2 GeV/c. For track momenta between 0.5 GeV/c and 1.2 GeV/c, a variable limit is placed: $\Delta\lambda < [(p_{lab} - 0.5)/0.7]$.
- The *continuity* of the IFR cluster is defined as $T_c = \frac{N_L}{L-F+1}$, where L and F are the last and first layers with hit. T_c is expected to be 1.0 for muons penetrating an ideal detector whereas is expected smaller for hadrons. We require $T_c > 0.3$ for tracks with $0.3 < \theta_{lab} < 1.0$ (i.e. in the Forward End Cap to remove beam background).
- The observed number of hit strips in each RPC layer is used to impose the conditions on the average number of hits, $\bar{m} < 8$, and the standard deviation, $\sigma_m < 4$.
- The strip clusters in the IFR layers are combined to form a track and fit to a third degree polynomial, with the quality of the fit selected by the condition $\chi^2_{fit}/DOF < 3$. In addition, the cluster centroids are compared to the extrapolated charged track, with the requirement $\chi^2_{trk}/DOF < 5$.

The muon identification efficiency has been measured using $\mu^+\mu^-(\gamma)$ events and two-photon production of $\mu^+\mu^-$ pairs. The misidentification rates for pions, kaons, and protons are extracted from selected data samples. The performance of the muon identification algorithm is summarized in Fig. 2-19, in terms of the muon identification efficiency and the per track probability that a hadron is misidentified as a muon. Only tracks in the fiducial volume, i.e. with a polar angle in the range $20.6 < \theta_{lab} < 135.9°$, are considered. The errors shown are statistical only, the systematic error is dominated by variations in the performance of the IFR as a function of position and time.

3

Event Reconstruction

The analysis relies on:

- the fully reconstruction of B mesons,
- the reconstruction of event quantities based on the particles in the rest of the event,
- the selection of high energy photons.

The building blocks for the reconstruction of these quantities are described in this chapter together with the algorithm used in the B reconstruction (the so called Semi-exclusive reconstruction[1] [58]).

3.1 Track selection

Tracks are selected using the criteria described in Sec. 2.3.3 with additional cuts. Track coming from $\Lambda \to p\pi$ candidates and γ conversions ($\gamma \to e^+e^-$) are removed. Also discarded are those tracks identified as electrons or muons (see Sec. 2.5 and 2.6). Finally a kaon/pion mass assignment is done according to a PID selection (see Sec. 2.4).

3.1.1 Recoil selection

For the definition of the quantities in the rest of the event (B_{recoil}), the requirements on charged tracks need to be stringent in order to ensure well known efficiencies and minimal backgrounds.

The track selection is summarized in Tab. 3-1.

- A cut on the distance of closest approach to the beam spot in the $x-y$ plane ($|d_{xy}| < 1.5\,\mathrm{cm}$) and along the z axis ($|d_z| < 10\,\mathrm{cm}$) is applied. This reduces fake tracks and background tracks not originating from the vicinity of the interaction point.
- For tracks with $p_\perp > 0.2$ at least one DCH hit is required. This cut is not used for low momentum tracks since slow pions produced (for instance in the $D^* \to D^0\pi$ decays) would be rejected.
- A cut on the maximum momentum of $p_{lab} < 10\,\mathrm{GeV}/c$, where p_{lab} is the laboratory momentum of the track is applied. This removes tracks not compatible with the beam energies.
- Tracks are required to be within the polar angle acceptance of the detector: $0.410 < \theta_{lab} < 2.54$ rad. This ensures a well-understood tracking efficiency.

[1] Several control samples have been used to produce the Figures in the following and the statistics does not always correspond to the final sample (81.9 fb^{-1}).

- Tracks with transverse momentum $p_\perp < 0.18\,\mathrm{GeV}/c$ do not reach the EMC and therefore they will spiral inside the drift chamber ("loopers"). The tracking algorithms of *BABAR* will not combine the different fragments of these tracks into a single track. Therefore dedicated cuts have been developed to reject track fragments compatible with originating from a looper based on their distance from the beam spot. In order to identify looper candidates, the minimal difference in $p_\perp$, ϕ and θ to all other tracks in the event is determined. Tracks passing selection criteria (see Tab. 3-1), different for same-sign and opposite-sign track pairs, are flagged as loopers and only the track fragment with $|d_z|$ closest to the beam spot is retained.

  These criteria remove roughly 13% of all low-momentum tracks in the central part of the detector. On average, they lower the mean charged multiplicity per B meson by less than 1%.

- Two tracks very closely aligned to each other are called "ghosts". These cases arise when the tracking algorithms splits the DCH hits in two track fragments. If two tracks are very close in phase space (as defined in Tab. 3-1), only the track with the largest number of DCH hits is retained. This ensures that the fragment with the better momentum measurement is kept in the analysis.

Table 3-1. *Summary of track selection criteria.*

Select tracks with	Selection criteria
distance in $x-y$ plane	$\lvert d_{xy}\rvert < 1.5\,\mathrm{cm}$
distance in z axis	$\lvert d_z\rvert < 10\,\mathrm{cm}$
minimum number of DCH hits	$N_{Dch} > 0$ if $p_\perp > 0.2\,\mathrm{GeV}/c$
maximum momentum	$p_{lab} < 10\,\mathrm{GeV}/c$
geometrical acceptance	$0.410 < \theta_{lab} < 2.54$ rad
Reject tracks if	**$\Delta p_t = 100\,\mathrm{MeV}$ to other tracks and**
loopers ($p_\perp < 0.18\,\mathrm{GeV}/c$)	Same sign: $\lvert\Delta\phi\rvert < 220$ & $\lvert\Delta\theta\rvert < 215$ mrad
	Opposite sign: $\lvert\Delta\phi\rvert < 190$ & $\lvert\Delta\theta\rvert < 300$ mrad
ghosts ($p_\perp < 0.35\,\mathrm{GeV}/c$)	$\lvert\Delta\phi\rvert < 220$ & $\lvert\Delta\theta\rvert < 215$ mrad

Only tracks above 300 MeV/c are considered as kaon candidates. The kaon selection is performed using variables based on information from the DRC, the DCH and the SVT. Likelihood functions are computed separately for charged and neutral particles, as products of three terms, one for each detector subsystem and then combined, see Sec.2.4.

To reconstruct K_S candidates, pairs of oppositely charged tracks are kinematically fit with the constraint that they originate from a common vertex. No constraint is applied on the invariant mass of the pair, but a $\pm 3\sigma$ cut is imposed: $0.486 < m_{\pi^+\pi^-} < 0.510\,\mathrm{GeV}/c^2$. It is furthermore required that the daughters of the K_S candidate are not part of the B_{reco} candidate. The calculation of the hadron X_s system makes use of the daughter tracks of the K_S candidate.

3.2 Neutral selection

Selection criteria on neutral candidates are applied in order to ensure well known efficiencies and minimal backgrounds. The experimental signature of a $B \to X_s\gamma$ decay is the presence of an isolated high energetic photon in the event, a dedicated selection, described in Sec. 4.1, is therefore applied on high energetic photons.

Neutral particles are selected as EMC local maxima energy depositions which are not matched to any track. These energy clusters originate mostly from photons, thus momenta and angles are assigned to be consistent with photons originating from the beam-beam interactions.

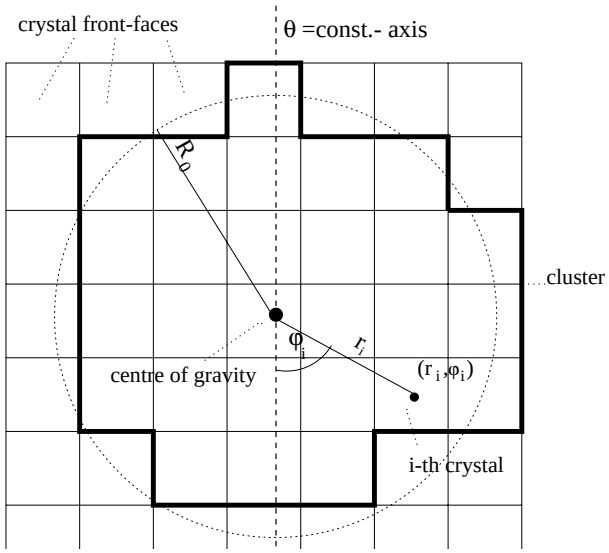

Figure 3-1. *Definition of the variables r_i, φ_i and R_0*

The neutral selection is summarized in Tab. 3-2.

Bumps are required to be within the calorimeter acceptance of the detector: $0.410 < \theta < 2.54$ rad. A cut on the minimum energy $E_\gamma^{\rm lab} > 80\,{\rm MeV}$ of neutrals is applied to remove low energy photons associated with beam related backgrounds.

Additional backgrounds are due to hadronic interactions, either by K_L or neutrons.

These backgrounds can be fought by applying requests on the shape of the calorimeter clusters. In order to describe the lateral energy distributions of showers, the following variables are defined: N, the number of crystals associated with the shower, E_i, the energy deposited in the i-th crystal, numbering them such that $E_1 > E_2 > \ldots > E_N$, and r_i, φ_i, the polar coordinates in the plane perpendicular to the line pointing from the interaction point to the shower center centered in the cluster centroid (see Fig. 3-1). Using these variables, one can define the variable

$$LAT = \frac{\sum_{i=3}^{N} E_i r_i^2}{\sum_{i=3}^{N} E_i r_i^2 + E_1 r_0^2 + E_2 r_0^2}, \tag{3.1}$$

where r_0 is the average distance between two crystals, which is approximately 5 cm for the *BABAR* calorimeter. This variable is constructed to discriminate between electromagnetic and hadronic showers based on their average properties. The sum starting from $i = 3$ omit the two crystals containing the highest amounts of energy. Electrons deposit most of their energy in two or three crystals, so that the value of LAT is small for electromagnetic showers. Multiplying the energies by the squared distances enhances the effect for hadronic showers, compared with electromagnetic ones.

Another useful shape variable is the ratio of the energy deposited in the 9 closest crystals from the cluster centroid over the energy deposited in the 25 closest crystals($S9S25$).

Since the fake photons background is not present in the daughters of the fully reconstructed B_{reco} , the rejection of this background has been studied comparing the photon candidates participating to the reconstructed B_{reco} and the rest of them. One of the problems of this approach is that the energy spectrum of the clusters is not identical in the two

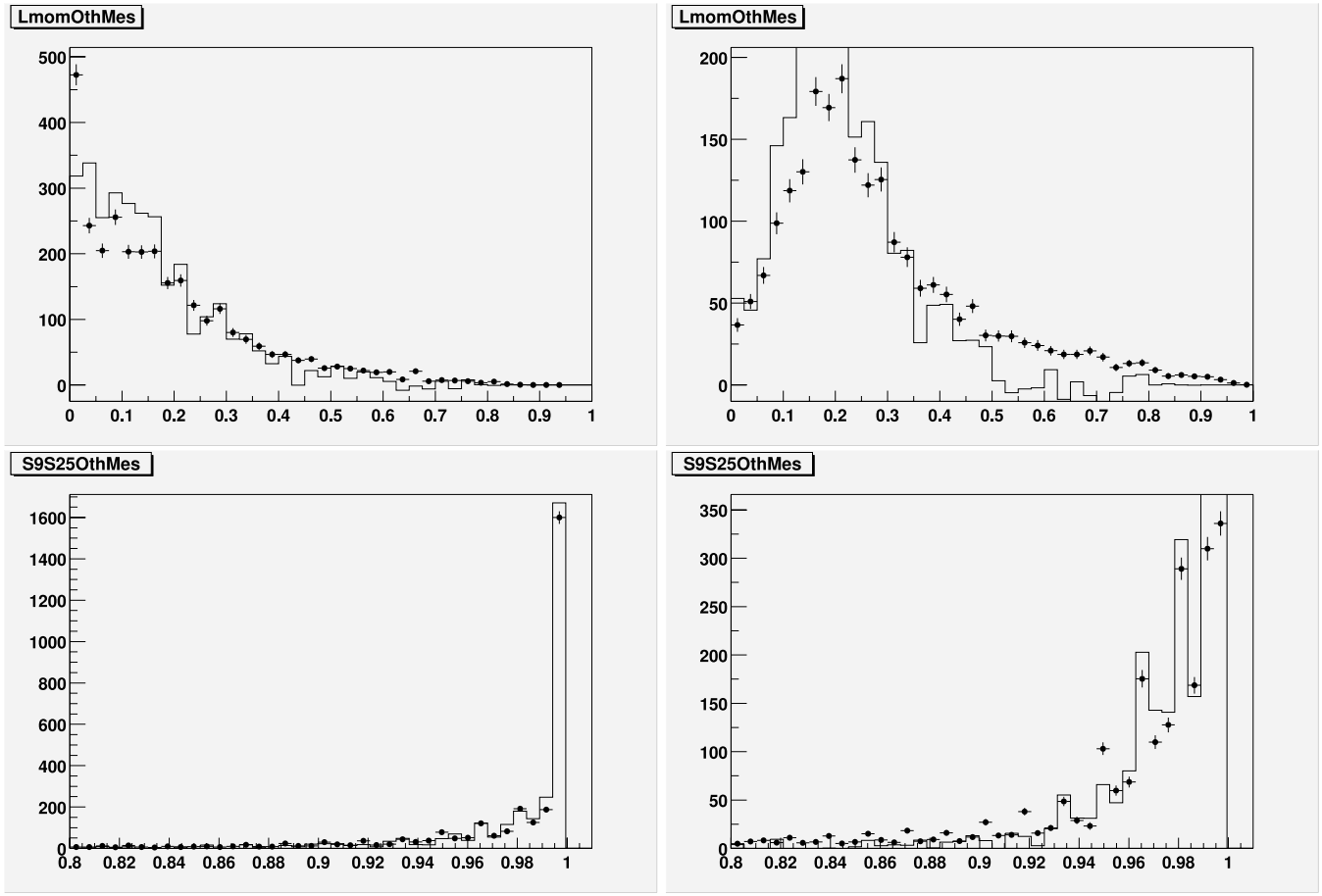

Figure 3-2. *Lateral momentum, LAT, (top row) and S9S25 (bottom row) distributions for photon candidates below (left column) and above (right column) 200 MeV. The histograms represent the reconstructed side while the dots represent the recoil side.*

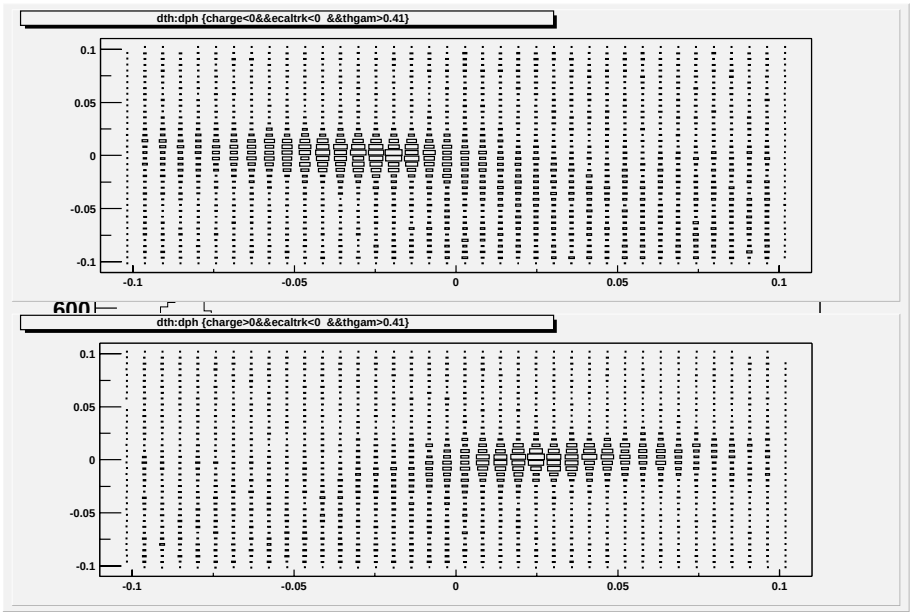

Figure 3-3. *Correlation plot between $d\phi$ (y axis in radiants) and $d\theta$ (x axis in radiants) for positively charged tracks (top) and negatively charged ones (bottom).*

samples. This has been accounted for by re-weighting the recoil side photons to match the spectrum in the reco side. Fig. 3-2 shows the comparison between the reco side (signal dominated) and the recoil side (signal and background) distributions of the lateral moment and S9S25.

The following criteria are applied: $0.05 <$LAT< 0.5 and $S9S25 > 0.9$.

These cuts are applied to all the recoiling photons except the $B \to X_s\gamma$ candidate photon ($E_\gamma > 1.3\,\mathrm{GeV}$) for which a dedicated selection is applied as described in Sec. 4.1.

The possibility to confuse, deposits from charged particles as neutral clusters, has also been investigated. Such clusters are due to inefficiencies in the algorithm that matches tracks and EMC clusters and lead to double counting of their energies. In order to study them, the distances in ϕ ($d\phi$) and θ ($d\theta$) with respect to all the tracks which do not have a matched cluster, are considered. Fig. 3-3 shows the $d\phi$ - $d\theta$ correlation plot. There is a clear evidence of unmatched clusters that are rejected by the cuts described in Tab. 3-2. They reject 1.2% of the neutral candidates in MonteCarlo and 4.2% in data. This difference is not understood, but without this selection there would be differences in Data-MonteCarlo efficiency.

Table 3-2. *Summary of neutral selection criteria.*

Selection Criteria	Cut value
Neutral energy	$E_\gamma > 80\,\mathrm{MeV}$
LAT	$0.05 <$LAT< 0.5
$S9S25$	$S9S25 > 0.9$
unmatched clusters	$\|d\theta\| < 30mrad$
	charge$> 0\&\& -30 < d\phi < 70mrad$
	charge$< 0\&\& -70 < d\phi < 30mrad$

3.3 Meson Reconstruction

3.3.1 π^0 reconstruction

The use and control of a wide portion of the π^0 energy spectrum is needed in this analysis. For instance, lowest energy π^0 s are used to reconstruct the $D^{*0} \to D^0\pi^0$ decays while the decay products in the $B \to D\ \pi\pi^0$ channel have quite large momentum.

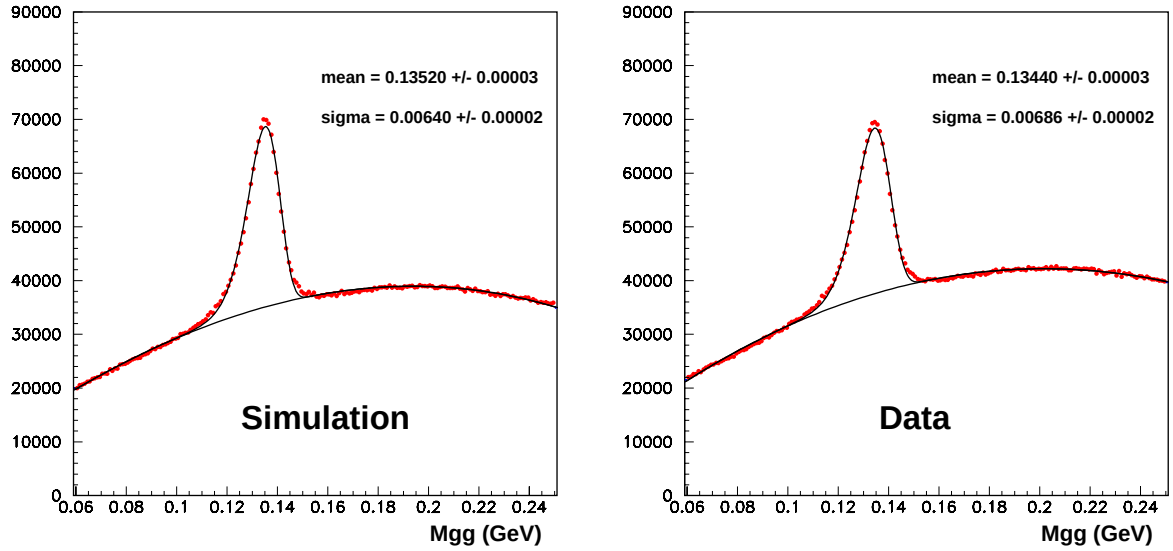

Figure 3-4. *π^0 peaks for simulated events and for data.*

The π^0 s are reconstructed using pairs of neutral clusters with a lower energy cut at 30 MeV and applying a cut on the LAT variable (the lateral shape of the calorimeter deposit). The resulting π^0 ought to have an energy above 200 MeV. A mass region of (110–155) MeV, corresponding to $(-4\sigma\ -\ +3\sigma)$, is applied. In Fig. 3-4 invariant masses and their resolutions for simulated events and real data are shown.

3.3.2 K^0_S reconstruction

K^0_S are reconstructed pairing all possible tracks of opposite sign, and looking for the 3D point (vertex) which is more likely to be common to the two tracks. The algorithm is based on a χ^2 minimization and it uses as a starting point for the vertex finding the closest approach in 3D. No constraint is applied on the invariant mass of the pair, but a $\pm 3\sigma$ cut is imposed: $0.486 < m_{\pi^+\pi^-} < 0.510\,\mathrm{GeV}$. Fig. 3-5 shows the comparison data-Monte-Carlo for in the invariant mass of the $\pi^+\pi^-$ system.

3.3.3 D reconstruction

The D mesons is reconstructed in a large variety of channels listed in Tab. 3-3.

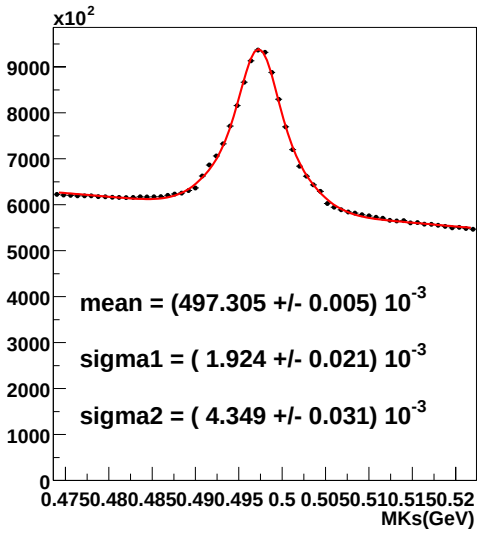

Figure 3-5. *Mass distributions for $K^0_S \to \pi^+\pi^-$. The distribution is fitted with a sum of a double Gaussian and a first order polynomial function.*

The D^0 is reconstructed in the modes $D^0 \to K\pi$ $D^0 \to K3\pi$ $D^0 \to K\pi\pi^0$ $D^0 \to K^0_S\pi\pi$. The charged tracks originating from a D meson are required to have a minimum momentum of 200 MeV/c for the $D^0 \to K\pi$ and 150 MeV/c for the remaining three modes. The D^0 candidates are required to lie within $\pm 3\sigma$, calculated on an event-by-event basis, of the nominal D^0 mass. All D^0 candidates must have momentum greater than 1.3 GeV/c and lower than 2.5 GeV/c in the $\Upsilon(4S)$ frame. The lower cut is done to reduce combinatorics, the upper is due to the kinematic endpoint of the D^0 coming from a $B \to D^0 X$ decay or $B \to D^{*+} X$ with $D^{*+} \to D^0\pi^+$. A vertex fit is performed, where a χ^2 probability greater than 0.1% is required. Selection criteria are summarized in Tab. 3-4.

D^+ candidates are reconstructed in the modes $D^+ \to K^-\pi^+\pi^+$, $D^+ \to K^-\pi^+\pi^+\pi^0$, $D^+ \to K^0_S\pi^+$, $D^+ \to K^0_S\pi^+\pi^0$, $D^+ \to K^0_S\pi^+\pi^+\pi^+$. The minimum charged track momentum is required to be 200 MeV/c. D^+ candidates are required to have an invariant mass within $\pm 3\sigma$, calculated on an event-by-event basis, of the nominal D^+ mass. The D^+ candidates must have momentum greater than 1.0 GeV/c in the $\Upsilon(4S)$ frame for the three cleanest modes ($D^+ \to K^-\pi^+\pi^+$, $D^+ \to K^0_S\pi^+$ and $D^+ \to K^0_S\pi^+\pi^0$) and greater than 1.6 GeV/c for the two remaining ones ($D^+ \to K^-\pi^+\pi^+\pi^0$ and $D^+ \to K^0_S\pi^+\pi^+\pi^+$). Moreover all D^+ candidates must have momentum lower than 2.5 GeV/c in the $\Upsilon(4S)$ frame, as the D^0 case. A vertex fit is performed and a χ^2 probability greater than 0.1% is required. Selection criteria are summarized in Tab. 3-5.

D^{*+} candidates are formed by combining a D^0 with a pion which has momentum greater than 70 MeV/c. Only the channel $D^{*+} \to D^0\pi^+$ is reconstructed since $D^{*+} \to D^+\pi^0$ events enter in the $B \to D^+ X$ category as explained in the next section. A vertex fit for the D^{*+} is performed using the constraint of the beam spot to improve the angular resolution for the soft pion. A fixed $\sigma = 30$ $\mu\mathrm{m}$ is used to model the beam spot spread in the vertical direction. The fit is required to converge, but no cut is applied on the probability of χ^2. After fitting, selected D^{*+} candidates are required to have Δm within $\pm 3\sigma$ of the measured nominal value.

D^{*0} candidates are reconstructed by combining a selected D^0 with either a π^0 or a photon having momentum less than 450 MeV/c in the $\Upsilon(4S)$ frame. The minimum momentum for the π^0 corresponds to 70 MeV while the photons are required to have an energy greater than 100 MeV. For $D^{*0} \to D^0\pi^0$ selected D^{*0} candidates are required to have Δm within 4 MeV/c^2 of the nominal value while the window is wider for $D^{*0} \to D^0\gamma$ ($127\,\mathrm{MeV}/c^2 < \Delta m < 157\,\mathrm{MeV}/c^2$).

Selection criteria for D^{*0} and D^{*+} are summarized in Tab. 3-6.

Decay mode	**B.F.(%)**
$D^* \to D^0\pi$; $D^0 \to K\pi$	2.55 ± 0.06
$D^* \to D^0\pi$; $D^0 \to K3\pi$	5.0 ± 0.2
$D^* \to D^0\pi$; $D^0 \to K\pi\pi^0$	8.8 ± 0.6
$D^* \to D^0\pi$; $D^0 \to K^0_S\pi\pi$ ($K^0_S \to \pi^+\pi^-$)	1.35 ± 0.08
$D^+ \to K\pi\pi$	9.1 ± 0.6
$D^+ \to K^0_S\pi$ ($K^0_S \to \pi^+\pi^-$)	0.94 ± 0.06
$D^+ \to K\pi\pi\pi^0$	6.4 ± 1.1
$D^+ \to K^0_S\pi\pi\pi$ ($K^0_S \to \pi^+\pi^-$)	2.38 ± 0.31
$D^+ \to K^0_S\pi\pi^0$ ($K^0_S \to \pi^+\pi^-$)	3.5 ± 1.0
$D^{*0} \to D^0\pi^0$; $D^0 \to K\pi$	2.35 ± 0.12
$D^{*0} \to D^0\pi^0$; $D^0 \to K3\pi$	4.6 ± 0.3
$D^{*0} \to D^0\pi^0$; $D^0 \to K\pi\pi^0$	8.1 ± 0.7
$D^{*0} \to D^0\pi^0$; $D^0 \to K^0_S\pi\pi$ ($K^0_S \to \pi^+\pi^-$)	1.2 ± 0.1
$D^{*0} \to D^0\gamma$; $D^0 \to K\pi$	1.44 ± 0.19
$D^{*0} \to D^0\gamma$; $D^0 \to K3\pi$	2.82 ± 0.18
$D^{*0} \to D^0\gamma$; $D^0 \to K\pi\pi^0$	5.0 ± 0.4
$D^{*0} \to D^0\gamma$; $D^0 \to K^0_S\pi\pi$ ($K^0_S \to \pi^+\pi^-$)	0.7 ± 0.1
$D^0 \to K\pi$	3.80 ± 0.09
$D^0 \to K3\pi$	7.46 ± 0.31
$D^0 \to K\pi\pi^0$	14.0 ± 0.9
$D^0 \to K^0_S\pi\pi$	2.03 ± 0.12

Table 3-3. *D Meson decay modes and the corresponding Branching Fractions as in [60].*

3.4 Semi-exclusive Reconstruction Method

The aim of the Semi-exclusive reconstruction is to get as many as possible B mesons reconstructed in fully hadronic modes in order to study the properties of the recoiling B .

Since B^0 mesons mostly decay into charged $D^{(*)}$ mesons while B^- mesons decay into the neutral $D^{0(*)}$ mesons, only such modes are considered. Tab. 3-7 shows the relevant branching fractions of the B mesons decaying predominantly into fully hadronic final states.

The Semi-exclusive reconstruction comprises the following steps:

- reconstruct all possible decay modes $B \to DX$, where the X system is a combination of π^+,π^0, K^+ and K^0_S, with total charge equal to ± 1, and including a maximum of 7 particles, 5 charged tracks and 2 neutrals;
- study the structure of the X system looking for resonances in the signal and studying the shape of the background (Sec. 3.4.2);
- identify submodes and create subcategories according to the their multiplicity and to the structure of the X system (e.g. $D\pi\pi^0$, $M_{\pi\pi^0} < 1.5\,\mathrm{GeV}/c^2$). For each mode, the most relevant parameter is the *apriori-purity* of the mode: the ratio $S/\sqrt{S+B}$ where S and B are the signal and combinatorial background respectively, as estimated from an M_{ES} fit on data (Sec. 3.4.2);

	$D^0 \to K\pi$	$D^0 \to K\pi\pi^0$	$D^0 \to K3\pi$	$D^0 \to K^0_S\pi\pi$
m_D invariant mass window	$\pm$ 15 MeV	$\pm$ 25 MeV	$\pm$ 15 MeV	$\pm$ 20 MeV
Charged tracks: lower $p*$ cut	$> 200\,\mathrm{MeV}/c$	$> 150\,\mathrm{MeV}/c$		
D^0 upper $p*cut$	$< 2.5\,\mathrm{GeV}/c$			
D^0 lower $p*cut$	$> 1.3\,\mathrm{GeV}/c$			
Vertex fit	$\chi^2 > 0.01$			

Table 3-4. *Selection criteria for D^0 modes.*

	$D^+ \to K\pi\pi$	$D^+ \to K^0_S\pi$	$D^+ \to K^0_S\pi\pi^0$	$D^+ \to K\pi\pi\pi^0$	$D^+ \to K\pi\pi\pi$
m_D invariant mass window	$\pm$ 20 MeV	$\pm$ 20 MeV	$\pm$ 30 MeV	$\pm$ 30 MeV	$\pm$ 30 MeV
D^+: lower $p*$ cut	$> 1.0\,\mathrm{GeV}/c$			$> 1.6\,\mathrm{GeV}/c$	
D^+: upper $p*$ cut	$< 2.5\,\mathrm{GeV}/c$				
Charged tracks: lower p cut	$> 200\,\mathrm{MeV}/c$				
Vertex fit	$\chi^2 > 0.01$				

Table 3-5. *Selection criteria for D^+ reconstruction.*

Criteria	**Cut**
$D^{*+} \to D^0\pi^+$	
Vertexing and χ^2	beam spot constraint($\sigma_y = 30$ μm), convergence
$m(D^0\pi^+) - m(D^0)$	$\pm 3\sigma$ MeV/c^2
$p^*(\pi^+)$	[70,450] MeV/c
$D^{*0} \to D^0\pi^0$	
$m(D^0\pi^0) - m(D^0)$	± 4 MeV/c^2
$p^*(\pi^0)$	[70,450] MeV/c
$p^*(D^{*0})$	$1.3 < p^* < 2.5$ GeV/c
$D^{*0} \to D^0\gamma$	
$m(D^0\gamma) - m(D^0)$	[127,157] MeV/c^2
$E^*(\gamma)$	[100,450] MeV
$p^*(D^{*0})$	$1.3 < p^* < 2.5$ GeV/c

Table 3-6. *Summary of cuts for D^{*+} and D^{*0} selection*

- determine a mode by mode combinatorial background rejection, in order to account for different background levels depending on the number on the number of charged tracks and, above all, on the number of π^0 s in the reconstructed mode (Sec. 3.4.3);
- rank the submodes according to their purity and yields and study the significance as a function of the number of used modes in order to maximize the statistical significance of the sample (Sec. 3.4.4);
- group the submodes with similar purity;
- resolve the multiple candidates (Sec. 3.4.4).

mode	branching fraction (%)
$B \to D^{*\pm} X$	22.5 ± 1.5
$B \to D^{\pm} X$	23.9 ± 1.9
$B \to D^{*0}/\overline{D}^{*0} X$	26.0 ± 2.7
$B \to D^{0}/\overline{D}^{0} X$	63.9 ± 3.0
$B \to D_s^{+} X$	10.5 ± 2.6
$B \to D^{-(*)} D_s^{(*)}$	4.8 ± 1.2
$B \to D^{(*)} \overline{D}^{(*)} K$	7.1 ± 2.3
$B^0 \to D^{-(*)} D^{+(*)}$	~ 1.0

Table 3-7. *Inclusive and Exclusive branching fractions relevant to this analysis as measured in [60].*

The starting point of the Semi-exclusive selection is the D^0, D^+, D^*, D^{*0} meson reconstruction as described in Sec. 3.3.3.

Next, clean lists of charged pions and kaons, π^0, and K_s^0 are needed to be combined to the D meson to form the B candidated.

Pairs of opposite charge hadrons ($V^0 = h^+h^-$) and quartets of hadrons ($W^0 = h^+h^-h^+h^-$) are created using the list of charged tracks. If both the K_s^0 decay products are among the tracks used for a V^0 or a W^0, the two tracks are replaced by the K_s^0 (i.e. a V^0 would become a K_s^0 and a W^0 either a $K_s^0\ \pi\pi$ or a $K_s^0\ K_s^0$).

We accept B candidates with $M_{ES} > 5.28\,\mathrm{GeV}/c^2$ and in a ΔE windows varying from $30\,\mathrm{MeV}$ to $80\,\mathrm{MeV}$ depending on the mode.

3.4.1 Definition of ΔE and M_{ES}

Two main variables are used to select B candidates, to extract the yields and to define a sideband region to study the background: ΔE and M_{ES}.

- The *energy difference* ΔE is defined (making use of energy conservation) as:

$$\Delta E = E_B^* - \sqrt{s}/2\,, \tag{3.2}$$

  where E_B^* is the energy of the B candidate in the $\Upsilon(4S)$ rest frame (CM) and where $\sqrt{s}$ is the total energy of the e^+e^- system in the CM rest frame. The resolution of this variable is affected by the detector momentum resolution and by the particle identification since a wrong mass assignment implies a shift in ΔE . Signal events are Gaussian distributed in ΔE around zero, continuum and part of the $b\ \overline{b}$ background can be fitted with a polynomial distribution and background, due to misidentification, gives shifted Gaussian peaks. The resolution of this variable depends essentially on the reconstructed B mode and can vary from 20 MeV to 40 MeV. It can be worsen by two factors: charged tracks multiplicity in the B mode and π^0 multiplicity.

- The *beam energy-substituted mass* is defined as:

$$M_{ES} = \sqrt{(\sqrt{s}/2)^2 - p_B^{*2}}\,, \tag{3.3}$$

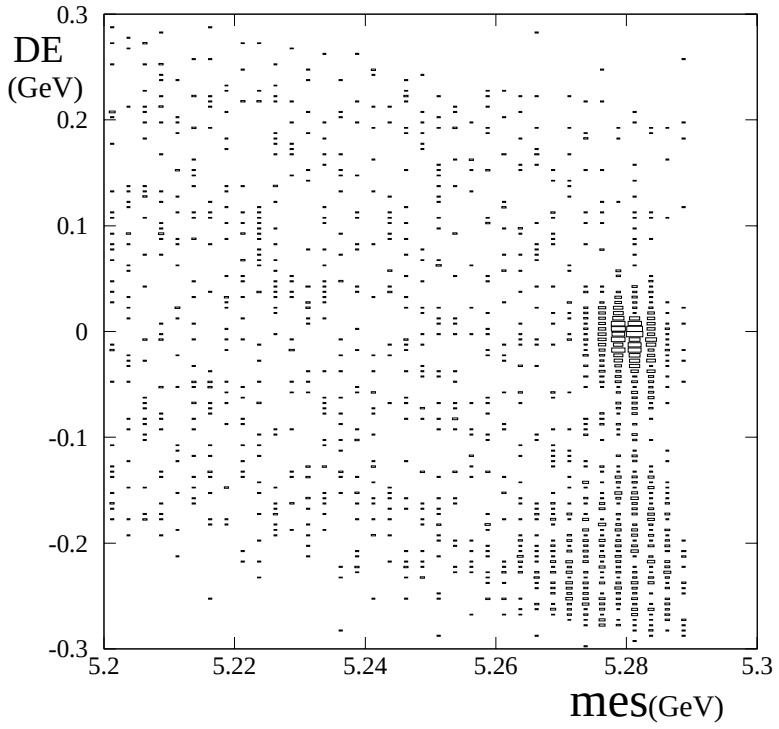

Figure 3-6. *ΔE versus M_{ES} for the decay , $B \to D^{*+}\pi^-$ with $D^0 \to K\pi$.*

where p^* is the B candidate momentum in the CM rest frame. It is clear that, since $|p_B^*| \ll \sqrt{s}/2$, the experimental resolution on M_{ES} is dominated by beam energy fluctuations. To an excellent approximation, the shapes of the M_{ES} distributions for B meson reconstructed in a final states with charged tracks only are Gaussian and practically identical. Otherwise the presence of neutrals in the final states, in case they are not fully contained in the calorimeter, can introduce tails.

It is important to notice that, since the sources of experimental smearing are uncorrelated (beams energy for M_{ES} and detector momentum resolution for ΔE), M_{ES} and ΔE also are in practice uncorrelated (Fig. 3-6).

The background shape in M_{ES} is parameterized using the ARGUS function [61]:

$$\frac{dN}{dM_{ES}} = N \cdot M_{ES} \cdot \sqrt{1-x^2} \cdot \exp\left(-\xi \cdot (1-x^2)\right) \tag{3.4}$$

where $x = M_{ES}/m_{\max}$ and the parameter ξ is determined from a fit. The $m_{\max}$, that represent the endpoint of the ARGUS distribution, is fixed in the fit to M_{ES}, since it depends only on the beam energy.

ARGUS shapes describes well both continuum ($c\overline{c}$ and uds) and $b\overline{b}$ background events, as shown in Fig. 3-7.

The signal component is fitted using a Crystal Ball function [62]:

- if $M_{ES} > m - \sigma \cdot a$

$$\frac{dN}{dM_{ES}} = N \cdot \frac{1}{\sqrt{2 \cdot \pi} \cdot \sigma} \cdot \exp\left(-\frac{1}{2} \cdot \frac{(M_{ES}-m)^2}{\sigma^2}\right) \tag{3.5}$$

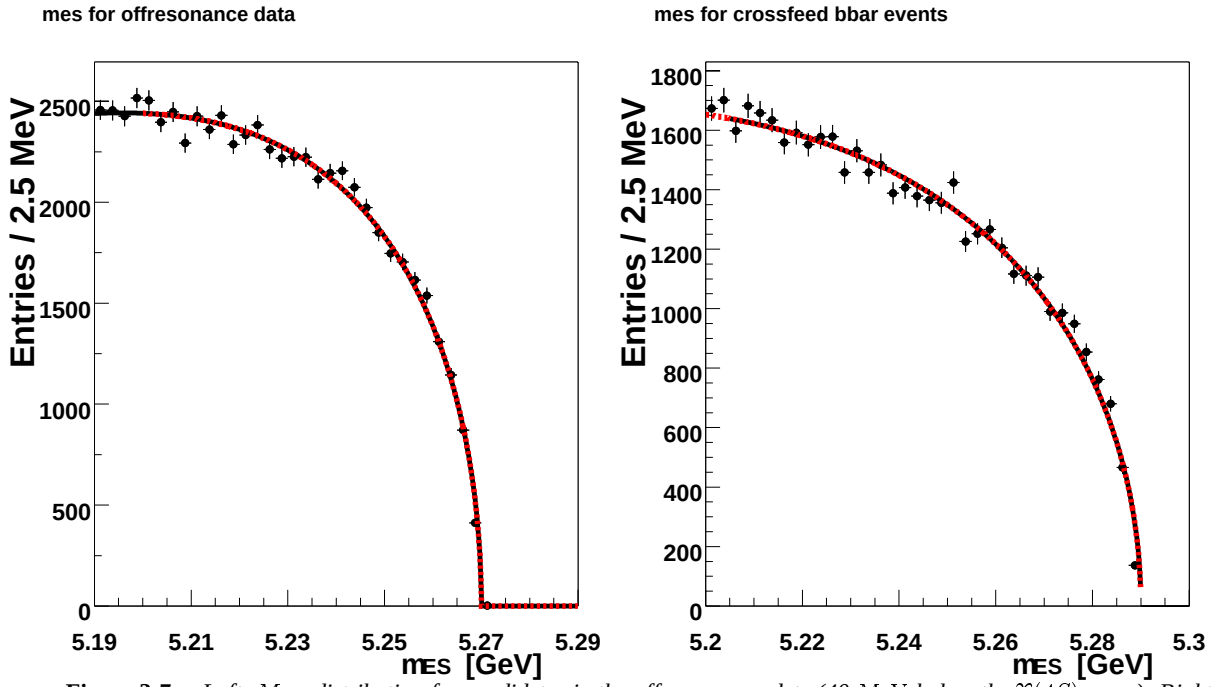

Figure 3-7. *Left: M_{ES} distribution for candidates in the off-resonance data (40 MeV below the $\Upsilon(4S)$ mass). Right: M_{ES} distribution for $b\overline{b}$ background (B^0 reconstructed as B^+). ARGUS shape fit is superimposed in both cases.*

- and if $M_{ES} < m - \sigma \cdot a$

$$\frac{dN}{dM_{ES}} = N \cdot \frac{1}{\sqrt{2 \cdot \pi} \cdot \sigma} \cdot \left(\frac{n}{a}\right)^n \exp\left(-\frac{1}{2} \cdot a^2\right) \frac{1}{\left(\frac{(M_{ES}-m)}{\sigma} + \frac{n}{a} - a\right)^n} \tag{3.6}$$

The radiative tail of this function can take into account possible not fully contained reconstructed π^0. Then the left tail of the distribution depends on the reconstructed B mode and in particular on the number of π^0. Fig. 3-8 shows the fitted shape on the Monte-Carlo for modes with no π^0, one π^0 an two π^0 s.

The maximum total number of floating parameters in the M_{ES} fits is 7. Two of them are for the ARGUS shape, while the remaining five parameters are for the Crystal Ball one.

3.4.2 Study of the X system

A detailed study of the X system, looking for resonances in the signal and background shape was performed. This is meant to optimize the overall purity since a relatively dirty mode could perhaps be split into a very clean and a very dirty one. An example is shown in Fig. 3-9, where the mode $B \rightarrow D\pi\pi\pi$ is analyzed.

In the upper plot, the a_1 line shape is clearly visible, but there is a significant contribution at higher masses. There is a large contribution above 1.5 MeV (non-resonant contribution and π_2). There is also a narrow structure around the D_s^+ mass which might be due to a non negligible $D_s^+ \rightarrow 3\pi$. Above 2 GeV/c^2 just a small amount of signal is present but the combinatoric background is very large, especially for the dirty D meson modes.

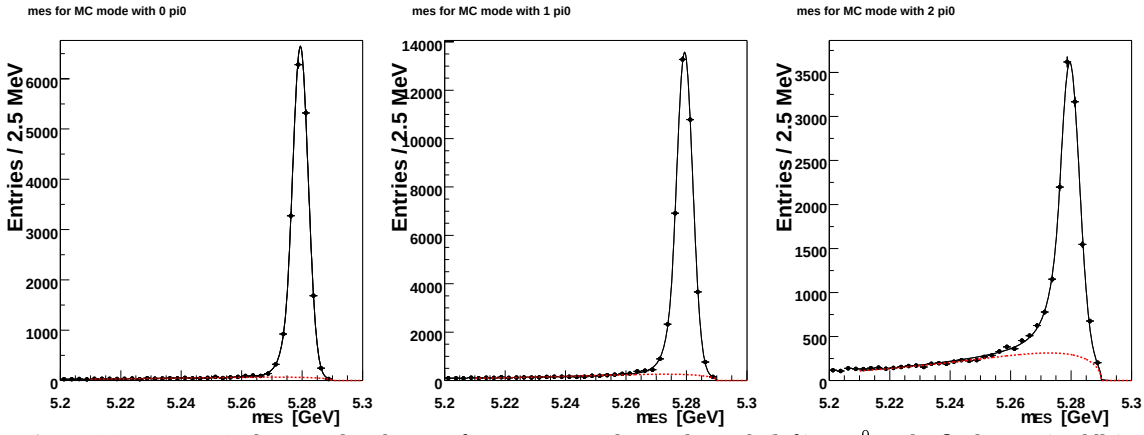

Figure 3-8. *MonteCarlo M_{ES} distributions for reconstructed B modes with (left) no π^0 in the final state, (middle) 1 π^0 in the final state and (right) 2 π^0's in the final state. The fit function is a sum of Crystal Ball and ARGUS function.*

In order to further investigate this interpretation the lower plots of Fig. 3-9 show the invariant masses plots of pairs of tracks in the X system for the a_1 ($M_X < 1.5\,\mathrm{GeV}/c^2$) and the π_2 ($1.5\,\mathrm{GeV}/c^2 < M_X < 2.\,\mathrm{GeV}/c^2$) regions separately. While the a_1 plot clearly shows a ρ signal, the π_2 shows both the f_2 and the ρ as expected from the decays of the π_2. To properly understand the final state the Dalitz analysis should be done, but this is not the purpose here that is meant to isolate dirty regions from clean ones. Two sub-modes are defined depending on whether M_X is smaller than 1.5 GeV/c^2 or it is between 1.5-2.0 GeV/c^2, without requiring the the sub-mode belonging to a precise resonance structure.

Finally the number of B modes is 52 (53 for the D^+ seed). The total number of modes is 1097. A summary is shown in Tab. 3-8.

3.4.3 ΔE selection

Once all the possible reconstruction modes are identified, a window in ΔE and a criterion to pick up among several candidates in a given mode have to be determined.

The ΔE resolutions are determined from the ΔE distributions before requesting the best candidates and they depend essentially on the number of charged tracks and, above all, on the number of π^0 s in the only X system (since the reconstructed D meson is mass constrained). For the modes without π^0 s a fit with a linear background and a Gaussian is performed and 2 σ symmetric windows are taken. In the case of modes with at least a π^0, the situation is worse. First of all there are too many candidates per event. Requiring that only the 10 candidates with the smallest $|\Delta E|$ are taken, can create a bias in the ΔE distribution. Therefore only the cleanest modes are used to determine a common window for all modes including π^0 s. Moreover the presence of π^0 makes the distribution asymmetric.

The ΔE window varies from $-45 < \Delta E < 30\,\mathrm{MeV}$ in the modes without π^0 s, to $-90 < \Delta E < 60$ in the modes with 2 π^0 s.

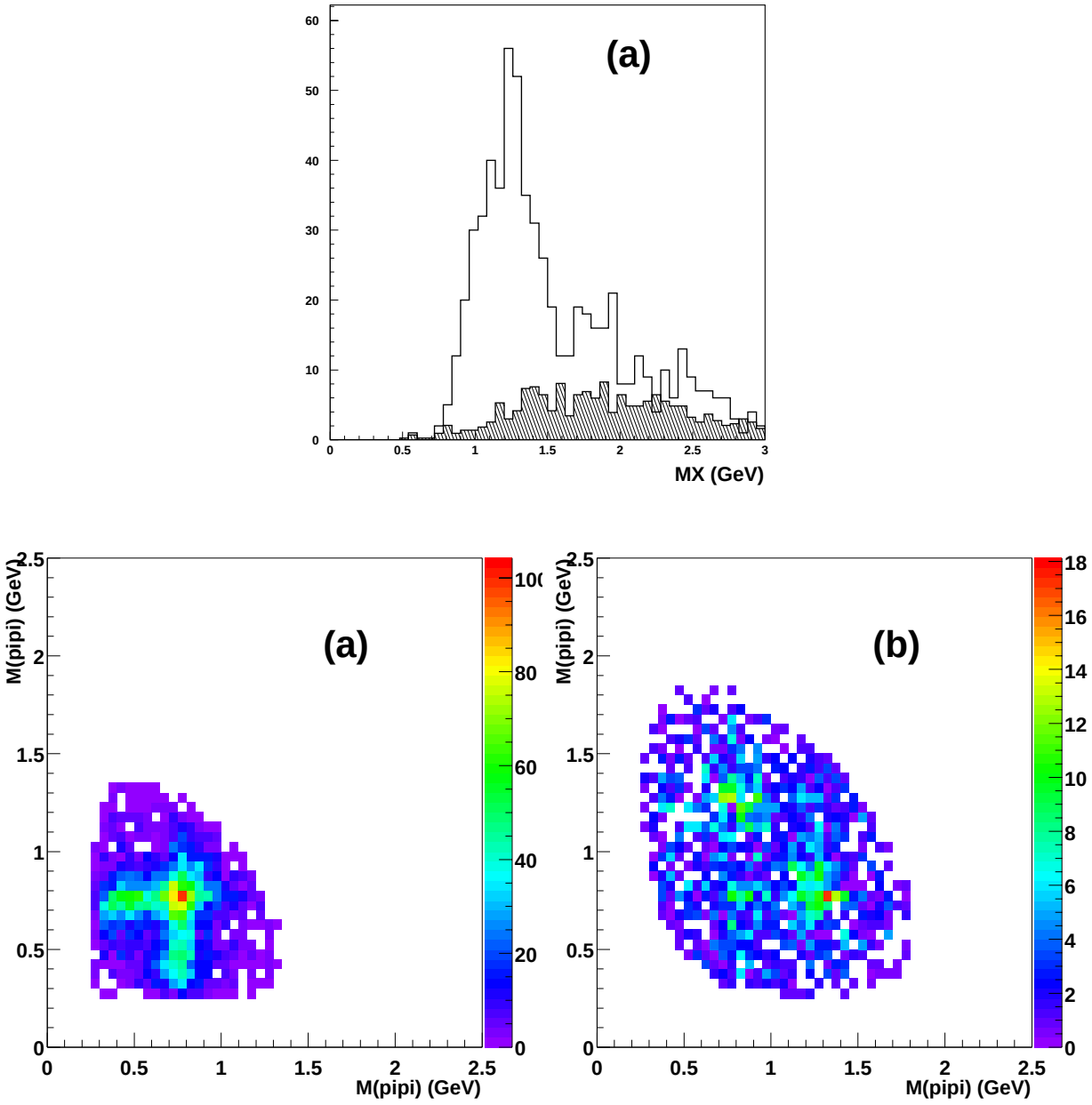

Figure 3-9. *a) M_X distribution for the $D^*3\pi$ on the reduced sample (20 fb-1). Only $D^* \to D^0, D^0 \to K\pi$ is plotted,plots show the properly normalized background (hatched histogram), as evaluated from sidebands. $M_{12} - M_{13}$ scatter plots for the three pions system for the mass region around the b) a_1 ($M_X < 1.5\,\mathrm{GeV}/c^2$) or c) the π_2 ($1.6 < M_X < 2.0\,\mathrm{GeV}/c^2$).*

Channel	pre-seed mode	number of B modes	total number of modes
$B^+ \to D^0 X$	$D^0 \to K^-\pi^+$	52	208
	$D^0 \to K^-\pi^+\pi^0$	52	
	$D^0 \to K^0_S\pi^+\pi^-$	52	
	$D^0 \to K^-\pi^+\pi^+\pi^-$	52	
$B^0 \to D^+ X$	$D^+ \to K^-\pi^+\pi^+$	53	265
	$D^+ \to K^-\pi^+\pi^+\pi^0$	53	
	$D^+ \to K^0_S\pi^+$	53	
	$D^+ \to K^0_S\pi^+\pi^0$	53	
	$D^+ \to K^0_S\pi^+$	53	
$B^+ \to D^{*0} X$	$D^{*0} \to D^0\pi^0$, $D^0 \to K^-\pi^+$	52	416
	$D^{*0} \to D^0\pi^0$, $D^0 \to K^-\pi^+\pi^0$	52	
	$D^{*0} \to D^0\pi^0$, $D^0 \to K^0_S\pi^+\pi^-$	52	
	$D^{*0} \to D^0\pi^0$, $D^0 \to K^-\pi^+\pi^+\pi^-$	52	
	$D^{*0} \to D^0\gamma$, $D^0 \to K^-\pi^+$	52	
	$D^{*0} \to D^0\gamma$, $D^0 \to K^-\pi^+\pi^0$	52	
	$D^{*0} \to D^0\gamma$, $D^0 \to K^0_S\pi^+\pi^-$	52	
	$D^{*0} \to D^0\gamma$, $D^0 \to K^-\pi^+\pi^+\pi^-$	52	
$B^0 \to D^{*+} X$	$D^{*+} \to D^0\pi^+$, $D^0 \to K^-\pi^+$	52	208
	$D^{*+} \to D^0\pi^+$, $D^0 \to K^-\pi^+\pi^0$	52	
	$D^{*+} \to D^0\pi^+$, $D^0 \to K^0_S\pi^+\pi^-$	52	
	$D^{*+} \to D^0\pi^+$, $D^0 \to K^-\pi^+\pi^+\pi^-$	52	
TOTAL			1097

Table 3-8. *Summary of the number of Semi-exclusive modes.*

3.4.4 Multiple candidates and definition of purity

Two kinds of multiple candidates are possible: multiple candidates can be reconstructed in the same submode and many reconstructed submodes per event are also possible.

If there are multiple candidates in the same submode the candidate with the minimum ΔE is used and one candidate per submode is selected.

The selection of the best B among different submodes cannot use the ΔE criterion because the modes with higher combinatoric background would be privileged with respect to the clean ones, thus introducing a bias. The idea is to find an unbiased criterion for choosing a signal event based on a $a-priori$ probability. The $a-priori$ probability here is given by the purity of the mode, determined by fitting the M_{ES} distribution.

The selection of the best B in the event is based on the choice of the reconstructed mode with the highest purity.

The modes are ranked according to their purity and are added up to the sample one at a time. At each addition of a mode the yield increases and the purity decreases. This method is very useful once the composition of the modes has to be optimized for the analysis of the recoil. The significance $S/\sqrt{S+B}$ is computed as a function of the number of added modes and the best composition is chosen. An example for $B^0 \to D^{*+} X$ case is shown in Fig. 3-10.

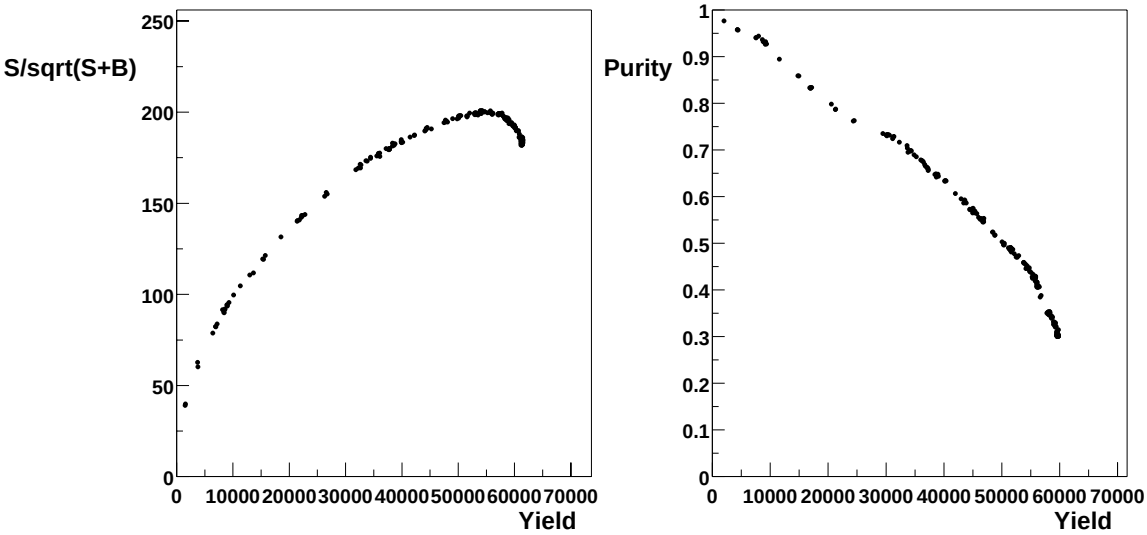

Figure 3-10. *Dependence of the quality factor $S/\sqrt{S+B}$ as a function of the yield when adding modes for the $B^0 \to D^{*+}X$ case. Statistics corresponds to 80 fb^{-1}.*

An integrated purity (referred as int-pur) is defined lumping together all the modes with purity higher or equal to the mode which is considered and meaning the purity of the overall sample.

It has to be noted that both the purities and the integrated purities are used in the following to rank the modes although after the selection on the recoil the actual purity is in general different in value.

3.5 Data and MonteCarlo samples

3.5.1 Data

This analysis is based on a total integrated on-peak luminosity of 81.9 fb^{-1}, recorded in the years 1999–2002. They correspond to about 88 million $B\overline{B}$ pairs. The off-peak data, corresponding to 9.6 fb^{-1}, were used as a control sample to check the fit to the M_{ES} variable for the continuum events (see Sec. 3.4.4).

The final yields depend on the cut on the purity. In Tab. 3-9 the yields for four different levels of purity are summarized. The total reconstructed modes amount to $\sim 5\%$ of the total B decay modes, this leads, for the Semi-exclusive reconstruction, to an overall efficiency of $\sim 0.4\%$, once reconstruction efficiency has been taken into account. The absolute efficiency is not needed in this analysis since the normalization is taken from the number of reconstructed B's before the selection.

3.5.2 MonteCarlo samples

The MonteCarlo samples used in this analysis are summarized in Tab. 3-10.

Channel	final pur.$> 80\%$	final pur.$> 50\%$	single mode pur.$> 10\%$	**final selection**
$B^+ \to D^0 X$	19120 ± 170	54120 ± 370	95204 ± 660	100040 ± 640
$B^0 \to D^+ X$	11070 ± 130	25720 ± 260	55830 ± 480	62349 ± 550
$B^+ \to D^{*0} X$	18600 ± 170	44270 ± 330	75350 ± 580	82050 ± 640
$B^0 \to D^{*+} X$	20670 ± 170	50300 ± 340	55560 ± 390	45729 ± 310
Total B^+	37720 ± 240	98390 ± 500	170560 ± 880	182091 ± 905
Total B^0	31740 ± 210	76020 ± 430	111390 ± 620	108080 ± 630
Total	69460 ± 320	174410 ± 660	281950 ± 1080	290208 ± 1111

Table 3-9. *Yields from Semi-exclusive reconstruction for different levels of purity for 80 fb^{-1} of data.*

3.5.2.1 Signal Simulation

A detailed description of the signal model has been given in Sec. 1.4. In the signal sample, one of the two B decays in $B \to X_s\gamma$. For the other B there are the two options, the so-called generic and cocktail B decays.

For *generic* event samples, the B meson decays without restrictions. Generic $B\overline{B}$ MonteCarlo represents the full simulation of all possible decays of the B meson and it should represent an unbiased event sample.

Cocktail samples contain only specific hadronic decay modes for the B mesons, corresponding to a subset of the modes used in the semi-exclusive reconstruction of the hadronic tag and where Semi-exclusive has a very high efficiency, thus resulting in a sample with higher purity use for cross-checks and high statistics test.

Different kinds of *signal* MonteCarlo samples are used in this analysis. The first one contains only resonant exclusive $B \to K^*(892)\gamma$ decay. The second one is based on the non-resonant $b \to s\gamma$ inclusive model. Several shapes, corresponding to different choices of the b quark mass are generated.

We will refer as KNxxx to indicate that Kagan & Neubert model [34] has been used with "xxx" being the value of the b quark mass expressed in MeV and divided by 10.

Each $\mathcal{B}(B \to K^*\gamma)$ is set to the weighted average of the *BABAR* measurements for the two charge states [44]. The non-resonant $B \to X_s\gamma$ is set to the world weighted average (Sec. 1.5).

For both of them, resonant and non-resonant, cocktail and generic sample are generated. The amount of generated events , the assumed Branching Ratio and the equivalent luminosity is detailed in Tab. 3-10. Luminosity for cocktail samples, is evaluated from the number of events in the M_{ES} peak.

3.5.2.2 $B\overline{B}$ events

$240\,\mathrm{fb}^{-1}$ of generic $B\overline{B}$ are used to simulated the data sample. Generic $B\overline{B}$ contain also signal events, those are modeled in a different way with respect to the signal described in Sec. 1.4. The resonant branching ratio is set to 4.5×10^{-5}. The non-resonant signal branching ratio is choose in such a way that the total branching ratio is set to 3.29×10^{-4} in agreement with Kagan-Neubert theoretical expectation [34]. A cut-off $m_{X_s}^{cut-off} = 1.1\,\mathrm{GeV}/c^2$ is applied as fitted in [52]. Moreover the ratio of the charm and beauty quark masses $z = m_c/m_b$ is set to 0.29 in agreement with [34].

Table 3-10. *Monte Carlo and data sets. KNxxx = Kagan & Neubert model [34] with "xxx" the value of the b quark mass. Each $\mathcal{B}(B \to K^*\gamma)$ is set to the weighted average of the BABAR measurements for the two charge states [44]. The non-resonant $\mathcal{B}$ is set to the world weighted average (sec.1.5).*

Data Set	1' B mode	Events	# breco	Cross Section or $\mathcal{B}$	Luminosity
uds	-			$2.09\,\text{nb}$	$109.63\,\text{fb}^{-1}$
$c\overline{c}$	-			$1.30\,\text{nb}$	$95.84\,\text{fb}^{-1}$
$B^0\overline{B}^0$	generic		387000 ± 834	$0.543\,\text{nb}$	$240\,\text{fb}^{-1}$
B^+B^-	generic		801000 ± 1280	$0.543\,\text{nb}$	$240\,\text{fb}^{-1}$
$B^0 \to K^{*0}(892)\gamma$	generic	111000	212 ± 16	$4.03 \pm 0.43 \times 10^{-5}$	$2518\,\text{fb}^{-1}$
$B^\pm \to K^{*\pm}(892)\gamma$	generic	136000	400 ± 25	$4.03 \pm 0.43 \times 10^{-5}$	$3083\,\text{fb}^{-1}$
$B^0 \to X_s^0\gamma$ (KN465)	generic	81000	152 ± 15	$3.34 \pm 0.38 \times 10^{-4}$	$221\,\text{fb}^{-1}$
$B^\pm \to X_s^\pm\gamma$ (KN465)	generic	75000	232 ± 18	$3.34 \pm 0.38 \times 10^{-4}$	$204\,\text{fb}^{-1}$
$B^0 \to X_s^0\gamma$ (KN480)	generic	113000	244 ± 19	$3.34 \pm 0.38 \times 10^{-4}$	$309\,\text{fb}^{-1}$
$B^\pm \to X_s^\pm\gamma$ (KN480)	generic	109000	332 ± 23	$3.34 \pm 0.38 \times 10^{-4}$	$298\,\text{fb}^{-1}$
$B^0 \to X_s^0\gamma$ (KN495)	generic	79000	134 ± 13	$3.34 \pm 0.38 \times 10^{-4}$	$216\,\text{fb}^{-1}$
$B^\pm \to X_s^\pm\gamma$ (KN495)	generic	79000	263 ± 19	$3.34 \pm 0.38 \times 10^{-4}$	$216\,\text{fb}^{-1}$
$B \to K^*\gamma$	cocktail	10000	1134 ± 36		$5284\,\text{fb}^{-1}$
$B \to X_s\gamma$ (KN465)	cocktail	50000	5676 ± 83		$3088\,\text{fb}^{-1}$
$B \to X_s\gamma$ (KN480)	cocktail	100000	11116 ± 116		$6050\,\text{fb}^{-1}$
$B \to X_s\gamma$ (KN495)	cocktail	50000	5448 ± 80		$2968\,\text{fb}^{-1}$

3.5.2.3 Non $B\overline{B}$ events

The non-$B\overline{B}$ MonteCarlo consists of $c\overline{c}$ and $u\overline{u}$, $d\overline{d}$, $s\overline{s}$ events. These samples have been used, to check the M_{ES} shape (Sec. 3.4.4).

The M_{ES} shapes and yields for data, generic $B\overline{B}$, generic signal (KN480 and resonant) are shown in Fig. 3-11. Similar plots for the cocktail sample are in Fig. 3-12.

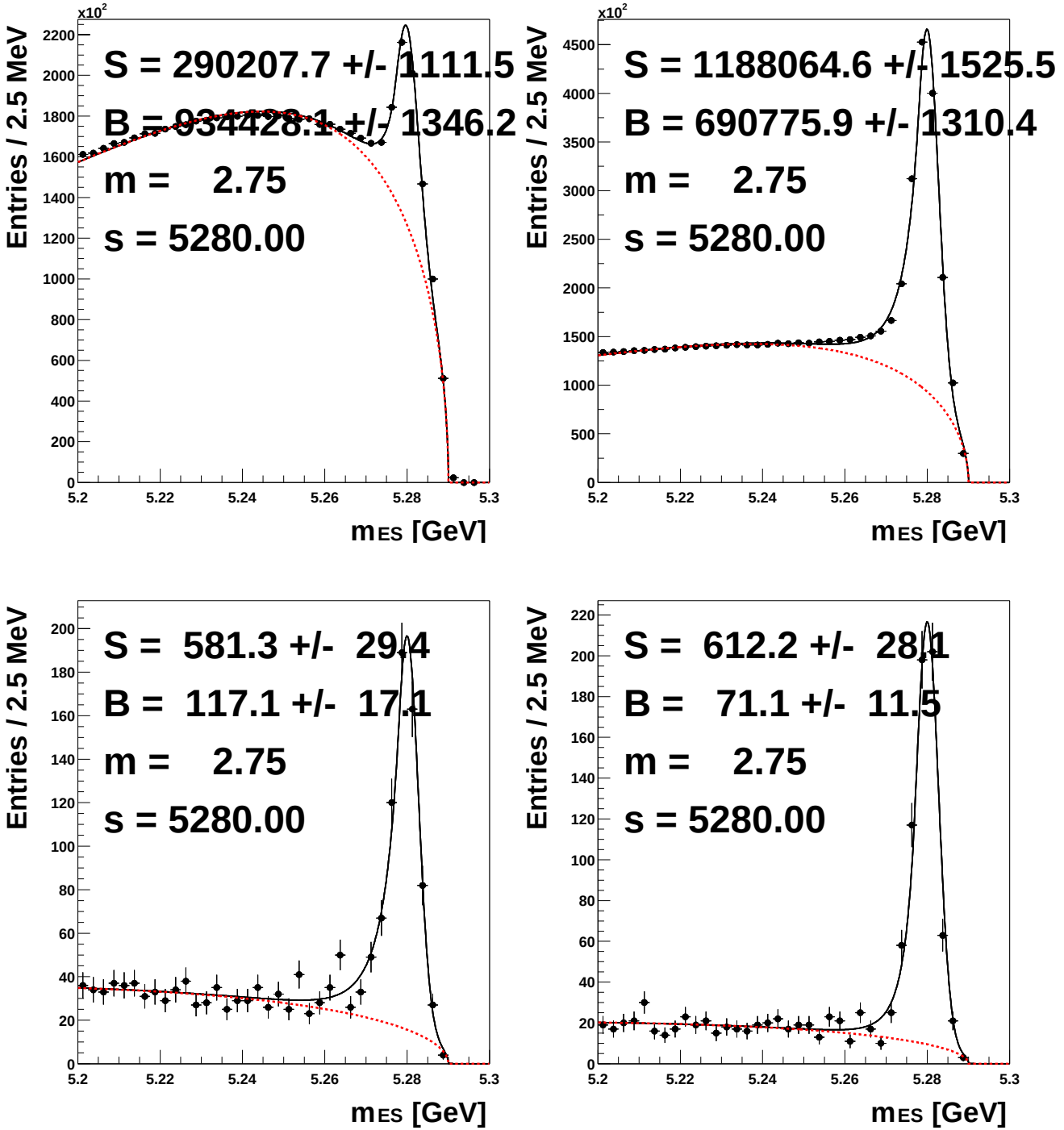

Figure 3-11. *Event yields for all seeds combined without additional requirement on the recoiling system. Top left: data sample. Top right: generic $B\overline{B}$ MonteCarlo sample. Bottom left: generic KN480 MonteCarlo signal sample. Bottom right: $B \to K^*\gamma$ MonteCarlo sample. The numbers printed on each plot indicate signal yield (S) and background yield (B), both in the signal region defined by $M_{ES} > 5.27\,\mathrm{GeV}/c^2$; peak (m) and width (s) of the signal Gaussian.*

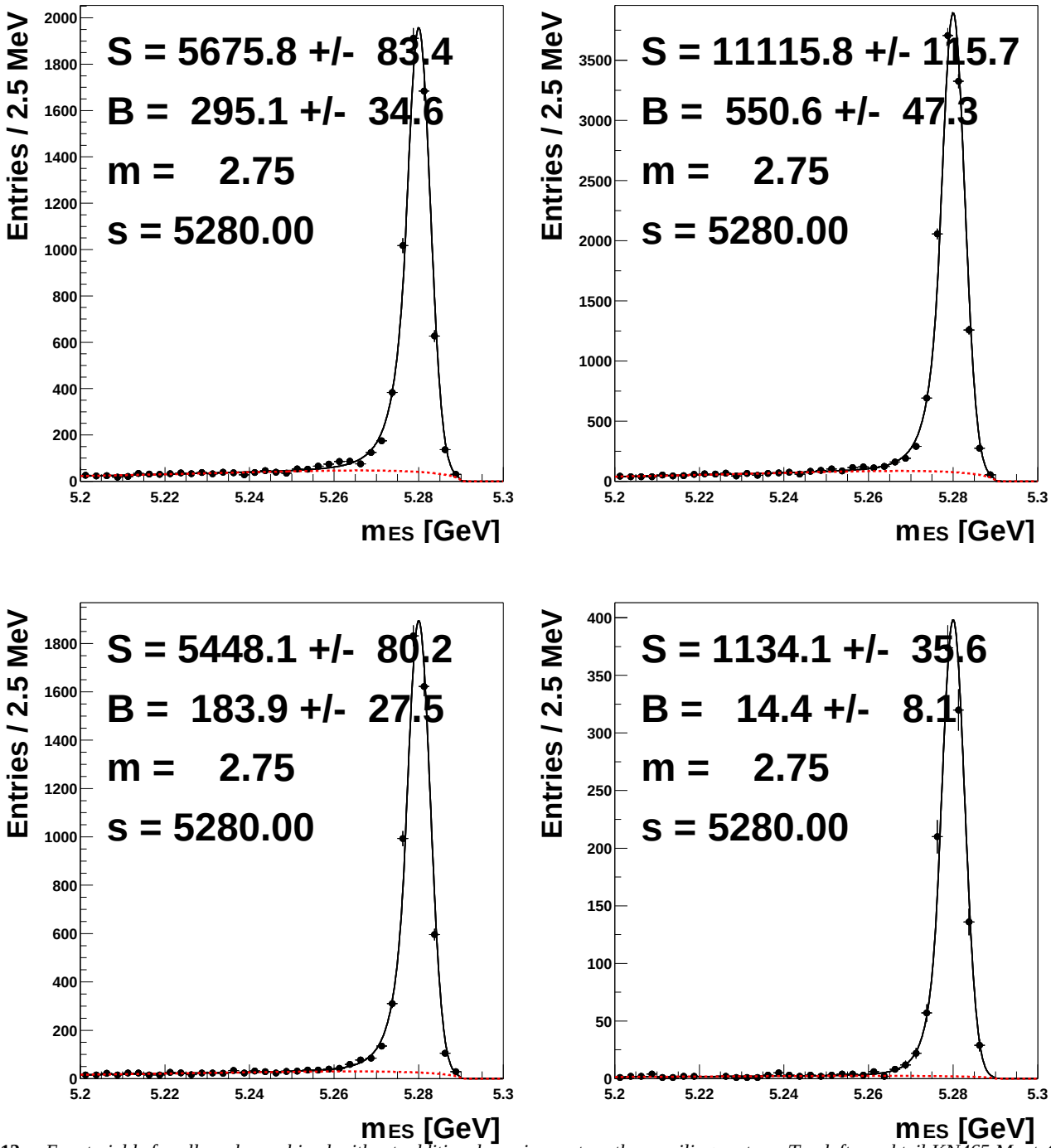

Figure 3-12. *Event yields for all seeds combined without additional requirement on the recoiling system. Top left: cocktail KN465 MonteCarlo sample. Top right: cocktail KN480 MonteCarlo sample. Bottom left: cocktail KN495 MonteCarlo sample. Bottom right: cocktail $B \to K^*\gamma$ MonteCarlo sample. The numbers printed on each plot indicate signal yield (S) and background yield (B), both in the signal region defined by $M_{ES} > 5.27\,\mathrm{GeV}/c^2$; peak (m) and width (s) of the signal Gaussian.*

4

Measurement of $\mathcal{B}(B \to X_s\gamma)$

This measurement is based on the study of high energy photons recoiling to fully reconstructed B 's. This technique offers many advantages:

- A very clean environment. One of the two B mesons from the decay of the $\Upsilon(4S)$ is reconstructed in a fully hadronic mode (see Fig. 4-1). We will refer it as B_{reco} . The remaining particles of the event originate from the other B , referred as B_{recoil} .
- The B_{recoil} 4-vector is measured, and hence all relevant kinematic quantities are known in the B_{recoil} rest frame. This information is advantageous for signal selection since the photon spectrum is not smeared from the unknown boost of the B mesons in the $\Upsilon(4S)$ frame like fully inclusive analysis. In the analysis we will refer as E_γ as the photon energy in B rest frame.
- Absolute luminosity and and B reconstruction efficiencies are not needed since normalization is taken from the number of reconstructed B's before the selection. This avoids errors from incorrectly luminosity estimates.
- The purity of the B_{reco} sample can be adjusted selecting only a sub-sample of the reconstructed modes on the tag side.
- Continuum events can be subtracted on the B_{reco} side performing a fit toM_{ES} as explained in Sec. 3.4.4 without using off-resonance data, of which much fewer statistics than on-peak data are available.
- Since the kinematics are over-constrained, the resolution on the reconstructed quantities, such as the mass of the hadronic system m_{X_s}, can be improved by using a kinematic fit.
- The fully hadronic reconstruction of one B in the decay determines the tagging of the charge and flavour of the B 's allowing to measure $BR(B \to X_s\gamma)$ and α_{CP} in B^0 and B^+ separately.

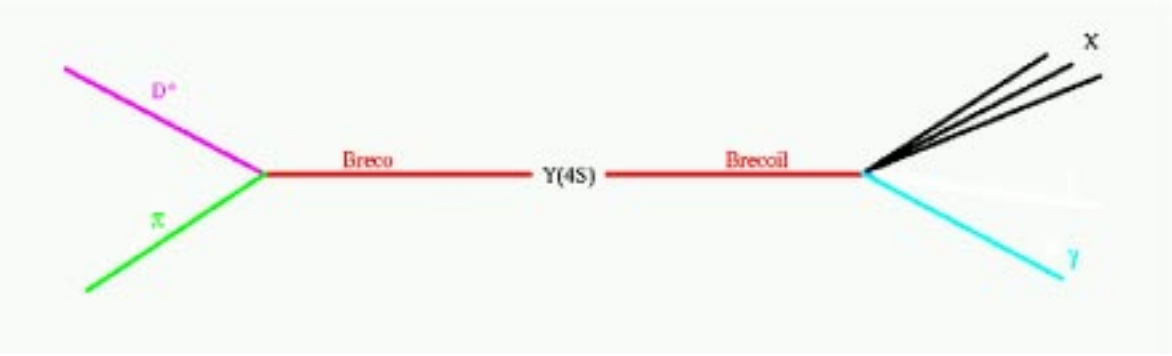

Figure 4-1. *$B \to X_s\gamma$ events in the recoil of fully reconstructed B 's*

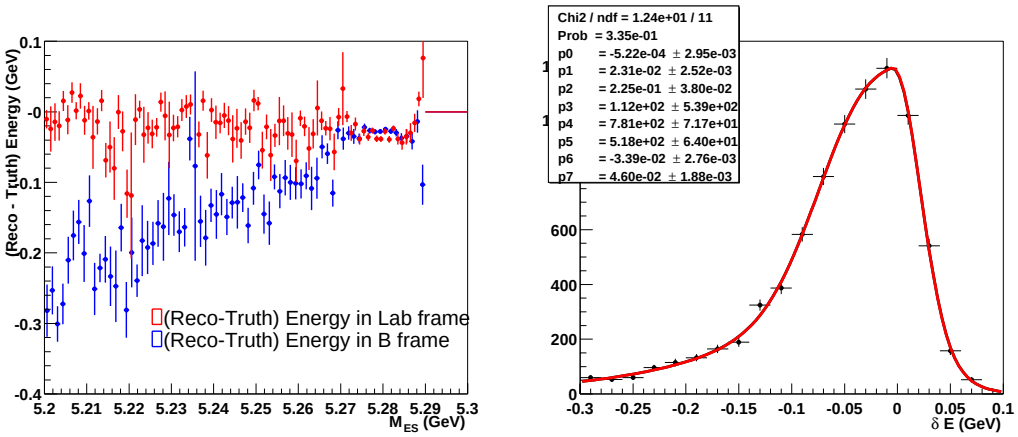

Figure 4-2. *Left: the difference δE between the photon reconstructed energy E^{reco} and truth generated energy E^{truth} versus M_{ES} distribution in the B_{recoil} frame (blue) and laboratory frame (red) in signal MonteCarlo sample. Right: δE distribution (combinatorial background subtracted) in MonteCarlo sample.*

The high energy photon selection is detailed in Sec. 4.1. Section 4.2 describes the selection criteria used for background rejection. The optimization of these criteria is given in Sec. 4.3. The Data-MonteCarlo comparison is reported in Sec. 4.4. Sec.4.5 and 4.6 describe the measurement technique and results.

4.1 High energy photon selection

The experimental signature of a $B \to X_s\gamma$ decay is the presence of an isolated high energetic photon in the event.

Detailed studies have been performed on the reconstruction and efficiency of high energy photons. Selection criteria are applied in order to ensure well known efficiencies and minimal backgrounds. In this chapter different variables, relevant to the analysis, are introduced; the optimization of selection criteria will be explained in Sec. 4.3.

- Photons with $E_\gamma > 1.3\,\mathrm{GeV}$ are selected. In case of multiple candidates, the most energetic one is selected. Multiple high energy photons hardly ever occur due to the kinematic constraints. They occur in 1.5% of the cases with $E_\gamma > 1.3\,\mathrm{GeV}$ but only 0.2% with $E_\gamma > 1.9\,\mathrm{GeV}$ (signal region).
- In order to remove poorly reconstructed clusters due to noisy or dead channels, at least 4 crystals are required to be fired by the EMC shower associated to the selected photon. Bump center of gravities are moreover required to be within the calorimeter acceptance of the detector: $0.410 < \theta < 2.54$ rad.
- Unmatched tracks (see Sec. 3.2), are removed. They occur in 0.1% of cases in MonteCarlo simulation and 0.4% in Data.
- The photon energy is boosted from the laboratory frame, where it is measured, into the B_{recoil} frame in which the analysis is performed. The B_{recoil} four-momentum is defined as:

$$P^{B_{recoil}} = P^{\Upsilon(4S)} - P^{B_{reco}} \,. \tag{4.1}$$

The $P^{\Upsilon(4S)} = P^{e+} + P^{e-}$ is known, the $P^{B_{reco}}$ can be calculated since the B_{reco} is reconstructed in a fully hadronic decay. Therefore the correctness of the boost, and of quantities computed in B_{recoil} frame, depends on the B_{reco} reconstruction. In the left plot of Fig. 4-2 the difference δE between the photon reconstructed

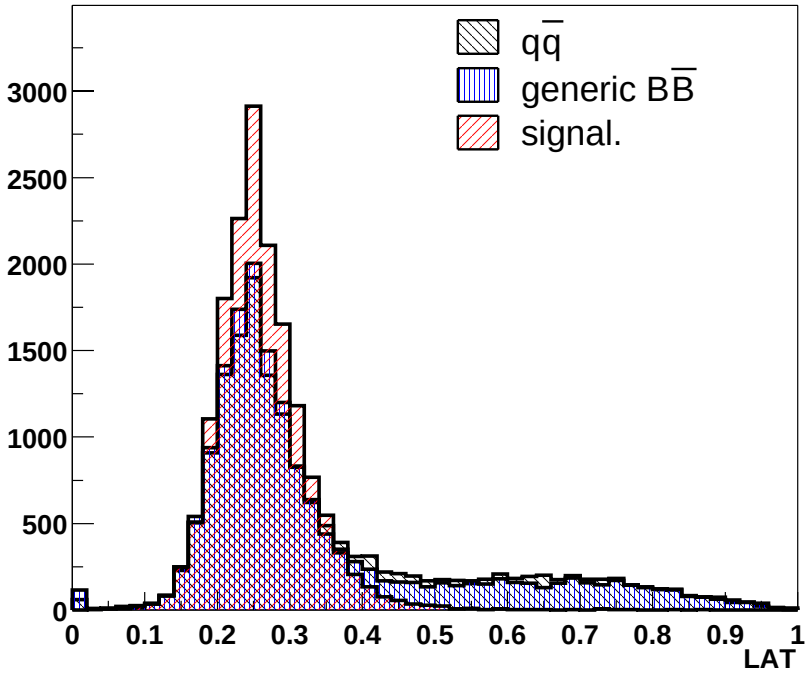

Figure 4-3. *LAT distribution for $B\overline{B}$, signal and $q\overline{q}$ events in MonteCarlo sample.*

energy E^{reco} and truth generated energy E^{truth} versus M_{ES} distribution is shown in the B_{recoil} frame (blue) and laboratory frame (red) in MonteCarlo sample. A strong correlation is present in the B_{recoil} frame; a poorly reconstructed B ($M_{ES} < 5.27\,\mathrm{GeV}/c^2$) leads to an under-estimate of both the boost and the reconstructed photon energy.

Therefore, in order to properly take into account the energy and M_{ES} correlation in the combinatorial background subtraction, the energy distribution is divided in several bins, and for each of them, the combinatorial background is subtracted from an M_{ES} fit. This technique is applied to all the variables used in the analysis. The right plot of Fig. 4-2 shows the δE distribution once the combinatorial background has been properly subtracted. A fit to the sum of a Crystal Ball plus an Gaussian function is superimposed. This is not meant to extrapolate any relevant information for the analysis, studies on the photon resolution and calibration are done on control sample as explained in Sec. 5.6. This is a check intended to show we are subtracting the combinatorial background in the correct way: no bias in the reconstructed energy is observed.

- In order to reduce hadronic fakes and merged π^0, the LAT variable (see Sec. 3.2) is used. In Fig. 4-3 the distribution for $B\overline{B}$, signal and $q\overline{q}$ events in MonteCarlo sample is shown, photons are required to have $LAT < 0.45$.

- The main source of background is due to γ coming from a $\pi^0 \to \gamma\gamma$ and $\eta \to \gamma\gamma$ decay. A $\pi^0(\eta)$ veto is applied in order to reject those events. The $M_{\gamma\gamma}$ invariant mass of the selected photons and any other photon in the recoil with $E_\gamma^{\mathrm{lab}} > 40(315)\,\mathrm{MeV}$ is computed and shown in Fig. 4-4. The choice of the minimum energy for the photons has been optimized for π^0 and η mass regions separately. In Fig. 4-5 the $M_{\gamma\gamma}$ invariant mass in $B\overline{B}$ MonteCarlo (left) and data (right) sample is shown in the π^0 mass region. A fit to the sum of a Crystal Ball plus a Gaussian function is superimposed. The $M_{\gamma\gamma}$ invariant mass in the η mass region is shown in Fig. 4-6, a fit

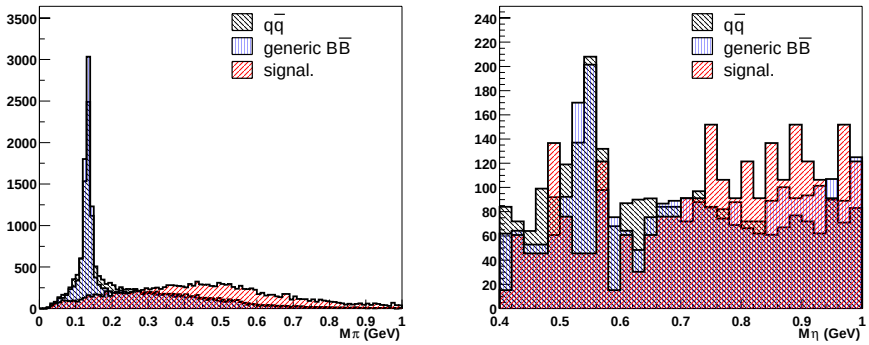

Figure 4-4. *$M_{\gamma\gamma}$ invariant mass of the selected photon and any other photon in the recoil with $E_\gamma^{\rm lab} > 40\,{\rm MeV}$ (left plot) and $E_\gamma^{\rm lab} > 315\,{\rm MeV}$ (right plot) in MonteCarlo sample.*

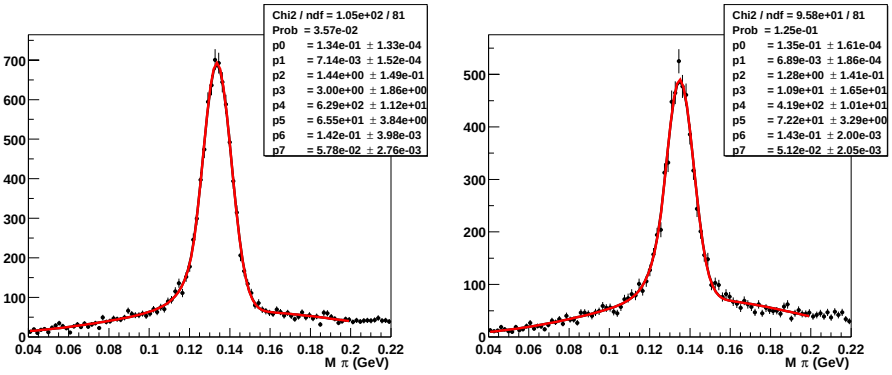

Figure 4-5. *$M_{\gamma\gamma}$ invariant mass in $B\overline{B}$ MonteCarlo (left) and data (right) sample in the π^0 mass region. A fit to the sum of a Crystal Ball plus a Gaussian function is superimposed.*

to the sum of a Crystal Ball plus a first order polynomial function is superimposed. High energy photon whose $M_{\gamma\gamma}$ lies in a mass window $115(508) < M_{\gamma\gamma} < 155(588)\,{\rm MeV}/c^2$ are vetoed.

- Since signal events have low multiplicity with respect to $q\overline{q}$ and generic $B\overline{B}$ events, the EMC bump-isolation discriminate the background. The left plot of Fig. 4-7 shows the distance between the selected photon and any other neutral bumps in the calorimeter. This variable is correlated to the $\pi^0(\eta)$ veto previously discussed; in fact in most of the cases the two photons making a $\pi^0(\eta)$ have, for kinematic reasons, EMC bumps close to each other on the calorimeter surface (right plot in Fig. 4-7). Anyway, it could be useful in rejecting events in which the $\pi^0(\eta)$ veto fails or the photon comes from other sources. Events for which the bump distance is lower than 40 cm are discarded.

4.2 Background rejection criteria

The main source of background is due to high energy photons in $q\overline{q}$ events that fail the π^0 and η veto.

The number of continuum events in the signal region can be estimated and subtracted from a fit to the M_{ES} distribution, but it is important to reduce this background in order to minimize the statistical error of the measurement.

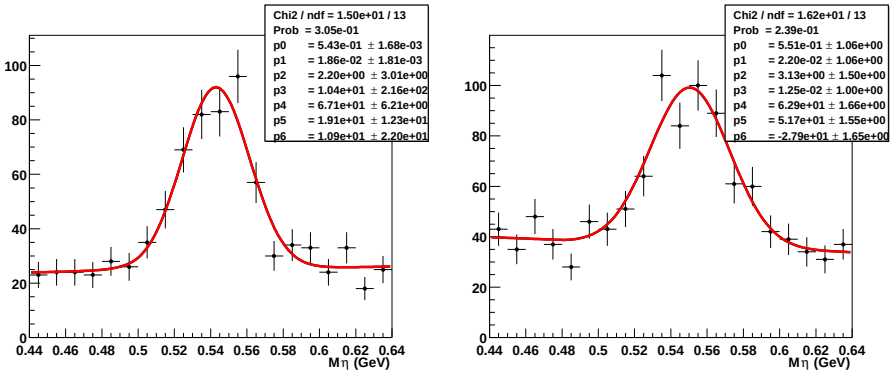

Figure 4-6. *$M_{\gamma\gamma}$ invariant mass in $B\overline{B}$ MonteCarlo (left) and data (right) sample in the η mass region. A fit to the sum of a Crystal Ball plus a first order polynomial function is superimposed.*

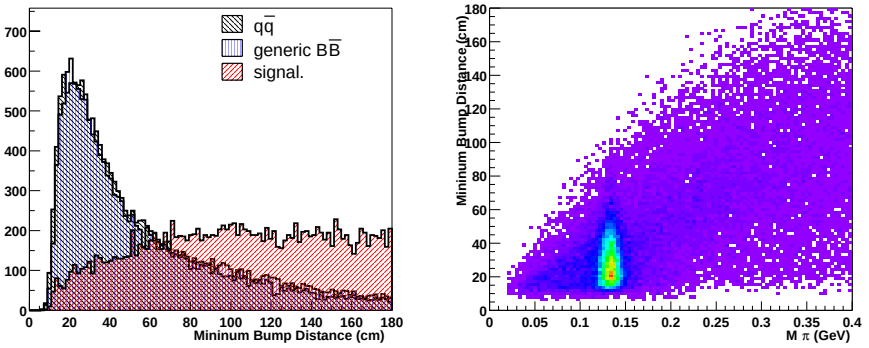

Figure 4-7. *Left plot:Distance between the selected photon and any other neutral bumps in the calorimeter. Right plot:correlation between the $M_{\gamma\gamma}$ invariant mass and the bump distance in $B\overline{B}$ MonteCarlo sample.*

4.2.1 Discriminant variables

There are many variables showing a discriminating power against this background: these are based on the different topology of $q\overline{q}$ events with respect to $B\overline{B}$ event (Fig. 4-8). In a true signal event, $B\overline{B}$ pair are produced via the $\Upsilon(4S)$ resonance. In the $\Upsilon(4S)$ rest frame, the B mesons have low momenta, so that the decay of each B meson is nearly isotropic. An additional feature of a signal event is that there is no correlation between the directions of the decay products coming from each of the two B mesons.

In a light-quark (u, d, s) continuum event, the event shape has a pronounced two-jet structure, so there is a strongly preferred direction characterizing the whole event. B candidates from such an event will therefore tend to have less isotropic decay shapes in the $\Upsilon(4S)$ rest frame, and there will also be correlations between the directions of the decay products of the two B meson candidates, since they will tend to lie within the two jets. In a $c\overline{c}$ event, the jet structure is still present, but is less pronounced, so shape variables will provide less discriminating power for this type of background.

Moreover some of these variables are helpful in rejecting background coming from $B\overline{B}$ over signal events as explained during this section.

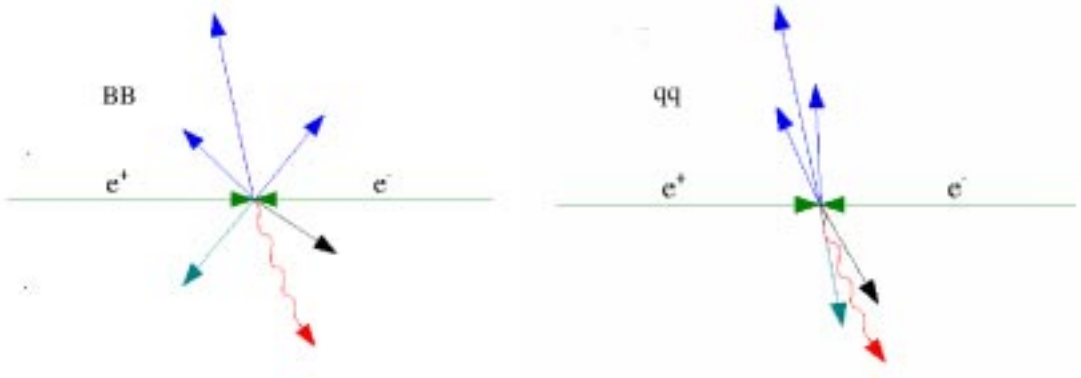

Figure 4-8. *Topology of the event for $B\overline{B}$ (left figure) and $q\overline{q}$ (right figure) in $\Upsilon(4S)$ rest frame.*

- **Thrust**
  The thrust axis of an event, $\hat{T}$, is defined as the direction which maximizes the sum of the longitudinal momenta of the particles. Thrust, T, is related to it [64] by

$$T = \frac{\sum_i |\hat{T} \cdot \mathbf{p}_i|}{\sum_i |\mathbf{p}_i|}. \tag{4.2}$$

  The allowed range of T is (0.5, 1), where $T \sim 1$ corresponds to a highly directional event, and T = 0.5 corresponds to an isotropic event.

  In a typical background event for a two-body decay, the decay products of the B candidate each lie in one of the two jets, and they are therefore approximately back-to-back. Thus the decay axis of the B candidate is roughly collinear with the thrust axis for the rest of the event. For a true signal event, the B decay axis is uncorrelated with the thrust axis of the rest of the event, which in that case comes from the decay of the other B meson. The Thrust could be computed including all the particles (T) or only neutral particle (T_{neu}) in the event.

  Since in this analysis one B is fully reconstructed, several variables could be explored for rejecting background:

- the Thrust of the B_{reco} : T_{reco},
- the Thrust of the B_{recoil} : T_{recoil},
- the absolute value of the cosine of the angle between $\hat{T}_{reco}$ and $\hat{T}_{recoil}$: $|cos(\theta_{TBB})|$,
- the absolute value of the cosine of the angle between the photon and the $\hat{T}_{reco(il)}$ axis: $|cos(\theta_{\gamma Treco(il)})|$.

The distribution of these variables is shown in Fig. 4-9. The most effective one is $cos(\theta_{TBB})$ that peaks at 1 for continuum events and is flat for $B\overline{B}$ and signal events since in this case the two thrust axes are uncorrelated. The distribution of $|cos(\theta_{\gamma Treco(il)})|$ peak at 1 for signal events, in this case, in fact, the thrust axis is the photon axis itself.

- **Fox-Wolfram Moments**

  The Fox-Wolfram moments, H_l, are defined [65] as,

$$H_l = \sum_{i,j} \frac{|\mathbf{p}_i|.|\mathbf{p}_j|}{E_{\rm vis}^2} P_l(cos\theta_{ij}), \tag{4.3}$$

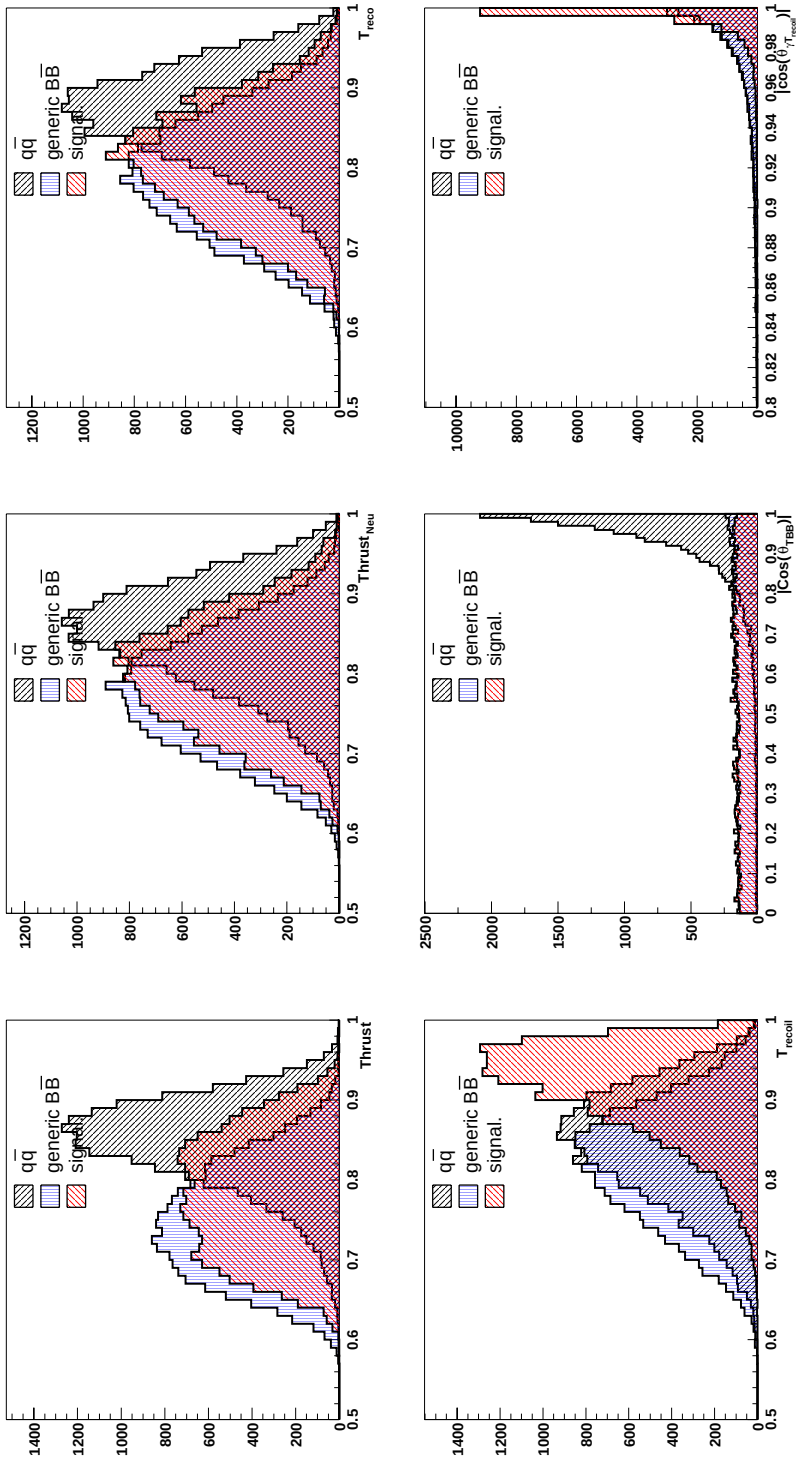

Figure 4-9. *Thrust variables distributions for $q\bar{q}$, $B\overline{B}$ and signal.*

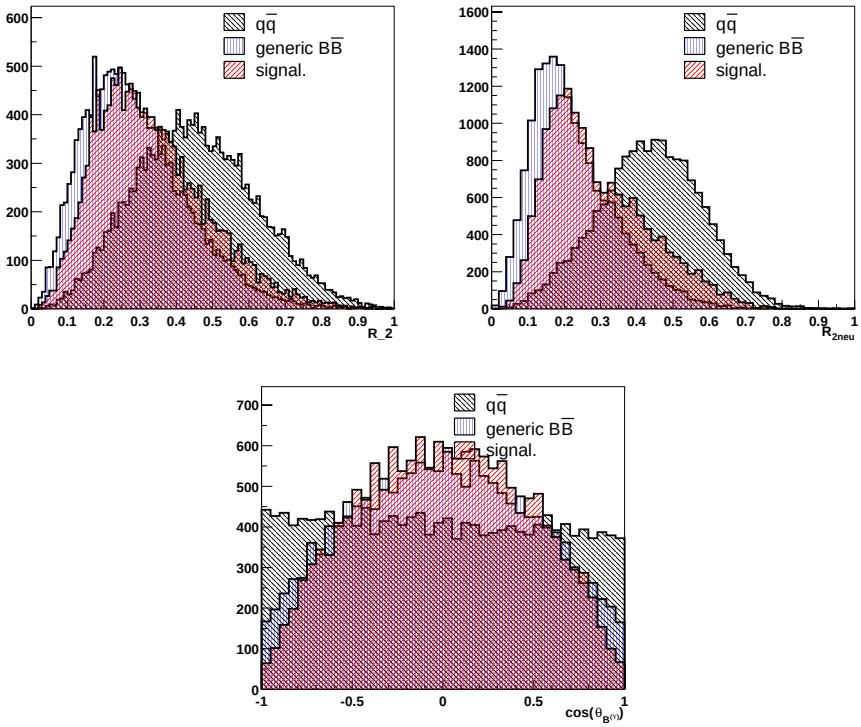

Figure 4-10. *R_2, R_{2neu} and $\cos(\theta_{B^*})$ distributions for $q\overline{q}$, $B\overline{B}$, signal events.*

where P_l are the Legendre polynomials, $\mathbf{p}_{i,j}$ are the particle momenta, θ_{ij} is the opening angle between particles i and j, and $E_{\rm vis}$ is the total visible energy of the event.

Neglecting particle masses, energy-momentum conservation requires that $H_0 = 1$. For 2-jet events, $H_1 = 0$ and $H_l \sim 1$ for l even, and $H_l \sim 0$ for l odd. For this application the ratio of Fox-Wolfram 2nd to 0th moments $R_2 = \frac{H_2}{H_0}$ is used as the discriminating variable. The distribution of R_2 including all the particles and only neutral particle (R_{2neu}) are shown in Fig. 4-10.

- $\cos(\theta_{B^*})$

  The B meson is a pseudo-scalar producted by the the vector meson $\Upsilon(4S)$: the angular momentum conservation forces the decay to be in a $\mathcal{P}$ wave, thus resulting in a $\sin^2(\theta_B)$ angular distribution of the B direction with respect to the beam axis in in $\Upsilon(4S)$ frame. For $q\overline{q}$ events, the distribution is expected to be flat.

  The distribution of $\cos(\theta_{B^*})$ is shown in Fig. 4-10: the asymmetry respect to zero is caused by the $\Upsilon(4S)$ Lorentz *boost*.

- **"Cleo" Energy Flow Cones**

  The total energy flowing along the photon direction is computed in cones of several angles, excluding the photon energy [66]. We will refer as $E^{syst}_{f(b),\theta}$ where $f(b)$ means that the cone is computed parallel or anti-parallel to the photon direction, θ is the opening angle, syst is the reference frame in which the cone si computed ($\Upsilon(4S)$, B) and a R suffix will be used to separate cones in which only the particles belonging to the B_{recoil} are used. Cones are effective in rejecting $q\overline{q}$ as $B\overline{B}$ background events. In $q\overline{q}$ events a large amount of energy in both forward and backward cones are expected while for signal events only a small amount of energy is expected, since the

X_s system goes back-to-back with respect to the photon. Morevoer a generic $B\overline{B}$, is characterized by a higher multiplicity than signal and therefore, more energy is expected to flow in small angles cones.

The Energy Cones distributions for different opening angle are shown in Fig. 4-11–4-16.

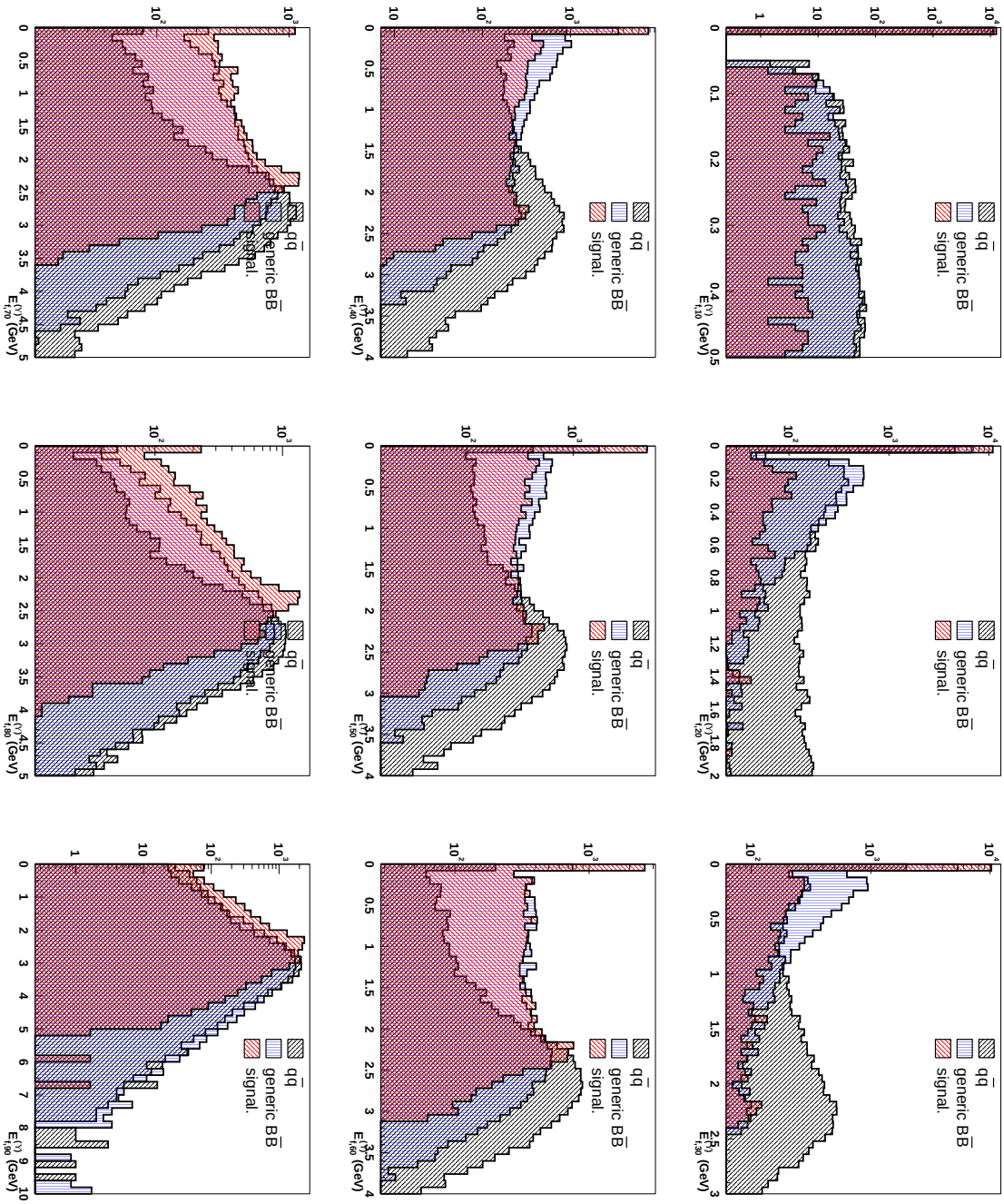

Figure 4-11. *$E^{\gamma(4S)}_{f,\theta}$ for $q\bar{q}$, $B\overline{B}$ and signal.*

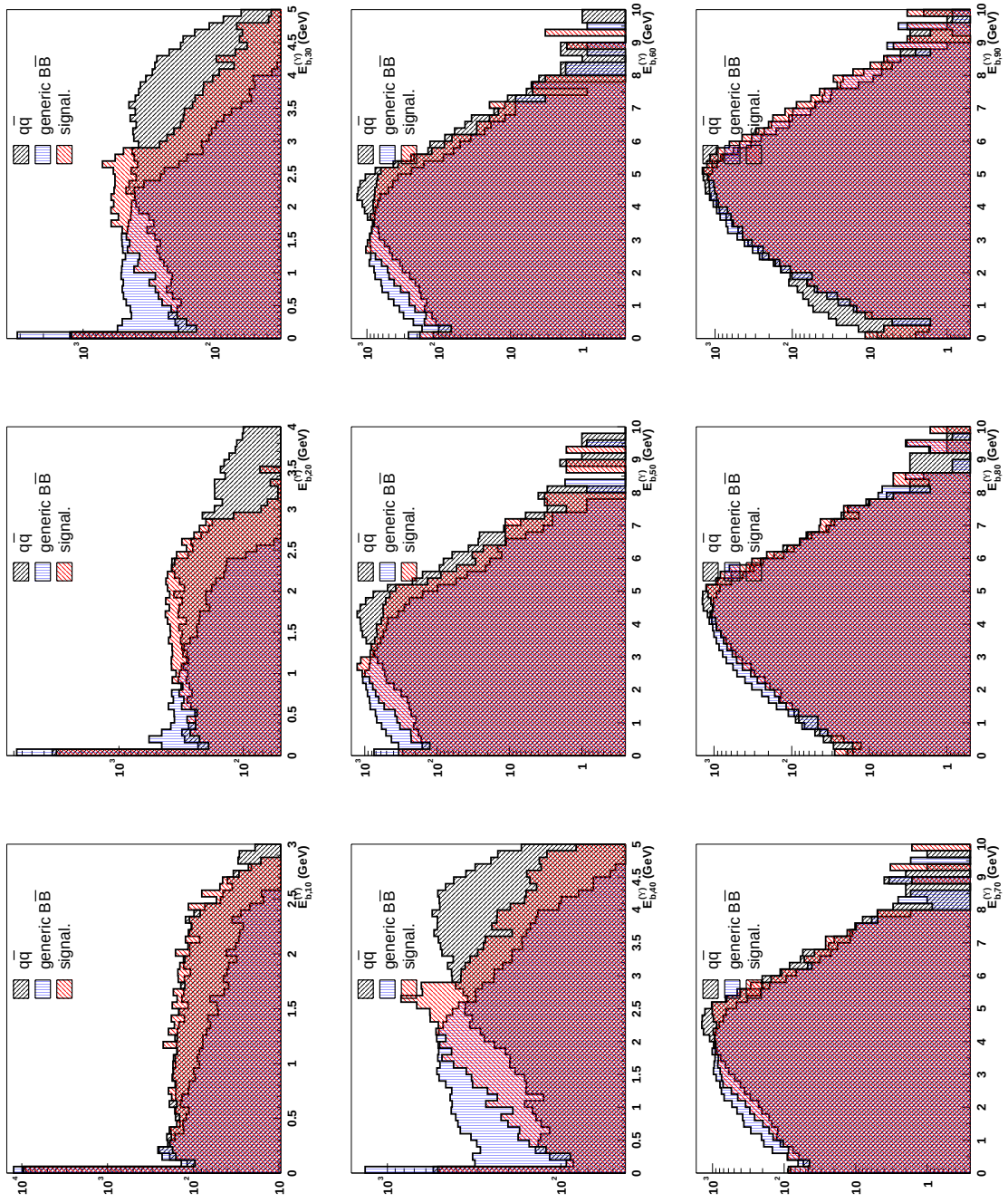

Figure 4-12. $E^{\Upsilon(4S)}_{b,\theta}$ *for* $q\overline{q}$, $B\overline{B}$ *and signal.*

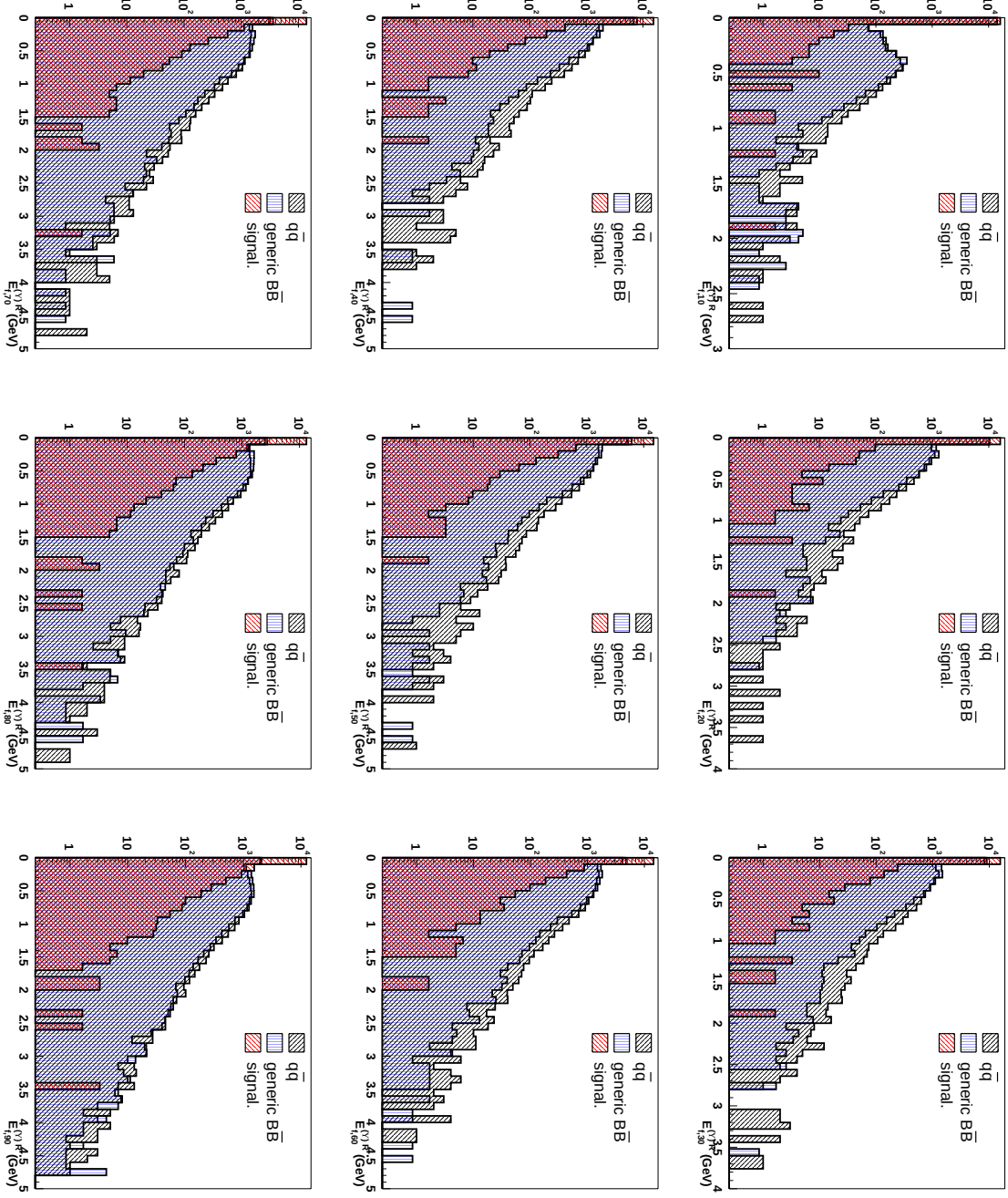

Figure 4-13. $E^{\Upsilon(4S),R}_{f,\theta}$ *for* $q\bar{q}$, $B\overline{B}$ *and signal.*

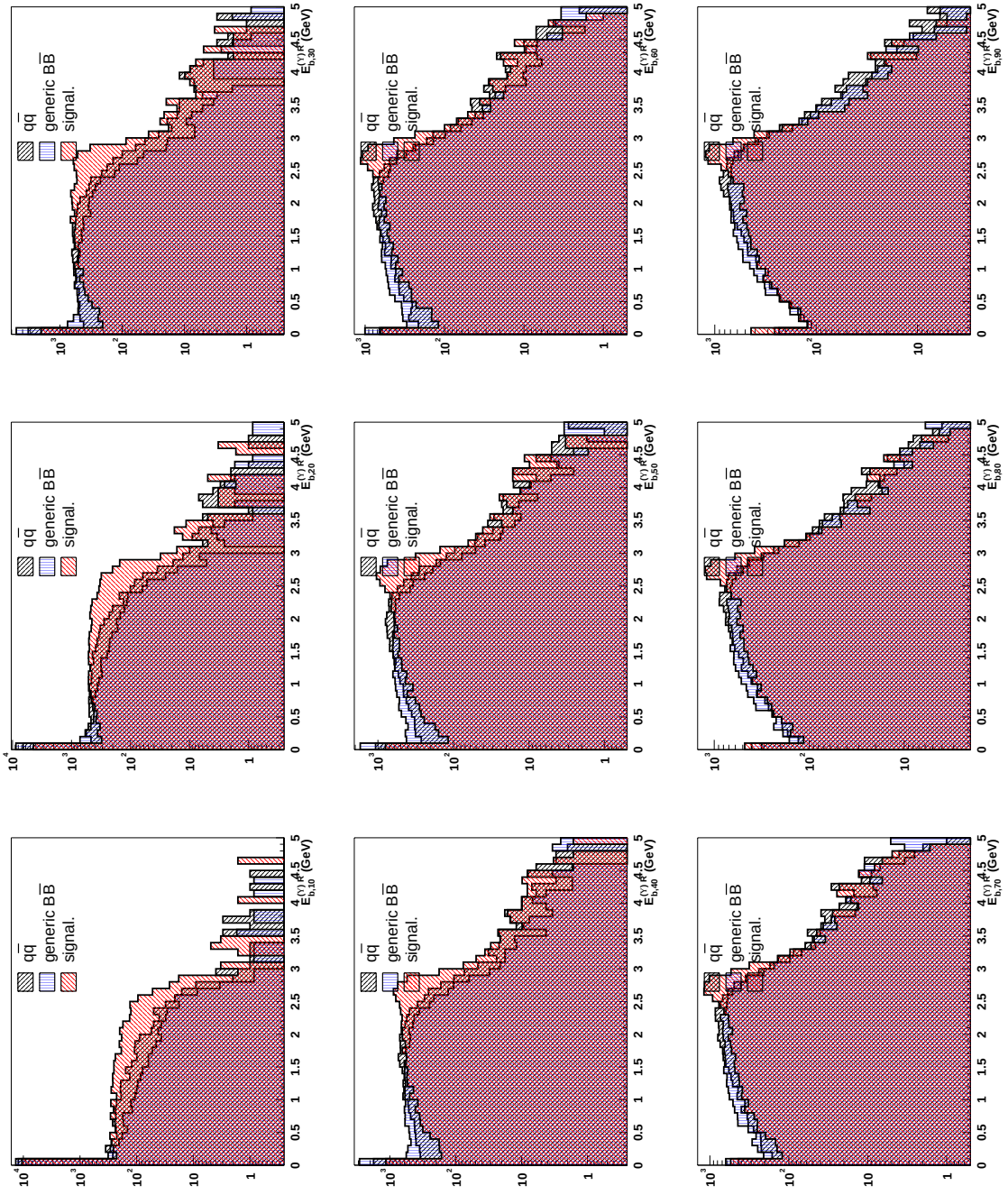

Figure 4-14. $E^{\Upsilon(4S),R}_{b,\theta}$ *for* $q\overline{q}$, $B\overline{B}$ *and signal.*

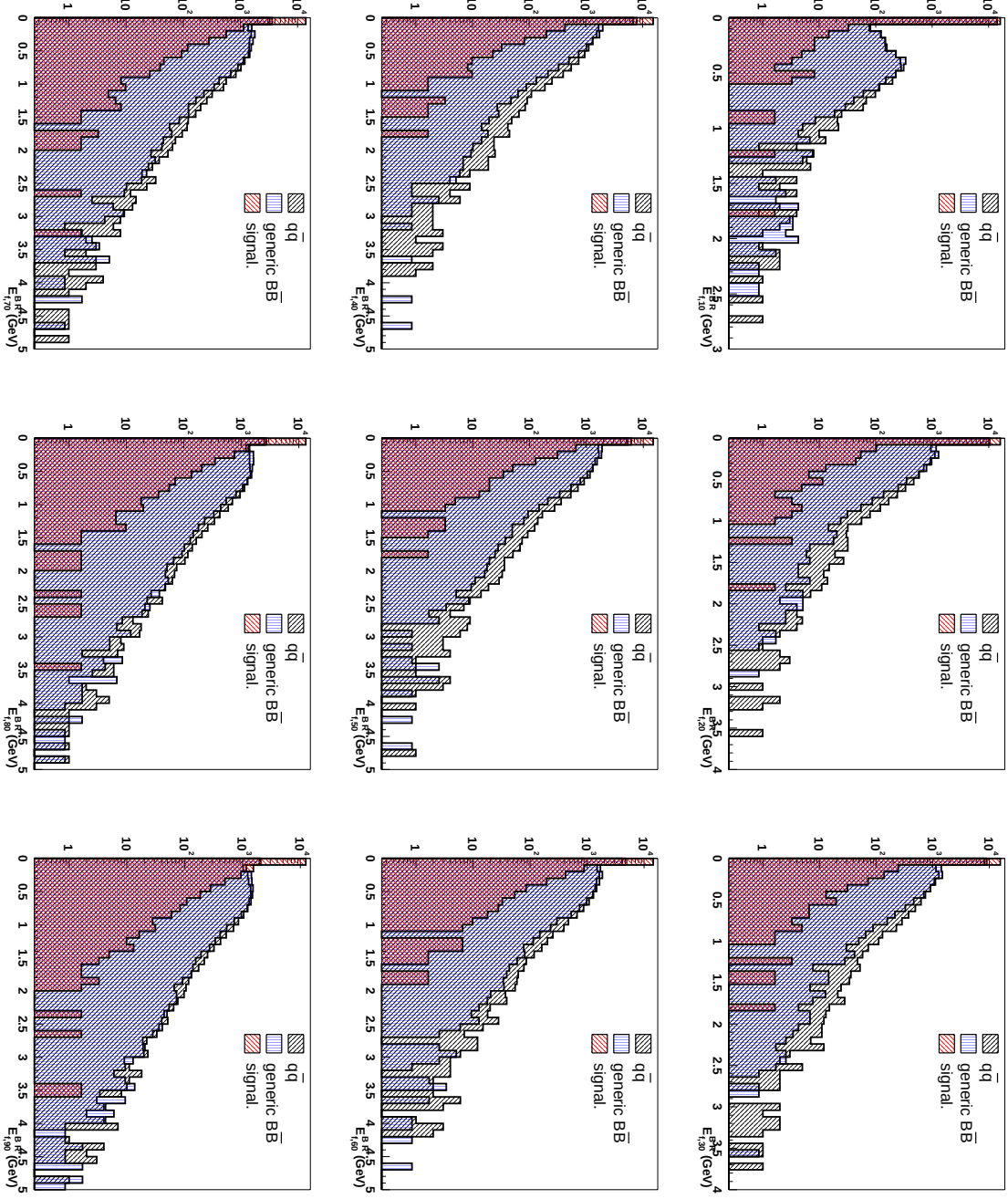

Figure 4-15. $E^{B,R}_{f,\theta}$ *for* $q\overline{q}$, $B\overline{B}$ *and signal.*

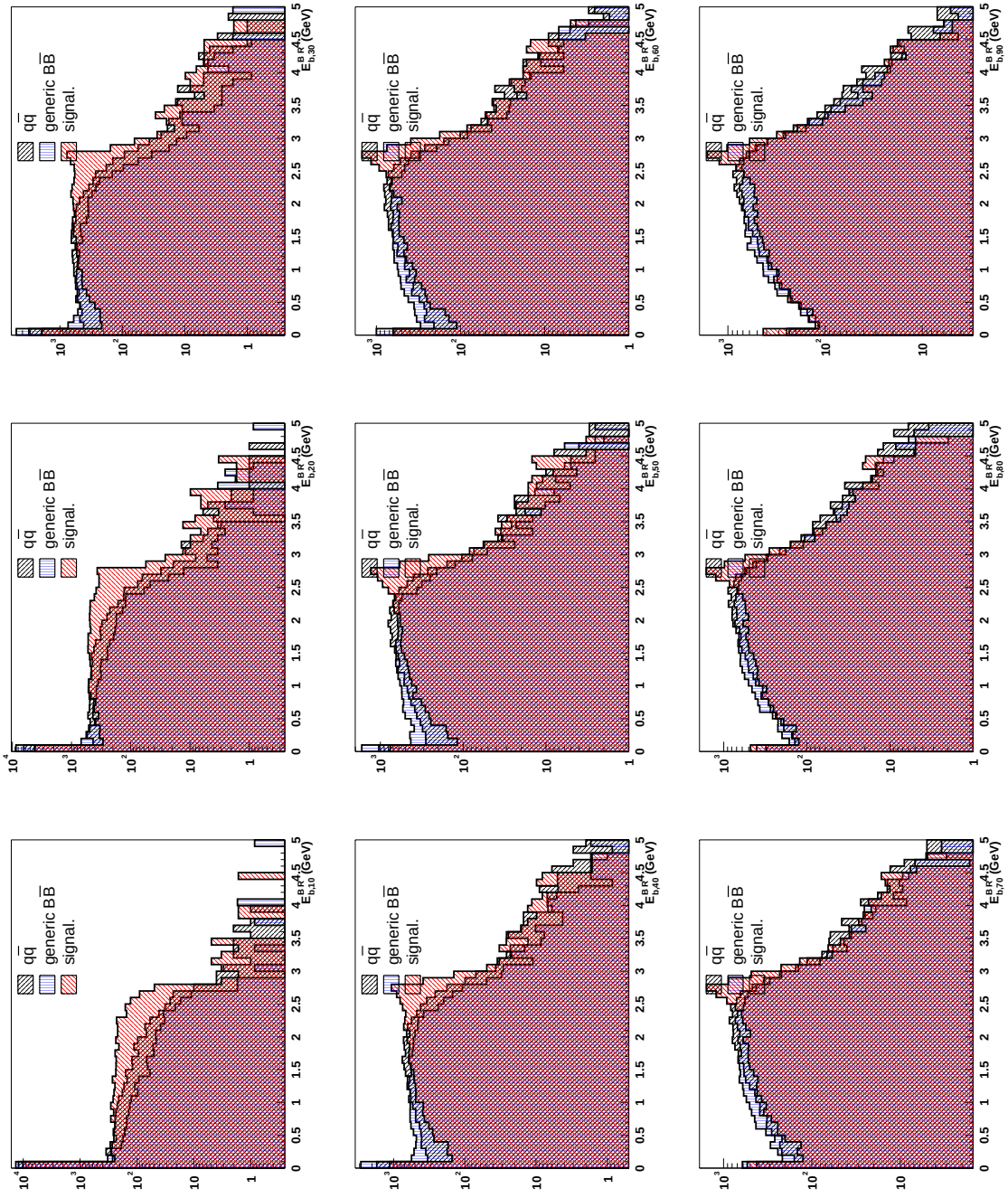

Figure 4-16. $E_{b,\theta^*}^{B,R}$ *for* $q\bar{q}$, $B\overline{B}$ *and signal.*

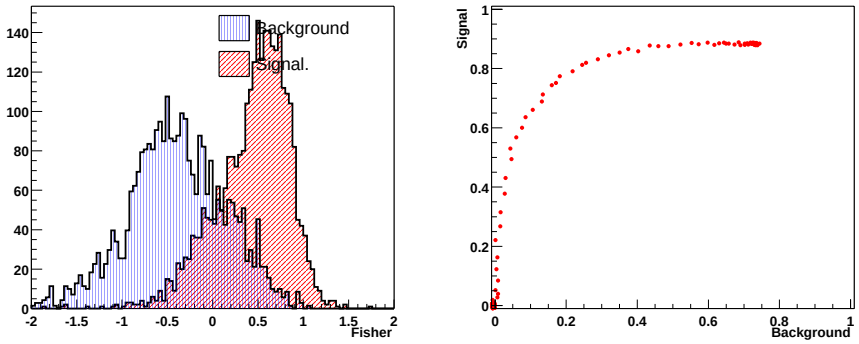

Figure 4-17. *Left plot: Fisher distribution for signal and background events. Right plot: Discriminant power of the Fisher with the signal(background) efficiency on vertical(horizontal) axis*

4.2.2 Linear Discriminant Analysis : $Fisher$

If there is no correlation between the variables, no information is lost in simply making separate requirementes on each one, otherwise a linear combinations of variables is needed to fully exploit their power rejection.

In Linear Discriminant Analysis [67], also known as the Fisher method, the discriminating variables which characterize the events, are combined linearly to provide the best separation between the two classes of events:

$$\mathcal{F} = \sum_{i=1}^{N} \alpha_i x_i. \tag{4.4}$$

The discrimination task consists of determining an axis in the R^N space of the discriminating variables such that the two classes are maximally separated. In order to apply this method, one needs to know just the mean values of each variable over the full sample, ($\bar{\mu}$), the means over signal and background separately, ($\bar{\mu}_b$, $\bar{\mu}_s$), and the total variance-covariance matrix, $U_{ij}^{b,s}$, that characterizes the dispersion of the events relative to the center of gravity of their own sample. The distance between the projected points will naturally be maximum along the direction defined by the line between μ_b and μ_s. Then the segment $(\bar{\mu}_b, \bar{\mu}_s)$ is the projection axis.

The coefficients in Eq. 4.4 could be easily computed from the equation:

$$\alpha_i = \sum_{j=1}^{N} (U^b + U^s)_{ij}^{-1} (\mu_j^b - \mu_j^s). \tag{4.5}$$

For an inclusive analysis it is important that the selection efficiency is flat across the energy spectrum and m_{X_s} system, in order to avoid to introduce model dependent bias. It is therefore not advisable to use variables strongly correlated to the photon energy and m_{X_s} system in the Fisher. The linear correlation of each variable with the photon energy and the charged and neutral multiplicity has been evaluated. In Tab. 4-1 the linear correlation coefficient ρ between the photon energy, charged and neutral multiplicity and all other variables used for background discrimination is reported.

Only variables that have good discrimination power and low energy and multiplicity linear dependence($\rho < 0.15$) are used in the Fisher: T, T_{neu}, T_{reco}, $|cos(\theta_{\gamma Trecoil})|$, $|cos(\theta_{TBB})|$, R_2, R_{2neu}, $E_{f,20}^{\Upsilon(4S)}$, $E_{f,30}^{\Upsilon(4S)}$, $E_{f,40}^{\Upsilon(4S)}$, $E_{f,50}^{\Upsilon(4S)}$,

Table 4-1. *The correlation coefficient ρ bwtween all variables ans the photon energy.*

Variable	ρ_{E_γ}	ρ_{nNeu}	ρ_{nCh}		Variable	ρ_{eg}	ρ_{neu}	ρ_{nCh}
$\|cos(\theta_{TBB})\|$	0.003	0.008	0.011		$E^{\Upsilon(4S)R}_{f,70}$	-0.155	0.10	0.132
R_2	0.069	0.086	-0.16		$E^{\Upsilon(4S)R}_{f,80}$	-0.185	0.11	0.147
R_{2neu}	0.149	-0.058	-0.05		$E^{\Upsilon(4S)R}_{f,90}$	-0.222	0.13	0.164
T	0.138	-0.05	-0.04		$E^{\Upsilon(4S)R}_{b,10}$	0.183	-0.06	-0.00
T_{neu}	0.074	0.07	-0.15		$E^{\Upsilon(4S)R}_{b,20}$	0.237	-0.05	0.069
T_{recoil}	0.456	-0.20	-0.18		$E^{\Upsilon(4S)R}_{b,30}$	0.203	-0.02	0.157
T_{reco}	0.070	-0.076	0.177		$E^{\Upsilon(4S)R}_{b,40}$	0.139	0.015	0.237
$E^{\Upsilon(4S)}_{f,10}$	0.001	-0.004	0.006		$E^{\Upsilon(4S)R}_{b,50}$	0.074	0.052	0.289
$E^{\Upsilon(4S)}_{f,20}$	-0.006	0.011	0.000		$E^{\Upsilon(4S)R}_{b,60}$	0.019	0.078	0.323
$E^{\Upsilon(4S)}_{f,30}$	-0.013	0.004	0.019		$E^{\Upsilon(4S)R}_{b,70}$	-0.019	0.099	0.343
$E^{\Upsilon(4S)}_{f,40}$	-0.015	0.016	0.018		$E^{\Upsilon(4S)R}_{b,80}$	-0.050	0.11	0.359
$E^{\Upsilon(4S)}_{f,50}$	-0.022	0.015	0.016		$E^{\Upsilon(4S)R}_{b,90}$	-0.071	0.12	0.368
$E^{\Upsilon(4S)}_{f,60}$	-0.017	0.009	0.025		$E^{B\ R}_{f,10}$	-0.025	0.003	0.025
$E^{\Upsilon(4S)}_{f,70}$	-0.021	0.018	0.029		$E^{B\ R}_{f,20}$	-0.043	0.02	0.037
$E^{\Upsilon(4S)}_{f,80}$	-0.047	0.021	0.052		$E^{B\ R}_{f,30}$	-0.067	0.038	0.055
$E^{\Upsilon(4S)}_{f,90}$	-0.079	0.027	0.053		$E^{B\ R}_{f,40}$	-0.085	0.046	0.067
$E^{\Upsilon(4S)}_{b,10}$	0.199	-0.078	-0.03		$E^{B\ R}_{f,50}$	-0.109	0.07	5 0.089
$E^{\Upsilon(4S)}_{b,20}$	0.228	-0.073	0.015		$E^{B\ R}_{f,60}$	-0.130	0.08	6 0.110
$E^{\Upsilon(4S)}_{b,30}$	0.182	-0.039	0.072		$E^{B\ R}_{f,70}$	-0.142	0.09	5 0.127
$E^{\Upsilon(4S)}_{b,40}$	0.119	-0.013	0.122		$E^{B\ R}_{f,80}$	-0.179	0.112	0.143
$E^{\Upsilon(4S)}_{b,50}$	0.066	0.005	0.159		$E^{B\ R}_{f,90}$	-0.219	0.1	3 0.163
$E^{\Upsilon(4S)}_{b,60}$	0.027	0.018	0.187		$E^{B\ R}_{b,10}$	0.197	-0.07	0.001
$E^{\Upsilon(4S)}_{b,70}$	0.002	0.043	0.200		$E^{B\ R}_{b,20}$	0.242	-0.054	0.074
$E^{\Upsilon(4S)}_{b,80}$	-0.018	0.056	0.223		$E^{B\ R}_{b,30}$	0.203	-0.020	0.168
$E^{\Upsilon(4S)}_{b,90}$	-0.037	0.070	0.229		$E^{B\ R}_{b,40}$	0.136	0.014	0.244
$E^{\Upsilon(4S)R}_{f,10}$	-0.028	0.007	0.028		$E^{B\ R}_{b,50}$	0.071	0.054	0.294
$E^{\Upsilon(4S)R}_{f,20}$	-0.043	0.027	0.036		$E^{B\ R}_{b,60}$	0.015	0.084	0.327
$E^{\Upsilon(4S)R}_{f,30}$	-0.066	0.042	0.054		$E^{B\ R}_{b,70}$	-0.022	0.099	0.348
$E^{\Upsilon(4S)R}_{f,40}$	-0.085	0.045	0.071		$E^{B\ R}_{b,80}$	-0.053	0.116	0.363
$E^{\Upsilon(4S)R}_{f,50}$	-0.117	0.072	0.096		$E^{B\ R}_{b,90}$	-0.072	0.126	0.371
$E^{\Upsilon(4S)R}_{f,60}$	-0.133	0.084	0.114		$\|cos(\theta_{\gamma Trecoil})\|$	0.154	-0.016	-0.031
$\cos(\theta_{B^*})$	0.005	-0.120	-0.001		$\|cos(\theta_{\gamma Treco})\|$	0.088	-0.011	0.0797

$E_{f,60}^{\Upsilon(4S)}$, $E_{f,70}^{\Upsilon(4S)}$, $E_{f,80}^{\Upsilon(4S)}$, $E_{f,90}^{\Upsilon(4S)}$, $E_{b,40}^{\Upsilon(4S)}$, $E_{b,50}^{\Upsilon(4S)}$, $E_{b,60}^{\Upsilon(4S)}$, $E_{f,20}^{\Upsilon(4S)R}$, $E_{f,30}^{\Upsilon(4S)R}$, $E_{f,40}^{\Upsilon(4S)R}$, $E_{f,50}^{\Upsilon(4S)R}$, $E_{f,20}^{BR}$, $E_{f,30}^{BR}$, $E_{f,40}^{BR}$, $E_{f,50}^{BR}$, $E_{f,60}^{BR}$

The Fisher distribution in signal and background events is shown in the left plot of Fig. 4-17.

The Fisher discriminant takes into account only one class of background while in this analysis two different types of background are present: some variables (see for example the $E_{b,40}^{\Upsilon(4S)}$ cone in Fig. 4-11) show a different distribution for signal, $q\overline{q}$ and $B\overline{B}$. In this case the Fisher could not give the best signal-background separation.

4.2.3 Background composition

After the whole selection, the main source of residual background is due to $B\overline{B}$ events. The composition of the background in the region $E_\gamma > 1.3\,\mathrm{GeV}$ has been studied in detail by using $\sim 240\,\mathrm{fb}^{-1}$ of $B\overline{B}$ MonteCarlo simulated events:

- $\sim 10\%$ of the background is composed by fake photons (mainly neutrons and K_L) that are not removed by the quality cuts on the photon.
- $\sim 90\%$ is due to high energy $\pi^0 (\sim 70\%)$ and $\eta (\sim 27\%)$ for which the veto does not work[1].

It has been found that if the second photon in $\pi^0(\eta) \to \gamma_1\gamma_2$, is soft ($E_{\gamma_2} < 100\,\mathrm{MeV}$), in 70% of the cases is not reconstructed even if it's within the calorimeter acceptance.

The decays from which π^0 and η are produced are summarized in Tab. 4-2. They are divided into two sub-samples: decays for which the $\pi^0(\eta)$ is directly generated from a B decay ($B \to \pi^0 X$), and those for which the $\pi^0(\eta)$ is produced in a secondary decay.

Table 4-2. *Composition of the background for events that fail the $\pi^0(\eta)$ veto in the region $E_\gamma > 1.3\,\mathrm{GeV}$.*

	Background Type	$\pi^0(\%)$	$\eta(\%)$
prompt decays	neutral B	9.6	31
	charged B	11	49
secondary decays	ρ	**69**	-
	D^0	7.6	9.5
	Other source	2.8	11.5

The background sources listed above account for 97.2% (for π^0 case) and 89.5% (for η case) of the total background at $E_\gamma > 1.3\,\mathrm{GeV}$.

To further analyze the background composition, decays in which a π^0 is generated by a ρ decay, have been studied. In 70% of the cases (40% of total background), the π^0 is generated throught the following decay chain: $B \to D^*\rho, \rho \to \pi^0\pi^+, \pi^0 \to \gamma_1\gamma_2$

[1] It's also present a small amount of background (3%) coming from $\omega(\eta') \to \gamma\gamma$ that is negligible and therefore not further studied in this section.

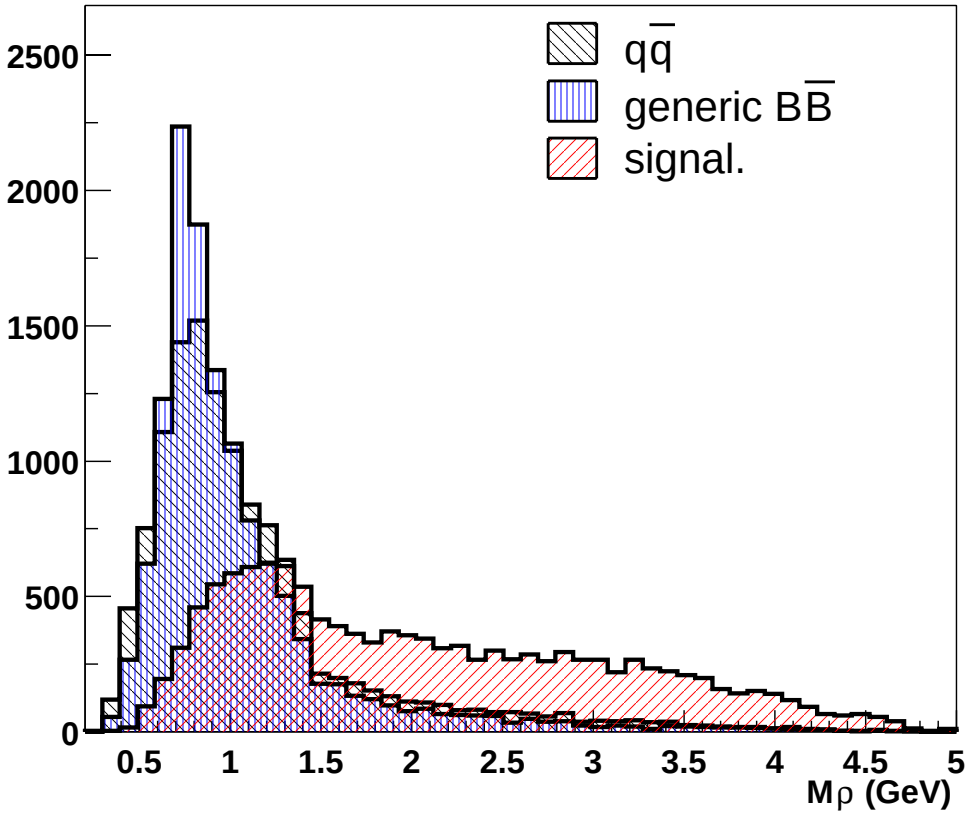

Figure 4-18. *$M(\pi^0,\pi)$ distribution for $q\overline{q}$, $B\overline{B}$, signal events*

In order to reject those events a ρ veto is applied. Since the lost photon is soft($E_{\gamma_2} < 100\,\mathrm{MeV}$), the direction and the energy of the π^0 could be approximated by the direction and energy of the energetic photon ($E_{\gamma_1} > 1.3\,\mathrm{GeV}$):

$$(\theta,\phi,E)_{\pi^0} \sim (\theta,\phi,E)_{\gamma_1} \tag{4.6}$$

The absolute value of three vector momentum $|\vec{P_{\pi^0}}|$ is calculated making the pion mass hypothesis: $|\vec{P_{\pi^0}}| = \sqrt{E^2_{\pi^0} - M^2_{\pi^0}}$. The π^0 is then combined with all the particles belonging to the B_{recoil} that are identified as charged pions and the invariant mass $M(\pi^0,\pi)$ is computed. In case of charged B decays, charge correlation is applied since the ρ and B have same sign charge in a two body decay.

The $M(\pi^0,\pi)$ distribution is shown in Fig. 4-18 for $B\overline{B}$, signal and $q\overline{q}$ events in MonteCarlo sample. Events for which $620\,\mathrm{MeV}/c^2 < M(\pi^0,\pi) < 920\,\mathrm{MeV}/c^2$ are vetoed.

4.3 Selection criteria optimization

Selection criteria have been optimized in order to minimize the statistical error in the extraction of $B \to X_s\gamma$ signal events. The $B \to X_s\gamma$ branching fraction, as explained in Sec. 4.5, is extracted from a fit to the E_γ distribution

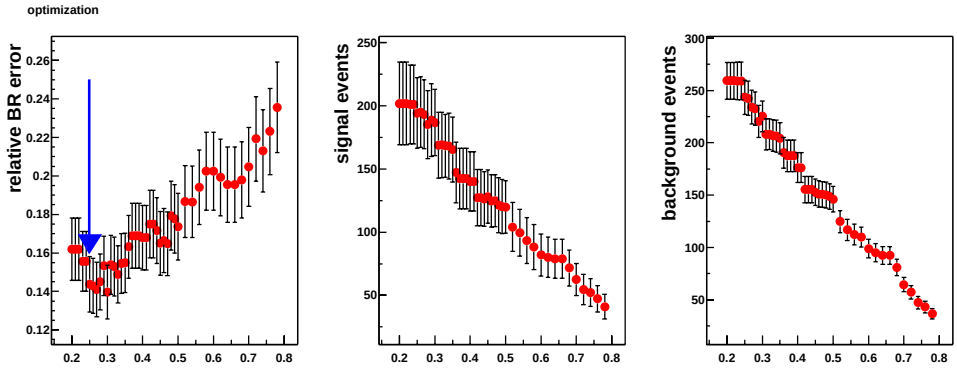

Figure 4-19. *Relative branching fraction error (left), the number of $B \to X_s\gamma$ eve nts (middle) and the number of background events (right) as a function of the int-pur cut as estimated on MonteCarlo simulation.*

on events that pass selection criteria. The optimization is performed using cocktail signal MonteCarlo and $B\overline{B}$, for modeling data, normalized to the same luminosity. The optimization is done iteratively: a first run is performed in order to find approximated values for the selection variables, which are then used as input for a second run of optimization. The final selection for each variable the optimization is done with all cuts applied except the one on the scanned variable.

The set of variables subject to optimization are: int-pur, LAT, π^0, η and ρ veto mass windows, minimum bump distance, Fisher.

In Fig. 4-19–4-23 the relative branching fraction error (left), the number of $B \to X_s\gamma$ events (middle) and the number of background events (right) as a function of the scanned variable, is shown.

- Int-pur optimization is shown in Fig. 4-19. A cut at 0.25 is applied.
- The LAT optimization is shown in Fig. 4-20. A cut at 0.45 is applied.
- The π^0 optimization is shown in Fig. 4-21. The scan is done in concentric mass windows around the π^0 nominal mass, on the horizontal axis the width of the mass windows is reported as a function of the fit resolution $\sigma = 7\,\mathrm{MeV}/c^2$ as estimated on MonteCarlo simulation. Event for which $115\,\mathrm{MeV}/c^2 < M_{\gamma\gamma} < 155\,\mathrm{MeV}/c^2$ are vetoed.
- The η optimization is shown in Fig. 4-22. The optimization is done as for π^0 veto, the resolution σ is $19\,\mathrm{MeV}/c^2$. Event for which $508\,\mathrm{MeV}/c^2 < M_{\gamma\gamma} < 588\,\mathrm{MeV}/c^2$ are vetoed.
- The minimum bump distance optimization is shown in Fig. 4-23. The left distribution shows a minimum at 60 cm. For an inclusive analysis it is important that the selection efficiency is flat across the energy spectrum and m_{X_s} system, in order to avoid to introduce model dependent bias. It is therefore not advisable to use variables strongly correlated to the photon energy and m_{X_s} system in the Fisher. The minimum bump distance could be related to the multiplicities of the X_s system. For this reason we apply a softer requirement on this variable:$40cm$.
- The Fisher optimization is shown in Fig. 4-24. A cut at $F > 0.2$ is applied.
- The ρ optimization is shown in Fig. 4-25. The optimization is done as for π^0 veto, the resolution σ is $150\,\mathrm{MeV}/c^2$. Events for which $620\,\mathrm{MeV}/c^2 < M(\pi^0, \pi) < 920\,\mathrm{MeV}/c^2$ are vetoed.

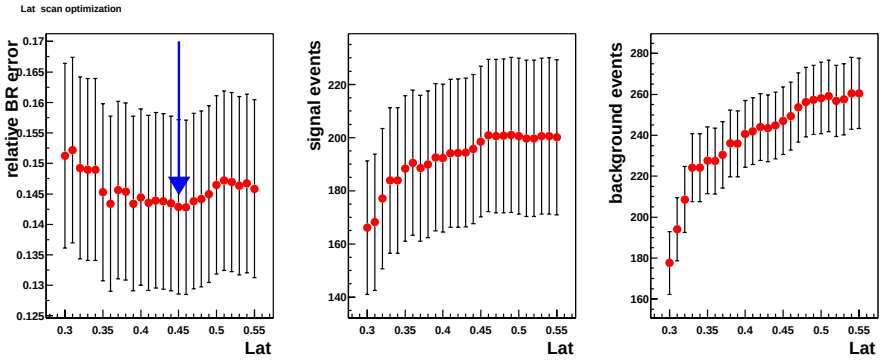

Figure 4-20. *Relative branching fraction error (left), the number of $B \to X_s\gamma$ eve nts (middle) and the number of background events (right) as a function of the LAT cut as estimated on MonteCarlo simulation.*

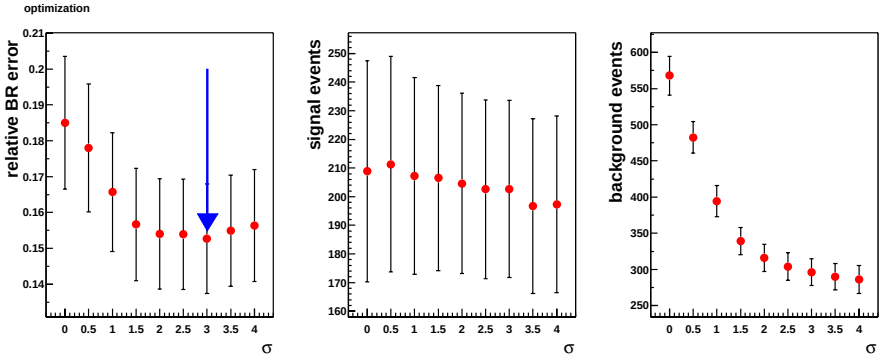

Figure 4-21. *Relative branching fraction error (left), the number of $B \to X_s\gamma$ eve nts (middle) and the number of background events (right) as a function of the π^0 mass windows width $\sigma = 7\,\mathrm{MeV}/c^2$ as estimated on MonteCarlo simulation.*

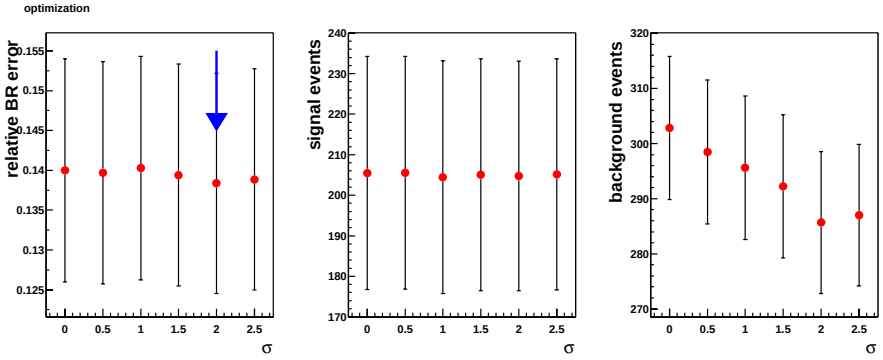

Figure 4-22. *Relative branching fraction error (left), the number of $B \to X_s\gamma$ eve nts (middle) and the number of background events (right) as a function of the η mass windows width $\sigma = 19\,\mathrm{MeV}/c^2$ as estimated on MonteCarlo simulation.*

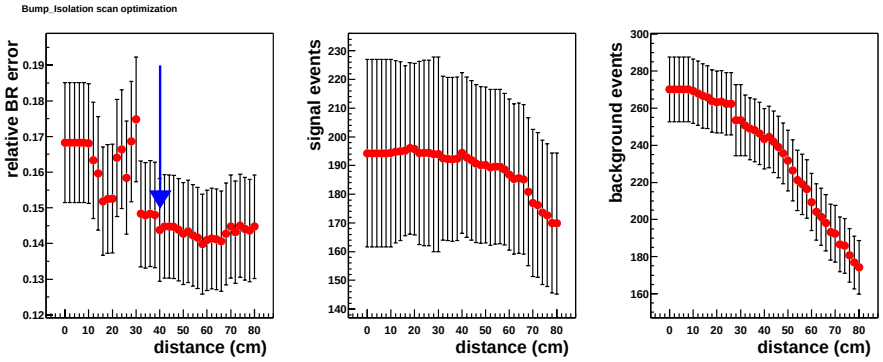

Figure 4-23. *Relative branching fraction error (left), the number of $B \to X_s\gamma$ events (middle) and the number of background events (right) as a function of the bump-isolation cut as estimated on MonteCarlo simulation.*

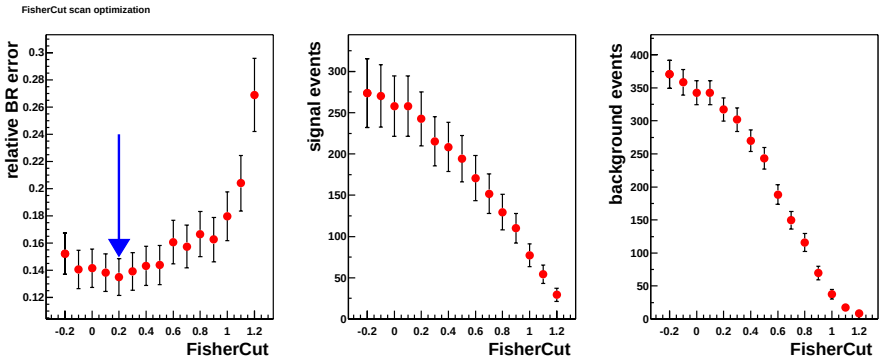

Figure 4-24. *Relative branching fraction error (left), the number of $B \to X_s\gamma$ eve nts (middle) and the number of background events (right) as a function of the Fisher cut as estimated on MonteCarlo simulation.*

The selection criteria for $B \to X_s\gamma$ events are summarized in Tab. 4-3

The cumulative efficiencies of these cuts (not including B reconstruction efficiency) are shown in Tab. 4-4.

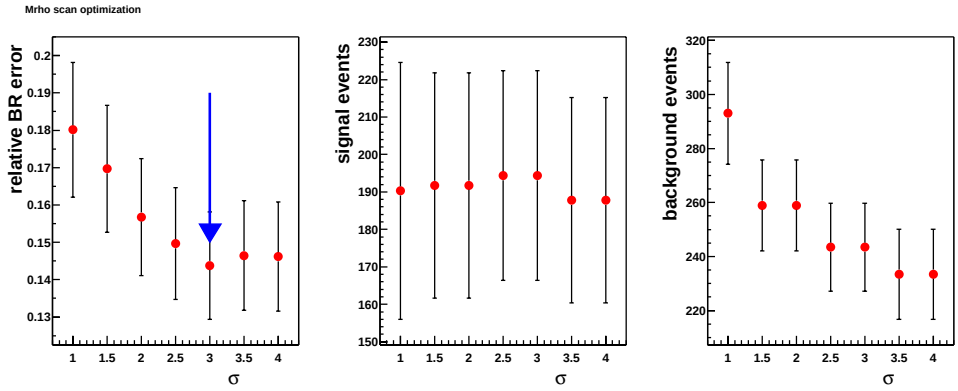

Figure 4-25. *Relative branching fraction error (left), the number of $B \to X_s\gamma$ eve nts (middle) and the number of background events (right) as a function of the $M(\pi^0, \pi)$ mass windows width $\sigma = 150\,\mathrm{MeV}/c^2$.*

Table 4-3. *Selection criteria for $B \to X_s\gamma$ events.*

Summary of selection Criteria	
B_{reco} candidate	int-pur> 0.25
Minimum photon energy	$E_\gamma > 1.3\,\mathrm{GeV}$
Quality cut	LAT< 0.45
Bump isolation cut	Bump separation$> 40cm$
π^0 veto	$115\,\mathrm{MeV}/c^2 < M_{\gamma\gamma} < 155\,\mathrm{MeV}/c^2$
η veto	$508\,\mathrm{MeV}/c^2 < M_{\gamma\gamma} < 588\,\mathrm{MeV}/c^2$
Fisher	$F > 0.2$
ρ veto	$620\,\mathrm{MeV}/c^2 < M(\pi^0, \pi) < 920\,\mathrm{MeV}/c^2$

Table 4-4. *Event selection cumulative cut efficiencies.*

Efficiency	**Data** (%)	**Gen** $B\overline{B}$ **(%)**	**Gen** $B \to X_s\gamma$(%)
E_γ	2.59 ± 0.06	2.62 ± 0.02	74 ± 6
int-pur	0.17 ± 0.01	0.197 ± 0.005	65 ± 5
LAT	0.152 ± 0.014	0.130 ± 0.004	64 ± 5
π^0 veto	0.071 ± 0.008	0.055 ± 0.003	56.1 ± 4.7
η veto	0.070 ± 0.008	0.053 ± 0.003	56.0 ± 4.6
Bump separation	0.063 ± 0.007	0.042 ± 0.002	52.8 ± 4.4
$Fisher$	0.051 ± 0.005	0.031 ± 0.002	43.7 ± 3.8
ρ veto	0.039 ± 0.004	0.022 ± 0.002	39.6 ± 3.6

4.4 Data-Montecarlo comparison

A good description of the relevant variables by the Monte-Carlo simulation is important for this analysis.

A π^0 control sample is defined applying all the requirements used in the analysis but inverting the π^0 veto, i.e. accepting events whose $M_{\gamma\gamma}$ lies in the windows $115\,\mathrm{MeV}/c^2 < M_{\gamma\gamma} < 155\,\mathrm{MeV}/c^2$, and removing the neutral bump distance requirement. This sample contains a negligible amount of signal and it is used to test the Data-MonteCarlo agreement in an independent sample.

Fig. 4-26–4-29 show comparisons of the most important variables for data and MonteCarlo simulations, both for signal (upper plots) and π^0 control sample (lower plots). Although some differences are observed, the overall agreement is good. Where differences are seen, the induced systematic effects are studied and they are discussed in Chapter 5.

Each plotted variable is divided in several bins and for each of them a background subtraction with the appropriate M_{ES} sideband distribution is performed.

Histograms are normalized to equal area. Each pair of histograms is tested for compatibility with a χ^2 test.

The Data-MonteCarlo agreement for all the variables entering the $Fisher$ are shown in App.A.

4.5 Measurement technique

4.5.1 Basic Concepts

The $B \to X_s\gamma$ branching ratio is extracted using the distribution of the energy of the most energetic photon E_γ in the event. A fit to the E_γ distribution is performed on events that pass selection criteria used to reject the $B\overline{B}$ and continuum background.

The goal of this analysis is to measure the branching ratio as:

$$\mathcal{B}(B \to X_s\gamma) = \frac{N_{sig}^{true}}{N_B^{true}} = \frac{N_{sig}}{N_B^{meas}\epsilon_{sel}} \times \frac{\epsilon_t^{all}}{\epsilon_t^{sig}} = \frac{(N^{meas} - BG)}{N_B^{meas}\epsilon_{sel}} \times \frac{\epsilon_t^{all}}{\epsilon_t^{sig}}, \tag{4.7}$$

where:

- $N^{meas} = N_{sig} + BG$ is the total number of candidates after all the analysis cuts in the region $E_\gamma > E_\gamma^{\min}$. The extraction of the remaining background BG contained in N^{meas} is described in Sec. 4.5.2.
- N_B^{meas} is the number of reconstructed B candidates with int-pur> 0.25 and before the rest of the selection. The combinatorial background is subtracted using the sidebands of the M_{ES} distribution as explained in Sec. 3.4.4.
- ϵ_{sel} is the efficiency for detecting $B \to X_s\gamma$ decays in the sample. It is extracted on MonteCarlo simulation.
- $\epsilon_t^{all,sig}$ is the B_{reco} reconstruction efficiency for tagging a B_{reco} in a generic and signal B decay.

The factor $\frac{\epsilon_t^{all}}{\epsilon_t^{sig}}$ represents the ratio of the efficiencies for finding a B_{reco} in events with a generic and signal decay in the recoiling B respectively. Due do the different multiplicities we expect this ratio to be slightly different for the two classes of events.

The $B \to X_d\gamma$ component is subtracted and it is calculated by using the theory input. According to the SM expectation, the $B \to X_d\gamma$ and the $B \to X_s\gamma$ branching fractions are in fact in the ratio $|V_{td}/V_{ts}|^2$ and the computaion

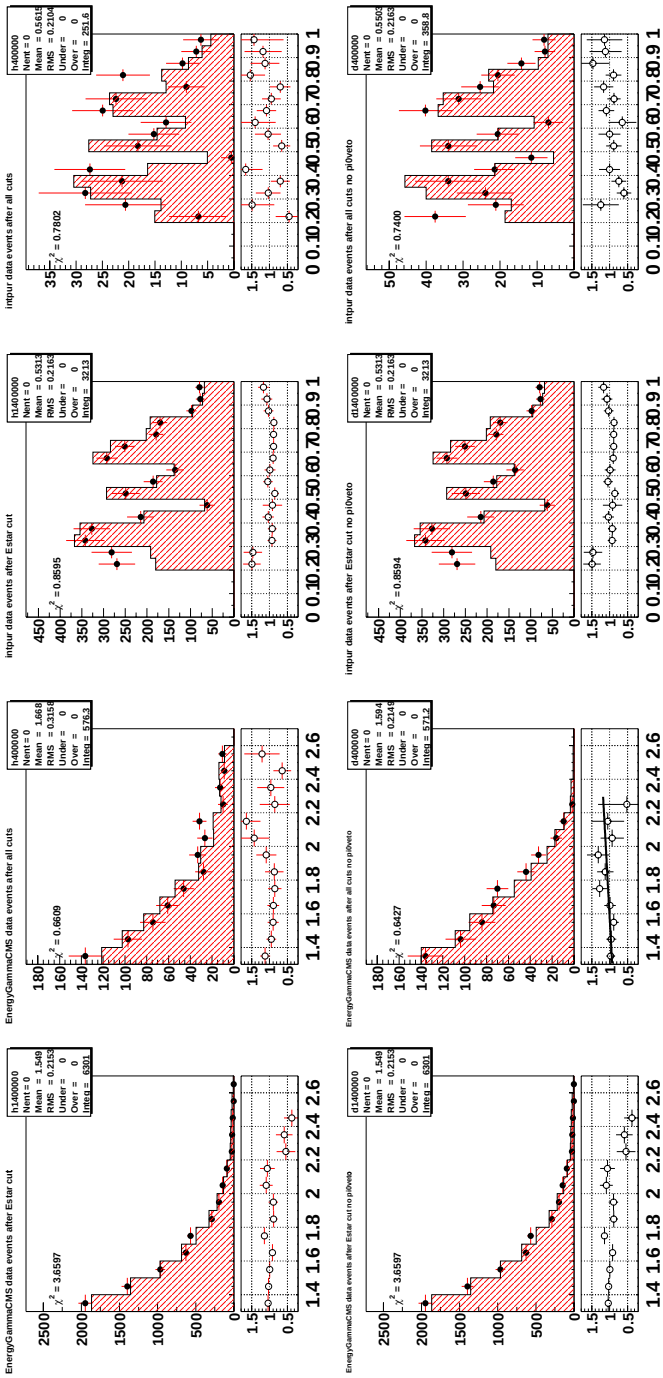

Figure 4-26. *Data-MonteCarlo agreement (side-bands subtracted) for signal sample (top row) and anti-Veto sample(bottom row). The first and second column display the energy spectrum (before any cuts and after all cuts), the third and fourth display int-pur spectrum(before any cuts and after all cuts). The χ^2 gives the probability of consistency of the histograms as obtained from a χ^2 test.*

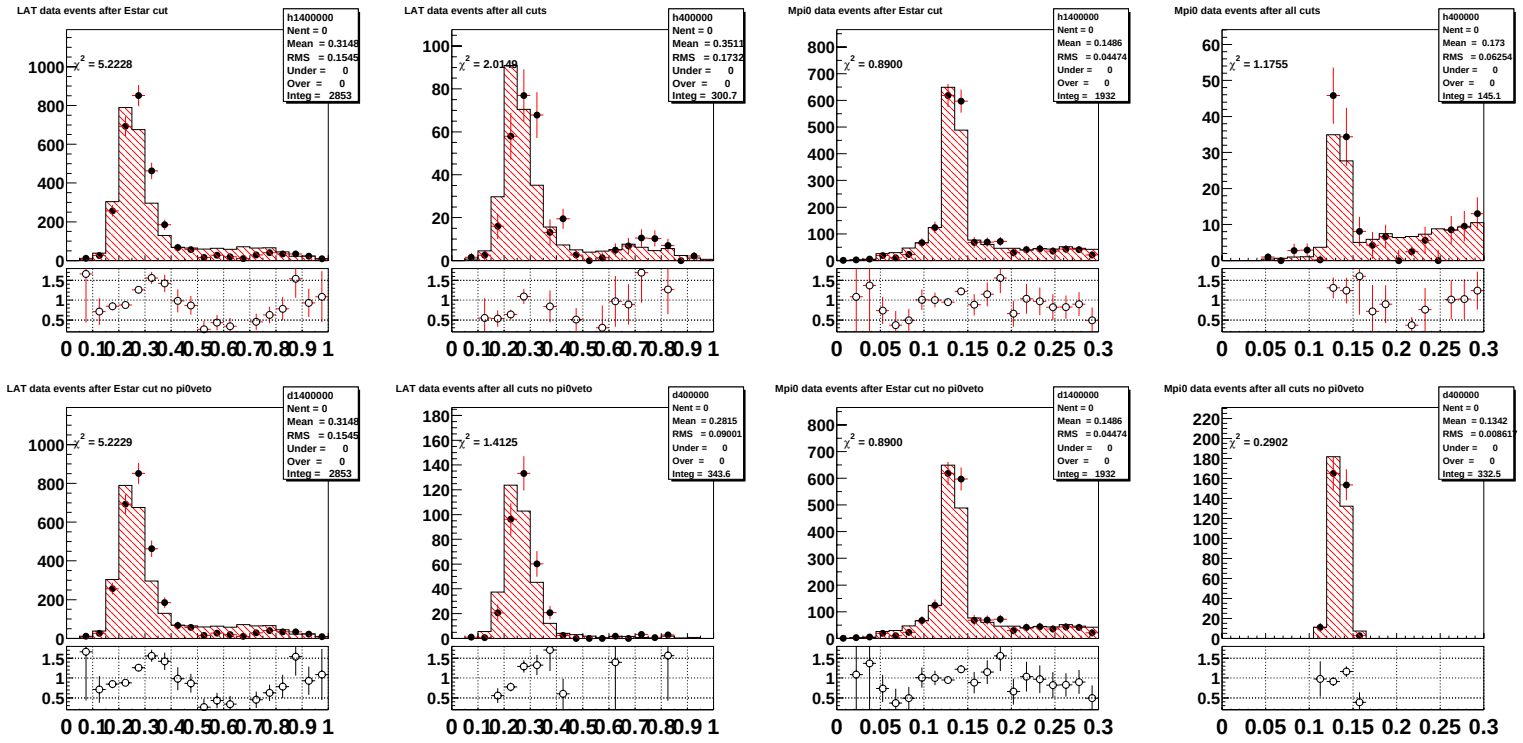

Figure 4-27. *Data-MonteCarlo agreement (side-bands subtracted) for signal sample (top row) and anti-Veto sample(bottom row). The first and second column display the LAT spectrum (before any cuts and after all cuts), the third and fourth display $M\pi^0$ spectrum(before any cuts and after all cuts). The χ^2 gives the probability of consistency of the histograms as obtained from a χ^2 test.*

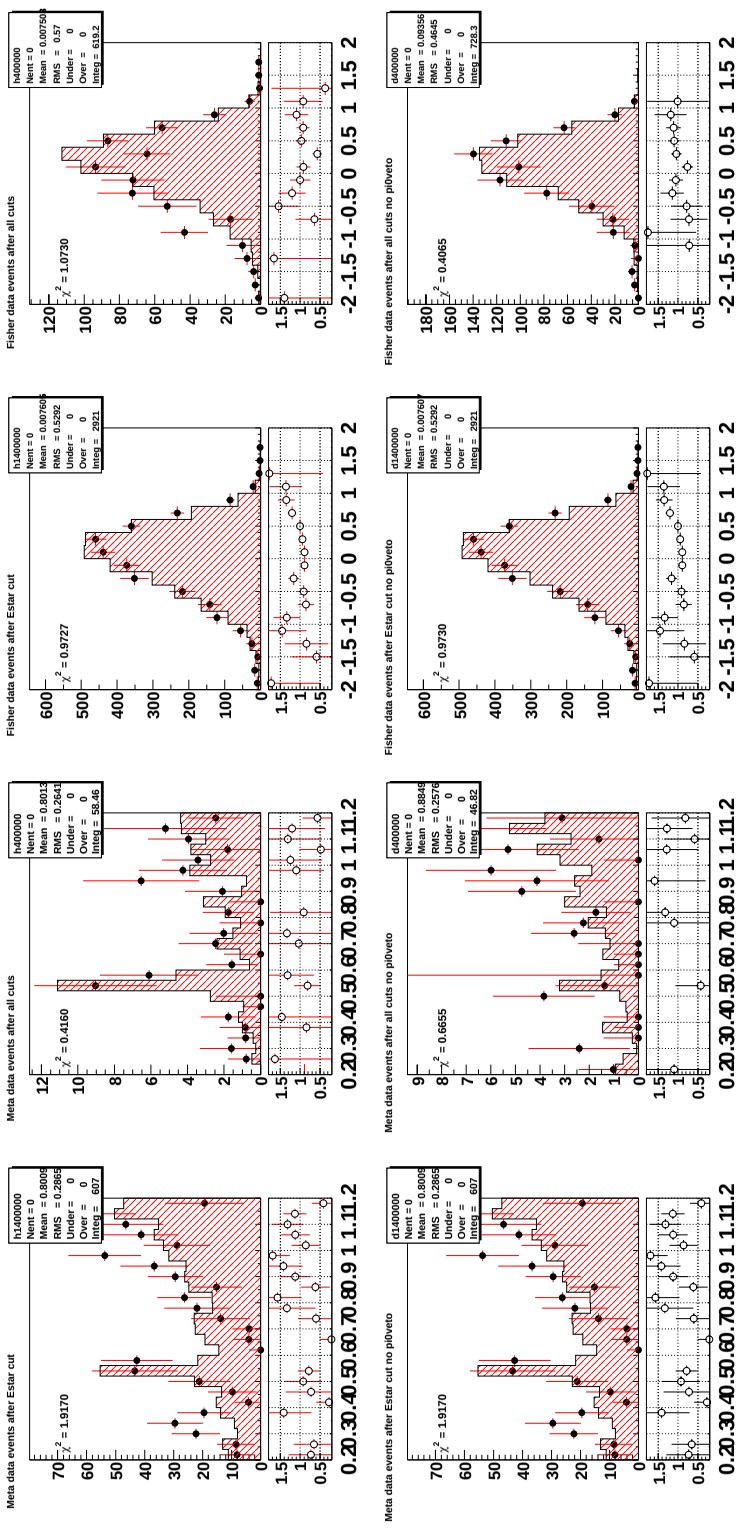

Figure 4-28. *Data-MonteCarlo agreement (side-bands subtracted) for signal sample (top row) and anti-Veto sample(bottom row). The first and second column display M η spectrum (before any cuts and after all cuts), the third and the fourth column display Fisher spectrum (before any cuts and after all cuts). The χ^2 gives the probability of consistency of the histograms as obtained from a χ^2 test.*

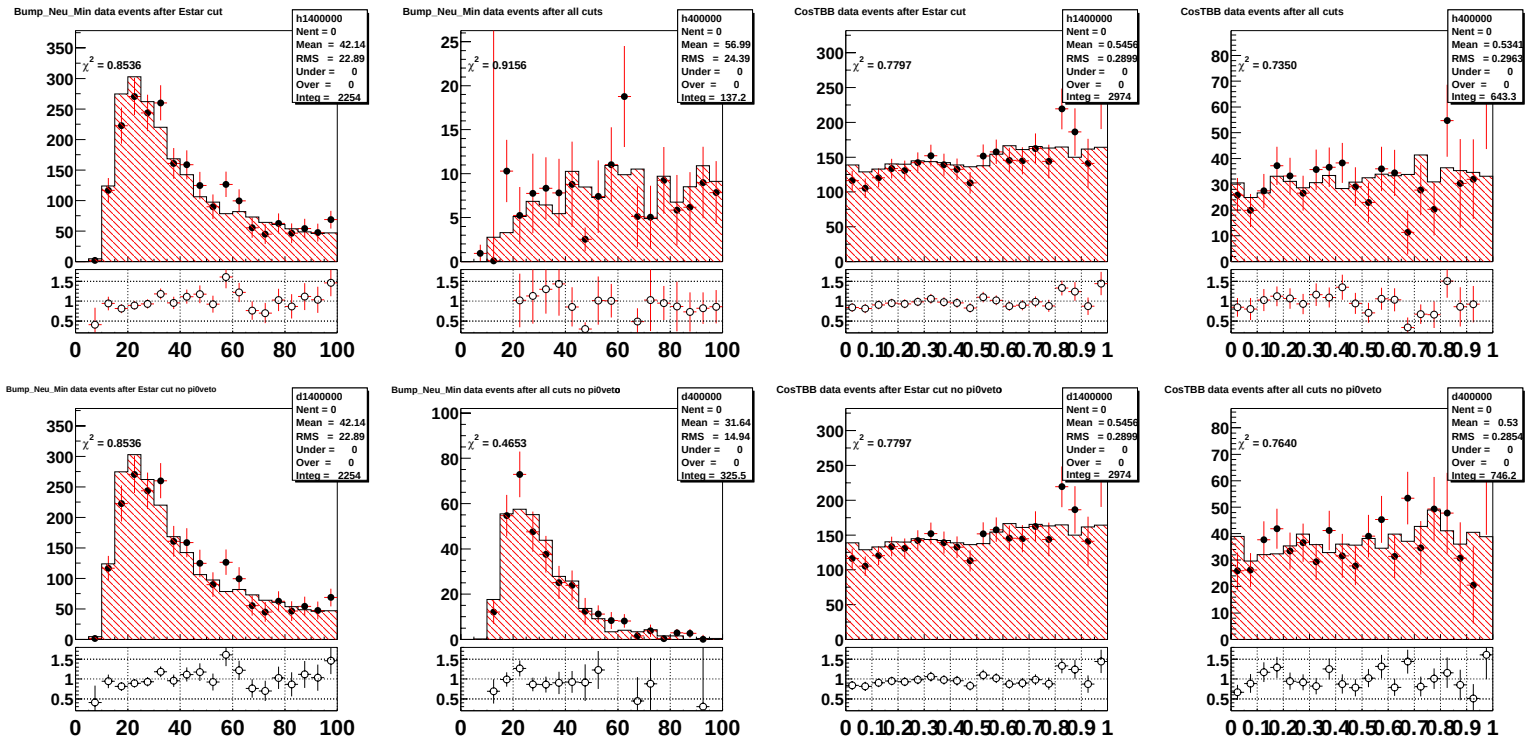

Figure 4-29. *Data-MonteCarlo agreement (side-bands subtracted) for signal sample (top row) and anti-Veto sample(bottom row). The first and second column display Neutral Bump Distance spectrum (before any cuts and after all cuts), the third and the fourth column display $|cos(\theta_{TBB})|$ spectrum (before any cuts and after all cuts). The χ^2 gives the probability of consistency of the histograms as obtained from a χ^2 test.*

has been done assuming same efficiency for the two different categories of events. Therefore the branching ratio is corrected by $(4.0 \pm 1.6)\%$, assuming the validity of the SM suppression factor $|V_{td}/V_{ts}|^2$.

In the following, the extraction of the signal events N_{sig} is described and the results are discussed. The tests and validations performed to make sure that the fitting procedure is correct are presented in Sec. 4.5.5.

4.5.2 Extraction of the signal events: N_{sig}

The event sample for $B \to X_s\gamma$, selected by the criteria described in Sec. 4.3, still contains sizable backgrounds.

Combinatorial background is generated from events for which the particles of the B_{reco} candidate do not originate from a single B meson. This component includes background from continuum and is subtracted in each E_γ bin performing a fit to the measured M_{ES} distribution (as described in Sec. 3.4.4).

Peaking background is generated in events for which the selected γ comes from a non-signal B decay.

The number of signal events $N_{sig} = N^{meas} - BG$, with $E_\gamma > E_\gamma^{\min}$, is extracted from a binned χ^2 fit to the measured E_γ distribution. A binned likelihood technique would not be correct here because it would impose Poisson errors on the individual bins, instead of the actual errors from the M_{ES} fits.

The measured E_γ distribution, N_i^{meas}, is fit bin-by-bin to the sum of two distributions, the signal N_i^{sig} and the peaking background BG,

$$\mu_i = C_s N_i^{sig\,MC} + C_b N_i^{bkgd\,MC}, \tag{4.8}$$

their shapes are derived from MonteCarlo simulation and their relative normalization is determined by a binned χ^2 fit.

The χ^2 function is:

$$\chi^2(C_s, C_b) = \sum_i \left(\frac{N_i^{meas} - \mu_i(C_s, C_b)}{\sqrt{\delta N_i^{meas\,2} + \delta N_i^{MC\,2}}} \right)^2 \tag{4.9}$$

where N_i^{meas} is the number of observed events, δN_i^{meas} and δN_i^{MC} are the corresponding statistical errors coming from the M_{ES} fits for data and MonteCarlo models respectively. C_s, C_b are the normalizations of the two components which are free parameters of the fit. The last bin is chosen to contain all events with $E_\gamma > E_\gamma^{\min}$, such that does not depend on signal E_γ shape. The fitted number of signal events is:

$$N^{sig} = N_{last}^{meas} - C_b N_{last}^{bkgd,MC}. \tag{4.10}$$

For each component the MonteCarlo is properly adjusted and re-weighted in order to match the ratio of charged and neutral B events in the data.

The extraction of N_{sig} proceeds in two steps as follows:

- the M_{ES} distributions for selected intervals in E_γ are fitted to extract N_i^{meas} as shown in Fig. 4-30, plots 1-14. Plot 15 shows the M_{ES} fit for events with $E_\gamma > 1.9\,\mathrm{GeV}$. The M_{ES} distribution is fit to the sum of a Cristal Ball plus an Argus function (see Sec. 3.4.4). bhe peak value m, the r.m.s. σ, and n parameter of the Crystal Ball function are fixed from an M_{ES} fit to the data sample with very high purity (int-pur> 0.95) and before the selection. The result of the fit is shown in Fig. 4-31. The following parameters are extracted: $m = 5.28\,\mathrm{GeV}, \sigma = 2.75\,\mathrm{MeV}, n = 5$.

  A fit to the total sample in all the energy range ($1.3\,\mathrm{GeV} < E_\gamma < 2.7\,\mathrm{GeV}$) and after the whole selection is performed to extract the a parameter of the Crystal Ball function. Then these four parameters are fixed in each E_γ bin (assuming that signal and background shape does not depend on E_γ) while the ARGUS function

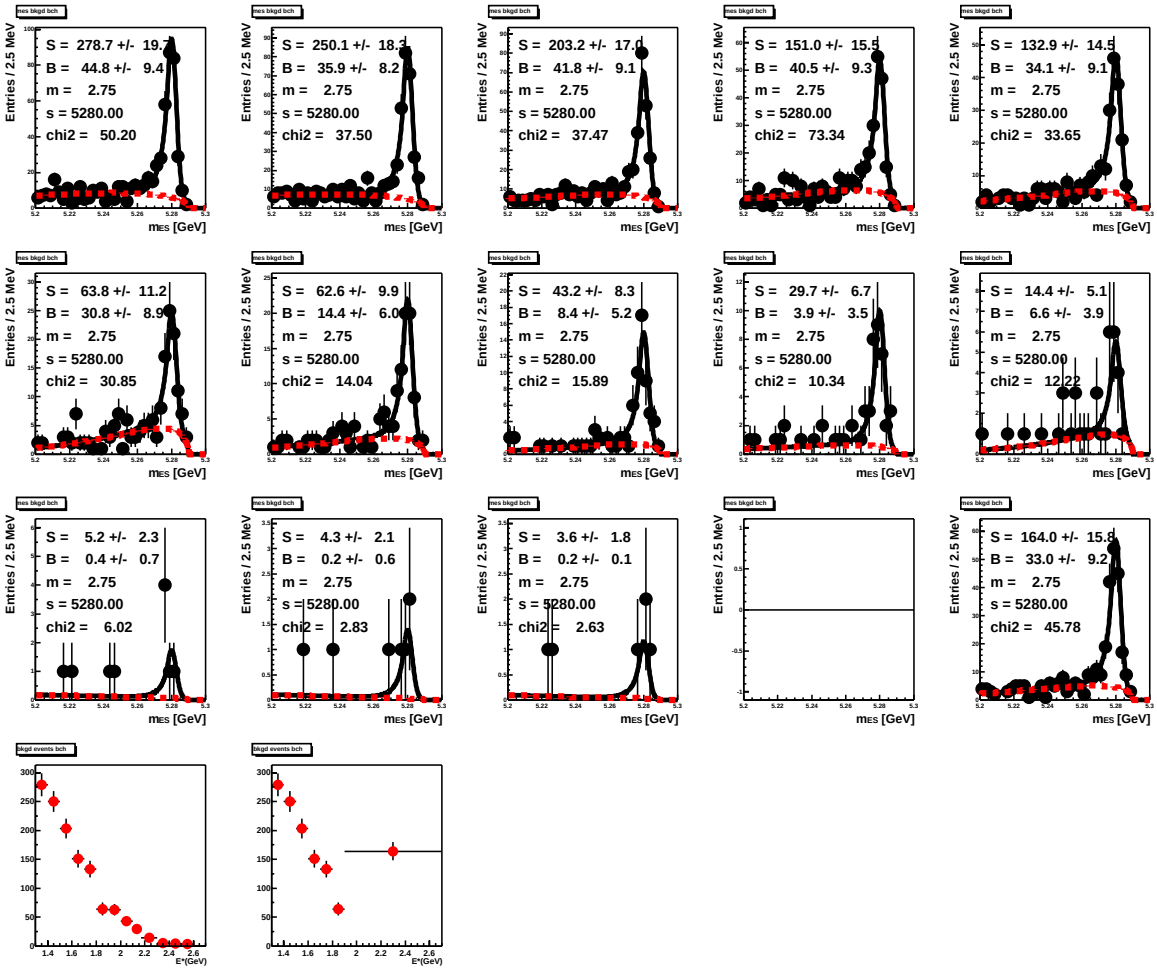

Figure 4-30. *Generic MonteCarlo: an example of fits to M_{ES} distributions for selected bins in (plots 1-12). Plot 13 shows the M_{ES} fit for events with $E_\gamma > 1.9\,\mathrm{GeV}$. The last two plots show the resultant distribution, N_i^{meas}, for each E_γ bin and grouping events with $E_\gamma > 1.9\,\mathrm{GeV}$ in a single bin.*

parameters and the Crystal Ball normalization are floated. These four parameters are also fixed in the extraction of normalization samples. The last two plots of Fig. 4-30 show the resultant distribution, N_i^{meas}, for each E_γ bin and grouping events with $E_\gamma > E_\gamma^{\min} = 1.9\,\mathrm{GeV}$ in a single bin.

- the result of the χ^2 fit to the E_γ distribution in generic MonteCarlo sample is illustrated in Fig. 4-32. On the left, the data are compared to the fit, indicating the two contributions, signal $C_s N_i^{sig}$ backgrounds $C_b N_i^{bkgd\,Mc}$. The plot in the middle shows the same comparison with a finer binning in the low E_γ region. On the right, the background subtracted signal distribution, $N_i^{meas} - C_b N_i^{bkgd\,Mc}$, is shown.

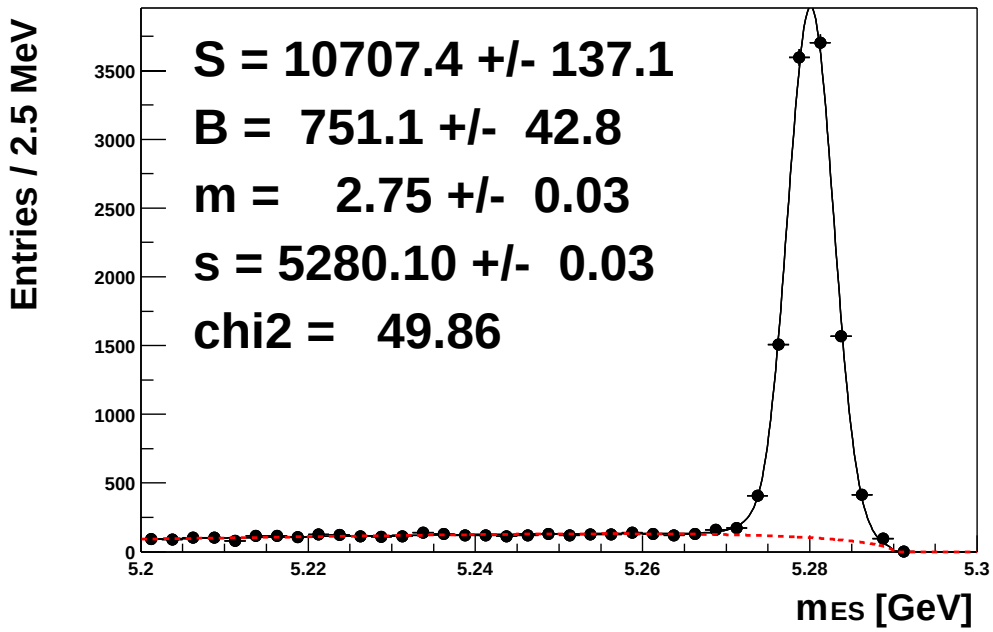

Figure 4-31. *Data sample: fit to M_{ES} distributions with int-pur > 0.95, before the selection.*

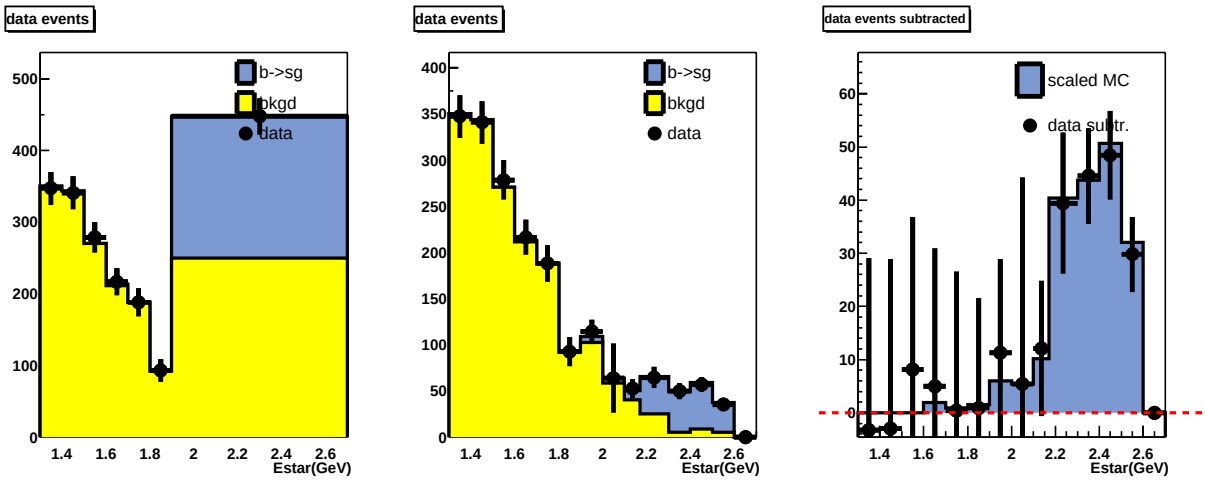

Figure 4-32. *An example of the fit to the E_γ distribution on generic MonteCarlo. Left: fit result with background (yellow), and all (blue) shapes superimposed. Middle: same as in the left plot with the finer binning. Right: E_γ distribution subtracted of the backgrounds (binning as in the middle plot).*

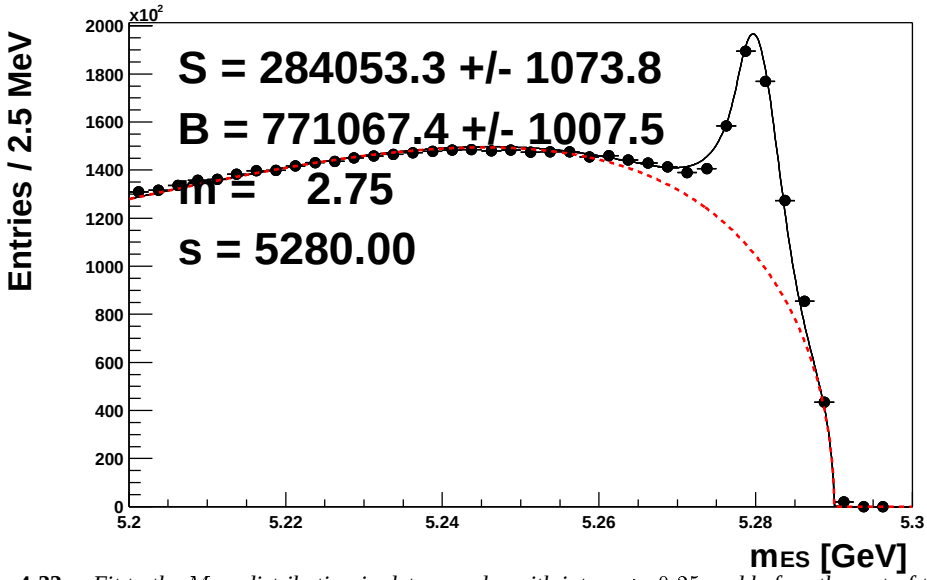

Figure 4-33. *Fit to the M_{ES} distribution in data sample, with int-pur > 0.25 and before the rest of the selection, used to extract N_B^{meas} from the data.*

4.5.3 Extraction of B_{reco} sample events: N_B^{meas}

For normalization purposes, N_B^{meas} is obtained from a fit to the M_{ES} distribution with int-pur > 0.25 and before the rest of the selection. The result of the fit on data is shown in Fig. 4-33. The number of reconstructed B 's is 284053 ± 1074.

4.5.4 Efficiency corrections

The factor $\frac{\epsilon_t^{all}}{\epsilon_t^{sig}}$ represents the ratio of the efficiencies for finding a B_{reco} in events with a generic and signal decay in the recoiling B respectively. It's estimated from $\sim 240\,\text{fb}^{-1}$ of generic MonteCarlo: the number of generic decays is scaled to the branching ratio generator value, and compared to the number of signal events. Both of them are extracted from an M_{ES} fit before the selection. A ratio $\frac{\epsilon_t^{sig}}{\epsilon_t^{all}} = 1.24 \pm 0.07$ is found. The uncertainty takes into account the M_{ES} fit errors and is dominated from the low statistics signal sample(~ 450 events).

The selection efficiency is estimated to be $\epsilon_{sel} = 0.396 \pm 0.036$, it is determined from a M_{ES} fit before and after the selection on a generic signal MonteCarlo sample.

4.5.5 Fit validations

4.5.5.1 Fit on MonteCarlo Samples

As a cross-check the full analysis has been performed on MonteCarlo samples. A fit on $\sim 240\,\text{fb}^{-1}$ of generic MonteCarlo is performed. The signal model is taken from the signal component of the generic $B\overline{B}$: the generated

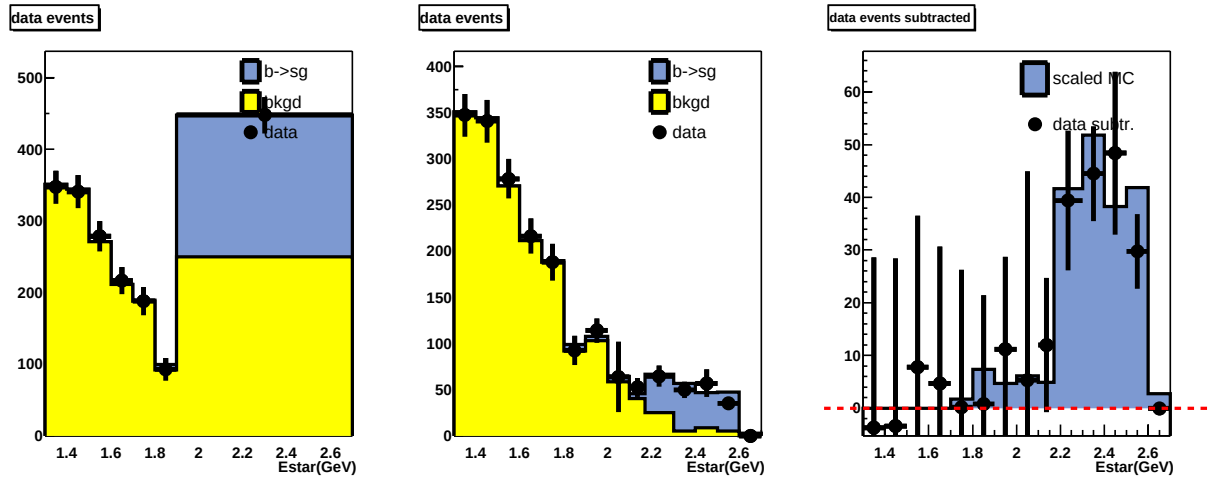

Figure 4-34. *A fit to the E_γ distribution on MonteCarlo sample. Left: fit result with background (yellow), and all (blue) shapes superimposed. Middle: same as in the left plot with the finer binning. Right: E_γ distribution subtracted of the backgrounds (binning as in the middle plot).*

value for the branching ratio is 3.29×10^{-4} with a $B \to K^*(892)\gamma$ over non-resonant ratio of $\sim 14\%$ and $m_{X_s}^{cut-off} = 1.1\,\mathrm{GeV}/c^2$. Fig. 4-32 shows the fit, $\chi^2/DOF = 0.015$, resulting in

$$\mathcal{B}(B \to X_s\gamma) = (3.16 \pm 0.43(stat.)) \times 10^{-4}, \tag{4.11}$$

a value in good agreement with the input value.

A second fit, on the same generic MonteCarlo sample, is performed with the signal modeled as explained in Sec. 3.5.2.1: a $B \to K^*(892)\gamma$ over non-resonant ratio of $\sim 12\%$ and $m_{X_s}^{cut-off} = 1.03\,\mathrm{GeV}/c^2$. The result of the fit, shown in Fig. 4-34, is:

$$\mathcal{B}(B \to X_s\gamma) = (3.43 \pm 0.46(stat.)) \times 10^{-4}, \tag{4.12}$$

with a $\chi^2/DOF = 0.046$. The results is in agreement with the input generator value even if the m_{X_s} cut-off and the mixture of resonant and non-resonant components used for signal modeling are slightly different. This effect is evident is the high energy region $E_\gamma > 2.4\,\mathrm{GeV}$ where the effect of the cut-off is relevant.

A third fit is performed modeling the signal from an higher statistics indipendent MonteCarlo sample. The signal is modeled as in the previous fit and the result is shown in Fig. 4-35:

$$\mathcal{B}(B \to X_s\gamma) = (3.07 \pm 0.41(stat.)) \times 10^{-4}, \tag{4.13}$$

with a $\chi^2/DOF = 0.027$. Also this value is compatible with the generator one.

4.5.5.2 Fit to the π^0 control sample

A useful cross-check can be performed on data using the π^0 control sample defined in Sec. 4.4, i.e. inverting the π^0 veto and removing the bump isolation requirement. The resulting branching ratio (Fig. 4-36) is compatible with the absence of signal: $N_{sig} = 0.5 \pm 10$.

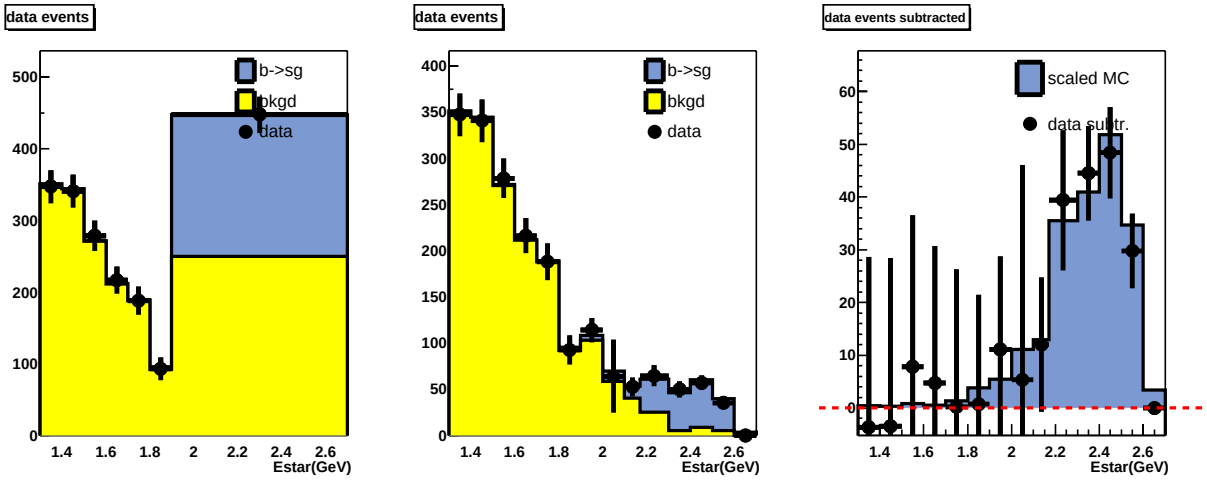

Figure 4-35. *A fit to the E_γ distribution on generic MonteCarlo sample with signal modeled from an indipendent MonteCarlo sample. Left: fit result with background (yellow), and all (blue) shapes superimposed. Middle: same as in the left plot with the finer binning. Right: E_γ distribution subtracted of the backgrounds (binning as in the middle plot).*

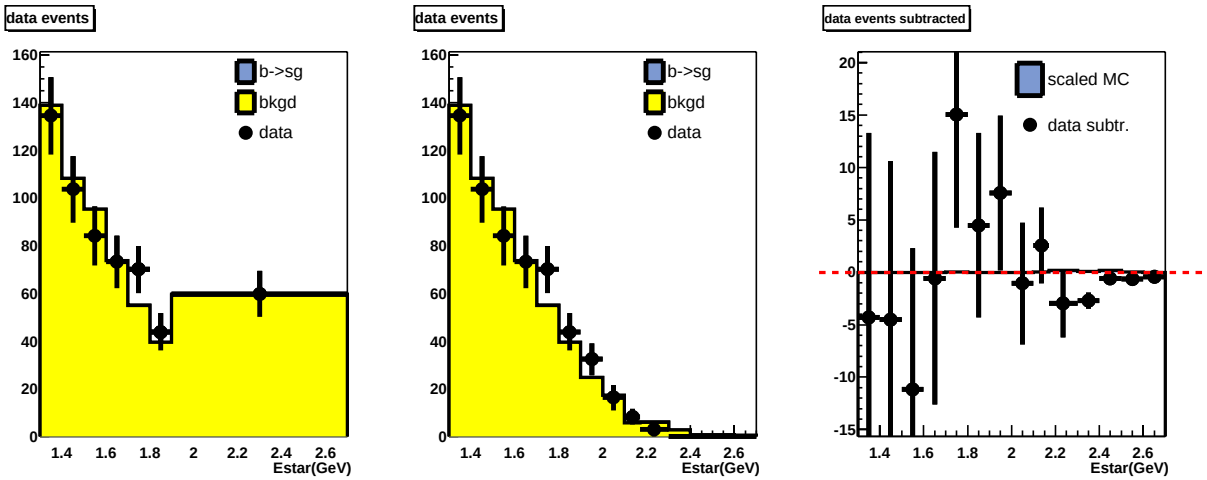

Figure 4-36. *A fit to the E_γ distribution on the π^0 control sample. Left: fit result with background (yellow), and all (blue) shapes superimposed Middle: same as in the left plot with the finer binning. Right: E_γ distribution subtracted of the backgrounds (binning as in the middle plot).*

4.6 Results

Figures 4-37 shows the fit results for data. The agreement in the background shape is good ($\chi^2/DOF = 0.93$). The result of the fit is:

$$\mathcal{B}(\mathbf{B \to X_s \gamma}) = (\mathbf{3.82 \pm 0.98(stat.)}) \times \mathbf{10^{-4}}. \tag{4.14}$$

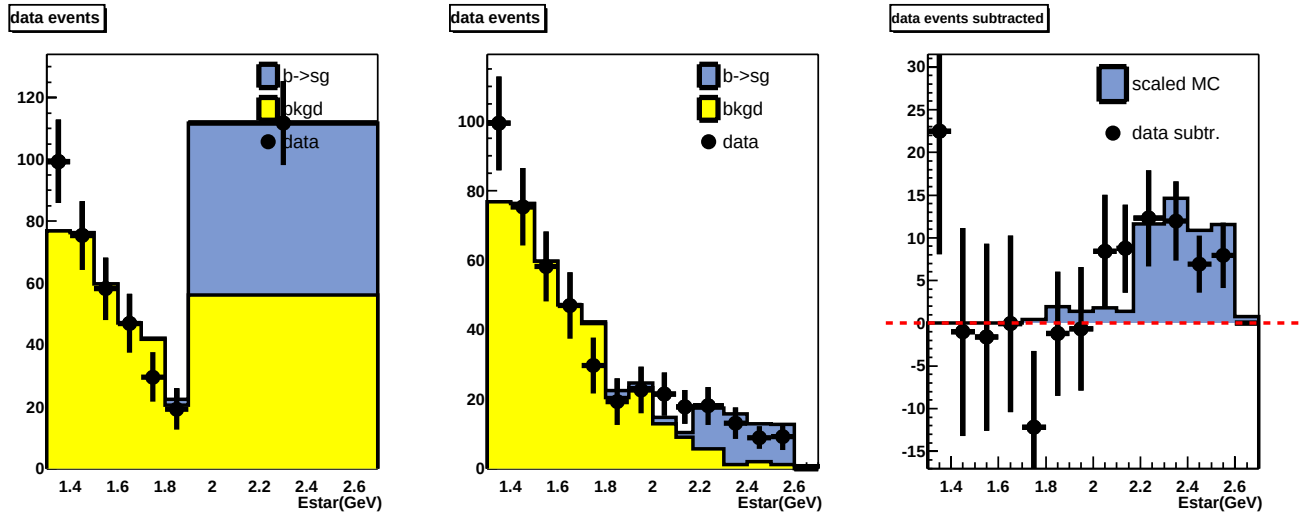

Figure 4-37. *DATA: χ^2 fit to the signal distribution. Left: fit result with background (yellow), and all (blue) shapes superimposed. Middle: same as in the left plot with the finer binning. Right: E_γ distribution subtracted of the backgrounds (binning as in the middle plot).*

The results for neutral and charged B are, respectively:

$$\mathcal{B}(\mathbf{B^0 \to X_s^0 \gamma}) = (\mathbf{5.93 \pm 1.98(stat.)}) \times \mathbf{10^{-4}}. \tag{4.15}$$

$$\mathcal{B}(\mathbf{B^\pm \to X_s^\pm \gamma}) = (\mathbf{2.70 \pm 1.10(stat.)}) \times \mathbf{10^{-4}}. \tag{4.16}$$

The results on the B^0 and B^+ samples are combined in order to extract the charged over neutral branching fraction ratio $R_{\pm/0}$:

$$\mathbf{R_{\pm/0}} = \frac{\mathcal{B}(\mathbf{B^\pm \to X_s^\pm \gamma})}{\mathcal{B}(\mathbf{B^0 \to X_s^0 \gamma})} = \mathbf{0.46 \pm 0.24(stat.)}. \tag{4.17}$$

Figures 4-38, 4-39, 4-40, 4-41, 4-42 show, respectively, all the M_{ES} fit on data, for $B^{\pm}$ and B^0 separately, the E_γ distribution, the M_{ES} fit to E_γ distribution after the whole selection in the energy range $1.3\,\mathrm{GeV} < E_\gamma < 2.7\,\mathrm{GeV}$, the fit results for $B^{\pm}$ and B^0 separately.

Fig. 4-45 shows the fit results for different theoretical signal models.

Table 4-5 and Fig. 4-46, shows the results for a variety of subsamples: charged and neutral B mesons, Run1 and Run2, for different level of Semi-exclusive reconstruction purity and for two different theoretical models. All the results are compatible.

The direct CP asymmetry is:

$$\alpha_{\mathbf{CP}}(\mathbf{B^0}) = \frac{\alpha_{\mathbf{CP}}^{\mathbf{meas}}(\mathbf{B^0})}{(\mathbf{1-2}\chi)} = \frac{\mathbf{\Gamma}(\mathbf{\bar{B}^0 \to X_s}\gamma) - \mathbf{\Gamma}(\mathbf{B^0 \to X_s}\gamma)}{\mathbf{\Gamma}(\mathbf{\bar{B}^0 \to X_s}\gamma) + \mathbf{\Gamma}(\mathbf{B^0 \to X_s}\gamma)} = \mathbf{-0.24 \pm 0.48(stat.)}, \quad (4.18)$$

for neutral B decays and:

$$\alpha_{\mathbf{CP}}(\mathbf{B^{\pm}}) = \frac{\mathbf{\Gamma}(\mathbf{B^- \to X_s}\gamma) - \mathbf{\Gamma}(\mathbf{B^+ \to X_s}\gamma)}{\mathbf{\Gamma}(\mathbf{B^- \to X_s}\gamma) + \mathbf{\Gamma}(\mathbf{B^+ \to X_s}\gamma)} = \mathbf{0.27 \pm 0.37(stat.)}, \quad (4.19)$$

for charged B decays.

The CP asymmetry weighted average is:

$$\alpha_{\mathbf{CP}} = \frac{\mathbf{\Gamma}(\mathbf{b \to s}\gamma) - \mathbf{\Gamma}(\mathbf{\bar{b} \to s}\gamma)}{\mathbf{\Gamma}(\mathbf{b \to s}\gamma) + \mathbf{\Gamma}(\mathbf{\bar{b} \to s}\gamma)} = \mathbf{0.02 \pm 0.30(stat.)}. \quad (4.20)$$

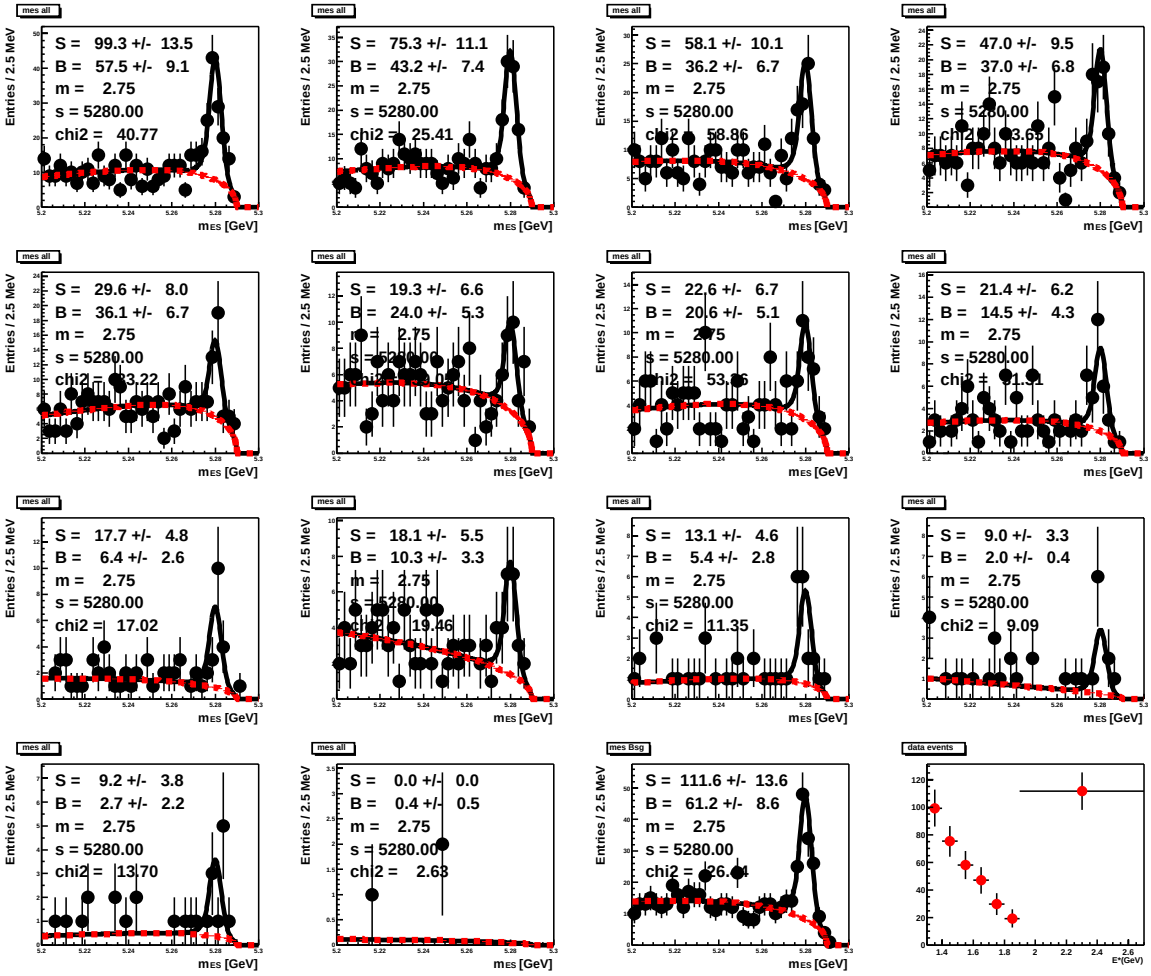

Figure 4-38. *DATA: Fits to the m_{ES} distributions in bins of E_γ.*

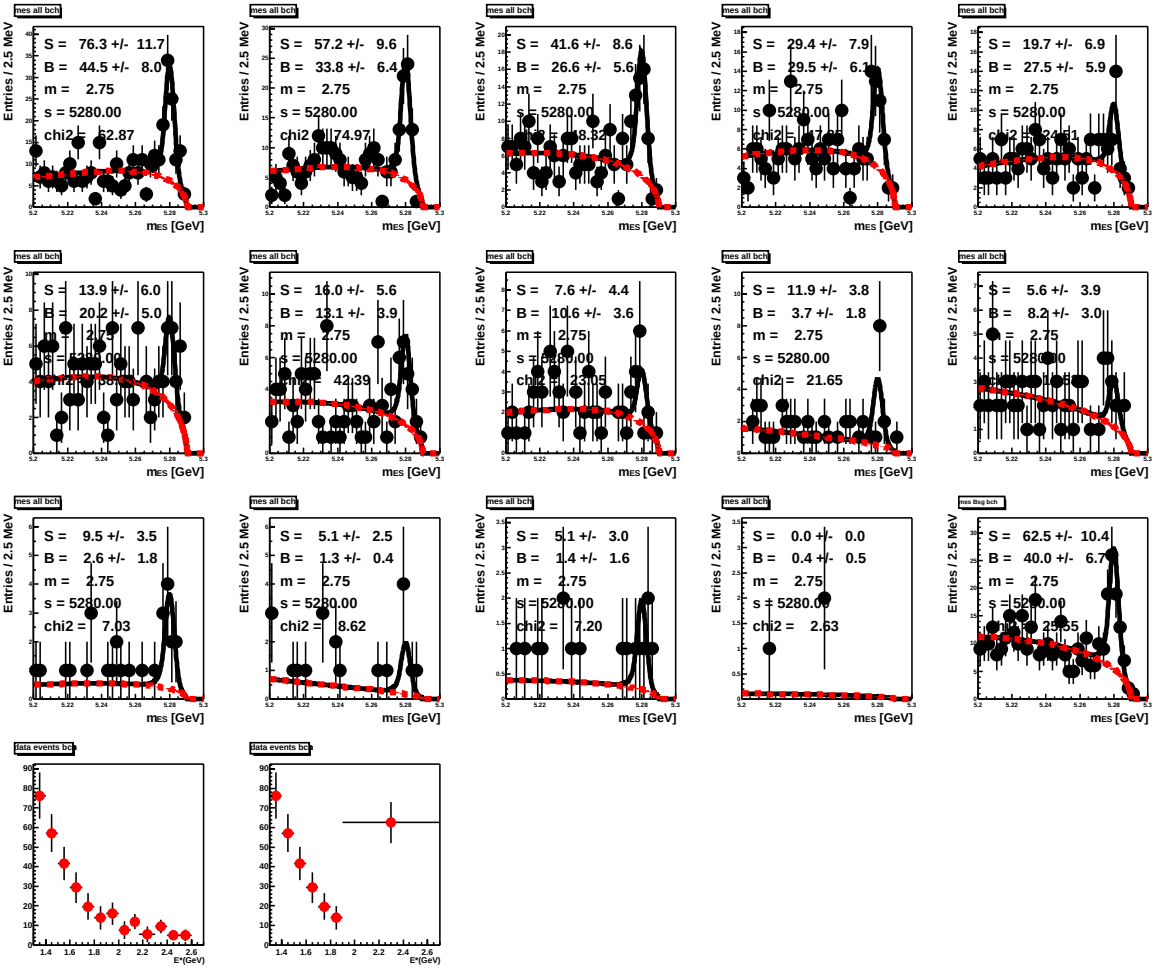

Figure 4-39. *DATA: Fits to the m_{ES} distributions in bins of E_γ for $B^\pm$.*

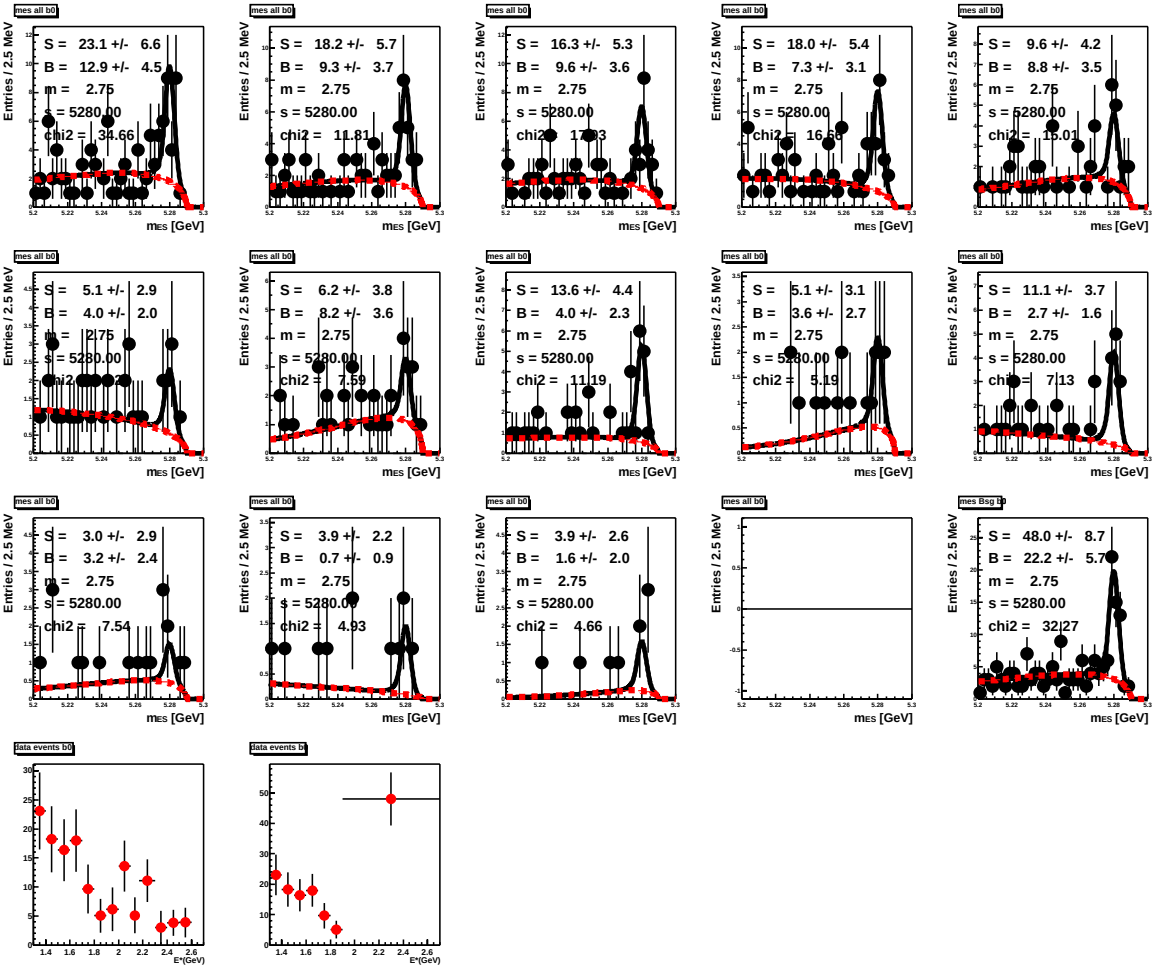

Figure 4-40. *DATA: Fits to the m_{ES} distributions in bins of E_γ for B^0.*

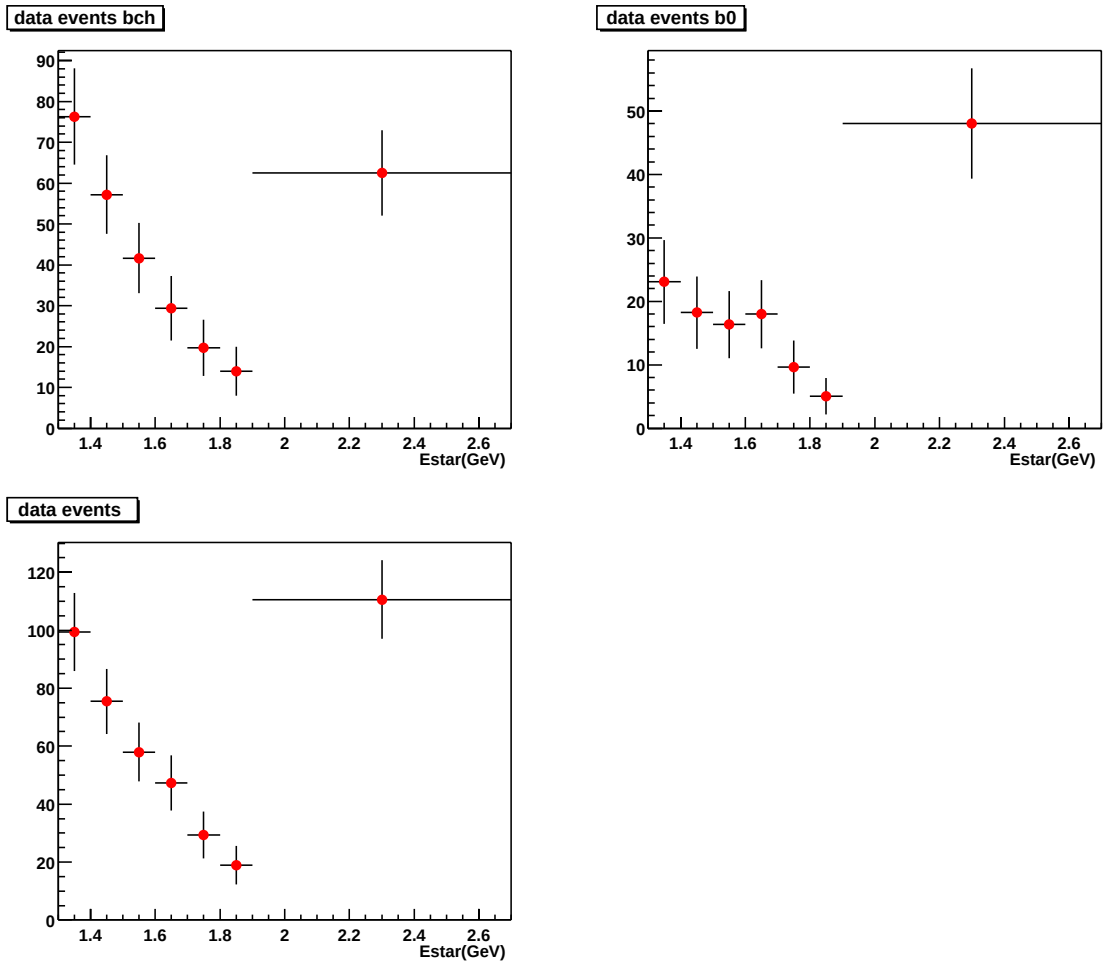

Figure 4-41. *DATA: Upper left: E_γ distribution for $B^\pm$. Upper right: E_γ distribution for B^0. Bottom left: combined results.*

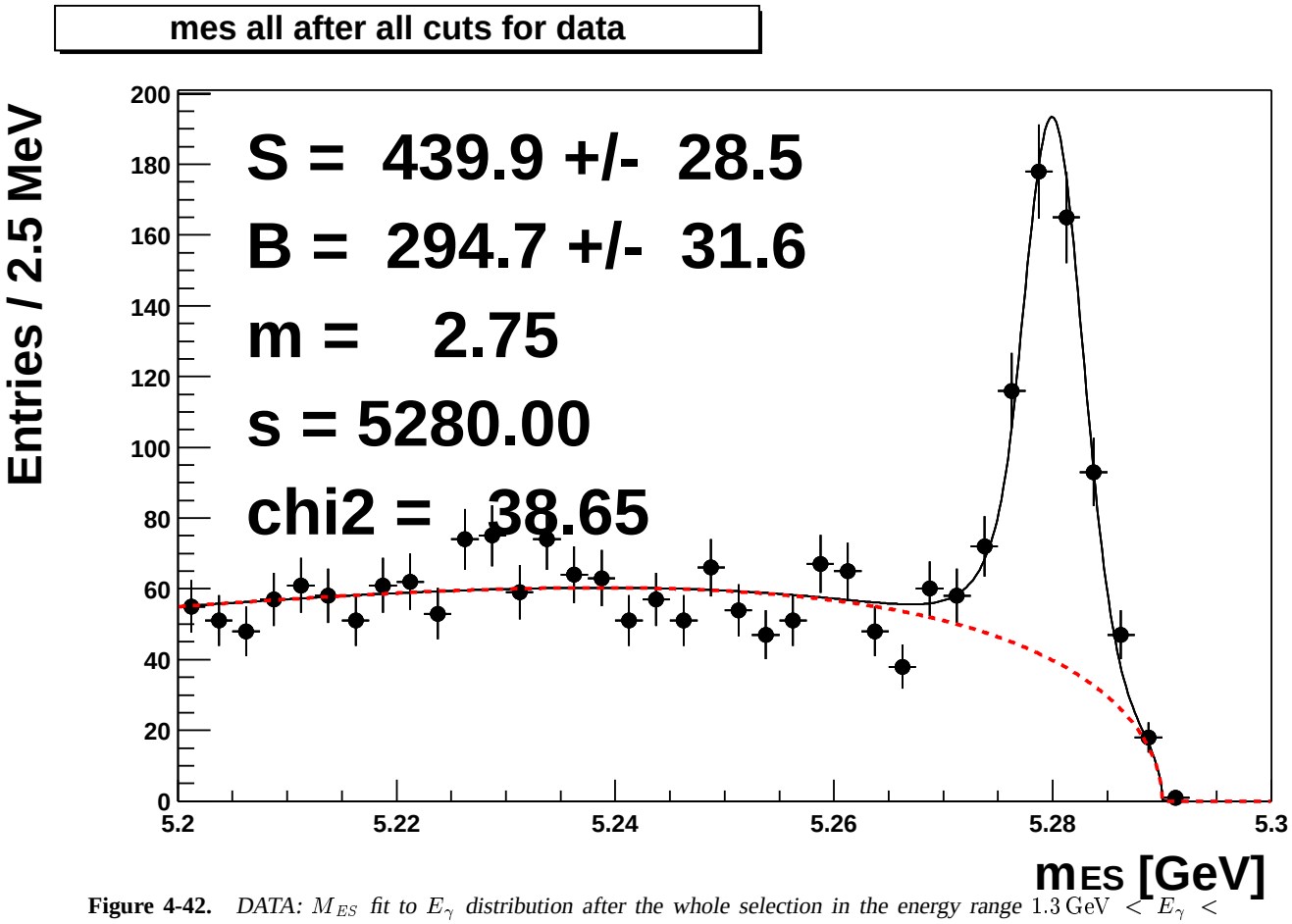

Figure 4-42. *DATA: M_{ES} fit to E_γ distribution after the whole selection in the energy range* $1.3\,\mathrm{GeV} < E_\gamma < 2.7\,\mathrm{GeV}$.

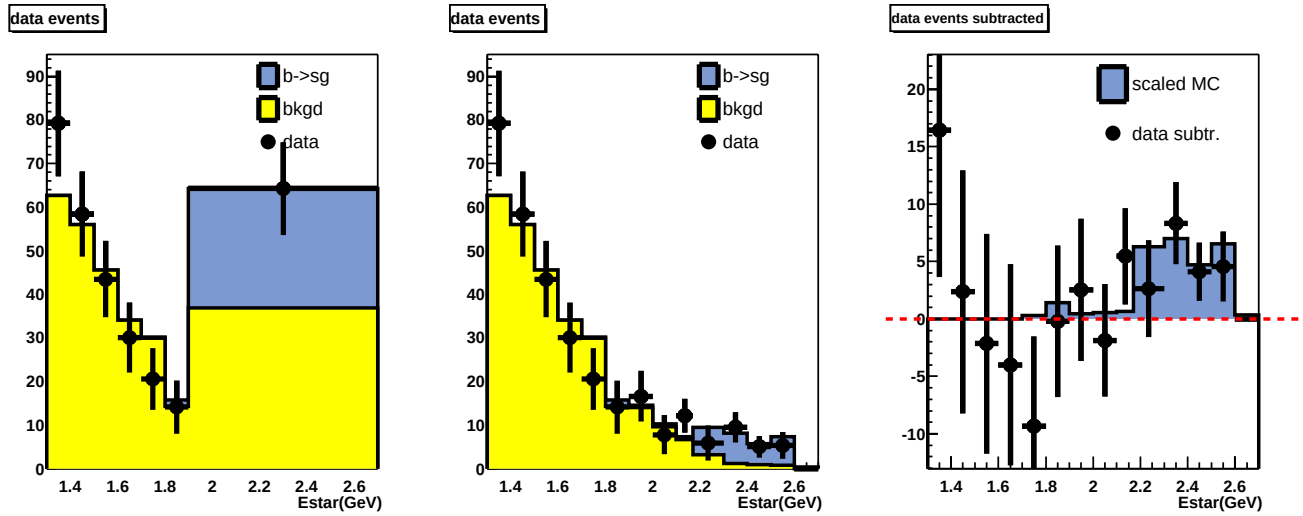

Figure 4-43. *DATA B^+ sample: χ^2 fit to the signal distribution. Left: fit result with background (yellow), and all (blue) shapes superimposed. Middle: same as in the left plot with the finer binning. Right: E_γ distribution subtracted of the backgrounds (binning as in the middle plot).*

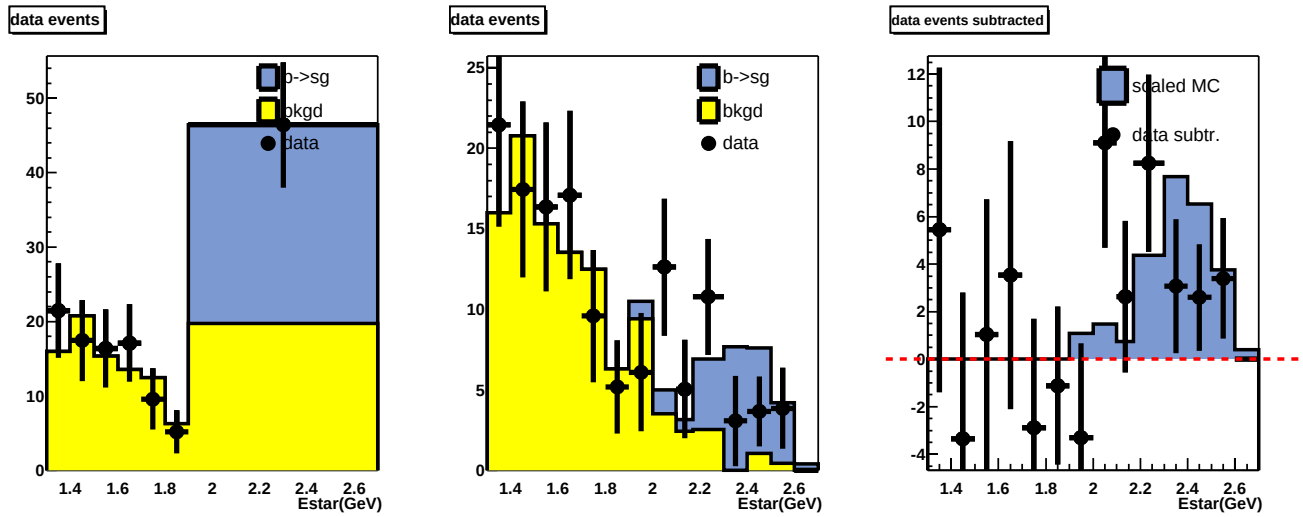

Figure 4-44. *DATA B^0 sample: χ^2 fit to the signal distribution. Left: fit result with background (yellow), and all (blue) shapes superimposed. Middle: same as in the left plot with the finer binning. Right: E_γ distribution subtracted of the backgrounds (binning as in the middle plot).*

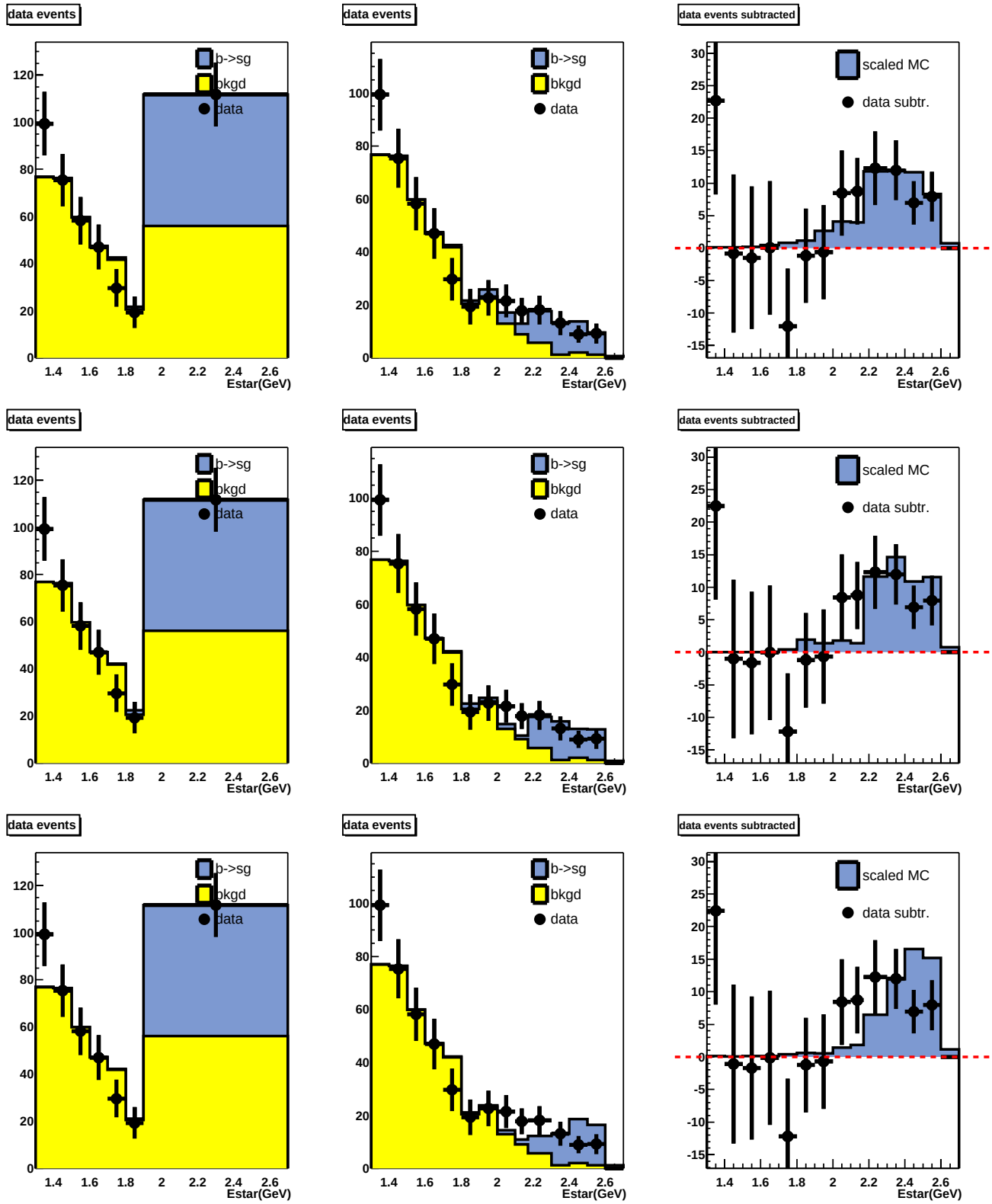

Figure 4-45. *DATA sample: χ^2 fit to the signal distribution. Upper plots: the fit is performed modeling the signal from a KN465 MonteCarlo sample. Middle plots: the fit is performed modeling the signal from a KN480 MonteCarlo sample(the default value). Bottom plots: fit is performed modeling the signal from a KN495 MonteCarlo sample. Left: fit result with background (yellow), and all (blue) shapes superimposed. Middle: same as in the left plot with the finer binning. Right: E_γ distribution subtracted of the backgrounds (binning as in the middle plot).*

Table 4-5. Summary of the fit parameters for data.

Parameter	N^{meas}	N_{sig}	BG	N_B^{meas}	$\epsilon_t^{all}/\epsilon_t^{sig}$	ϵ_{sel}	$\mathcal{B}(B \to X_s\gamma)(*10^{-4})$
all events	111.6 ± 13.5	55.5 ± 14.2	56.1 ± 4.7	284054 ± 1074	1.24 ± 0.07	0.396 ± 0.036	3.82 ± 0.98
B^0	46.4 ± 8.4	26.6 ± 8.9	19.7 ± 3.1	106442 ± 577	1.16 ± 0.11	0.348 ± 0.055	5.93 ± 1.98
$B^{\pm}$	64.3 ± 10.6	27.4 ± 11.1	36.8 ± 3.6	177685 ± 903	1.28 ± 0.08	0.426 ± 0.048	2.70 ± 1.10
RunI	19.7 ± 5.4	9.4 ± 5.7	9.3 ± 1.7	44300 ± 170	1.24 ± 0.07	0.396 ± 0.03	4.08 ± 2.0
RunII	92.9 ± 12.3	44.6 ± 13.0	48.4 ± 4.3	239741 ± 907	1.24 ± 0.07	0.396 ± 0.03	3.62 ± 1.05
intpur> 0.8	23.6 ± 5.0	14.2 ± 5.2	9.4 ± 1.6	58180 ± 287	1.08 ± 0.12	0.45 ± 0.09	4.7 ± 1.7
$0.5 <$intpur< 0.8	46.3 ± 8.3	21.6 ± 8.7	24.7 ± 2.9	123656 ± 595	1.21 ± 0.09	0.36 ± 0.05	3.86 ± 1.55
intpur< 0.5	54.0 ± 10.6	30.3 ± 11.1	23.6 ± 3.8	135290 ± 927	1.27 ± 0.12	0.41 ± 0.06	4.09 ± 1.50
KN465	111.6 ± 13.5	55.6 ± 14.2	55.9 ± 4.7	284054 ± 1074	1.24 ± 0.07	0.427 ± 0.01	3.52 ± 0.90
KN495	111.6 ± 13.5	55.4 ± 14.2	56.2 ± 4.7	284054 ± 1074	1.25 ± 0.07	0.47 ± 0.012	3.14 ± 0.80

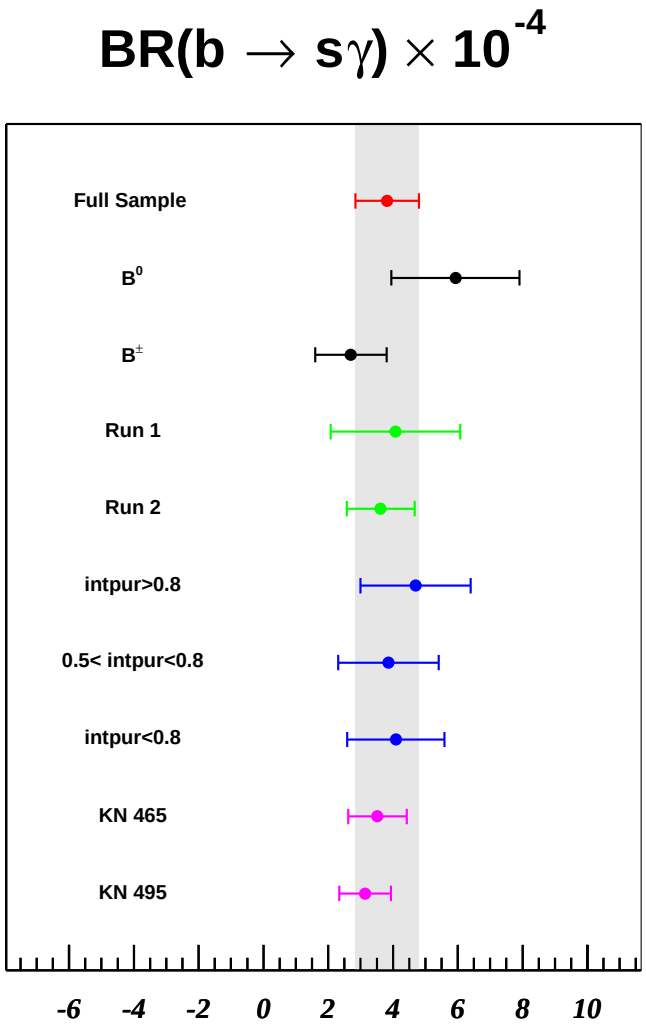

Figure 4-46. *Summary of the results for various sub-samples with statistical errors super-imposed. The vertical band represents the statistical error of this measurement.*

5

Systematic Uncertainties

In this inclusive analysis a large set of systematic uncertainties have to be taken into account. In the following, the possible systematic effects that can impact the individual ingredients of the branching ratio measurement used in the equation

$$\mathcal{B}(B \to X_s\gamma) = \frac{N_{sig}^{true}}{N_B^{true}} = \frac{N_{sig}}{N_B^{meas}\epsilon_{sel}} \times \frac{\epsilon_t^{all}}{\epsilon_t^{sig}} = \frac{(N^{meas} - BG)}{N_B^{meas}\epsilon_{sel}} \times \frac{\epsilon_t^{all}}{\epsilon_t^{sig}}. \quad (5.1)$$

are summarized:

- N_B^{meas} is the result of a fit to the M_{ES} distribution and it is therefore affected by its quality.
- N_{sig} is derived in two steps: N^{meas} is determined by a fit to the M_{ES} distribution and therefore sensitive to the quality the fit. $N_{sig} = N^{meas} - BG_u$ is determined by a fit to the E_γ distribution. It is therefore sensitive to the quality of MonteCarlo simulation.
- ϵ_{sel}. The selection efficiency for $B \to X_s\gamma$ events on the fully reconstructed sample is extracted from the MonteCarlo simulation. It is sensitive to the quality of the simulation of the reconstruction of tracks and neutral particles. Moreover, it depends on the theoretical model used to describe it (see Sec.1.3), since the signal E_γ spectrum shape and therefore the effectiveness the $E_\gamma^{\min}$ cut varies in different models.
- $\epsilon_t^{sig,all}$. A possible bias introduced by the selection of the Semi-exclusive reconstruction for the two classes of events could give rise to systematic effects.

5.1 $Breco$ composition and B^0-B^+ crossfeed

The fact that the MonteCarlo does not fully reproduce the data introduces possible differences in the B_{reco} sample composition. This effect can have an impact on the analysis in several ways. First of all the individual decays modes, depending on the multiplicity, may have different resolution in the kinematic quantities so that a difference in the B_{reco} composition might also result in a different resolution. Similarly the ratio of efficiencies $\epsilon_t^{all}/\epsilon_t^{sig}$ could be mode dependent and a not well reproduced composition could give a different ratio. Finally the cross-feed among the reconstructed modes and between B^0 and B^+ could be different in data and in MonteCarlo samples.

Fig. 5-1 shows the integrated purity for generic MonteCarlo and data sample that is an indicator of the sample composition.

Studies of the impact of the purity of the B_{reco} sample on the ratio $\epsilon_t^{all}/\epsilon_t^{sig}$ were performed. The measurement of $\mathcal{B}(B \to X_s\gamma)$ was repeated as a function of the purity of the B_{reco} sample. Fig. 5-2 shows the dependency of the result on the cut on the integrated purity, that is an indicator of the sample composition. The result is insensitive to the cut within the errors.

Another effect could be introduced by the B^0-B^+ cross-feed. In Fig. 5-3 M_{ES} for B^0 (left) and B^+ (right) cross-feed events is shown. The amount of these events corresponds to $(3.0 \pm 0.6)\%$ for B^+s and $(2.1 \pm 0.3)\%$ for B^0's. In order

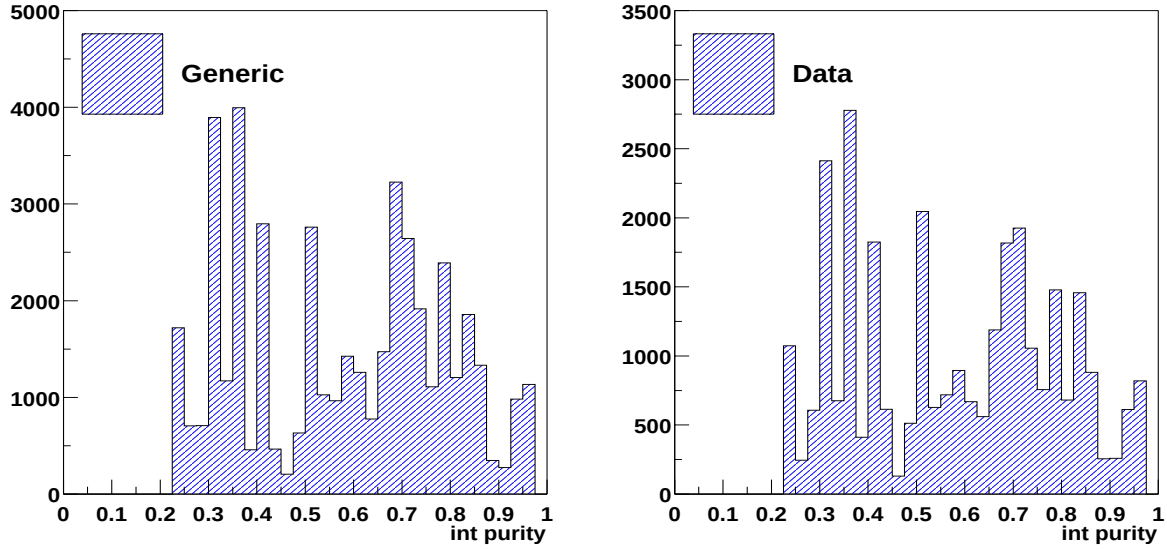

Figure 5-1. *Integrated purity for Generic MonteCarlo (left) and data (right), that is an indicator of the sample composition.*

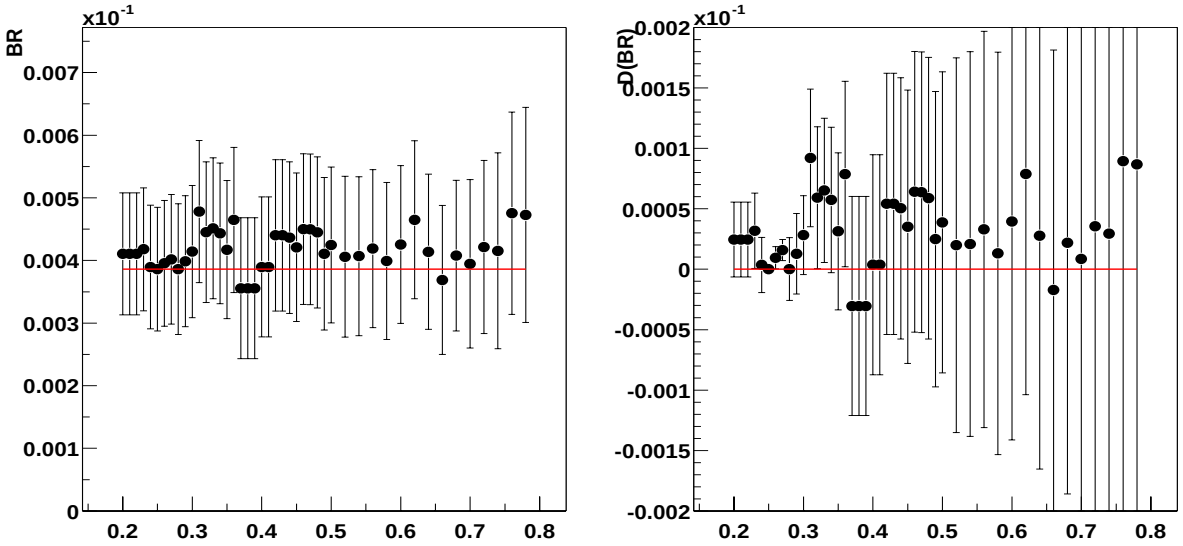

Figure 5-2. *Left: $\mathcal{B}(B \to X_s\gamma)$ result as a function of the integrated purity. Right: difference to the default analysis working point with uncorrelated errors shown.*

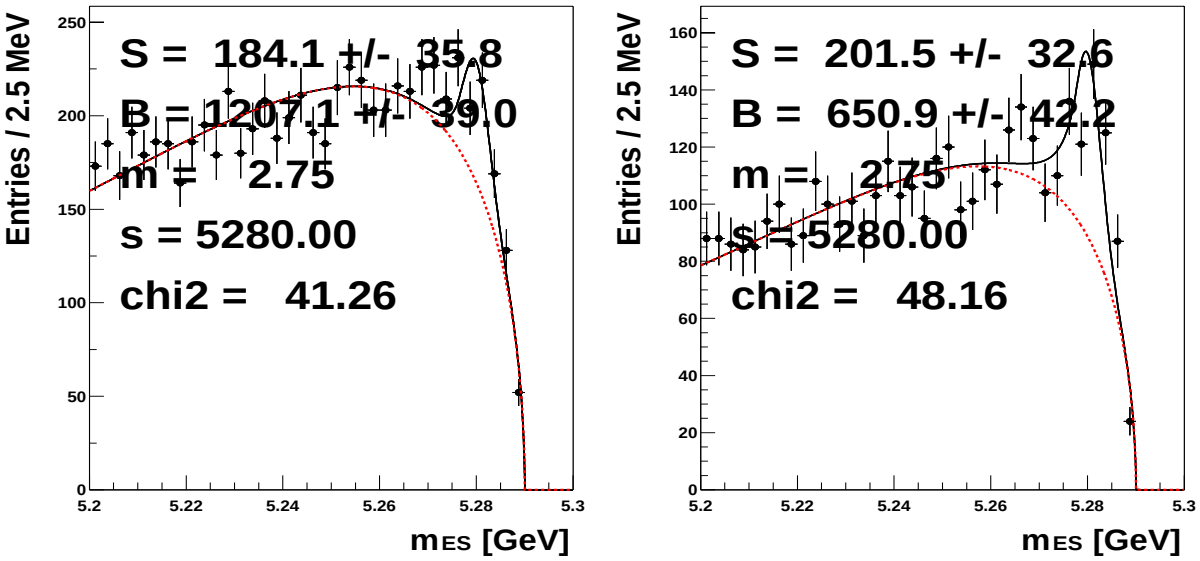

Figure 5-3. *M_{ES} distribution (for $E_\gamma > 1.3$ GeV photons) for crossfeed B^0 (left) and B^+ (right) events is shown.*

to check the impact of this effect, the data events were fitted using MonteCarlo model with and without cross-feed. The results are consistent. Finally, since all the effects are negligible and they were expected to be small, no systematic uncertainty is assigned to the B_{reco} composition.

5.2 $Breco$ reconstruction efficiency: $\epsilon_t^{all}/\epsilon_t^{sig}$

The ratio $\epsilon_t^{all}/\epsilon_t^{sig}$ of the efficiencies for finding a B_{reco} in events with a generic and signal decay in the recoiling B respectively is estimated to be 1.24 ± 0.07 as explained in Sec. 4.5.4. The 5.6% uncertainty is taken as systematics.

In high multiplicity $B\overline{B}$ events the probability of a wrong assignment of particles belonging to the B_{recoil} to the B_{reco} meson is higher than in signal events which are characterized by a few decay products on the recoiling side. The difference of this ratio from one is expected to become smaller requiring only the clean modes to be reconstructed in the B_{reco} sample. Fig. 5-4 shows the factor $\epsilon_t^{all}/\epsilon_t^{sig}$ as a function of the integrated purity. The ratio goes to one for high values of the integrated purity. The stability of the measured branching fraction as a function of the integrated purity (Fig. 5-2) makes the results reliable all over the int-pur spectrum.

5.3 MonteCarlo statistics

The finite available MonteCarlo statistics affects the measurement since it introduces an uncertainty in the shape of the background model. This is accounted for in the fit by the δN_i^{MC} term in Eq. 4.9. In order to separate this uncertainty from the purely statistical one, the measurement is repeated setting this term to zero. The statistical error obtained in this way is considered as statistical error (although the quoted central value is the one obtained with the default fit) and the difference in quadrature between the errors obtained with this fit and the default one is assigned to the systematic error as "MonteCarlo statistics". It's contribution is 8.4%.

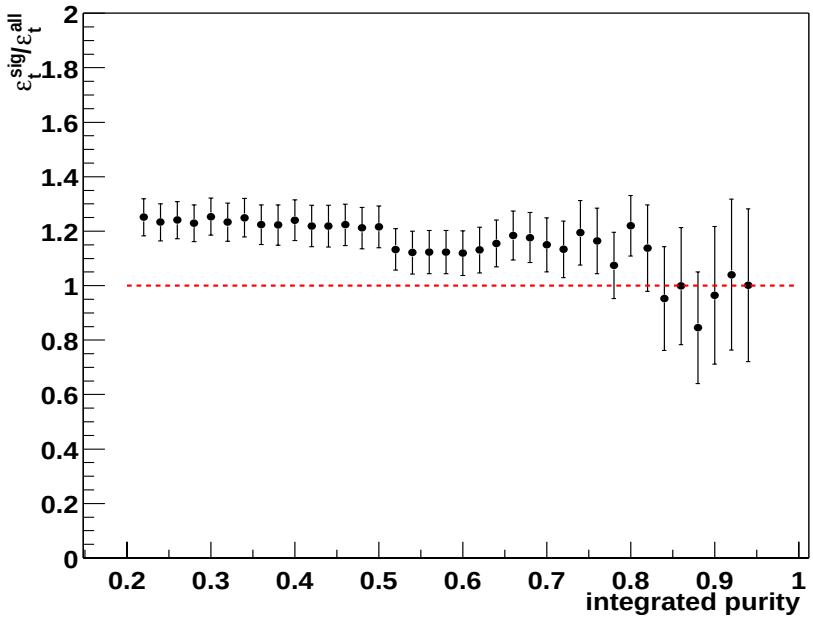

Figure 5-4. *The factor $\epsilon_t^{all}/\epsilon_t^{sig}$ as a function of the integrated purity.*

5.3.1 Efficiency from KN480 simulation

A systematic uncertainty is due to the limited Monte Carlo statistics for determining the signal efficiency. The central value of the efficiency in this analysis is based on Kagan-Neubert model with $m_b = 4.80\,\mathrm{GeV}/c^2$ and a $B \to K^*(892)\gamma$ over non-resonant ratio of 12%, thus resulting in a cut-off for the m_{X_s} system of $1.03\,\mathrm{GeV}/c^2$ (Sec.1.4) Taking into account the actual Monte Carlo statistics from Tab. 3-10, we find a 9% uncertainty in the efficiency.

5.4 Fit to the M_{ES} distribution

In the fits to the M_{ES} distributions the parameters other than the yields are fixed to values extracted from a high purity sample as explained in Sec. 4.5.2. In order to test the dependence on the mes signal shape, the systematic uncertainty due the choice of these parameters, their values are varied of $\sim 20\%$ of their value. The resulting uncertainty in $\mathcal{B}(B \to X_s\gamma)$ is 1%.

Different models have been used for the M_{ES} signal shape, a Gaussian function is used instead of the Crystal Ball function. The difference between the results obtained for the two fit functions, 4%, is taken as systematic error.

5.5 Binning effect

The effect of using a different binning (for $E_\gamma < 1.9\,\mathrm{GeV}$) in the fit and in the extraction of N_{sig} has been studied. Using different bin sizes and increasing the number of bins gives a systematic uncertainty of 1%.

energy range	smearing factor
30-100 MeV	3%
100-300 MeV	2.6%
300-600 MeV	1.6%
>600 MeV	0%

Table 5-1. *Smearing factor in different neutral energy bins.*

5.6 Neutral reconstruction

Differences between data and MonteCarlo simulation in the photon detection efficiency, resolution and calibration, can impact the E_γ distributions.

The photon efficiency is checked by considering a sample of τ lepton decays [68]. The study is performed using the τ hadronic decays that represent an abundant source of π^0 s. $e^+e^- \to \tau^+\tau^-$ events are selected identifying the decay $\tau \to e\nu\bar{\nu}$. The recoiling τ is then studied. The ratio $R = N(\tau \to h^\pm\pi^0)/N(\tau \to h^\pm\pi^0\pi^0)$ is computed both for data and MonteCarlo as a function of the π^0 energy in order to evaluate possible differences in efficiency. The photon efficiency is then adjusted to bring this ratio to 1.0. It is found that for isolated high energy photons no correction is required [69]. The statistical precision of this procedure gives a 2.5% systematic uncertainty.

The resolution has been studied [70] taking π^0 s from both $\tau \to h^\pm\pi^0$ and $\tau \to h^\pm\pi^0\pi^0$ decays. The π^0 mass is fitted in energy bins and the resolution (σ using a Gaussian fit) is then compared between data and MonteCarlo. The MonteCarlo resolution is changed applying a smearing factor such to be identical to data. The resulting smearing factors are shown in Tab. 5-1.

An estimate of the neutral systematics is performed switching off this extra smearing and comparing with the default $\mathcal{B}(B \to X_s\gamma)$. The systematics corresponds to 3%.

The calibration of the calorimeter is performed as a function of the laboratory energy and the polar angle $\cos\theta$ [57]. The energy scale of the electromagnetic calorimeter is being checked with symmetric $\eta \to \gamma\gamma$ decays and also a sample of photons from virtual Compton scattering [69]. With the η sample the two photons are both required to be in the same 500 MeV energy bin in the range $0.0 < E_{lab} < 3.0\,\mathrm{GeV}$. The invariant mass is compared with the nominal PDG mass. Any deviation in the mass is directly proportional to a deviation in energy scale. The largest deviation found, is 0.5%.

The dominant effect of a small shift in the energy scale is to change the signal efficiency of the energy cut. A 0.5% uncertainty in energy scale results in a 2.5% uncertainty in efficiency.

In the analysis photons isolated by $40\,\mathrm{cm}$ from any other EMC bump are required. To estimate the systematic uncertainty associated with this requirement radiative Bhabha photons are embedded from data in both generic $B\overline{B}$ data and MonteCarlo events and compare the efficiency of the isolation cut. This has been done for the $B \to K^*\gamma$ analysis in [41] (25 cm cut used) and the 2% derived there is taken as systematic.

The systematic uncertainty associated with $\pi^0(\eta)$ veto is estimated by embedding a photon in both off-resonance data and continuum MonteCarlo and comparing the π^0 mass distribution resulting from forming the combination of the high energy photon and any other photon in the event satisfying the requirements of Sec. 4.1. This has been done for the $B \to K^*\gamma$ analysis in reference [41] and the 1% derived there is quoted as systematic.

The photon spectrum is boosted from the laboratory frame, where it's measured, into the B_{recoil} frame in which the analysis is performed. A check has been performed to verify that the B_{recoil} boost is correctly estimated: the most

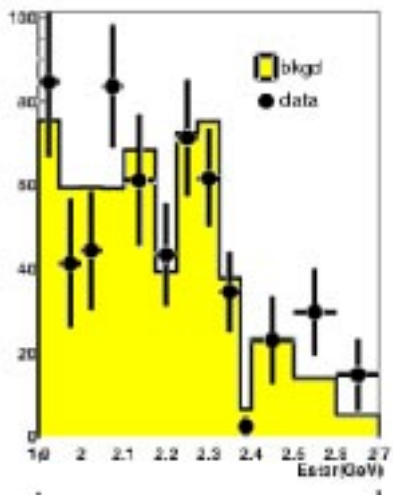

Figure 5-5. *Energy distribution of the most energetic charged π for generic $B\overline{B}$ MonteCarlo and data.*

energetic charged π is selected in order to isolate $B \rightarrow D\,\pi$ decays. In the B_{recoil} rest frame the π energy is known:

$$E_\gamma = \frac{m_B^2 - m_D^2}{2m_B} = 2.26\,\mathrm{GeV}. \tag{5.2}$$

The plot in Fig. 5-5 shows the energy distribution for data and generic $B\overline{B}$. Even if the selection is not optimized for $B \rightarrow D\,\pi$, a clear peak is visible in the region between $2.2\,\mathrm{GeV}$ and $2.3\,\mathrm{GeV}$. The low statistics of the selected sample does not allow to extract quantitative limits on the correctness of the boost. No systematic uncertainty is assigned to the B_{recoil} boost estimate.

5.7 Theoretical uncertainties

5.7.0.1 Dependence on the non-resonant Shape

The signal extrapolation below $E_\gamma < 1.9\,\mathrm{GeV}$ introduces uncertainties depending on the non-resonant model used for the signal shape (Sec. 1.3).

In the analysis, a Kagan-Neubert model with $m_b = 4.80\,\mathrm{GeV}/c^2$ and a $B \rightarrow K^*(892)\gamma$ over non-resonant ratio of 12%, with cut-off for the m_{X_s} system at $1.03\,\mathrm{GeV}/c^2$ (Sec.1.4), is used.

The prescription given by Kagan and Neubert [34] is to vary the b-quark mass m_b between 4.65 and 4.95 GeV/c^2. Variations of the parameter μ_π^2 in the shape function have a much smaller effect on the partially integrated branching ratio, and also the sensitivity to the functional form adopted for the shape function turns out to be small.

In each case the $m_{X_s}^{cut-off}$ is computed in order to satisfy the requirement that the discarded integral of the X_s spectrum below *cut-off* equals the $K^*(892)$ contribution. The $m_{X_s}^{cut-off}$ as a function of the m_b quark mass is reported in Tab. 5-2.

Varying the b-quark mass m_b between 4.65 and 4.95 GeV/c^2 a change in the selection efficiency of $\{-5\%, +5.7\%\}$ is observed.

m_b (GeV/c^2)	$m_{X_s}^{cut-off}$(GeV/c^2)
4.65	1.15
4.80	1.03
4.95	0.90

Table 5-2. *Choices of $m_{X_s}^{cut-off}$ for Kagan-Neubert model for several values of the b-quark mass m_b. These values satisfy the prescription [34] that the discarded integral of the X_s spectrum below m_{cutoff} equals the $K^*(892)$ contribution.*

5.7.0.2 Sensitivity to the assumed $B \to K^*(892)\gamma$ branching fraction

The $B \to K^*(892)\gamma$ is set to the weighted average of the *BABAR* measurements for the two charge states [44] $(4.03 \pm 0.43) \times 10^{-5}$. The dependence of signal efficiency on the fraction of $B \to K^*(892)\gamma$ in the signal model is tested varying the resonant branching fraction between the experimental errors keeping fixed the total branching fraction. A KN480 model is used for the non resonant branching ratio and the $m_{X_s}^{cut-off}$ is re-computed in each case.

This results in an efficiency change of $\{+0.6\%, -0.1\%\}$. The reason for the low sensitivity to such changes is that the selection efficiency is not much different for $B \to K^*(892)\gamma$ than for the continuum part of $B \to X_s\gamma$.

5.7.0.3 Sensitivity to the assumed $B \to X_s\gamma$ inclusive branching fraction

Although the $B \to X_s\gamma$ inclusive branching fraction is the ouput of this measurement the signal shape depends on the assumed value. The $B \to X_s\gamma$ is set to the world weighted average $(3.34 \pm 0.38) \times 10^{-4}$. The changing in the signal efficiency is tested varying the total branching ratio between the experimental error keeping the $B \to K^*(892)\gamma$ branching fraction fixed. A KN480 model is used for the non resonant branching ratio and the $m_{X_s}^{cut-off}$ is re-computed in each case. This results in an efficiency change of $\{-0.1\%, +0.6\%\}$.

5.7.0.4 Sensitivity to Boundary between resonant and non-resonant components

The signal model, described in Sec. 1.3, is composed of a mixture of $B \to K^*(892)\gamma$ and $B \to X_s\gamma$ with a sharp boundary at 1.03 GeV. In reality this boundary is rather of a smooth transition. To take this into account we compute an uncertainty by varying the boundary between 0.93 and 1.13 GeV/c^2 without varying either m_b or the K^* fraction. This results in an efficiency change of 1%.

5.7.0.5 Overall model-dependence uncertainty

Adding in quadrature the numbers in the previous four subsections, the overall model-dependence uncertainties on the efficiency is $\{-5.1\%, 5.8\%\}$:

5.8 $B \to X_d\gamma$ subtraction

The $B \to X_d\gamma$ component is subtracted by using the theory input that, according to the SM expectation, the $B \to X_d\gamma$ and the $B \to X_s\gamma$ branching fractions are in the ratio $|V_{td}/V_{ts}|^2$ and assuming same efficiency for the two different categories of events. Therefore the branching ratio is corrected down by $(4.0 \pm 1.6)\%$ of itself, the 1.6% error is taken as systematics.

5.9 Stability checks

The stability of the result has been tested running the entire analysis varying the main selection criteria: integrated purity, $Fisher$, LAT, neutral bump isolation, π^0 and ρ veto. The integrated purity and the $Fisher$ variables are scanned in the range 0.2 <int-pur< 0.8 and $-0.6 < F < 1$ respectively. The LAT variable is varied in the region $0.3 < LAT < 0.55$, where the Data-MonteCarlo agreement is not particularly good. The bump isolation is scanned over the range 10 <Bump isolation< 80 cm. The $\pi^0(\rho)$ veto is varied in the range $0 < \sigma < 4(2)$ of its resolution as estimated on MonteCarlo. In Fig. 5-6 the fit results are shown as a function of the main cut. In each plot all cuts are applied except the one on the scanned variable.

The results are stable, even changing the cut over a wide range which implies that the background shape is well estimated since the signal over background ratio varies sensitively within the the studied range. The result in the Fisher scan tends to shift to high values when the cut becomes very tight ($F > 0.4$), the current values used in this analysis ($F > 0.2$) is in a stable region. No systematic errors are applied.

5.9.1 Minimum Photon Energy Scan

The $B \to X_s\gamma$ branching ratio is extracted using the distribution of the energy of the most energetic photon E_γ in the event. Photons with $E_\gamma > E_{min} = 1.3\,\mathrm{GeV}$ are selected for this purpose. Events in the signal region ($1.9\,\mathrm{GeV} < E_\gamma < 2.7\,\mathrm{GeV}$) are extracted from a fit to the E_γ distribution.

Fig. 5-7 shows the relative branching fraction error (left), the number of $B \to X_s\gamma$ events (middle) and the number of background events (right) as a function of the choice of E_{min} as estimated on MonteCarlo simulation. The statistical error decreases as the minimum energy shifts to lower values. This is due to the fact that the error on the background component C_b in Eq. 4.10, becomes smaller enlarging the sideband region. The *working point* has been chosen considering also the systematic error.

The effect of changing the lower energy limit on the photon selection could have a different impact on data sample depending on the Data-MonteCarlo agreement in the photon spectrum. The π^0 control sample is used to test this agreement. Fig. 5-8 shows the photon spectrum for this sample after the whole selection, the Data over MonteCarlo ratio is fit with a first order polynomial function. The angular coefficient is fit as: 0.16 ± 0.14.

In order to quote a systematic error, the $\mathcal{B}(B \to X_s\gamma)$ is computed on data as a function on the minimum photon energy using the correction from the π^0 sample and re-weighting the MonteCarlo in oder to match the photon shape on data.The difference between this result and the *nominal* one with the correction switched off, is taken as systematics.

The errors coming from MonteCarlo simulation, Fig. 5-7, properly rescaled on data sample is added in quadrature to the systematic error previously calculated. The choice of $E_{min} = 1.3\,\mathrm{GeV}$ is a compromise between the necessity of a stable *working point* and the minimization of the relative branching fraction error. A 7.6% is quoted as systematics error.

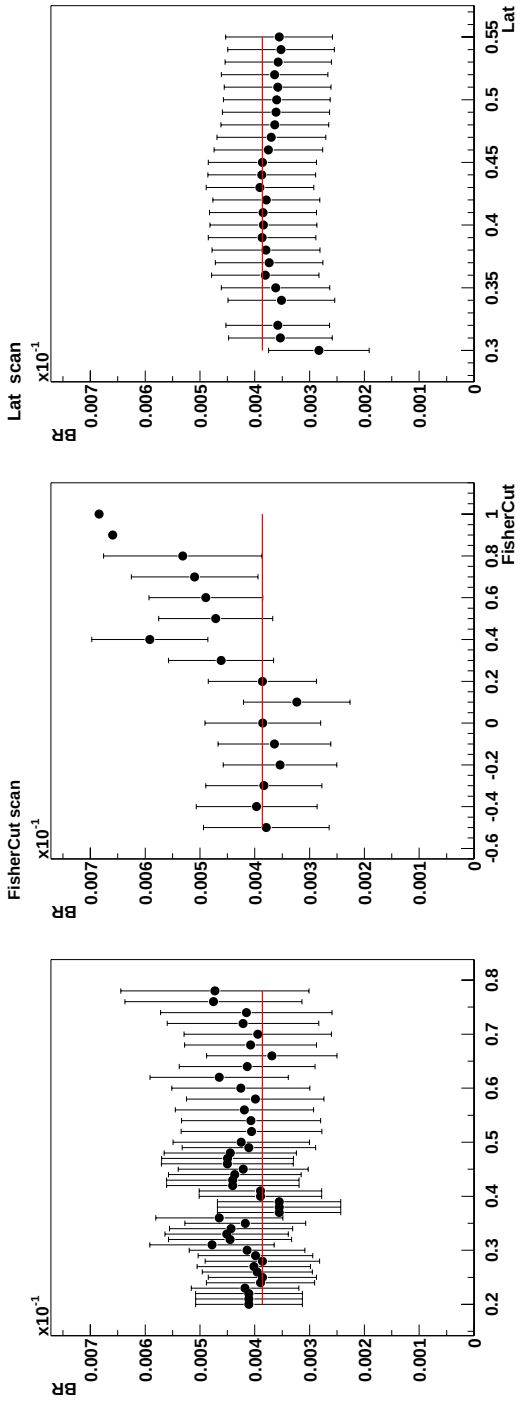

Figure 5-6. *Measurement of $BR(B \to X_s\gamma)$ as a function of the int-pur (upper left), $Fisher$ (upper middle), LAT (upper right) , bump distance isolation (bottom left), π^0 (bottom middle), ρ (bottom right) cut applied. Stastical errors are reported.*

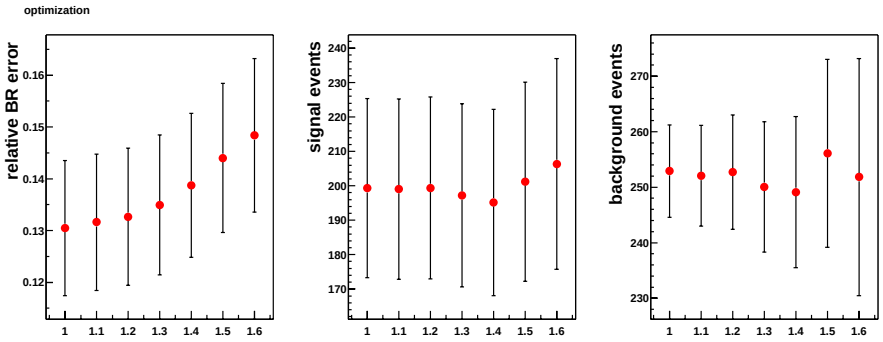

Figure 5-7. *Relative branching fraction error (left), the number of $B \to X_s\gamma$ eve nts (middle) and the number of background events (right) as a function of the LAT cut as estimated on MonteCarlo simulation.*

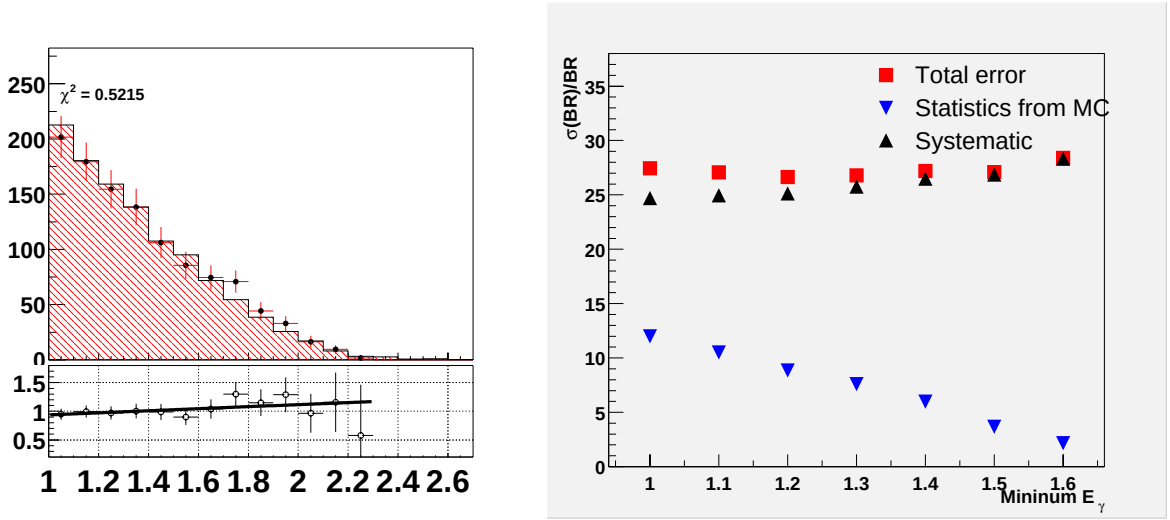

Figure 5-8. *Left plot:The Data-MonteCarlo comparison for the energy spectrum in π^0 control sample. The Data over MonteCarlo ratio is with a first order polynomial function. Right plot: statistical, systematics and total error on the $B \to X_s\gamma$ as a function of E_{min}*

.

5.10 Summary of the systematics

Systematic errors are summarized in Tab. 5-3.

The systematic error is mostly dominated by the MonteCarlo statistics in the extraction of the signal efficiency and in the uncertainty in the shape of the background model. These errors will decrease as soon as more simulated events will be available. The systematic error in the E_γ shape, extracted from the π^0 control sample, could be better understood and reduced when more statistics will be available. An improvement in the M_{ES} fit technique could reduce the error in the extraction of the yields. Moreover, the quite large error due to detector effects could be also better understood in the future. A reasonable estimate is that the total experimental systematic error can go below 5%.

Table 5-3. *The systematic uncertainties in the measurement of the BR($B \to X_s\gamma$).*

	Relative Uncertainty (%)
B_{reco} composition	-
$\epsilon_t^{sl}/\epsilon_t^u$	5.6
MonteCarlo statistics	8.4
signal efficiency	9.1
M_{ES} fit	4.1
χ^2 bins	1
photon selection	5.1
E_γ shape	7.6
Total experimental error	16.9
$B \to X_d\gamma$ subraction	1.6
model dependence	$^{+5.8}_{-5.1}$
Total theoretical error	$^{+6.0}_{-5.3}$

5.11 Propagation of errors in $R_{\pm/0}$ and α_{CP}

In order to propagate the errors in $R_{\pm/0}$ taking into account the correlations properly, the following procedure is adopted:

- errors are computed separately for neutral and charged B tags.
- they are grouped into correlated (σ_c^i, where $i = 0, +$ for B^0 and $B^\pm$), uncorrelated (σ_u^i) and anticorrelated (σ_a^i). These subtotals are computed separately for B^0 and $B^\pm$, adding the contributions in quadrature.
- the total covariance matrix is written as $V_{ij} = \delta_{ij}\sigma_c^i\sigma_c^j + \sigma_u^i\sigma_u^j + (2\delta_{ij} - 1)\sigma_a^i\sigma_a^j$
- the error on the ratio is propagated using $\widehat{V}$.

Errors are summarized in Tab. 5-4. The result is:

Table 5-4. *Correlated and uncorrelated uncertainties in the measurement of the ratio* $R_{\pm/0} = \mathcal{B}(B^{\pm} \to X_s^{\pm}\gamma)\mathcal{B}(B^0 \to X_s^0\gamma)$*. Errors are quoted as absolute values.*

	$\mathcal{B}(B^{\pm} \to X_s^{\pm}\gamma)$ (10^{-4})	$\mathcal{B}(B^0 \to X_s^0\gamma$ (10^{-4})
Branching fraction	2.70	5.93
	uncorrelated uncertanties	
Stat. err.	1.10	1.98
MonteCarlo stat.	0.37	0.66
Total uncorrelated error	1.16	2.07
	correlated uncertanties	
Fit technique	0.11	0.23
Photon efficiency	0.3	0.94
$\epsilon_t^{sl}/\epsilon_t^u$	0.15	0.16
Photon selection	0.13	0.38
E_γ shape	0.2	0.47
theo.	0.13	0.37
Total correlated error	0.46	1.3
	anticorrelated uncertanties	
crossfeed	0.08	0.09

$$\mathbf{R_{\pm/0} = \frac{\mathcal{B}(B^{\pm} \to X_s^{\pm}\gamma)}{\mathcal{B}(B^0 \to X_s^0\gamma)} = 0.46 \pm 0.24(stat.) \pm 0.09(syst.).} \quad (5.3)$$

The propagation of errors in the α_{CP} measurement is perfomed in the same way. Errors are summarized in Tab. 5-5.

The direct CP asymmetry is:

$$\mathbf{\alpha_{CP}(B^0) = \frac{\alpha_{CP}^{meas}(B^0)}{(1-2\chi)} = \frac{\Gamma(\bar{B}^0 \to X_s\gamma) - \Gamma(B^0 \to X_s\gamma)}{\Gamma(\bar{B}^0 \to X_s\gamma) + \Gamma(B^0 \to X_s\gamma)} = -0.24 \pm 0.48(stat.) \pm 0.20(syst.),} \quad (5.4)$$

for neutral B decays and:

$$\mathbf{\alpha_{CP}(B^{\pm}) = \frac{\Gamma(B^- \to X_s\gamma) - \Gamma(B^+ \to X_s\gamma)}{\Gamma(B^- \to X_s\gamma) + \Gamma(B^+ \to X_s\gamma)} = 0.27 \pm 0.37(stat.) \pm 0.09(syst.),} \quad (5.5)$$

Table 5-5. *Correlated and uncorrelated uncertainties in the measurement of the direct CP asymmetry. Errors are quoted as absolute values.*

	B^-	B^+	$\bar{B}^0$	B^0
Number of events	18.84	10.84	12.28	16.64
	uncorrelated uncertanties			
Stat. err.	8.4	7.3	5.9	7.1
MonteCarlo stat.	2.3	1.5	2.6	3
Total uncorrelated error	8.7	7.5	6.4	7.6
	correlated uncertanties			
Fit technique	0.8	0.4	0.5	0.7
Photon efficiency	2.1	1.2	1.9	2.7
Photon selection	1.0	0.6	0.6	0.8
E_γ shape	1.4	0.8	9.3	1.3
Total correlated error	2.8	1.6	2.3	3.2

for charged B decays.

The CP asymmetry weighted average is:

$$\alpha_{\mathbf{CP}} = \frac{\mathbf{\Gamma(b \to s\gamma) - \Gamma(\bar{b} \to s\gamma)}}{\mathbf{\Gamma(b \to s\gamma) + \Gamma(\bar{b} \to s\gamma)}} = \mathbf{0.02 \pm 0.32}. \tag{5.6}$$

where statistical and systematics error are added in quadrature.

6

Conclusions

The $B \to X_s\gamma$ branching ratio and direct CP asymmetry have been measured with a novel technique consisting in the study of high energy photons recoiling to fully reconstructed B 's. This reconstruction determines the flavor and the charge of the reconstructed B meson and allows , for the first time, to measure $BR(B \to X_s\gamma)$ and α_{CP} in B^0 and $B^\pm$ separately.

The signal spectrum is measured down to $1.9\,\mathrm{GeV}$, a value never reached in previous measurements. This allows to reduce the theoretical uncertainties due to the extrapolation in the unmeasured part of the energy spectrum.

The resulting $BR(B \to X_s\gamma)$ value is:

$$\mathcal{B}(\mathbf{B \to X_s\gamma}) = (\mathbf{3.82 \pm 0.98(stat.) \pm 0.65(syst.)^{+0.23}_{-0.20}(theo.)}) \times \mathbf{10^{-4}}. \quad (6.1)$$

The results for neutral and charged B are, respectively:

$$\mathcal{B}(\mathbf{B^0 \to X^0_s\gamma}) = (\mathbf{5.93 \pm 1.98(stat.) \pm 1.00(syst.)^{+0.36}_{-0.31}(theo.)}) \times \mathbf{10^{-4}}. \quad (6.2)$$

$$\mathcal{B}(\mathbf{B^\pm \to X^\pm_s\gamma}) = (\mathbf{2.70 \pm 1.10(stat.) \pm 0.45(syst.)^{+0.16}_{-0.14}(theo.)}) \times \mathbf{10^{-4}}. \quad (6.3)$$

The ratio of charged over neutral branching fraction is:

$$\mathbf{R_{\pm/0}} = \frac{\mathcal{B}(\mathbf{B^\pm \to X^\pm_s\gamma})}{\mathcal{B}(\mathbf{B^0 \to X^0_s\gamma})} = \mathbf{0.46 \pm 0.24(stat.) \pm 0.09(syst.)}. \quad (6.4)$$

The direct CP asymmetry is:

$$\mathbf{\alpha_{CP}(B^0)} = \frac{\mathbf{\Gamma(\bar{B}^0 \to X_s\gamma) - \Gamma(B^0 \to X_s\gamma)}}{\mathbf{\Gamma(\bar{B}^0 \to X_s\gamma) + \Gamma(B^0 \to X_s\gamma)}} = \mathbf{-0.24 \pm 0.48(stat.) \pm 0.20(syst.)}, \quad (6.5)$$

for neutral B decays and:

$$\alpha_{\mathbf{CP}}(\mathbf{B}^{\pm}) = \frac{\mathbf{\Gamma}(\mathbf{B}^{-} \to \mathbf{X_s}\gamma) - \mathbf{\Gamma}(\mathbf{B}^{+} \to \mathbf{X_s}\gamma)}{\mathbf{\Gamma}(\mathbf{B}^{-} \to \mathbf{X_s}\gamma) + \mathbf{\Gamma}(\mathbf{B}^{+} \to \mathbf{X_s}\gamma)} = \mathbf{0.27 \pm 0.37(stat.) \pm 0.09(syst.)}, \quad (6.6)$$

for charged B decays.

The α_{CP} weighted average is:

$$\alpha_{\mathbf{CP}} = \frac{\mathbf{\Gamma}(\mathbf{b} \to \mathbf{s}\gamma) - \mathbf{\Gamma}(\bar{\mathbf{b}} \to \mathbf{s}\gamma)}{\mathbf{\Gamma}(\mathbf{b} \to \mathbf{s}\gamma) + \mathbf{\Gamma}(\bar{\mathbf{b}} \to \mathbf{s}\gamma)} = \mathbf{0.02 \pm 0.32}. \quad (6.7)$$

where statistical and systematics error are added in quadrature.

In Fig. 6-1 the $B \to X_s\gamma$ branching ratio measured in this thesis is compared with the previous measurements. The vertical band represents the theoretical prediction [35]: $\mathcal{B}(B \to X_s\gamma) = (3.73 \pm 0.30) \times 10^{-4}$. The central value is in very good agremeent with theoretical expectation and compatible with previous measurements.

This measurement is already competitive. Nevertheless many improvements are still feasible. The statistical error represents the main source of uncertainties in the analysis. In the next years PEP-II will deliver higher and higher luminosity. By the year 2005 *BABAR* will have recorded an expected luminosity of 500 fb^{-1}. The statistical error will go down to 10%. The experimental systematic error is mostly dominated by the MonteCarlo statistics in the extraction of the signal efficiency and in the uncertainty in the shape of the background model, both of them will decrease as soon as more simulated events will be available. Moreover, the quite large error due to detector effects could be also better understood in the future. A reasonable estimate is that the total experimental systematic error can go below 5%.

By adding statistics not only the integral but also the E_γ shape can be measured allowing the extraction of the theoretical parameters m_b and μ_π^2. These parameters could be used for a better determination of the CKM matrix element V_{ub} since the shape function, to the lowest order in Λ_{QCD}/m_b, is the same in $B \to X_s\gamma$ and in $B \to X_u\ell\nu$ decays.

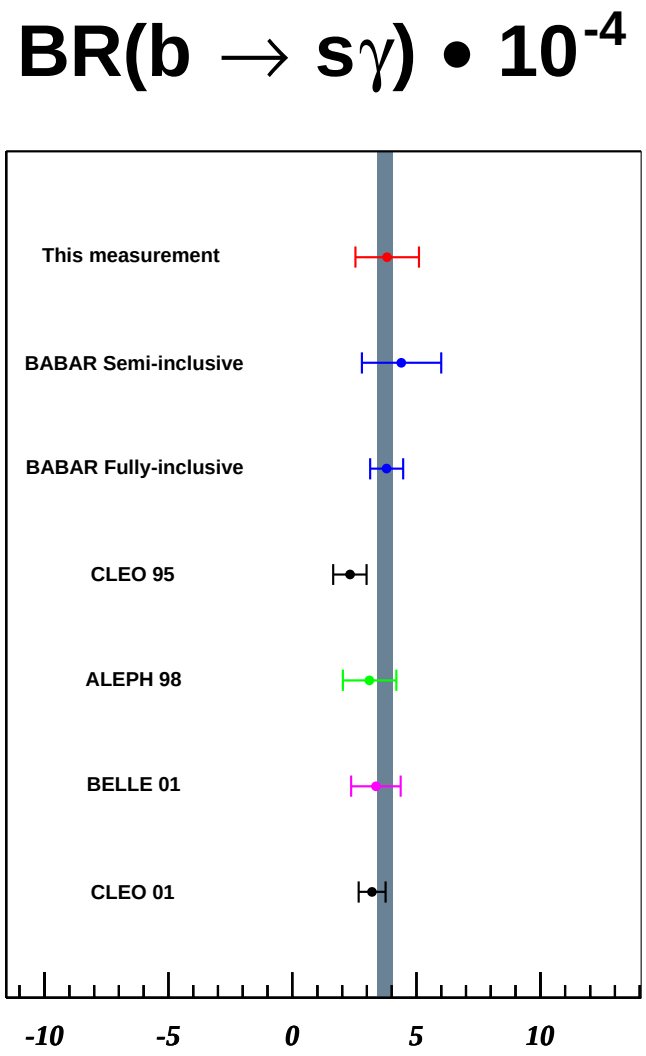

Figure 6-1. *$\mathcal{B}(B \to X_s\gamma)$ measurements versus theoretical predictions. The vertical band represents the theoretical prediction [35].*

A

Data-MonteCarlo comparison

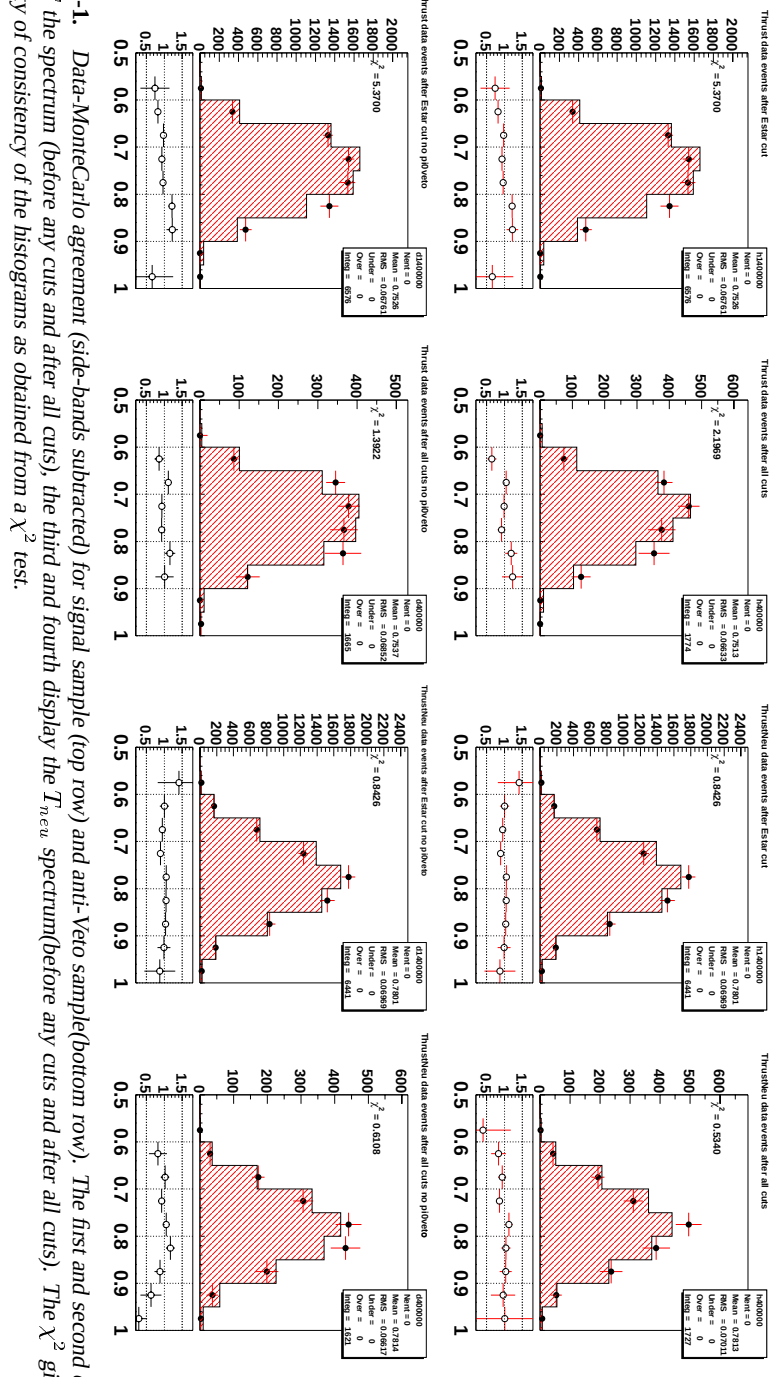

Figure A-1. *Data-MonteCarlo agreement (side-bands subtracted) for signal sample (top row) and anti-Veto sample(bottom row). The first and second column display T the spectrum (before any cuts and after all cuts), the third and fourth display the T_{neu} spectrum(before any cuts and after all cuts). The χ^2 gives the probability of consistency of the histograms as obtained from a χ^2 test.*

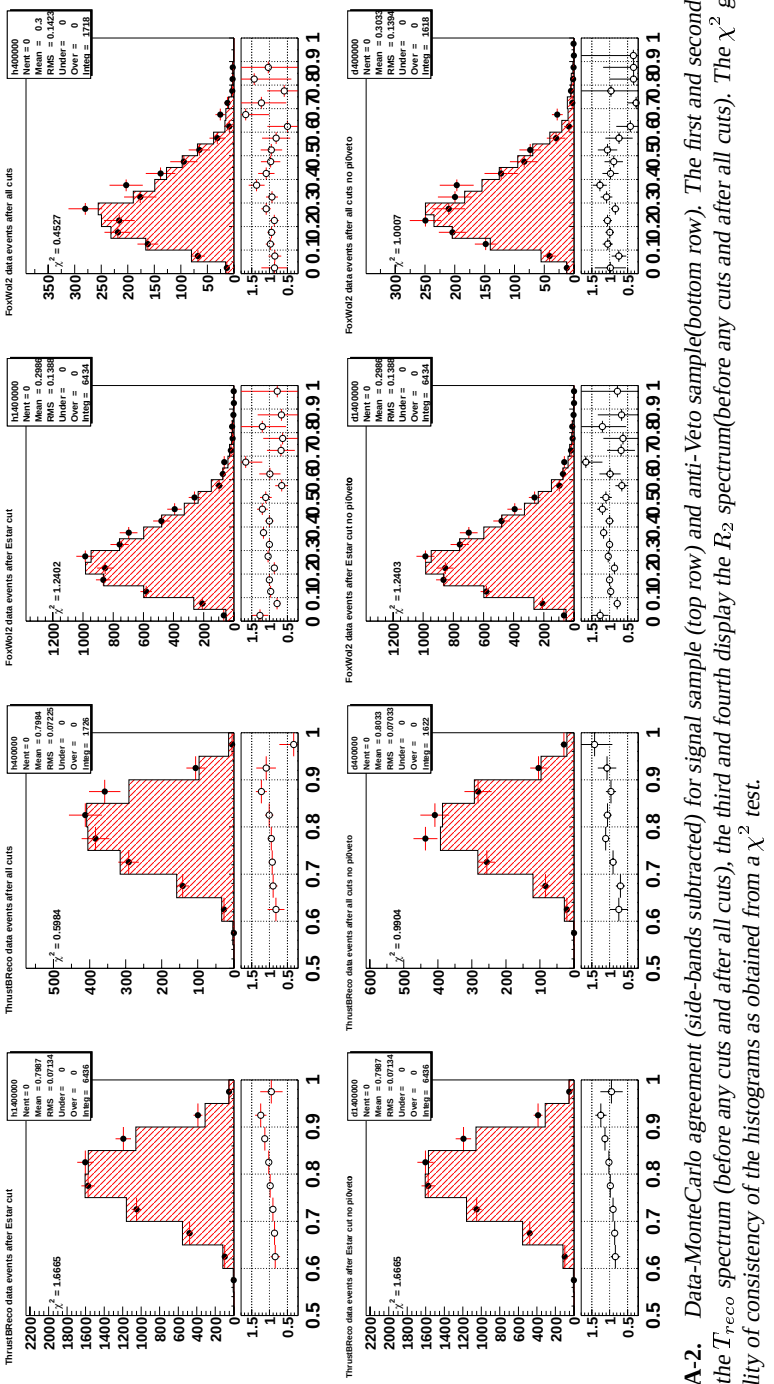

Figure A-2. *Data-MonteCarlo agreement (side-bands subtracted) for signal sample (top row) and anti-Veto sample(bottom row). The first and second column display the T_{rECO} spectrum (before any cuts and after all cuts), the third and fourth display the R_2 spectrum(before any cuts and after all cuts). The χ^2 gives the probability of consistency of the histograms as obtained from a χ^2 test.*

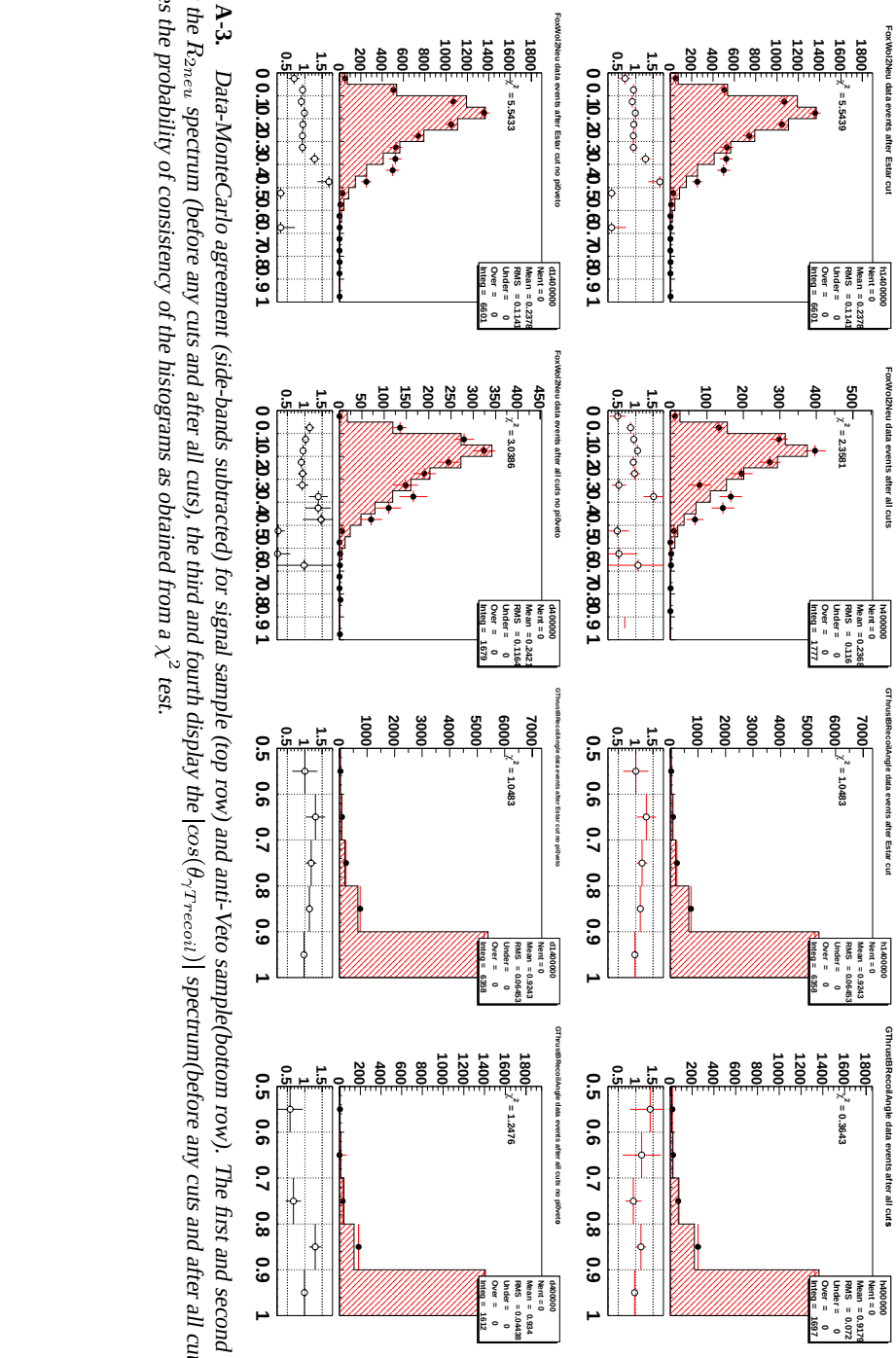

Figure A-3. *Data-MonteCarlo agreement (side-bands subtracted) for signal sample (top row) and anti-Veto sample(bottom row). The first and second column display the R_{2new} spectrum (before any cuts and after all cuts), the third and fourth display the $|cos(\theta_{\gamma Trecoil})|$ spectrum(before any cuts and after all cuts). The χ^2 gives the probability of consistency of the histograms as obtained from a χ^2 test.*

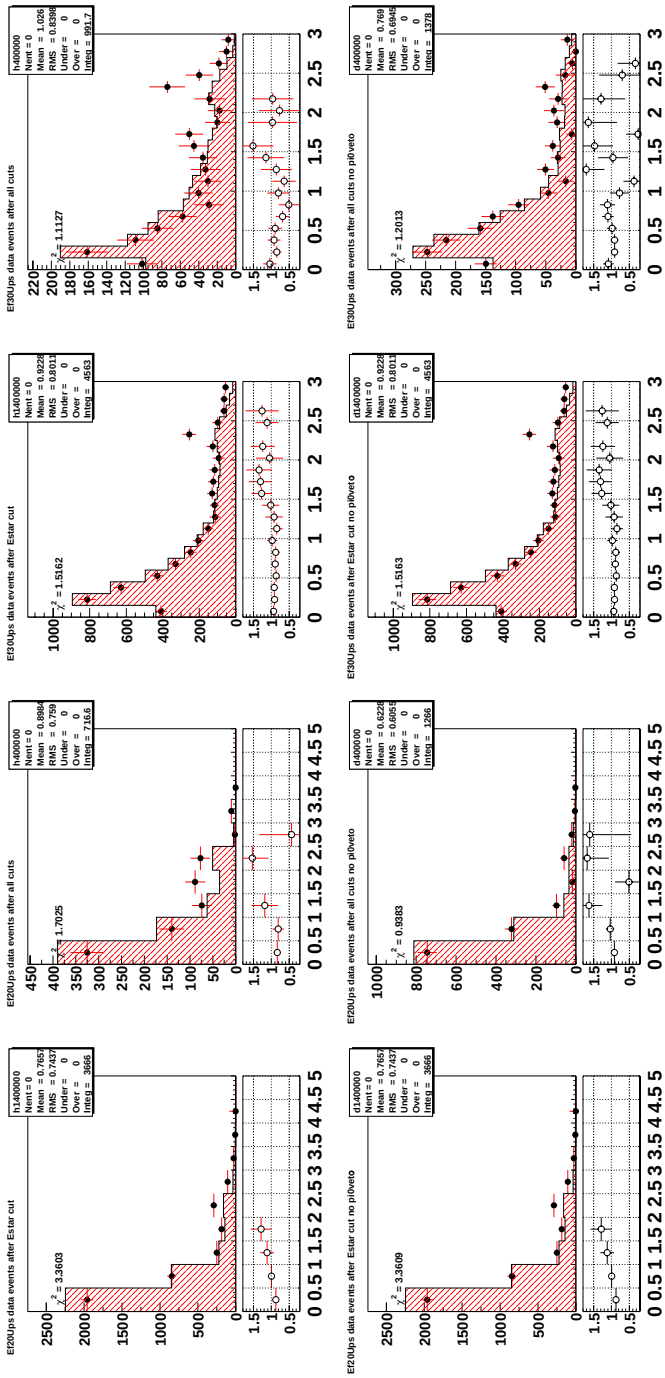

Figure A-4. *Data-MonteCarlo agreement (side-bands subtracted) for signal sample (top row) and anti-Veto sample(bottom row). The first and second column display the $E^{\Upsilon(4S)}_{f,20}$ spectrum (before any cuts and after all cuts), the third and fourth display the $E^{\Upsilon(4S)}_{f,30}$ spectrum(before any cuts and after all cuts). The χ^2 gives the probability of consistency of the histograms as obtained from a χ^2 test.*

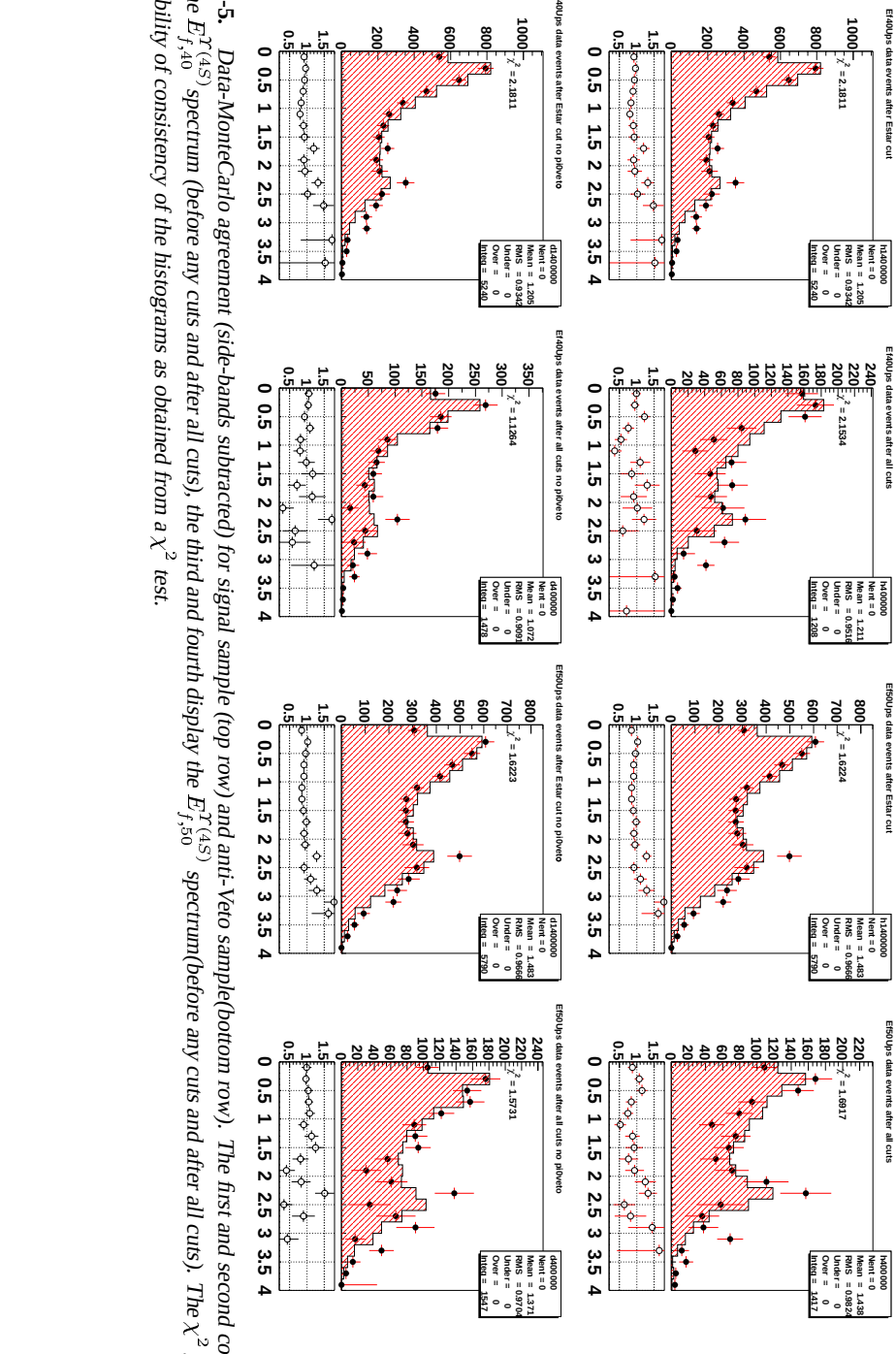

Figure A-5. *Data-MonteCarlo agreement (side-bands subtracted) for signal sample (top row) and anti-Veto sample(bottom row). The first and second column display the $E^{\Upsilon(4S)}_{f,40}$ spectrum (before any cuts and after all cuts), the third and fourth display the $E^{\Upsilon(4S)}_{f,50}$ spectrum(before any cuts and after all cuts). The χ^2 gives the probability of consistency of the histograms as obtained from a χ^2 test.*

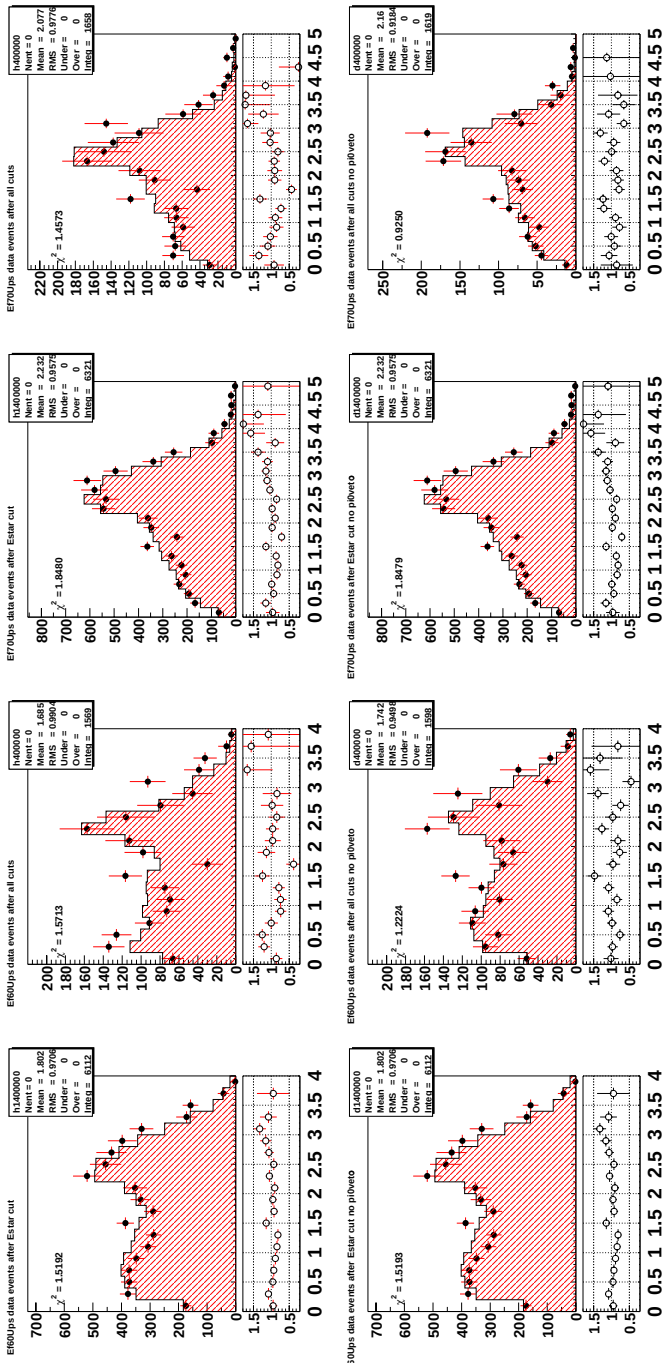

Figure A-6. *Data-MonteCarlo agreement (side-bands subtracted) for signal sample (top row) and anti-Veto sample(bottom row). The first and second column display the $E^{\Upsilon(4S)}_{f,60}$ spectrum (before any cuts and after all cuts), the third and fourth display the $E^{\Upsilon(4S)}_{f,70}$ spectrum(before any cuts and after all cuts). The χ^2 gives the probability of consistency of the histograms as obtained from a χ^2 test.*

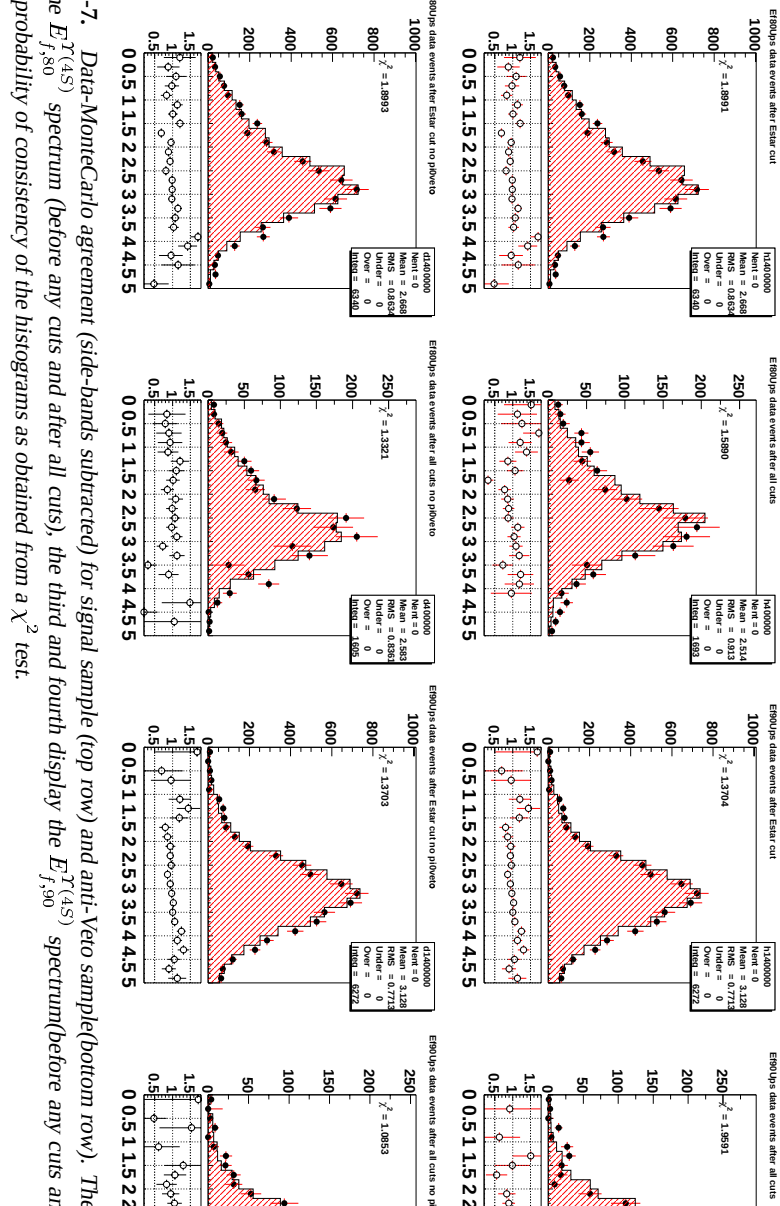

Figure A-7. *Data-MonteCarlo agreement (side-bands subtracted) for signal sample (top row) and anti-Veto sample(bottom row). The first and second column display the $E^{\Upsilon(4S)}_{f,80}$ spectrum (before any cuts and after all cuts), the third and fourth display the $E^{\Upsilon(4S)}_{f,90}$ spectrum(before any cuts and after all cuts). The χ^2 gives the probability of consistency of the histograms as obtained from a χ^2 test.*

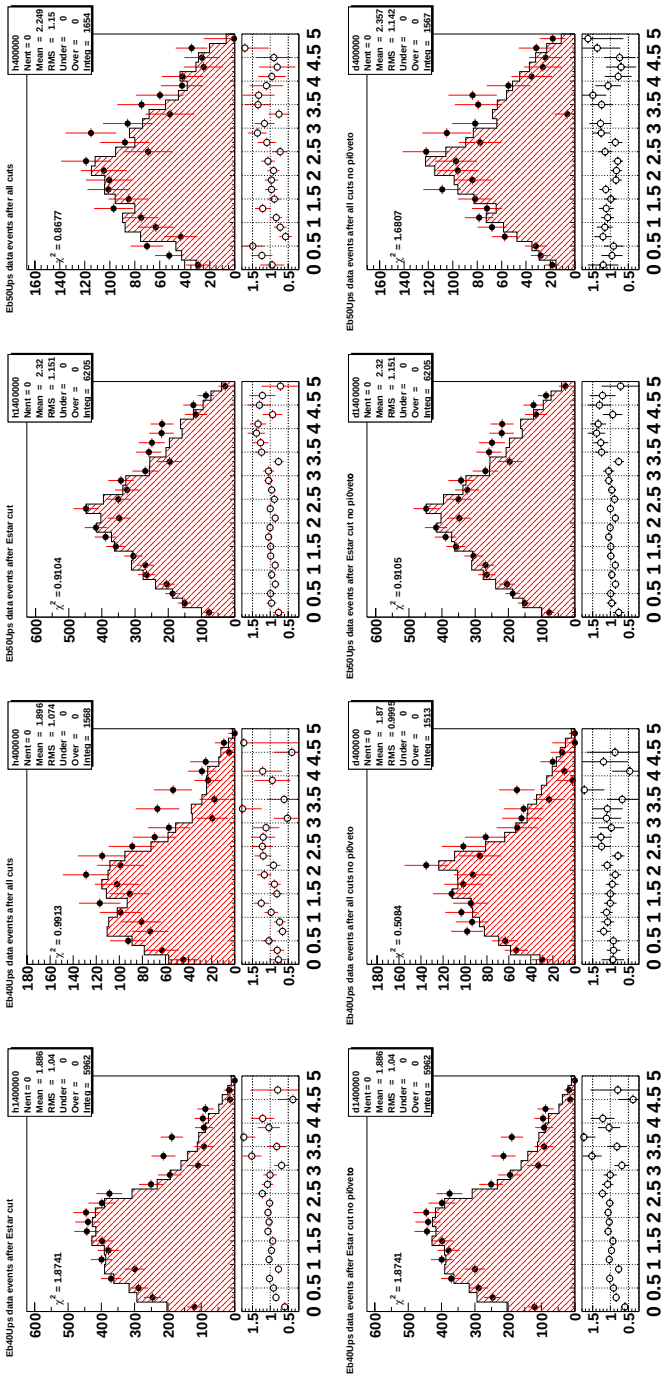

Figure A-8. *Data-MonteCarlo agreement (side-bands subtracted) for signal sample (top row) and anti-Veto sample(bottom row). The first and second column display the $E_{b,40}^{\Upsilon(4S)}$ spectrum (before any cuts and after all cuts), the third and fourth display the $E_{b,50}^{\Upsilon(4S)}$ spectrum(before any cuts and after all cuts). The χ^2 gives the probability of consistency of the histograms as obtained from a χ^2 test.*

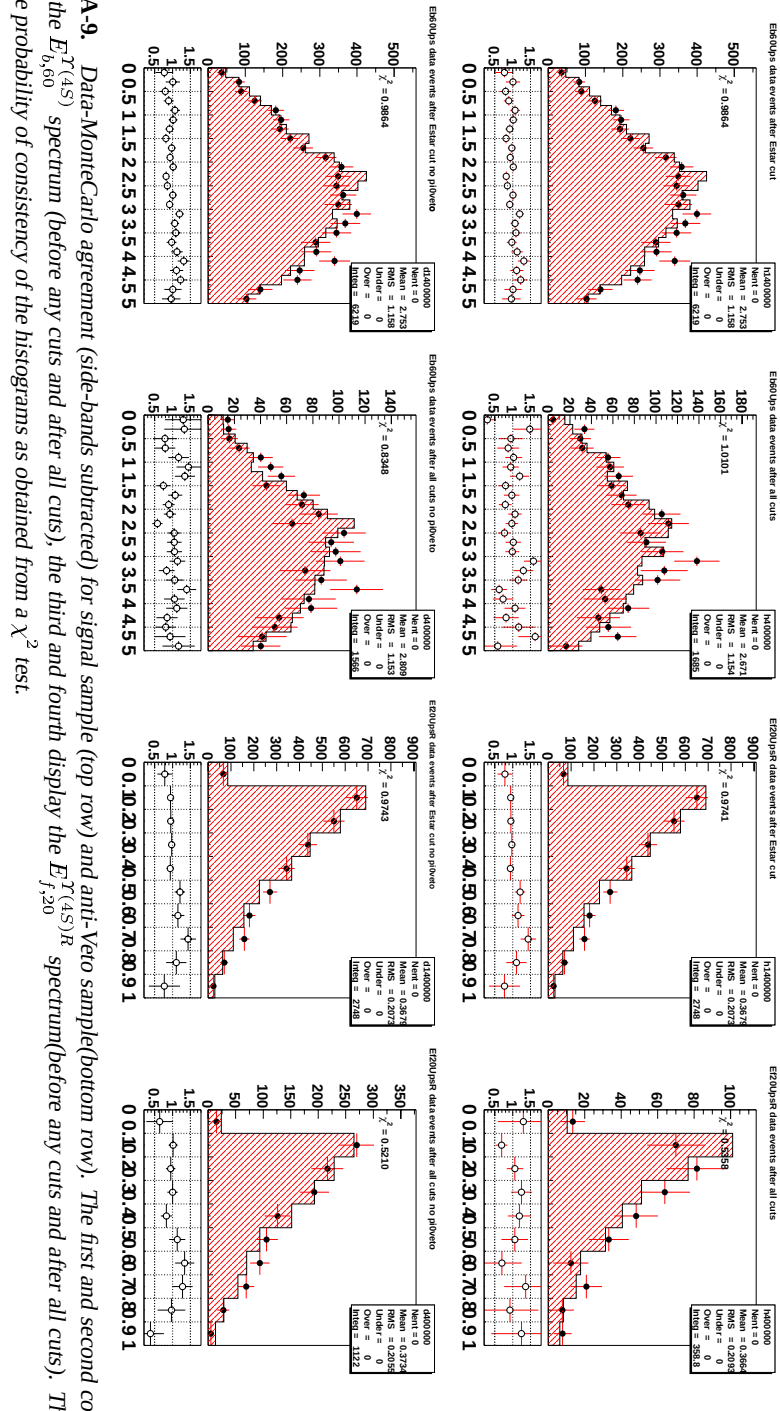

Figure A-9. *Data-MonteCarlo agreement (side-bands subtracted) for signal sample (top row) and anti-Veto sample(bottom row). The first and second column display the $E^{\Upsilon(4S)}_{\beta,60}$ spectrum (before any cuts and after all cuts), the third and fourth display the $E^{\Upsilon(4S)R}_{f,20}$ spectrum(before any cuts and after all cuts). The χ^2 gives the probability of consistency of the histograms as obtained from a χ^2 test.*

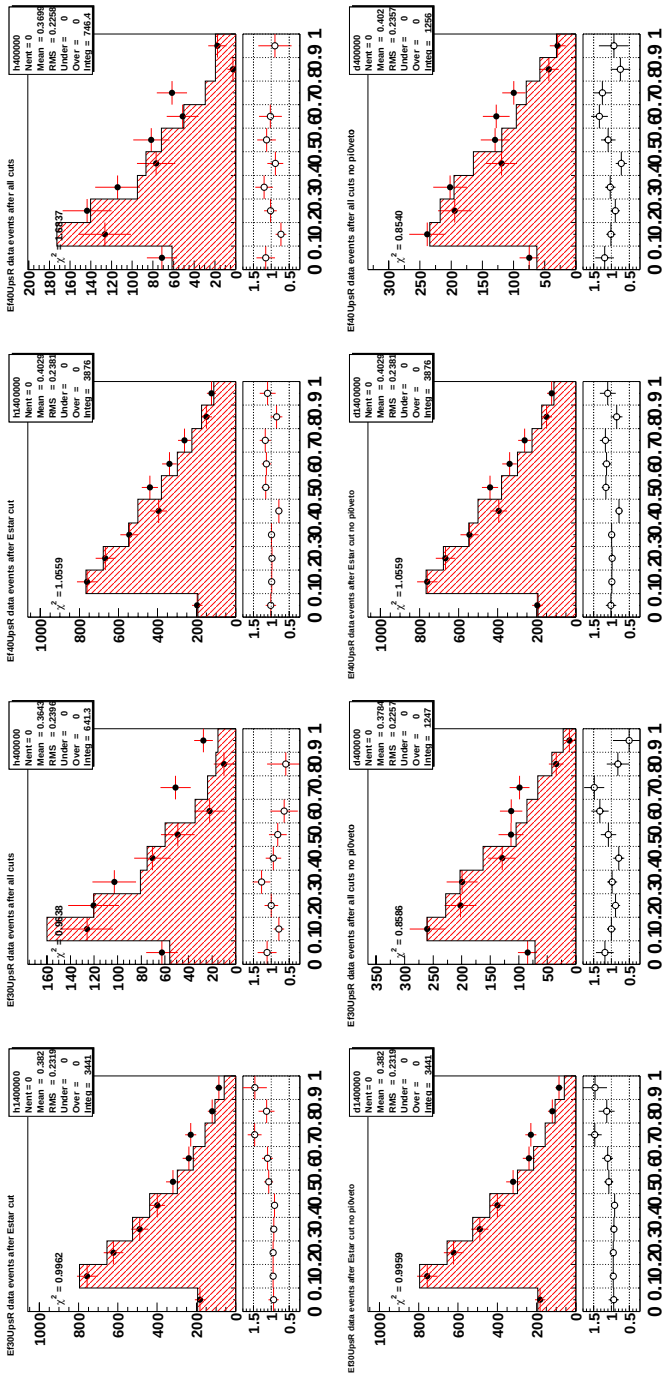

Figure A-10. *Data-MonteCarlo agreement (side-bands subtracted) for signal sample (top row) and anti-Veto sample(bottom row). The first and second column display the $E_{f,30}^{\Upsilon(4S)R}$ spectrum (before any cuts and after all cuts), the third and fourth display the $E_{f,40}^{\Upsilon(4S)R}$ spectrum(before any cuts and after all cuts). The χ^2 gives the probability of consistency of the histograms as obtained from a χ^2 test.*

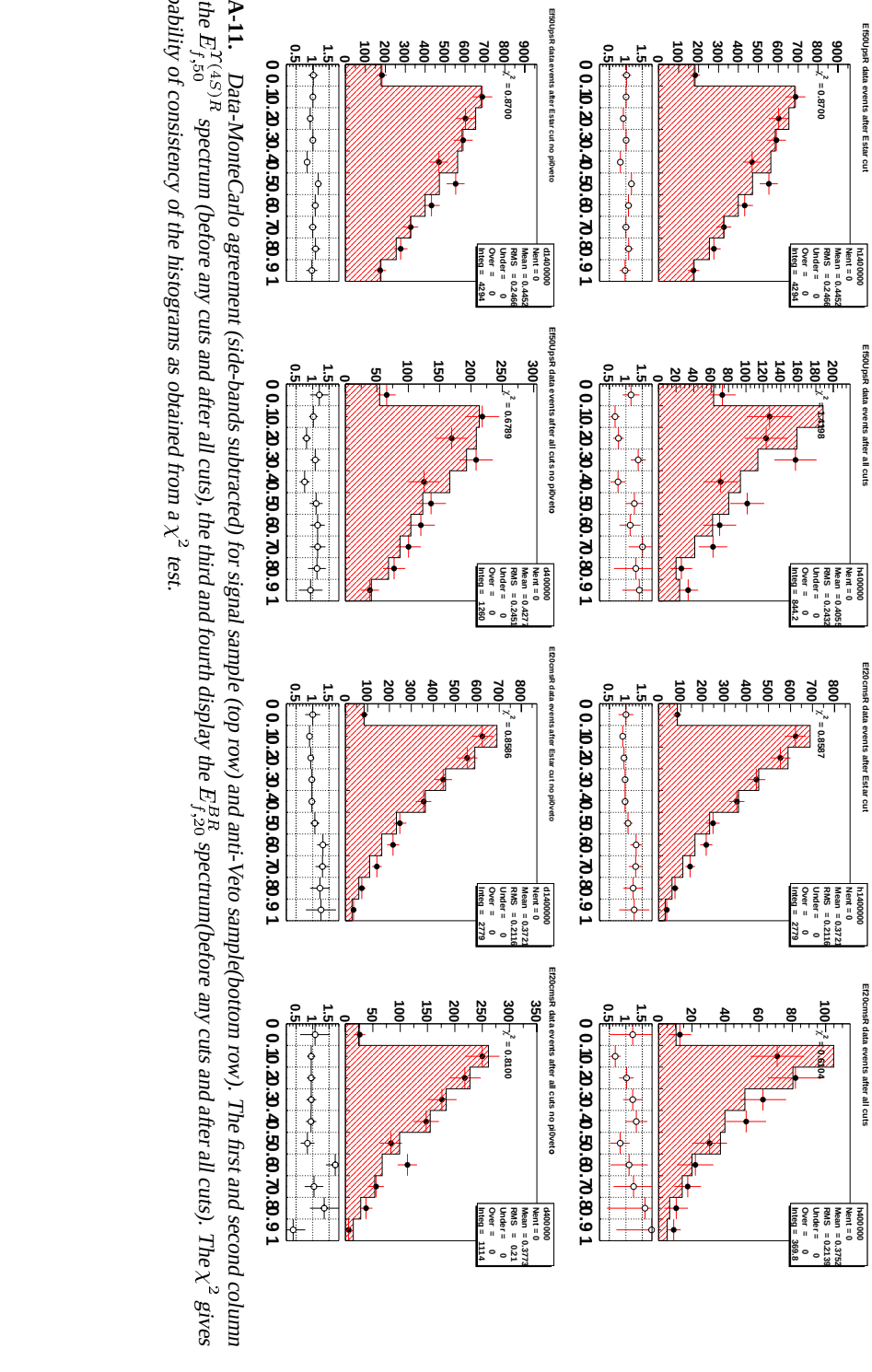

Figure A-11. *Data-MonteCarlo agreement (side-bands subtracted) for signal sample (top row) and anti-Veto sample(bottom row). The first and second column display the $E^{\Upsilon(4S)R}_{f,50}$ spectrum (before any cuts and after all cuts), the third and fourth display the $E^{BR}_{f,20}$ spectrum(before any cuts and after all cuts). The χ^2 gives the probability of consistency of the histograms as obtained from a χ^2 test.*

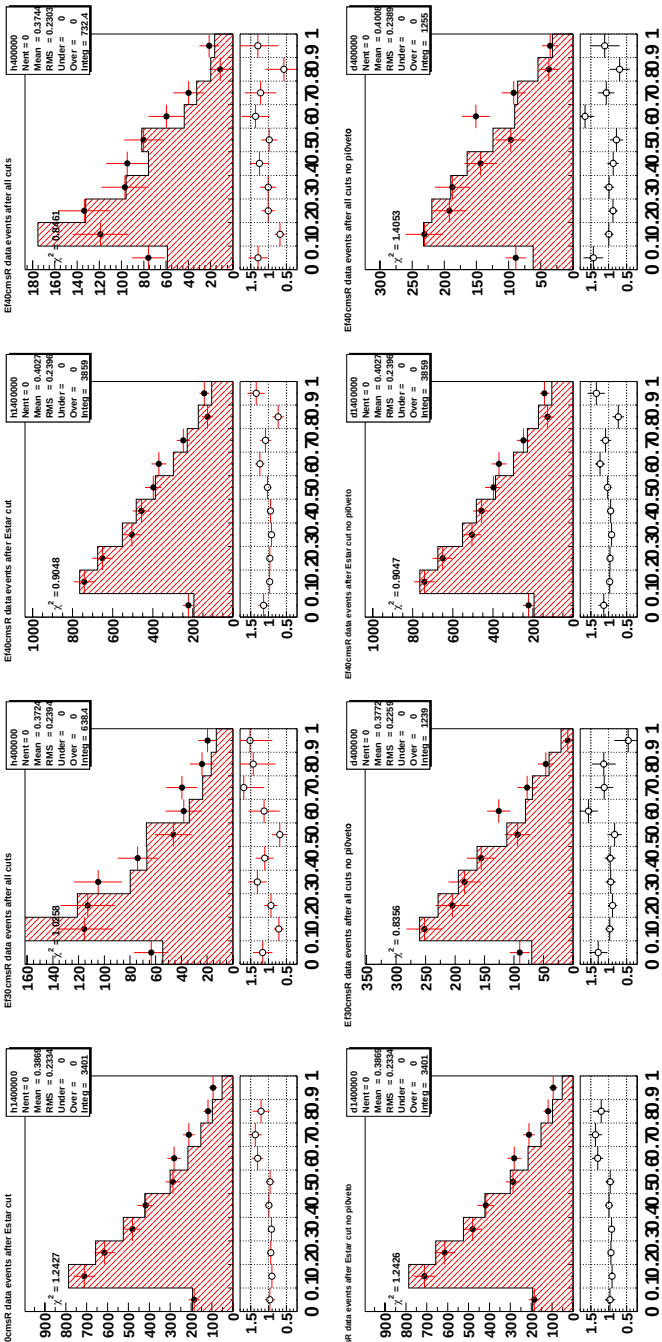

Figure A-12. *Data-MonteCarlo agreement (side-bands subtracted) for signal sample (top row) and anti-Veto sample(bottom row). The first and second column display the $E^{BR}_{f,30}$ spectrum (before any cuts and after all cuts), the third and fourth display the $E^{BR}_{f,40}$ spectrum(before any cuts and after all cuts). The χ^2 gives the probability of consistency of the histograms as obtained from a χ^2 test.*

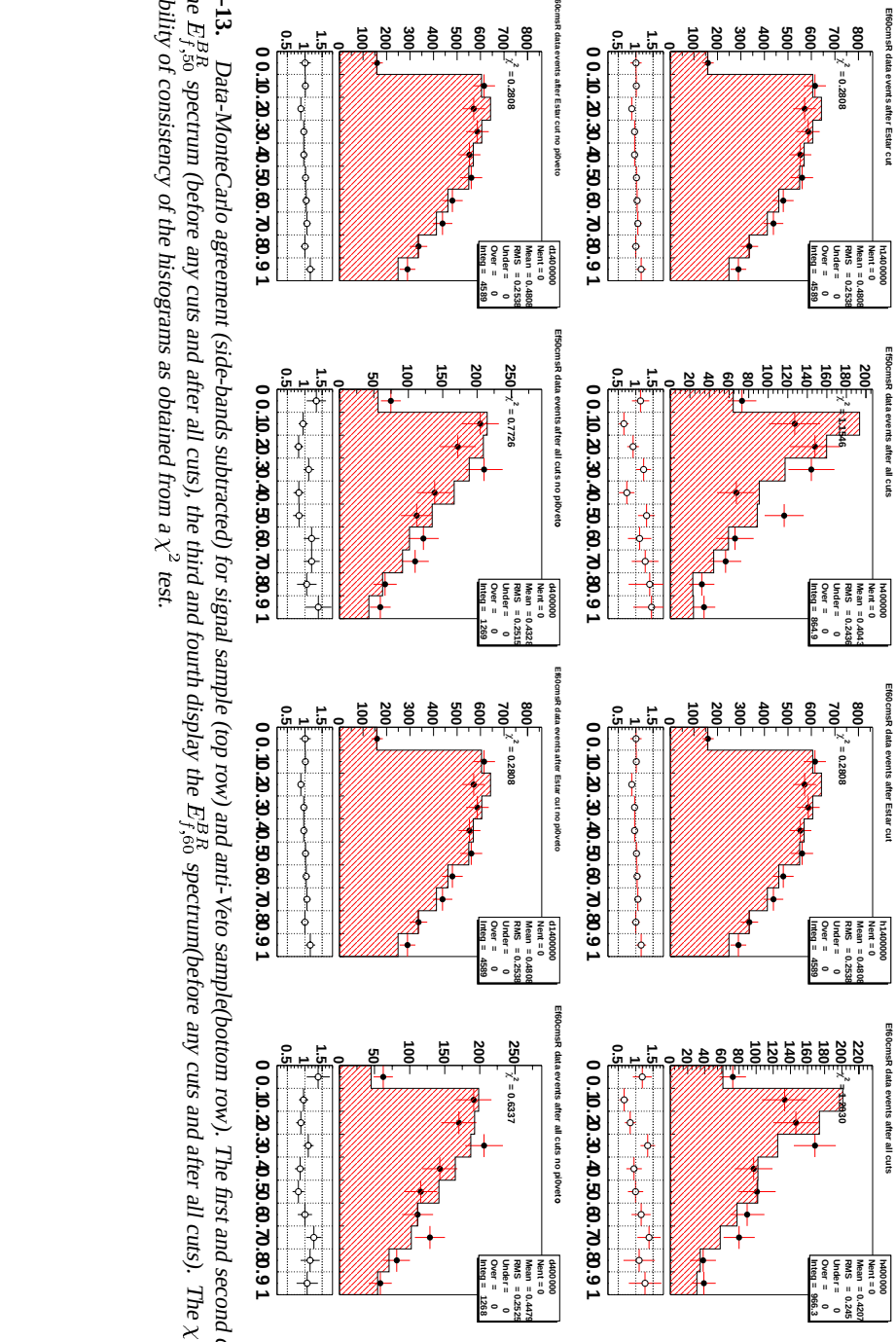

Figure A-13. *Data-MonteCarlo agreement (side-bands subtracted) for signal sample (top row) and anti-Veto sample(bottom row). The first and second column display the $E^{BR}_{f,50}$ spectrum (before any cuts and after all cuts), the third and fourth display the $E^{BR}_{f,60}$ spectrum(before any cuts and after all cuts). The χ^2 gives the probability of consistency of the histograms as obtained from a χ^2 test.*

Bibliography

[1] S.L. Glashow, Nucl. Phys. **22** (1961) 579;
S. Weinberg, Phys. Rev. Lett. **19** (1967) 1264;
A. Salam, in *Proc. 8th Nobel Symp.*, ed. N. Swartholm,
Almquist and Wiksells, Stockholm (1968).

[2] P. W. Higgs, Phys. Lett. **12**, 132 (1964).

[3] N. Cabibbo, Phys. Rev. Lett. **10** (1963) 531.

[4] M. Kobayashi and T. Maskawa, Prog. Th. Phys. **49** (1973) 652.

[5] L. Wolfenstein, Phys. Rev. Lett. **51** (1983) 1945.

[6] A. J. Buras, M. E. Lautenbacher and G. Ostermaier, Phys. Rev. D **50**, 3433 (1994) [arXiv:hep-ph/9403384].A. J. Buras, M.E. Lautenbacher and G. Ostermaier, *Phys. Rev.* **D50** (1994) 3433.

[7] I. I. Bigi, M. A. Shifman and N. Uraltsev, Ann. Rev. Nucl. Part. Sci. **47**, 591 (1997).

[8] I. I. Bigi and N. Uraltsev, Int. J. Mod. Phys. A **16**, 5201 (2001) [hep-ph/0106346];
M. A. Shifman, hep-ph/0009131.

[9] K. Wilson, Phys. Rev. **179**, 1499 (1969); D **3**, 1818 (1971).

[10] W. Zimmermann, Ann. Phys. **77**, 536 and 570 (1973).

[11] N. Isgur, M. B. Wise, Phys. Lett. B **232**, 113 (1989).

[12] A. F. Falk, [hep-ph/9610363], (1996).

[13] A. F. Falk, [hep-ph/0202092], (2002).

[14] M. Neubert, Nucl. Phys. B Proc. Suppl. **59**, 101 (1997).

[15] J. Chay, H. Georgi and B. Grinstein, Phys. Lett. B **247**, 399 (1990).

[16] T. Mannel and M. Neubert, *Phys. Rev.* **D50**, 2037 (1994).

[17] M. Neubert, *Phys. Rev.* **D49**, 3392 and 4623 (1994).

[18] I. I. Bigi, M. A. Shifman, N. G. Uraltsev and A. I. Vainshtein, Int. J. Mod. Phys. **A9**, 2467 (1994);
I. I. Bigi, M. A. Shifman, N. G. Uraltsev and A. I. Vainshtein, Phys. Lett. B **328**, 431 (1994).

[19] E. C. Poggio, H. R. Quinn and S. Weinberg, *Phys. Rev.* **D13**, 1958 (1976).

[20] I. I. Bigi, N. G. Uraltsev and A. I. Vainshtein, Phys. Lett. B **293**, 430 (1992); [Phys. Lett. B **297**, 477(E) (1993)];
I. I. Bigi, M. A. Shifman, N. G. Uraltsev and A. I. Vainshtein, Phys. Rev. Lett. **71**, 496 (1993);
I. I. Bigi *et al.*, Proceedings of the Annual Meeting of the Division of Particles and Fields of the APS, Batavia, Illinois, (1992), edited by C. Albright *et al.*, World Scientific, Singapore (1993), p. 610.

[21] B. Blok, L. Koyrakh, M. A. Shifman and A.I. Vainshtein, *Phys. Rev.* **D49**, 3356 (1994); [*Phys. Rev.* **D50**, 3572(E) (1994)].

[22] A. F. Falk and M. Neubert, *Phys. Rev.* **D47**, 2965 and 2982 (1993).

[23] A.V. Manohar and M. B. Wise, *Phys. Rev.* **D49**, 1310 (1994).

[24] A. Ali and I. Pietarinen, Nucl. Phys. B **154**, 519 (1979).

[25] C. H. Jin, W. F. Palmer and E. A. Paschos, Phys. Lett. B **329**, 364 (1994);
A. Bareiss and E. A. Paschos, Nucl. Phys. B **327**, 353 (1989).

[26] A. J. Buras, M. Misiak, [hep-ph/0207131], (2002).

[27] S. Bertolini, F. Borzumati and A. Masiero, Phys. Rev. Lett. **59** (1987) 180.

[28] N.G. Deshpande *et al.*, Phys. Rev. Lett. **59** (1987) 183.

[29] M. Misiak, Nucl. Phys. B **393**, 23 (1993) [Erratum-ibid. B **439**, 461 (1993)].

[30] C. Greub, T. Hurth and D. Wyler, Phys. Rev. D **54**, 3350 (1996) [hep-ph/9603404].

[31] K. Adel and Y. Yao, Phys. Rev. D **49**, 4945 (1994) [hep-ph/9308349].

[32] K. Chetyrkin, M. Misiak and M. Munz, Phys. Lett. B **400**, 206

[33] C. Greub and T. Hurth, Nucl. Phys. Proc. Suppl. **74**, 247 (1999) [hep-ph/9809468].

[34] A.L. Kagan and M. Neubert, Eur. Phys. J. C **7**, 5 (1999) [hep-ph/9805303].

[35] P. Gambino and M. Misiak, Nucl. Phys. B **611**, 338 (2001) [hep-ph/0104034].

[36] A. Ali and C. Greub, Z. Phys. C **49**, 431 (1991); Phys. Lett. B **361**, 146 (1995) [hep-ph/9506374].

[37] A. Ali and E. Pietarinen, Nucl. Phys. B **154**, 519 (1979).

[38] T. E. Coan *et al.* [CLEO Collaboration], hep-ex/0010075.

[39] K. Abe *et al.* [BELLE Collaboration], BELLE-CONF-0239.

[40] T. E. Coan *et al.* [CLEO Collaboration], Phys. Rev. Lett. **84**, 5283 (2000) [hep-ex/9912057].

[41] B. Aubert *et al.* [BABAR Collaboration], Phys. Rev. Lett. **88**, 101805 (2002) [hep-ex/0110065].

[42] K. Abe *et al.* [BELLE Collaboration], [hep-ex/0308038].

[43] A. L. Kagan and M. Neubert, Phys. Rev. D **58**, 094012 (1998) [hep-ph/9803368].

[44] *BABAR* Collaboration, B. Aubert *et al.*,, Phys. Rev. Lett. **8**8 101805 2002.

[45] A. Eisner, T. Pulliam, B. Schumm, T. Colberg, K. Schubert, S. Playfer, F. DiLodovico, V. Koptchev, S. Willocq, C. Jessop & H. Tanaka, "Measurement of $\mathcal{B}(B \to K^*\gamma)$ and Search for Direct CP-violation", *BABAR* Analysis Document # 33.

[46] Tilman Colberg, University of Dresden, "Measurement of the Decay Fractions, $\mathcal{B}(B^\pm \to K^{*\pm}(892)\gamma)$, $K^{*+} \to K^+\pi^0$ and $\mathcal{B}(B^0 \to K^{*0}(892)\gamma)$, $K^{*0} \to K^0_S\pi^0$", *BABAR* Analysis Document # 133.

[47] M. S. Alam *et al.* [CLEO Collaboration], Phys. Rev. Lett. **74**, 2885 (1995).

[48] S. Chen *et al.* [CLEO Collaboration], Phys. Rev. Lett. **87**, 251807 (2001) [hep-ex/0108032].

[49] R. Barate *et al.* [ALEPH Collaboration], Phys. Lett B. **429**, 169 (1998).

[50] K. Abe *et al.* [Belle Collaboration], Phys. Lett. B **511**, 151 (2001) [hep-ex/0103042].

[51] B. Aubert *et al.* [BABAR Collaboration], hep-ex/0207076.

[52] B. Aubert *et al.* [BABAR Collaboration], BABAR-CONF-02/025, SLAC-PUB-9308 (2002).

[53] R. Ammar *et al.* [CLEO Collaboration], Phys. Rev. Lett. **71**, 674 (1993).

[54] E. H. Thorndike [Cleo collaboration], hep-ex/0206067.

[55] S. Stone, hep-ph/0112008.

[56] C. Jessop, SLAC-PUB-9610.

[57] B.Aubert *et al.*, [*BABAR* Collaboration], SLAC-PUB-8569, [hep-ex/0105044].

[58] D. del Re *et al.*,, "Semi-exclusive B reconstruction", *BABAR* Analysis Document #271.

[59] C. H. Cheng [BABAR Collaboration], Int. J. Mod. Phys. A **16S1A** , 413 (2001) [arXiv:hep-ex/0011007].

[60] K. Hagiwara *et al.*, the Particle Data Group, *Review of Particle Physics D66*, 010001 (2002).

[61] H. Albrecht *et al.*, The ARGUS Collaboration, Z. Phys. C **4**8 543 1990.

[62] Crystal Ball Collaboration, A study of the radiative cascade transition between the upsilon-prime and upsilon resonances, DESY F31-86-02.

[63] see for istance *BABAR* Analysis Document # #287 "Measurements of $B^0\overline{B}^0$ Mixing Rate using Partially Reconstructed B^0 decays to $D^*l\nu$" and references therein.

[64] S. Brandt, Ch. Peyrou, R. Sosnowski, and A. Wroblewski, Phys. Lett. B **12**, 57 (1964); E. Fahri, Phys. Rev. Lett. **39**, 1587 (1977).

[65] G. C. Fox and S. Wolfram, Nucl. Phys. B **149**, 413 (1979).

[66] D.M. Asner *et al.* [CLEO Collaboration], Phys. Rev. D **53**, 1039-1050 (1996) [hep-ex/9508004].

[67] R. A. Fisher, Annals of Eugenics 7 (1936) 179; M. S. Srivastava and E. M. Carter, North Holland, Amsterdam (1983).

[68] The Neutrals Analysis Working group "Study of π^0 Reconstruction Efficiency in Run I Data Using $\tau\tau$ 1-on-1 Decays", *BABAR* Analysis Document # 196.

[69] The Neutrals Analysis Working group "Comparison between Monte Carlo and Data of the π^0 detection and reconstruction efficiency using τ 1-on-1 decays", *BABAR* Analysis Document # 378.

[70] Neutrals Analysis Working Group, "π^0 reconstruction in Run I", *BABAR* Analysis Document # 20.

[71] F. DiLodovico *et al.*,, "Study of $b \to s\gamma$ using the sum of exclusive modes", *BABAR* Analysis Document # 220.

[72] GEANT 3.15: R.Brun *et al.*, Report No. CERN DD/EE/84-1.

[73] T.Sjöstrand, *Comput. Phys. Commun.* **82**, 74 (1994); T.Sjöstra nd and M.Bengston *ibid.* **43**, 367 (1987); T.Sjöstrand, *ibid.* **39**, 347 (1986).

[74] P.Billoir, *Nucl.Instr.Methods* , A225 (1984) 225

[75] T. Brandt, "Likelihood Based Electron Identification", *BABAR* Analysis Documents #396 (2002).

[76] B.N. Ratcliff, SLAC-PUB-5946 (1992); B. N. Ratcliff, SLAC-PUB-6067 (1993); P. Coyle *et al*, *Nucl.Instr.Methods* , A343 (19 94) 292.